UNIVERSITY OF CALIFORNIA SAN DIEGO

Responses of the Southern Ocean in a Changing Climate

A dissertation submitted in partial satisfaction of the
requirements for the degree
Doctor of Philosophy

in

Oceanography

by

Jia-Rui Shi

Committee in charge:

Professor Lynne D. Talley, Co-Chair
Professor Shang-Ping Xie, Co-Chair
Professor Ian Eisenman
Professor Sarah T. Gille
Professor Jan Kleissl

2021

The dissertation of Jia-Rui Shi is approved, and it is acceptable in quality and form for publication on microfilm and electronically.

University of California San Diego

2021

TABLE OF CONTENTS

LIST OF FIGURES

LIST OF TABLES

ACKNOWLEDGEMENTS

I would like to thank my PhD advisors, Lynne and Shang-Ping, for giving me the opportunity and constant support to explore my interests. I would like to acknowledge my committee members, Dr. Sarah Gille, Dr. Ian Eisenman, and Dr. Jan Kleissl, for their advice and feedback on this dissertation. I would also like to thank Dr. Young-Oh Kwon, Dr. Susan Wijffels, and Dr. Amala Mahadevan at WHOI, for their advice and help during this special time.

I'm grateful for my parents, who constantly supporting and encouraging me. Thanks to Dr. Yue Wu and my son Ryan. I would not have made it through this process without you.

Chapter 2, in full, is a reprint of the material as it appears in *Journal of Climate*, 2018: Jia-Rui Shi, Shang-Ping Xie, and Lynne D. Talley, "Evolving Relative Importance of the Southern Ocean and North Atlantic in Anthropogenic Ocean Heat Uptake". The dissertation author was the primary investigator and author of this paper.

Chapter 3, in full, is a reprint of the material as it appears in *Journal of Climate*, 2020: Jia-Rui Shi, Lynne D. Talley, Shang-Ping Xie, Wei Liu, and Sarah T. Gille, "Effects of Buoyancy and Wind Forcing on Southern Ocean Climate Change". The dissertation author was the primary investigator and author of this paper.

Chapter 4, in full, has been submitted for publication of the material as it may appear in *Nature Climate Change*: Jia-Rui Shi, Lynne D. Talley, Shang-Ping Xie, Qihua Peng, Wei Liu, "Acceleration of the Southern Ocean Zonal Flow" (2021). The dissertation author was the primary investigator and author of this paper.

Chapter 5, in part, is a draft in preparation for submission for publication as “Spatial Pattern of the Southern Ocean Subsurface Warming: The Role of Ocean Jets”, by J.-R. Shi, S.-P. Xie, and L. D. Talley. The dissertation author was the primary investigator and author of this material.

VITA

2012	B.Eng. in Ocean Engineering, Shanghai Jiao Tong University
2015	M.Eng. in Ocean Engineering, Shanghai Jiao Tong University
2017	M.S. in Oceanography Scripps Institution of Oceanography, University of California, San Diego
2021	Ph.D., in Oceanography Scripps Institution of Oceanography, University of California, San Diego

PUBLICATIONS

Shi, J.-R., S.-P. Xie, and L. D. Talley, 2018: Evolving Relative Importance of the Southern Ocean and North Atlantic in Anthropogenic Ocean Heat Uptake. *J. Clim.*, **31**, 7459–7479.

Shi, J.-R., L. D. Talley, S.-P. Xie, W. Liu, and S. T. Gille, 2020: Effects of Buoyancy and Wind Forcing on Southern Ocean Climate Change. *J. Clim.*, **33**, 10003–10020.

Shi, J.-R., L. D. Talley, S.-P. Xie, Q. Peng, and W. Liu. Acceleration of the Southern Ocean Zonal Flow. Submitted.

ABSTRACT OF THE DISSERTATION

Responses of the Southern Ocean in a Changing Climate

by

Jia-Rui Shi

Doctor of Philosophy in Oceanography

University of California San Diego, 2021

Professor Lynne D. Talley, Co-Chair
Professor Shang-Ping Xie, Co-Chair

Based on Argo float observations, ocean heat content increase has mostly occurred in the Southern Ocean to the north of the Antarctic Circumpolar Current (ACC) over the past 15 years. In contrast, the upwelling of the pristine water dampens the warming within the ACC, creating an uneven warming in the Southern Ocean. In this dissertation, we utilize modern observational data sets and state-of-the-art climate model simulations to investigate the responses of the Southern Ocean in a changing climate.

We show that the equatorward displacement of maximum subsurface warming relative to maximum heat uptake is associated with mean overturning circulation from the zonal mean perspective. Using idealized model experiments, we decompose the Southern Ocean climate change driven by buoyancy forcing and wind stress change, respectively. We find that the ocean subsurface temperature and salinity change primarily stems from buoyancy forcing change instead of wind change. The subsurface warming pattern due to overturning circulation increases the meridional density gradient and enhances zonal geostrophic velocity in the upper layer. Therefore, we find a significant acceleration of the Southern Ocean zonal flow driven by the buoyancy forcing change. Based on observations, we also document a robust acceleration of Southern Ocean zonal flow at latitudes 48˚S-58˚S since 1993 (satellite altimetry) and since 2005 (Argo floats), supporting the attribution of the ACC acceleration to the greenhouse warming. Moreover, the spatial pattern of Southern Ocean subsurface warming is found to be anchored by the mean ocean jets based on model simulations. For regional responses, jet-scale overturning circulation straddling the strong ocean jets, such as Subantarctic Front and Agulhas Return Current, facilitates the warming on the equatorward, downwelling flank and suppresses the warming on the poleward, upwelling flank.

The research presented in this dissertation improves understanding of the physical processes controlling the Southern Ocean climate change and contributes to reliable future projections.

Chapter 1

Introduction

Making up 71% of the planet, the ocean is an important component of the climate system through its energy, mechanical, and gaseous exchanges with the atmosphere. The ocean plays a central role in mitigating climate change by absorbing large proportions of heat and carbon that are associated with human activities. The Fifth Assessment Report published by the Intergovernmental Panel on Climate Change (IPCC) in 2013 showed that the ocean has stored 93% of Earth's energy imbalance mainly caused by greenhouse gas (GHG) emissions over 1971-2010 (Rhein et al. 2013), manifested as a significant increase of ocean heat content (OHC). Hence, as a buffer to climate change, the world ocean slows the rate of global surface warming (von Schuckmann et al. 2016; Exarchou et al. 2015), remarkably.

Among all the ocean basins, the Southern Ocean south of 30°S dominates the ocean heat uptake (Roemmich et al. 2015; Frölicher et al. 2015; Shi et al. 2018), defined as the change of net surface heat flux, and stored a large amount of anthropogenic heat since the 1950s based on observations (Gille 2002, 2008) because of its unique geometry and circulation pattern, although it only occupies 30% of the global surface ocean area. The unique geometry manifests as the unblocked channel, the Drake Passage, which extends from the southern tip of South America (56˚S) to the northern tip of Palmer Peninsula in West Antarctica (62˚S) (Toggweiler and Samuels 1995). The Antarctic Circumpolar Current (ACC), composed of multiple jets, flows through the Drake Passage from west to east, providing connections among the world's major ocean basins.

Besides the property exchange in the horizontal direction, the steeply sloping isopycnals (surfaces of constant density) in geostrophic balance with the strong eastward flow of the ACC facilitates exchange between the deeper and upper layers of the ocean. The tilted isopycnals also provide potential energy feeding the vigorous eddy field (Rintoul 2018). The strong westerly wind is a primary driver of the upwelling of water masses in the Southern Ocean. The water masses at the outcrop regions interact with the atmosphere, moderating the warming of the surface south of the ACC, and then push equatorward due to Ekman transport. Therefore, improving our understanding of the unique features of the Southern Ocean is vital to interpreting past climate change, such as surface heat uptake, changes in ocean temperature, salinity, and the large-scale ocean circulation, thus enhancing the projections of future climate change.

Human GHG and aerosol emissions have given rise to a substantial anthropogenic climate change on a global scale over the past century (Myhre et al. 2013; von Schuckmann et al. 2016). As one example, the land and ocean surface temperature warms by 0.85˚C (0.65-1.06˚C) calculated by a linear trend over the period 1880 to 2012 (IPCC 2013). The historical effective radiative forcing (ERF) is estimated to be between -1.9 and -0.1 W/m^2 over the period 1750-2011 for anthropogenic aerosols (AAs), and between 2.6 and 3.2 W/m^2 for GHGs (Boucher et al. 2013). Besides the difference in the magnitude of their ERF, GHGs and AAs also have a very different spatial distribution. Due to their short atmospheric residence time and localized sources, AAs are mainly distributed in the Northern Hemisphere (NH), while GHGs are globally well mixed. Furthermore, AA forcing, represented as Aerosol Optical Depth (AOD), shows a distinct time evolution due to the history of industrial development and associated emission regulation (e.g. Shi et al. 2018; Deser et al. 2020). Anthropogenic ozone change is another radiative forcing agent responsible for regional climate change, especially surface climate around Antarctica associated

with Antarctic stratospheric ozone depletion (Thompson et al. 2011; Waugh et al. 2013). The global and regional responses to these fundamental drivers of historical climate change are widely discussed in previous literature through theoretical considerations and various kinds of modeling studies, including the responses of sea surface temperature (Xie et al. 2010, 2013; Wang et al. 2016a), precipitation (Held and Soden 2006; Zhang et al. 2007), and winds (Swart and Fyfe 2012; Lee and Feldstein 2013).

The Southern Ocean absorbs 75% of global ocean heat uptake based on phase 5 of the Coupled Model Intercomparison Project (CMIP5) historical runs including all of the anthropogenic and natural radiative forcings (Frölicher et al. 2015). The dominance of the Southern Ocean in heat uptake is strongly linked with wind-driven upwelling of pristine deep water, which delays warming at the surface, then carries heat content anomaly equatorward via the meridional overturning circulation (MOC), and makes the outcropping regions available to keep absorbing a great amount of excess heat from the atmosphere (Bryan et al. 1988; Manabe et al. 1990; Morrison et al. 2013, 2016; Armour et al. 2016; Liu et al. 2018; Shi et al. 2020). Another reason why the Southern Ocean absorbed significant quantities of heat from the atmosphere during the historical periods is that the Northern Hemisphere (NH) heat gain due to GHGs is largely compensated by the effect of AAs, leaving small heat uptake in the subpolar North Atlantic (Shi et al. 2018). Ocean circulation change is found to play a central role here: the weakening of the Atlantic Meridional Overturning Circulation (AMOC) in response to GHG radiative forcing leads to lower SST in the subpolar North Atlantic, and results in less heat loss from the ocean to the atmosphere. In contrast, a strengthening AMOC in response to aerosol forcing increases SSTs in the North Atlantic, resulting in more heat loss from the ocean. In the future scenarios, the Southern Ocean is projected to remain an important reservoir of anthropogenic heat; however, the role of

the North Atlantic will rise dramatically due to the expected decrease of aerosol emissions due to anticipated pollution controls. These results and associated physical processes are discussed in Chapter 2.

Besides the aforementioned radiative effect of the GHG or AA emissions, changes in surface wind stress can also change the ocean state, mechanically. For instance, based on model simulations, the poleward-intensification of Southern Hemisphere (SH) zonal wind forced by both stratospheric ozone depletion (Gillett 2003) and anthropogenic GHG emissions (Fyfe and Saenko 2006) results in an increase of the Southern Ocean mean flow MOC, which, however, is partially compensated by an increase in the eddy MOC (Gent 2016). The respective effects of buoyancy and wind (momentum) forcing on transient climate change in the Southern Ocean should be explored to help us understand the observed long-term change. Using partial-coupling model simulations (Liu et al. 2018), we found that the buoyancy forcing change accounts for 80% of total heat storage change and also dominates the upper layer freshening in the Southern Ocean (Shi et al. 2020). Wind stress change offsets this surface freshening by a strong wind-driven upwelling of saline waters in the MOC. Moreover, we found that buoyancy forcing change leads to an increase in baroclinic transport within the ACC due to an increase in the cross-stream density gradient, whereas wind stress change creates a more barotropic increase in circumpolar transport. These results and related physical processes are discussed in Chapter 3.

Coming back to observations, a complex set of changes has taken place in the Southern Ocean over the past several decades. The extratropical SH (20˚-60˚S) contributes 67%-98% of global upper 2000 m ocean heat content change, peaking at around 40˚S-45˚S, during the Argo era since 2006 (Roemmich et al. 2015). The deep ocean (≥ 2000 m) in the Southern Ocean has shown significant heat storage change in the past serval years, accounting for approximately 19% of total

excess heat (Purkey and Johnson 2010; Talley et al. 2016). Broadscale freshening was observed in the Southern Ocean based on Argo floats and other hydrographic data (Durack and Wijffels 2010; Swart et al. 2018), consistent with more net precipitation over the higher latitudes (wet-get-wetter mechanism; Durack et al. 2012). Moreover, only a minimal change was reported in ACC transport during recent decades despite strengthening winds (Boning et al., 2008), based on analyses of Argo profiling float and historical oceanographic data; an eddy saturation mechanism that limits ACC transport has been hypothesized (Munday et al. 2013). Similarly, a large number of previous publications focused on the effect of wind change on Southern Ocean climate change. However, with an additional decade of Argo and satellite altimeter data, we show that the zonal flow in the Southern Ocean has significantly accelerated within 48˚-58˚S since 1993, tightly linked with external buoyancy forcing changes. More evidence from observations and the comparisons between various model simulations and observations is shown in Chapter 4.

Since many previous studies and the contents in Chapters 3 and 4 are largely based on global zonal averaging, it is important to further understand the spatial patterns and regional responses in the Southern Ocean. For instance, the Southern Ocean excess heat is stored in different regions and layers of the basins (e.g. Sallée 2018). In contrast with the maximum OHC increase that occurred around 40˚S-45˚S in the global zonal mean (Roemmich et al. 2015; Armour et al. 2016; Swart et al. 2018), the actual maximum ocean warming extends from around 35˚S in the Atlantic sector to 55˚S in the Pacific sector, spanning 20˚ in latitude (2200 kilometers). This suggests that the physical mechanisms hypothesized for the zonally-averaged framework might only partially account for the regional responses. In Chapter 5, we show that the position of maximum OHC change is north of the ACC and highly correlated with the position of the zonal jet, according to results from a long list of CMIP5 and CMIP6 models. The jet-scale overturning

circulation (JSOC; Li and Lee 2017) can be a factor affecting the regional subsurface warming pattern since the destratification (decrease of vertical density gradient) in the downward branch of JSOC promotes the subduction of excess heat to the north of the jets. In addition, the warming spots around the western boundary currents suggest that the intensified southward advection of warm water also contributes to the regional warming pattern. We confirm again that wind change plays only a secondary role compared with buoyancy forcing change in determining the magnitude and pattern of Southern Ocean temperature change based on idealized simulations. The role of bathymetry in affecting the Southern Ocean subsurface warming pattern via stirring of the surface jets is also discussed in Chapter 5 by using a set of flat-bottom model simulations.

Chapter 2

Evolving Relative Importance of the Southern Ocean and North Atlantic in Anthropogenic Ocean Heat Uptake

2.1 Abstract

Ocean uptake of anthropogenic heat over the past 15 years has mostly occurred in the Southern Ocean, based on Argo float observations. This agrees with historical simulations from the Coupled Model Intercomparison Project phase 5 (CMIP5), where the Southern Ocean (south of 30˚S) accounts for 72%±28% of global heat uptake, while the contribution from the North Atlantic north of 30˚N is only 6%. Aerosols preferentially cool the Northern Hemisphere, and the effect on surface heat flux over the subpolar North Atlantic opposes the greenhouse gas (GHG) effect in nearly equal magnitude. This heat uptake compensation is associated with weakening (strengthening) of the Atlantic Meridional Overturning Circulation (AMOC) in response to GHG (aerosol) radiative forcing. Aerosols are projected to decline in the near future, reinforcing the greenhouse effect on the North Atlantic heat uptake. As a result, the Southern Ocean, which will continue to take up anthropogenic heat largely through the mean upwelling of water from depth, will be joined by increased relative contribution from the North Atlantic due to substantial AMOC slowdown in the 21st century. In the RCP8.5 scenario, the percentage contribution to global uptake is projected to decrease to 48%±8% in the Southern Ocean and increase to 26%±6% in the northern

North Atlantic. Despite the large uncertainty in the magnitude of projected aerosol forcing, our results suggest that anthropogenic aerosols, given their geographic distributions and temporal trajectories, strongly influence the high latitude ocean heat uptake and interhemispheric asymmetry through AMOC change.

2.2 Introduction

More than 90% of Earth's energy imbalance (EEI), mainly caused by the greenhouse gases (GHGs) emissions from industrial development, is stored in the ocean (Rhein et al. 2013; Trenberth et al. 2014). Increases in global ocean heat content (OHC) are robustly detected in both observations and model simulations (Levitus et al. 2012; Rhein et al. 2013; Roemmich et al. 2015; Riser et al. 2016; Liu et al. 2016; Cheng et al. 2016, 2017; Gleckler et al. 2016), illustrating the ocean's dominant role in slowing the rate of surface warming (von Schuckmann et al. 2016; Exarchou et al. 2015). The excess heat, defined as the change in heat content since pre-industrial time, enters the ocean through air-sea heat flux. The pattern of ocean heat uptake (heat taken up at the surface) is strongly associated with a multitude of complex climate processes, such as the concentration of atmospheric CO_2, aerosols, changing ocean circulation, cloud feedback, and eddies (Morrison et al. 2016).

The Southern Ocean has received much recent attention in the discussion of global heat uptake and heat storage. The dominance of the Southern Ocean in heat uptake is partly associated with wind-driven upwelling of cold deep water (Bryan et al. 1988; Manabe et al. 1990; Morrison and Hogg 2013; Frölicher et al. 2015). The upwelling of pristine deep water delays the Southern Ocean warming at the surface, then takes up a great amount of excess heat from the atmosphere, and then carries the heat content anomaly northward and downward into the thermocline via the

overturning circulation (Morrison et al. 2016; Armour et al. 2016). The enhanced heat uptake in the Southern Ocean has a profound impact on tropical climate change, displacing the intertropical convergence zone (ITCZ) and monsoons (Hwang et al. 2017).

GHGs are the most important radiative forcing that warms the global climate. Much previous work focuses on ocean heat uptake in the Southern Ocean in response to increased CO2 (the most important component in GHGs) (Bryan et al. 1988; Manabe et al. 1990, 1991; Kuhlbrodt and Gregory 2012; Marshall et al. 2015; Armour et al. 2016). For instance, in response to a quadrupling of CO2 in the Coupled Model Intercomparison Project phase 5 (CMIP5), enhanced heat uptake is found in both the Southern Ocean and the northern North Atlantic (Marshall et al. 2015). This suggests that the northern North Atlantic also plays an important role in the ocean uptake of anthropogenic heat. Climatologically, strong heat loss from the ocean to the atmosphere takes place in the subpolar North Atlantic (SPNA), leading to the formation of North Atlantic Deep Water (NADW) (Talley et al. 2011). The deep water formation is part of the Atlantic Meridional Overturning Circulation (AMOC) (Böning et al. 2006) through which the SPNA is tied to the ocean circulation and global heat transport (Robson et al. 2016; Zhang and Yan 2017; Heuzé 2017). An AMOC slowdown in response to the increasing CO2 results from the enhanced stratification of the upper water column due to the increased buoyancy flux into the SPNA (Thorpe et al. 2001; Gregory et al. 2005; Buckley and Marshall 2016). Associated with a weakening AMOC, less excess heat is transported to high northern latitudes, resulting in an SST cooling tendency in the SPNA and increased heat flux into to ocean (Wood et al. 1999; Russell and Rind 1999; Weaver et al. 2007; Kim and An 2013; Rugenstein et al. 2013; Winton et al. 2013; Gregory et al. 2016).

Anthropogenic aerosols are a second major radiative forcing for global climate change. Aerosols and GHGs have opposite effects: while GHGs warm, aerosols cool the earth. The global

historical GHG effective radiative forcing (ERF) is estimated at 2.5±0.4 Wm-2, while the ERF of the historical aerosols is about -1.0±0.4 Wm-2 in 2000 relative to 1850 based on the CMIP5 models (Shindell et al. 2015). Besides the difference in the magnitude of their ERF, GHG and anthropogenic aerosol forcings also show different spatial distributions. Due to their short residence time and localized emissions, anthropogenic aerosols are mainly distributed in the Northern Hemisphere (NH), while GHGs are well-mixed in the atmosphere. The geographically distributed anthropogenic aerosols can lead to cross-equatorial energy transport in both the ocean and atmosphere (Kang and Xie 2014; Acosta Navarro et al. 2017). The inter-hemispheric asymmetric climate responses, such as a southward shift of the intertropical convergence zone (ITCZ) and cross-equatorial wind, are dominated by the inhomogeneous aerosol forcing (Wang et al. 2016a,b).

Anthropogenic ozone change is another important radiative forcing agent responsible for regional climate change. The anthropogenic stratospheric ozone hole over Antarctica has been the focus of extensive Southern Hemisphere climate studies. Antarctic stratospheric ozone depletion has enhanced Southern Hemisphere westerly winds, affecting the surface climate around Antarctica (Thompson et al. 2011; Waugh et al. 2013). Southern Ocean sea surface temperature shows fast and slow responses—rapid cools followed by slow but persistent warming—due to ozone-hole forcing (Marshall et al. 2014; Ferreira et al. 2015). The ozone forcing fields, however, have large variations across the CMIP5 models with either interactive or prescribed ozone (Eyring et al. 2013; Frölicher et al. 2015).

In CMIP5 historical runs that include all of the anthropogenic (i.e., GHGs, aerosols, and ozone) and natural (i.e., solar irradiance and volcanoes) radiative forcings, the Southern Ocean (south of 30˚S) takes up as much as 75% of global oceanic heat gain (Frölicher et al. 2015). Based

on observations, the Southern Ocean has experienced continuous and monotonic long-term warming since around the 1960s (Gille 2002; Cheng et al. 2017). Furthermore, Roemmich et al. (2015) show that the extratropical Southern Hemisphere (20˚S-60˚S) contributes 67 to 98% of global upper ocean (above 2000m) heat content change during the Argo era since 2006. This large fraction of heat uptake in the Southern Ocean contrasts with much smaller ocean heat uptake in the SPNA in both historical simulations and observations, even taking into account the different sizes of the two regions. Could the relative importance of the SPNA and Southern Ocean change in the future as a result of changes in the relative strengths of the anthropogenic forcings?

The present study explores the underlying mechanisms for the long-term change of regional ocean heat uptake. By using the single-forcing simulations of CMIP5, we find that GHG radiative forcing itself is not enough to account for regional pattern of historical ocean heat uptake, especially in the SPNA. Historically, the impact of anthropogenic aerosols, which are mostly confined to the NH, is to nearly completely offset heat uptake due to GHGs in the SPNA. We find that this results from compensation of AMOC change due to GHGs by that due to anthropogenic aerosol forcing. In contrast to this small historical heat uptake in the SPNA, heat uptake is large in the Southern Ocean, where the GHG forcing dominates, somewhat reinforced by ozone forcing, and where aerosol forcing is weak. As anthropogenic aerosol emissions are expected to decrease while GHGs will continue to rise, the relative importance of the SPNA and Southern Ocean in future ocean heat uptake cannot be extrapolated from the historical change. Based on observations, historical period simulations, and future projections, our goal is to show the shifting relative importance of the two regions. We will show that the North Atlantic's role in global ocean heat uptake rises dramatically in the 21st century.

The rest of the paper is organized as follows. Section 2 describes the methods and data used. Section 3 discusses the surface heat flux response patterns under different model simulations over the historical period from 1861 to 2005. Section 4 investigates the patterns of ocean heat uptake in future projections from 2006 to 2100. Section 5 discusses the response of the AMOC to anthropogenic forcing and its impact on regional heat uptake. Section 6 further investigates the effect of anthropogenic aerosol reduction in future projections. Section 7 compares OHC changes between observations and simulations. Section 8 is a summary.

2.3 Data and Methods

2.3.1 Simulations

This study uses outputs of climate model simulations from the World Climate Research Program's CMIP5 (Taylor et al. 2012). We choose nine models that perform all of the following five experiments: GHG single-forcing (GHG), anthropogenic aerosol single-forcing (AERO), historical all-forcing simulations (HIST), and the Representative Concentration Pathway (RCP) RCP4.5 and RCP8.5 scenarios. The numbers of ensemble members for each model and each experiment are listed in Table 2.1. According to the conservation of energy, the heat budget for a particular body of water is (Talley et al. 2011):

$$Q_T = Q_{net} + Q_V \tag{2.1}$$

where QT is the rate of change in heat of the body of water, Qnet is the net surface heat flux, and QV is the advective heat flux by ocean circulation. Qnet is derived by summing turbulent flux (latent and sensible heat flux) and radiative flux (shortwave and longwave radiation) at the surface. In steady state (e.g., prior to the industrialization), $Q_T \approx 0$. With increasing GHGs, ocean takes up and stores the anthropogenic heat. Hereafter, we call changes in Qnet (represented by the

linear trend) the anthropogenic ocean heat uptake (through the surface), and time integration of Qnet relative to the pre-industrial steady state the cumulative heat uptake.

Here, we focus on the changes of Qnet and sea surface temperature (SST) during the historical period (1861-2005) and RCP scenarios (2006-2100). The multimember average for each model is obtained first and then the multi-model ensemble mean is made to reduce internal variability. In GHG (AERO) runs, GHGs (anthropogenic aerosols) are the only time-varying forcing agent, with other forcings fixed at the pre-industrial level. Besides GHG and AERO, we also use the ozone single-forcing runs (OZONE) from three CMIP5 models (Cionni et al. 2011) to investigate the effect of ozone on ocean heat uptake; because there are many fewer ozone ensemble members and because the tradeoff between AERO and GHG forcing dominates the ocean heat uptake, our analysis of ozone effects is not exhaustive, and is mostly included in the supplemental materials. The HIST runs are forced by historical estimates of changes in anthropogenic GHGs and aerosols, natural forcing (volcanoes and isolation), as well as changes in land use (Sheffield et al. 2013).

We also use 38 realizations from the CESM Large Ensemble Project ('LENS'), all of which use the same external forcing and model with small differences in the atmospheric initial condition (Kay et al. 2015). Therefore, the effects of external forcing and internal climate variability can be isolated by analyzing the ensemble mean and deviations, respectively. Historical and RCP8.5 external forcing from 1920 to 2100 (ensemble member 1 starts from 1850) is applied in LENS. We also use a modified RCP8.5 ensemble from CESM with aerosols fixed at their 2005 level ('2005AERO') (Xu et al. 2015) to identify the effect of changing anthropogenic aerosols in future projections. The difference between LENS and 2005AERO (15 realizations) is their aerosol trajectories.

An AMOC index is defined as the maximum volume transport stream function at 30˚N and is calculated for the first-member run (r1i1p1) from each CMIP5 model. The AMOC anomaly, relative to the 1861-1880 average in each model, is used to calculate the multi-model mean of the AMOC change. We also obtain the AMOC anomaly from the ensemble member 1 of LENS and 2005AERO. The AMOC anomaly of LENS is relative to the 1861-1880 mean, and the AMOC anomaly of 2005AERO is relative to the annual-mean of 2006.

Annual anomalies and 11-year running average are calculated for the analysis of air-sea heat flux and the AMOC intensity. We interpolate all model outputs to a regular 1˚x1˚ latitude-longitude grid to facilitate comparison.

2.3.2 Observations

Observed ocean temperature is compared with the simulations to assess their validity. Argo floats have been profiling ocean temperature in the upper 2000m since 2004 (Gould et al. 2004; Roemmich and Gilson 2009). Considering the large coverage gaps in 2004 and 2005 (Roemmich et al. 2015), we use the monthly gridded Argo temperature data (Roemmich and Gilson 2009) from the beginning of 2006. For a longer time series, extending to the deep ocean, we use the optimal interpolated EN4 potential temperature product from the Met Office Hadley Centre, which is available on a 1˚x1˚ grid with 42 vertical levels from the surface to about 5500m during 1900-2016 (Good et al. 2013). The Levitus et al. (2009) and Gouretski and Reseghetti (2010) methods are used to correct the XBT bias in EN4-L09 and EN4-G10 versions, respectively. We also use the monthly mean temperature product from the Institute of Atmospheric Physics (IAP) (Cheng et al. 2016, 2017) from 1940 to 2015 on a regular 1˚x1˚ grid with 41 vertical levels in the upper

2000m. The EN4 and IAP products include shipboard, MBT, XBT, and Argo temperature profiles. Observational data are listed in Table 2.2.

In this study, OHC is calculated by integrating the temperature profile within a certain layer and then multiplying by reference values of density (1025 kgm-3) and specific heat (3985 Jkg-1K-1) of seawater. OHC in different layers (0-300m, 0-700m, 0-2000m or below 2000m) is calculated for each observational dataset (Argo, EN4, and IAP). Subsurface potential temperature from LENS is also used to calculate the OHC and compare with observations. To suppress high-frequency noise, we apply a 5-year running average to the time series of the observed and LENS OHC. The time evolution of OHC is relative to the climatology from 1975 to 2012. Empirical orthogonal function (EOF) analysis is applied to the 0-2000m OHC in the northern North Atlantic (north of 30˚N) of IAP data from 1950 to 2015. A similar EOF analysis is applied to EN4-G10 from 1950 to 2016. A 5-year running average is applied before EOF analysis. The principal components are normalized by their respective standard deviations.

2.4 Historical responses to anthropogenic forcing

2.4.1 Ocean heat uptake

The CMIP5 multimodel ensemble mean net surface heat flux (Qnet) trends for the historical period (1861-2005) are shown in Figure 2.1. Positive (negative) trends indicate that the ocean is being heated (cooled). In HIST runs (Figure 2.1c), the Southern Ocean dominates ocean heat uptake. In GHG runs (Figure 2.1a), heat uptake in the northern North Atlantic is greatly intensified, while the Southern Ocean remains similar to HIST. Moreover, the long-term trends of Qnet and SST (Figure 2.2) in the Southern Ocean and SPNA are broadly of opposite sign. That is, where SST cools in the SPNA and is neutral in the high southern latitudes, the Qnet trend is

positive, towards less cooling. Where SST has warmed fastest, in the mid-latitude Gulf Stream, Kuroshio, Brazil, Agulhas Currents, the trend in Qnet is to greater cooling. The change of Qnet is thus damping the SST change in these critical regions, as shown by Armour et al. (2016). This correlation suggests that the air-sea heat flux Qnet is a strong function of the air-sea temperature difference, that that difference is largely due to changes in SST rather than in air temperature, and that the SST changes are due to anomalous advection.

In the GHG runs, the Southern Ocean and the northern North Atlantic are the most active regions that take up the anthropogenic heat (Figure 2.1a). Elsewhere the trend in Qnet is small and not well organized in space. In order to compare the trends in Southern Ocean (SO) and northern North Atlantic (NA) heat uptake poleward of 30° latitude quantitatively, the surface heat flux is integrated over the SO (south of 30˚S) and NA (30˚N-70˚N, 80˚W-10˚W). The time evolution of heat flux for each experiment referenced to the 1861-1880 average is shown in Figure 2.3. For the SO over the 20th century, the long-term heat flux trend from HIST runs (black) is 0.128 PW/century, which is close to the result from GHG runs (red, 0.178 PW/century). HIST runs capture the cooling effects of volcanic aerosols following volcano eruptions (Agung in 1963, El Chichon in 1982, and Pinatubo in 1991) (Ding et al. 2014; Smith et al. 2016), which are not included in the GHG or AERO runs. In contrast with the SO, for the NA, heat uptake is large in GHG (0.091 PW/century) but is small (0.030 PW/century) in HIST, which includes all radiative forcings.

The time series of cumulative heat uptake since 1861 (not shown) is similar to the time series of heat uptake. In HIST runs during the 20th century, the global ocean takes up 263±102 ZJ and the SO takes up 190±81 ZJ, accounting for 72%±28% of global ocean heat uptake, consistent with Frölicher et al (2015). During the same period, the NA takes up 16±82 ZJ, contributing only

6% of global heat uptake. The ratio of cumulative heat uptake between SO and NA is 11.8±13.9. Thus, the Southern Ocean dominates ocean heat uptake in the historical period. In GHG runs, the global ocean takes up 570±152 ZJ, which double the global ocean heat uptake in the HIST runs. The SO maintains about the same level of heat uptake (255±94 ZJ), while the NA takes up 137±41 ZJ accounting for 24%±11% of global cumulative ocean heat uptake. The NA heat uptake in GHG runs increases by around 7.5 times relative to HIST runs. The discrepancy of regional cumulative heat uptake between HIST and GHG indicates the influence of factors other than GHG.

2.4.2 Compensation between GHG and anthropogenic aerosols

Anthropogenic aerosols are an important radiative forcing that cools the global climate (Forster et al. 2007). The global map of long-term trend of Qnet due to the anthropogenic aerosol radiative forcing (AERO) is shown in Figure 2.1b. The geographically distributed anthropogenic aerosols cause enhanced SST cooling (Figure 2.2b) with more heat loss in the NH (Figure 2.1b) than the Southern Hemisphere (SH). The intensive heat loss takes place in the NA rather than the North Pacific even though aerosols are prevalent throughout the NH. This is primarily due to the greater sensitivity of the SPNA, where the mean mixed layers are about 10 times deeper than in the North Pacific (Holte et al. 2017). The Qnet trend pattern in AERO runs broadly opposes that in GHG runs (Figure 2.1a,b). The compensation between GHGs and aerosols is remarkable in the SPNA. This compensation is also clear in the zonally integrated trend in Qnet from the CMIP5 ensemble mean (Figure 2.4). The cross-correlation in the zonally integrated pattern is -0.60 between AERO and GHG runs, illustrating an overall similarity in the responses of ocean heat uptake to GHG and aerosol forcings (Xie et al. 2013, 2015). There is a linear relationship between regional ocean heat uptake and global radiative forcing shown in Figure A1. We sum the Qnet

trends from GHG and AERO runs (defined as GHG+AERO), denoted by the brown curve (Figure 2.4). The cross-correlation in meridional pattern between GHG+AERO and HIST is very high (0.95), indicating that oceanic heat uptake is forced to first order by GHGs and anthropogenic aerosols. It also suggests that the sum is a good approximation for the all-forcing simulations.

Tables 2.3 and 2.4 compare cumulative ocean heat uptake in the SO and NA in total amount and percentage to the global uptake from various runs. The SO to NA ratio of uptake is about 2:1 for GHG (warming), 1:2.6 for AERO (cooling) and 12:1 in the HIST (warming). The dominant SO uptake in HIST is a result of compensating NA uptake in response to GHG (137 ZJ) and AERO (-134 ZJ). The results from GHG+AERO and HIST are particularly close, implying that the historical response of heat uptake is mainly due to the combination of GHG and aerosol radiative forcing. Therefore we hypothesize that the impact of anthropogenic aerosols on ocean heat uptake accounts for much of the discrepancy between the HIST and GHG runs.

Other forcing agents, such as ozone, may also affect the pattern and magnitude of ocean heat uptake. The zonally integrated Qnet trend of ozone runs (OZONE) is represented by the green curve (the ensemble mean of 3 CMIP5 models) in Figure A2. Here the result represents the effect of ozone concentration from both stratosphere and troposphere. The global average response of Qnet trend is smaller in the single forcing OZONE runs than in GHG and AERO runs. The Southern Ocean, however, shows marked heat uptake: enhanced westerly wind stress in the Southern Ocean due to stratospheric ozone depletion (Thompson et al. 2011; Ferreira et al. 2015) causes enhanced equatorward Ekman transport and hence this heat uptake. Furthermore, we find that the Qnet trend is smaller in ozone runs than that in GHG and AERO runs in the mid-latitudes of the NH. We also sum the Qnet trends from GHG, AERO, and OZONE runs (defined as GHG+AERO+OZONE) (Figure A2). We note an offset between HIST and

GHG+AERO+OZONE, which may result from the nonlinear effect of forcing agents when prescribed together, but could instead be due to the small number of CMIP5 ozone single-forcing experiments.

2.5 Future projections

The global aerosol optical depth (AOD) and CO2 concentrations used for the historical (HIST) and future projection (RCP8.5) runs of GFDL-CM3 over the 20th and 21st century are shown in Figure 2.5. Anthropogenic aerosol forcing, represented by AOD, in CMIP5 historical simulations increases rapidly over the 20th century due to industrial development. It peaks at the beginning of the 21st century, and then is projected to decline during the RCP scenarios as countries begin to restrict aerosols out of the need to improve air quality and protect human health (Westervelt et al. 2015; Rotstayn et al. 2013). Unlike aerosols, GHGs including CO2 are projected to increase steadily. Thus, aerosol forcing offsets the warming effect of GHGs to some extent over the historical period; its reduction amplifies the GHG warming relative to the historical period in future projections (Xie et al. 2015).

The Qnet trends projected until 2050 in the RCP4.5 and RCP8.5 scenarios are shown in Figure 2.6. The zonally integrated patterns of Qnet trend (Figure 6c) differ markedly from HIST (Figure 2.4) in the NH extratropics. The biggest difference is that heat uptake is projected to greatly intensify in the northern North Atlantic (Figure 2.6a,b compared with Figure 2.1c). Comparison of the time series of NA and SO ocean heat uptake over the period from 1900 to 2100 (Figure 2.7a) shows a rapid increase in heat uptake takes place in the NA (solid curves) at the beginning of the 21st century, while the SO heat uptake continues its historical rise. Given the steady rise of CO2 concentration, this rapid increase in NA uptake is associated with the change of anthropogenic

aerosol forcing. With anthropogenic aerosol emissions declining in future projections, the NA heat uptake increases to the same order of magnitude as the SO heat uptake (Figure 2.7a), despite its much smaller area. In the future, more and more excess heat is projected to be stored in the ocean through the North Atlantic.

Heat flux trends in the SO and NA in various runs and their ensemble means are shown in Figure 2.7b, separated according to single forcing GHG and AERO runs, as well as the HIST and projected RCP4.5 and RCP8.5 runs. The relative trends in the SO vs. the NA for the GHG and AERO are shown by the straight line fits. These straight lines envelop the future scenarios (RCP4.5 & RCP8.5) despite the large spread across models, which implies that GHG and AERO remain the dominant forcings in the future projections. According to Tables 2.3 and 2.4, from 2006 to 2100, the percentage of global heat uptake contributed by the SO decreases to 52%±9% (48%±8%) for the RCP4.5 (RCP8.5). The contribution of the NA increases to 28%±7% for the RCP4.5 and 26%±6% for the RCP8.5. The SO and NA ratio of cumulative heat uptake is about 2:1, which is much smaller than that during the historical period (12:1). That is, the relative importance of the SO and NA in anthropogenic heat uptake evolves due to the very different trajectories of GHGs (increasing) and anthropogenic aerosols (decreasing).

2.6 AMOC responses to anthropogenic forcing

The long-term mean (1960-2005) meridional overturning stream function is illustrated in Figure 2.8, for the Atlantic Ocean north of 30˚S and for the Southern Ocean south of 30°S, based here on the first realization of the LENS. The Atlantic Meridional Overturning Circulation (AMOC) index is defined as the maximum stream function at 30˚N. The multi-model ensemble mean change in AMOC intensity, relative to the average over 1861-1880 in each model, is shown

in Figure 2.9. The AMOC has almost no trend (-0.03 Sv/decade), only decadal variability, in the HIST runs covering the 20th century. In contrast, the GHG and AERO runs weakened (-0.21 Sv/decade) and strengthened (0.19 Sv/decade) the AMOC, respectively, hence nearly compensating each other, as seen above for North Atlantic heat uptake (Delworth and Dixon 2006). The robustness of this result is apparent in the eight CMIP5 models that are averaged in Figure 2.9, six of which similarly show only a small AMOC trend, both positive and negative (-0.1< AMOC trend <0.1 Sv/decade), in their HIST runs, despite large variation (from ~10Sv to ~30Sv) in the mean AMOC intensity among models (Figure A3). Thus, even though the global GHG radiative forcing is larger than the aerosol forcing in magnitude (about 2:1 ~ 3:1), their impacts on AMOC strength are comparable.

In future projections, with continuing increase in GHG but decrease in aerosol forcing, the AMOC slows down dramatically in RCP4.5 (-0.42 Sv/decade from 2006 to 2050) and RCP8.5 (-0.67 Sv/decade from 2006 to 2100) (Figure 2.9). These trends are much larger than the trend in the historical period, because the GHGs are not compensated by aerosols.

The rapid slowdown of the AMOC in RCP4.5 and RCP8.5 is consistent with the rapid increase of the NA heat uptake (Figure 2.7a), suggesting influence of ocean circulation on the regional ocean heat uptake. When the climate warms due to GHG increase, surface temperature increases and salinity decreases (not shown, but due to increased precipitation and sea ice melt), which together decrease the upper ocean density. This strengthens the stratification and hence weakens deep convection and the AMOC intensity. When the AMOC slows, poleward heat transport diminishes over the North Atlantic, resulting in a cooling tendency in SPNA SST (Winton et al. 2013; Marshall et al. 2015; Drijfhout et al. 2012; Buckley and Marshall 2016). The decreasing SPNA SST is associated with intensified surface heat flux into the ocean (Rugenstein

et al. 2013; Winton et al. 2013; Gregory et al. 2016). When more excess heat is absorbed by the SPNA, with increasing precipitation and sea ice melt, surface water in the SPNA becomes even less dense, increasing the stability of the water column and further weakening the AMOC (Delworth and Dixon 2006; Cheng et al. 2013; Menary et al. 2013). Thus there is a positive feedback between the SPNA surface heat flux and the AMOC intensity. Therefore it appears that the enhanced SPNA heat uptake is strongly tied to the change of ocean circulation, in particular, the AMOC. The processes that govern heat uptake changes in the SO under anthropogenic forcings are entirely different, primarily affected by the climatological currents (Marshall et al. 2015; Morrison et al. 2016; Liu et al. 2018).

2.7 Effect of anthropogenic aerosol reduction in future projections

To further investigate the effect of projected declining aerosols on regional heat uptake, we use two experiments from CESM: LENS and AERO2005 (section 2.1). The differences between the responses from 2005AERO, which fixes aerosols at the 2005 level, and RCP8.5 of LENS, which projects a decline in aerosols, reveal the effect of the reduced aerosols and their precursors (such as SO2 and NO2) in future projections. The long-term trends (2006-2100) of Qnet and SST from LENS, 2005AERO and the difference between them are shown in Figure 2.10. For both LENS and 2005AERO, Qnet trend features an intense, positive heat uptake change in the NA (Figure 2.10a,b). Ocean heat uptake is locally enhanced where SST warming (contours) is reduced, illustrating that surface heat flux is mainly driven by the ocean on multidecadal timescale (Gulev et al. 2013). For 2005AERO, the increased heat uptake is primarily attributed to continued GHG increase. Subtracting the Qnet response in 2005AERO runs from that in LENS (Figure 2.10c), we

find a remarkable positive trend in the SPNA, while changes are negligible elsewhere. Thus, the intensified heat uptake in the SPNA in LENS is partly attributed to the aerosol reduction.

Area-integrated heat uptake and cumulative heat uptake are calculated to quantify the contribution of the declining aerosols (Figure 2.11). From 2006 to 2100, the NA heat flux trend is 0.428 PW/century in RCP8.5 of LENS, while only 0.287 PW/century in 2005AERO (Figure 2.11a). Despite the dominance of GHGs in radiative forcing in RCP8.5, one-third of that heat flux trend in the NA is due to the declining anthropogenic aerosols because the aerosol forcing is mostly restricted to the NH. At the end of the 21st century, the heat uptake rate by the NA catches up with that of the SO in RCP8.5.

In the 20th century, the time evolution of cumulative heat uptake of LENS shows small changes in the NA (3±21 ZJ) but a remarkable increase in the SO (190±11 ZJ) (Figure 2.11b), consistent with the CMIP5 results (Table 2.3). The large standard deviation in the NA shows that internal variability is an important factor affecting the regional heat uptake. In RCP8.5 of LENS, at the end of the 21st century, the cumulative heat uptake change in the NA (712±22 ZJ) is comparable to that in the SO (964±13 ZJ). In 2005AERO, the cumulative heat uptake in the NA decreases to 503±17 ZJ. The reduced aerosols account for 29% of cumulative heat uptake in the NA in RCP8.5. In addition, the global ocean heat uptake decreases by 15% if aerosol emissions are fixed at 2005-levels. We can further deduce that with a weaker GHG forcing than RCP8.5 (such as RCP2.6), the relative contribution of the declining anthropogenic aerosols to heat uptake will become larger.

Moreover, in 2005AERO with aerosol fixed instead of declining from 2006 to 2100, the AMOC slows down by -0.53 Sv/decade, less than half of the result from the LENS, in which aerosols decline (-1.23 Sv/decade) (Figure 2.11c). This shows that the declining anthropogenic

aerosols permit more rapid slowdown of the AMOC (Menary et al. 2013) and result in enhanced heat uptake in the NA in the future.

2.8 Comparison with observations of ocean heat content

For comparison with observations, we primarily use ocean heat content (OHC) rather than Qnet because OHC is based on subsurface temperature profiles which are measured with high accuracy, while surface heat fluxes are indirectly calculated and suffer from large uncertainties in algorithm (Valdivieso et al. 2017). OHC change is determined by Qnet globally while the differences between OHC and Qnet trend patterns are due to ocean circulation. Note that our purpose is not to analyze the ocean heat budget, which is closed in the models, but rather to assess the model representation of ocean heat.

The spatially integrated, regional OHC changes in the upper 2000m in the North Atlantic (NA) north of 30°N and Southern Ocean (SO) south of 30°S are shown in Figure 2.12, based on observations (Argo, IAP, EN4-L09, and EN4-G10) and simulations (LENS). In the NA, the observed OHC trend is relatively flat from 1960 to 1996, followed by a sharp rise afterward in all data sets, and then a decrease since 2006. In the SO, OHC features a robust rise after 1960. The contrast in OHC change between the NA and SO is consistent with the change of cumulative heat uptake obtained from the aforementioned simulations.

External forcing and internal variability as well as natural forcing affect the decadal-to-multi-decadal climate change (Hansen et al. 2011). For instance, Terray (2012) concludes that the anthropogenic forcings account for the warming trend in the North Atlantic SST over the last three decades, while the internal variability is very strong in the SPNA, contributing to the multi-decadal SST swings. Here we focus on how the external forcing and internal variability affect the OHC

change in the NA. In order to isolate the contributions of forced and internal variability, we apply an EOF analysis to the OHC integrated over the upper 2000m in the NA. The first two modes based on the IAP data are shown in Figure 2.13. The leading mode explains about 43% of the total variance, with a dipole pattern between the subpolar and subtropical North Atlantic. The leading principal component (PC1) shows two major phase shifts during 1950-2015 (Figure 2.13c), which is synchronized with the North Atlantic Oscillation (NAO) index from NOAA (https://www.ncdc.noaa.gov/teleconnections/nao/). The Atlantic multidecadal Oscillation (AMO) index from NOAA (https://www.esrl.noaa.gov/psd/data/timeseries/AMO/) is also shown in Figure 2.13b. The cross-correlation between PC1 and NAO is 0.77, suggesting that the first mode of atmospheric circulation significantly affects the OHC change in the North Atlantic north of 30°N (McCarthy et al. 2015; Delworth et al. 2017). The cooling of the SPNA and the warming of the subtropical gyre is associated with the positive phase of NAO (Lozier et al. 2008; Zhang and Yan 2017). Specifically, the enhanced westerlies in the SPNA during positive NAO drive increased heat loss (Duchez et al. 2016; Robson et al. 2016). The second principal component (PC2), which explains about 28% of the variance, is nearly constant from 1960 to 1996, followed by a rapid rise. EOF2 features enhanced warming along the Gulf Stream and a cooling in the SPNA, resembling the trend of the ensemble mean of LENS (Figure 2.15b). Therefore, EOF2 seems to reflect the response to external radiative forcing. PC2 suggests that the northern North Atlantic has become more active in anthropogenic heat uptake during the most recent two decades. We have also applied the EOF analysis to the OHC of EN4-G10 (Figure A4). The spatial patterns and PCs are similar to those of the IAP product.

Based on the second mode of the EOF analysis (Figure 2.13d), we select two 37-year periods for the OHC change comparison: 1) 1960-1996, when PC2 is relatively flat; 2) 1979-2015,

which includes a rapid increase of OHC and the NAO effect is nearly averaged out based on Figure 2.13c. The comparison of the OHC trend between IAP data and the LENS ensemble mean for the first period, 1960-1996 is shown in Figure 2.14. The pattern of LENS ensemble mean behaves as a reference here, representing the external forcing effects on OHC change. There is broad agreement in the Southern Ocean where the zonally integrated heat gain from both IAP data and LENS shows a pronounced trend (Figure 2.14c,d). The upper 2000m of the SO accounts for about 74% (103%) of global heat storage change in IAP data (the ensemble mean of LENS). During this period, major differences between the observations and simulation are found in the North Atlantic. This is due to the internal multidecadal variability, captured in the observed EOF1 (Figure 2.13c), which overwhelms the external forcing signal. For the second period of 1979-2015 (Figure 2.15), in the NA, the external forcing signal increases rapidly (Figure 2.13d), leading to a different spatial pattern, which is similar to the pattern of LENS ensemble mean (Figure 2.15b). The relative importance of the SO in global heat content change decreases to 39% and 51% in IAP data and LENS, respectively (Figure 2.15c,d). Thus we show that the external forcing signal is stronger and detectable in recent decades. In addition, IAP data show much more tropical warming relative to the LENS ensemble, which seems to be related to internal variability. The largest discrepancies of OHC change between IAP and EN4 data are found in the Southern Ocean from 1960 to 1996 (compare Figure 2.14c and Figure A5c), which is probably due to sparse observations over the period (Wang et al. 2017).

In future projections (RCP8.5 from 2015 to 2100), the North Atlantic and Arctic show remarkable increases in heat storage (Figure 2.16a). During this period, the Southern Ocean only explains about 32% of global OHC change. This is comparable to the percentage of global anthropogenic heat absorbed by the whole Atlantic north of 30˚S (24%). Although the Southern

Ocean OHC trend increases in recent decades (Figure 2.17a), the percentage of the Southern Ocean to global OHC change decreases (Figure 2.17b).

Heat transport due to ocean circulation (as represented by Figure 2.7) can strongly affect the heat storage pattern (Winton et al. 2013; Frölicher et al. 2015; Tamsitt et al. 2016), and are responsible for the discrepancies between the ocean heat storage and uptake patterns in the same regions (Frölicher et al. 2015; Armour et al. 2016). First of all, the SO peak is at 55˚S in the heat uptake pattern (Figure 2.4) but around 42~45 ˚S in heat content change pattern (Figure 2.14c,d). The displacement is primarily due to advection by the equatorward Ekman transport (Tamsitt et al. 2016; Armour et al. 2016). The smaller percentage of the SO to global OHC change (32%) than the values in cumulative heat uptake shown in Table 2.4 may also be attributed to ocean adjustment. Furthermore, the much smoother OHC trend (Figure 2.15d) with a nearly uniform increase in the top 300m layer is most likely due to ocean ventilation. More work is needed to investigate the response of ocean heat uptake and storage to ocean circulation in a two-dimensional (latitude-longitude space) or three-dimensional (latitude-longitude-depth space) sense.

2.9 Summary

The Southern Ocean accounts for 72%±28% of global heat uptake in historical runs during the 20th century in the CMIP5 ensemble. We have shown that the Southern Ocean's historical dominance relative to the same latitude range of the North Atlantic is due to the compensating effects of anthropogenic aerosol cooling and GHG warming on the surface heat flux for the first order over the North Atlantic and AMOC intensity. In GHG single-forcing simulations for the historical period, the Southern Ocean's contribution to global uptake is much smaller at 45%±10%, with a large contribution from the northern North Atlantic (24%±11%). Anthropogenic aerosols

preferentially cool the NH, causing a large heat loss in the northern North Atlantic that opposes the GHG heating. The compensating aerosol effect is small over the Southern Ocean, and therefore this region dominates the historical global anthropogenic heat uptake, which is driven mainly by GHGs with a much smaller contribution from ozone (Figure A2).

This pattern of historical heat uptake cannot be extrapolated into the future, however, as anthropogenic aerosols are projected to decrease due to environmental regulation. In future projections, the Southern Ocean continues to absorb heat at an increasing rate, but the North Atlantic greatly increases its heat uptake due to the projected reduction in aerosol forcing. The consequence is that the Southern Ocean's percent contribution to global heat uptake decreases to about 50% while the northern North Atlantic uptake increases to about 27%. Using simulations from CESM, we show that the anticipated reduction in anthropogenic aerosols causes surface heat uptake to increase by about 30% in the northern North Atlantic and about 15% globally. The varying relative importance between the Southern Ocean and North Atlantic heat uptake between historical and future periods is determined by the different spatial distributions and trajectories of GHG and anthropogenic aerosol radiative forcing.

Heat losses (gains) in the SPNA are accompanied by strengthening (weakening) of the AMOC in the AERO (GHG) runs. In the GHG runs, as an example, less heat is advected to the high latitude North Atlantic due to the weakening AMOC intensity (Winton et al. 2013), leading to lower SSTs in the SPNA. This cooler surface water results in less heat loss from the ocean to the atmosphere, increasing the stratification of the upper ocean, which then further weakens the AMOC intensity. This positive feedback between AMOC and North Atlantic heat uptake sustains the weakening of AMOC intensity and intensification of regional heat uptake (Gregory et al. 2016; Buckley and Marshall 2016). This illustrates that ocean circulation change induced by

anthropogenic forcing can strongly affect the pattern of heat uptake in the North Atlantic, while the Southern Ocean heat uptake is primarily driven by background ocean circulation (Marshall et al. 2015; Morrison et al. 2016; Liu et al. 2018). For instance, Liu et al. (2018) demonstrates that the background ocean circulation accounts for about 80% of Southern Ocean heat storage change, while the remaining 20% is due to wind-induced ocean circulation change.

It is likely that, in the late 20th century, the lack of a significant observed decreasing trend in the AMOC, despite an increase in global ocean heat uptake, is due to the strongly moderating influence of anthropogenic aerosols, which preferentially affect the North Atlantic. The recent observations of the AMOC intensity from the RAPID array (Cunningham et al. 2007) at 26.5˚N show that the AMOC has weakened substantially over the past decade since 2004, consistent with from model simulations. However, the observed magnitude of the decreasing trend (about -0.5 Sv/yr) from 2004 to 2012 (Smeed et al. 2014; Roberts et al. 2014) is much larger than that projected to occur in the 21st century (about -0.1 Sv/yr; Cheng et al. 2013). The internal AMOC variability seems to be responsible for the observed slowdown of the AMOC over the past decade, but the anthropogenic forcing effect cannot be ruled out (Smeed et al. 2014; Jackson et al. 2016). At least one decade of continuous observations is required to diagnose the influence of the external climate forcing on the AMOC (Roberts et al. 2014). Such observations will also test the projected increase in anthropogenic heat uptake in the subpolar North Atlantic.

GHG radiative forcing by itself fails to explain the pattern of historical ocean heat uptake change. Our study reveals the important role of anthropogenic aerosols relative to greenhouse gases in regional ocean heat uptake, but the large uncertainty in the magnitude and spatial pattern of anthropogenic aerosol forcing (Myhre et al. 2013; Rotstayn et al. 2015; Hansen et al. 2011) is a barrier to fully quantifying its impact on global and regional climate change. Further studies are

necessary to improve the observation, understanding, and simulation of the complex aerosol effects on climate change. Another useful extension of our work should include quantifying the role of ocean circulation in high latitude heat budgets.

2.10 Acknowledgments

J.-R. Shi is supported by the U.S. National Science Foundation (AGS-1637450) and the Southern Ocean Carbon and Climate Observations and Modeling project (SOCCOM) under National Science Foundation Award (PLR-1425989). We acknowledge the World Climate Research Programme's Working Group on Coupled Modeling, which is responsible for CMIP5, and we thank the climate modeling groups for producing and making available the model output. The CESM LENS and 2005AERO simulations are available on the Earth System Grid (www.earthsystemgrid.org). The Argo data used here were collected and made freely available by the International Argo Program and by the national programs that contribute to it (http://argo.ucsd.edu). IAP product is available on Climate Data Guide (https://climatedataguide.ucar.edu/climate-data/ocean-temperature-analysis-and-heat-content-estimate-institute-atmospheric-physics). EN4 products are available on the Met Office Hadley Centre (https://www.metoffice.gov.uk/hadobs/en4/download-en4-2-0.html).

Chapter 2, in full, is a reprint of the material as it appears in *Journal of Climate*, 2018: Jia-Rui Shi, Shang-Ping Xie, Lynne D. Talley, "Evolving Relative Importance of the Southern Ocean and North Atlantic in Anthropogenic Ocean Heat Uptake". The dissertation author was the primary investigator and author of this paper.

Table 2.1: CMIP5 models used in this study. Numbers shown in columns of Model Experiments give the number of ensemble members used in various simulations: GHG single-forcing runs (GHG), anthropogenic aerosol single-forcing runs (AERO), historical runs (HIST), RCP4.5 and RCP8.5.

Institute	Model	Reference	Model Experiments				
			GHG	AERO	HIST	RCP4.5	RCP8.5
CCCma	CanESM2	von Salzen et al. (2013)	5	5	5	5	5
NCAR	CCSM4	Meehl et al. (2012)	3	3	3	3	3
NSF-DOE-NCAR	CESM1-CAM5	Hurrell et al. (2013)	1	3	3	3	3
CSIRO-QCCCE	CSIRO-Mk3-6-0	Rotstayn et al. (2012)	10	10	10	10	10
NOAA GFDL	GFDL-CM3	Donner et al. (2011)	3	3	3	3	1
NOAA GFDL	GFDL-ESM2M	Dunne et al. (2013)	1	1	1	1	1
NASA GISS	GISS-E2-R	Schmidt et al. (2014)	5	5	5	5	1
IPSL	IPSL-CM5A-LR	Dufresne et al. (2013)	1	1	1	1	1
NCC	NorESM1-M	Iversen et al. (2013)	1	1	1	1	1

Table 2.2: Observed data used in this study. Annual mean is applied to all the observed data.

Observation	Reference	Data	Depth	Period
Argo	Roemmich and Gilson (2009)	Temperature	0-2000m	2006-2016
IAP	Cheng et al. (2016)	Temperature	0-2000m	1940-2015
EN4-G10	Good et al. (2013); Gouretski and Reseghetti (2010)	Potential Temperature	0-5500m	1900-2016
EN4-L09	Good et al. (2013); Levitus et al. (2009)	Potential Temperature	0-5500m	1900-2016

Table 2.3: Cumulative ocean heat uptake (ZJ) in the SO (south of 30˚S), NA (30˚N-70˚N, 80˚W-10˚W) and global ocean simulated by the CMIP5 models. Values in brackets indicate the periods used to calculate the change of ocean heat uptake for different runs. The model uncertainties are estimated as one standard deviation across the models. CSIRO-Mk3-6-0 is excluded in HIST runs due to the negative trend of global cumulative heat uptake.

	GHG (1900-2000)	**AERO** (1900-2000)	**GHG+AERO** (1900-2000)	**HIST** (1900-2000)	**RCP4.5** (2006-2100)	**RCP8.5** (2006-2100)
SO	255±94	-52±62	202±116	190±81	829±145	1187±208
NA	137±41	-134±71	3±62	16±82	443±114	632±115
Global	570±152	-283±153	287±156	263±102	1580±114	2468±179

Table 2.4: The percentage of the SO and NA, defined as in Table 2.3, relative to global ocean cumulative heat uptake simulated by the CMIP5 models. Values in brackets indicate the periods used to calculate the change of ocean heat uptake for different runs. The model uncertainties are estimated as one standard deviation across the models. CSIRO-Mk3-6-0 is excluded in HIST runs due to the negative trend of global cumulative heat uptake.

Percentage	**GHG** (1900-2000)	**AERO** (1900-2000)	**GHG+AERO** (1900-2000)	**HIST** (1900-2000)	**RCP4.5** (2006-2100)	**RCP8.5** (2006-2100)
SO/Global	45%±10%	18%±25%	71%±51%	72%±28%	52%±9%	48%±8%
NA/Global	24%±11%	47%±26%	1%±42%	6%±39%	28%±7%	26%±6%

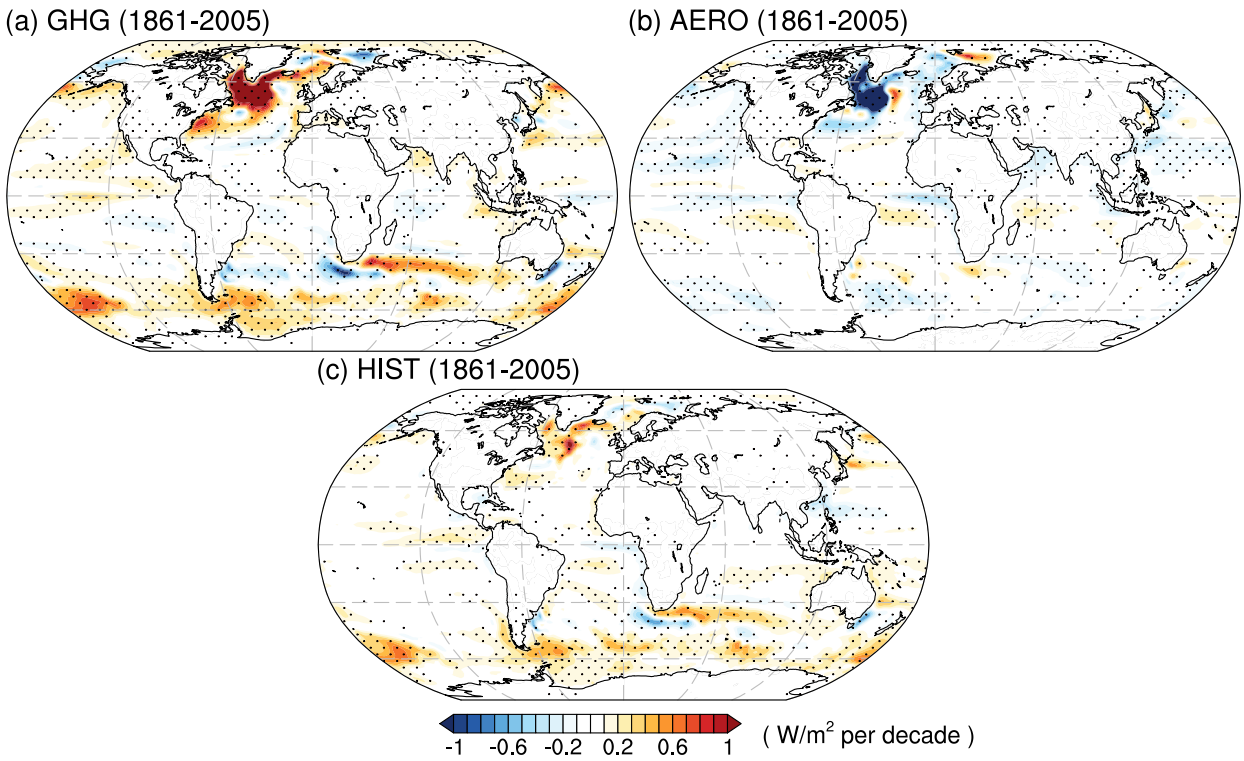

Figure 2.1: Trend of net surface heat flux (Qnet) (in W/m2 per decade) of the ensemble mean of 9 CMIP5 models in (a) GHG runs (1861-2005), (b) AERO runs (1861-2005) and (c) HIST runs (1861-2005). Positive indicates excess heat absorbed by the ocean. Stippling indicates regions exceeding 95% statistical significance computed from the two-tailed t-test.

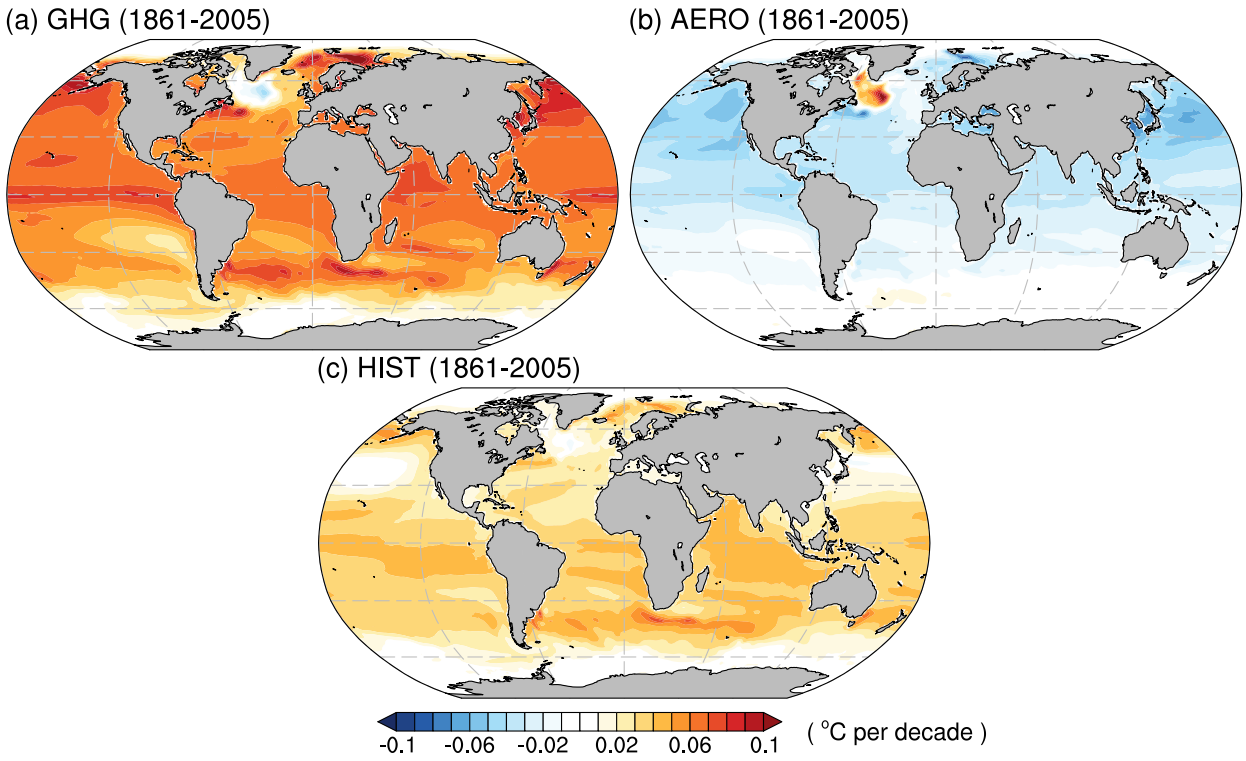

Figure 2.2: Trend of SST (in ˚C per decade) of ensemble mean of 9 CMIP5 models in (a) GHG runs (1861-2005), (b) AERO runs (1861-2005), (c) HIST runs (1861-2005). Positive indicates warming of surface sea water.

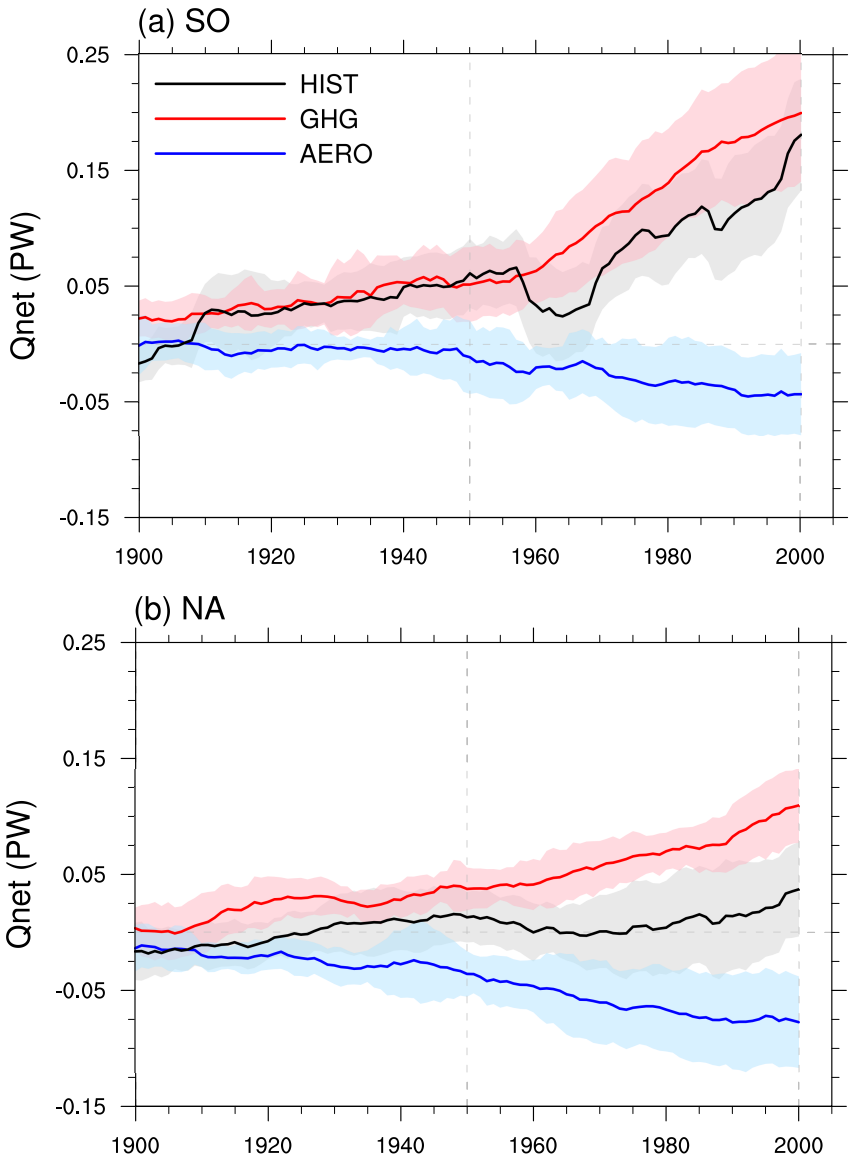

Figure 2.3: Time series of surface heat uptake area-integrated over (a) the SO (Southern Ocean, south of 30˚S) and (b) the NA (North Atlantic, north of 30˚N) in the 20th century from the ensemble mean of CMIP5 models. Different colors show the responses of HIST (black), GHG (red), and AERO (blue) runs. The shadings denote model uncertainties as one standard deviation across models. 11-year running average is applied to the time series.

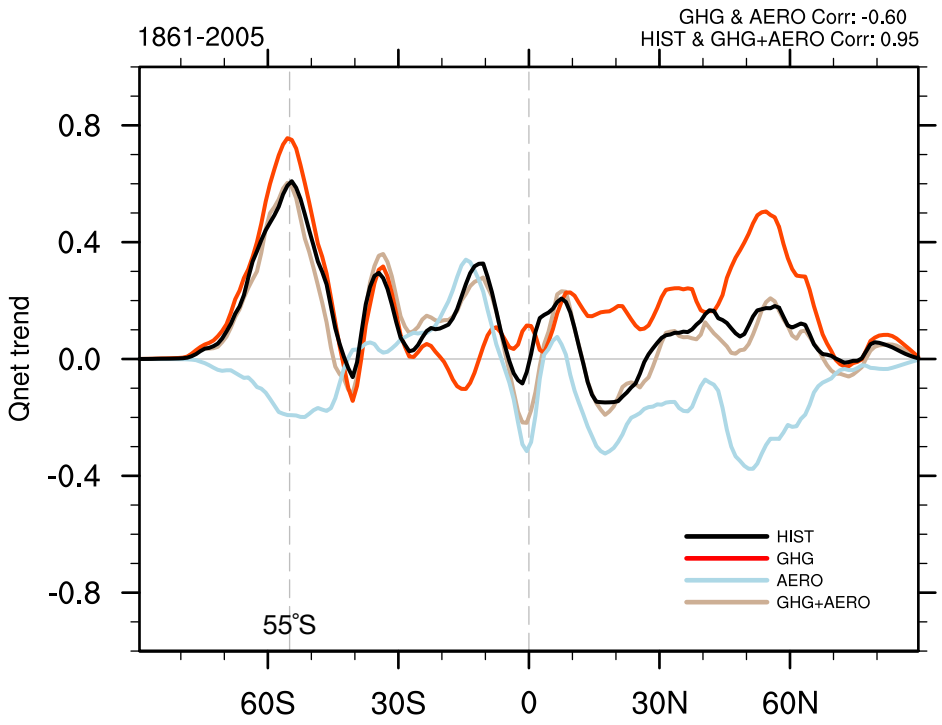

Figure 2.4: Zonally integrated Qnet trend (in TW/lat per decade) in GHG (red), AERO (blue) and HIST (black) runs from 1861 to 2005. The brown curve denotes the linear combination of responses of GHG and AERO (GHG+AERO). The first row at the top right corner indicates the correlation coefficient between heat flux responses of GHG and AERO runs. The second row, same as the first row, but for HIST and GHG+AERO. Positive represents the heat gain of the ocean. Similar calculations using the smaller ensemble of ozone runs are shown in the supplementary material, Figure A2.

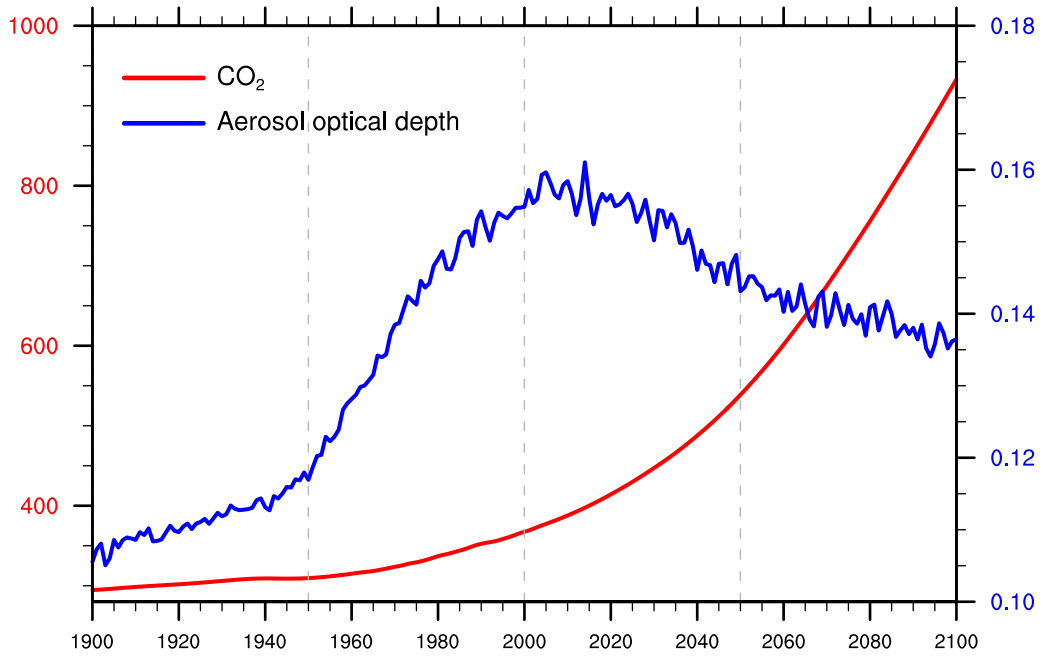

Figure 2.5: Global CO_2 concentration (red curve, ppm) and global mean ambient aerosol optical depth (AOD) at 550nm (blue curve) from 1900 to 2100. Data are from the HIST (1900-2005) and RCP8.5 (2006-2100) runs of GFDL-CM3.

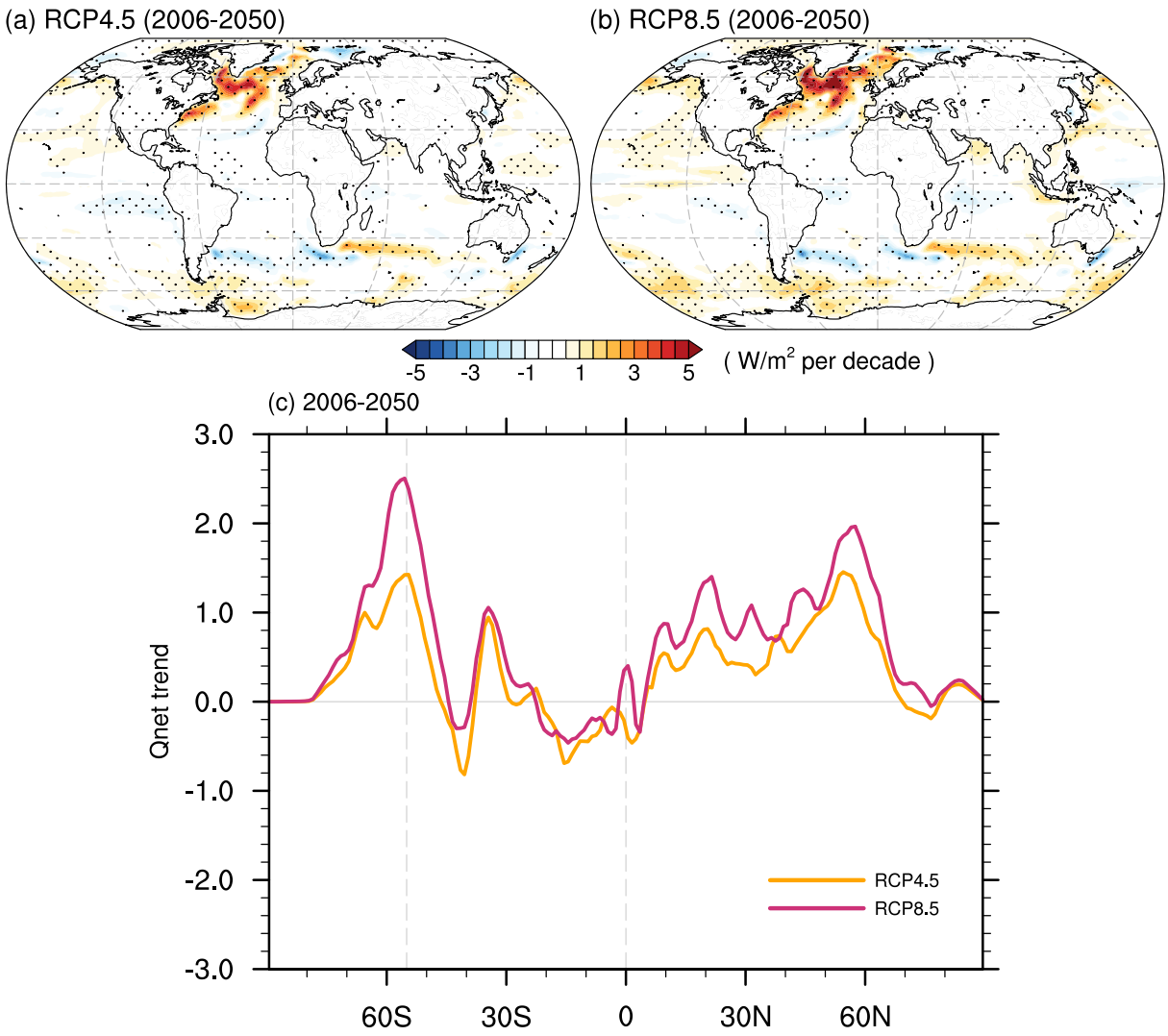

Figure 2.6: Qnet trend (in W/m^2 per decade) of the ensemble mean of 9 CMIP5 models in (a) RCP4.5 (2006-2050) and (b) RCP8.5 (2006-2050). Positive indicates excess heat absorbed by the ocean. Stippling indicates regions exceeding 95% statistical significance computed from the two-tailed t-test. (c) Zonally integrated Qnet trend in RCP4.5 (orange) and RCP8.5 (purple) from 2006 to 2050.

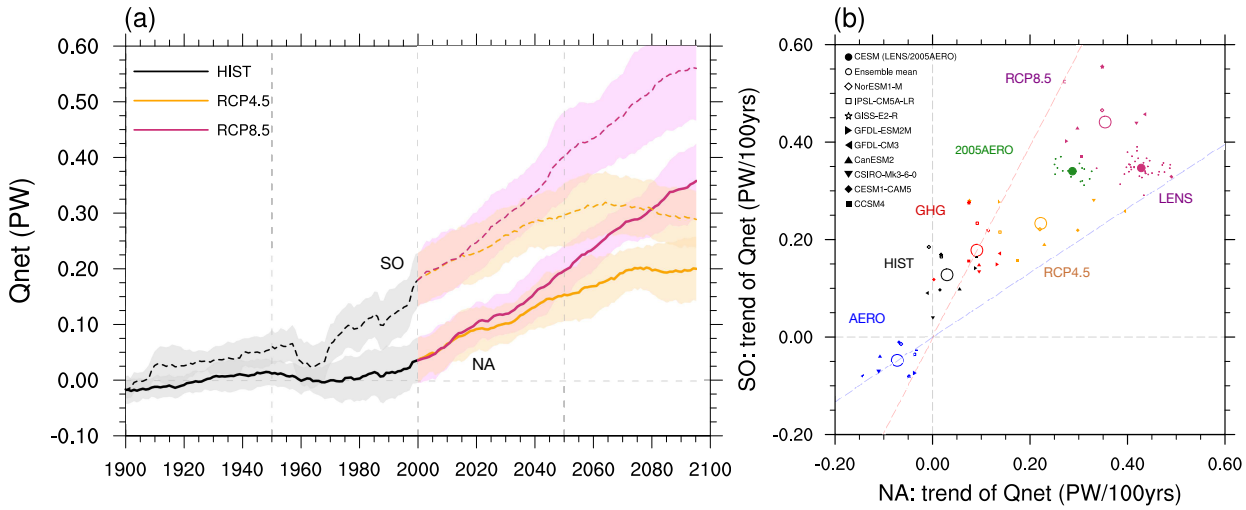

Figure 2.7: Time series of (a) heat uptake in the NA (30˚N-70˚N, 80˚W-10˚W; solid curves) and SO (south of 30˚S; dashed curves) relative to the average of 1861-1880 for various ensembles of CMIP5. Shading denotes model uncertainties as one standard deviation across models. (b) SO versus NA in heat uptake trend. The multimodel means are represented by hollow circles, with each model run denoted by small dots. The dashed red (blue) lines for the historical single forcing runs GHG (AERO) are plotted through the multimodel means (hollow circles), with their slopes based on all runs in the ensemble. The ensemble mean responses from LENS (purple) and 2005AERO (green) are also shown in the scatter plot (filled circle), with individual members denoted by smaller dots.

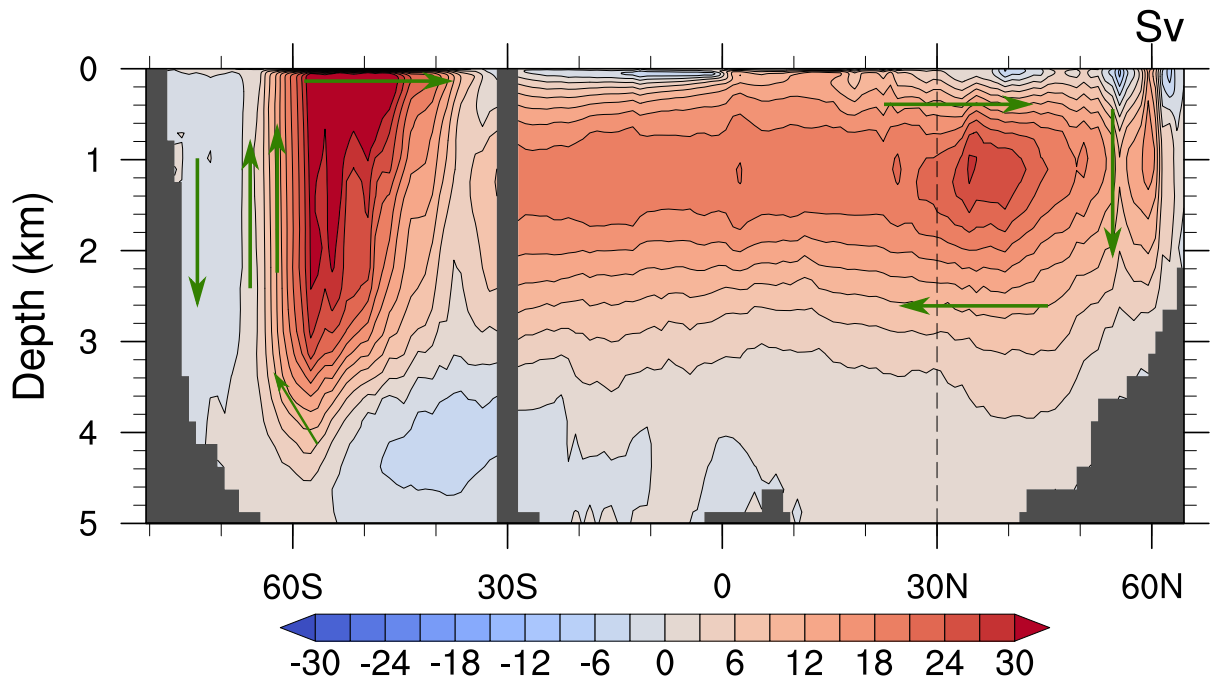

Figure 2.8: Long-term mean (from 1960 to 2005) meridional overturning stream function (in Sv) in the Atlantic Ocean (north of 30˚S) and in the Southern Ocean (south of 30˚S) from the first realization of the LENS. The stream function is calculated based on the sea water meridional velocity and is zonally integrated in the Atlantic and Southern Ocean, respectively. Red shading denotes clockwise circulation; blue shading denotes anticlockwise circulation. The AMOC index is defined as the maximum stream function at 30°N (dashed line).

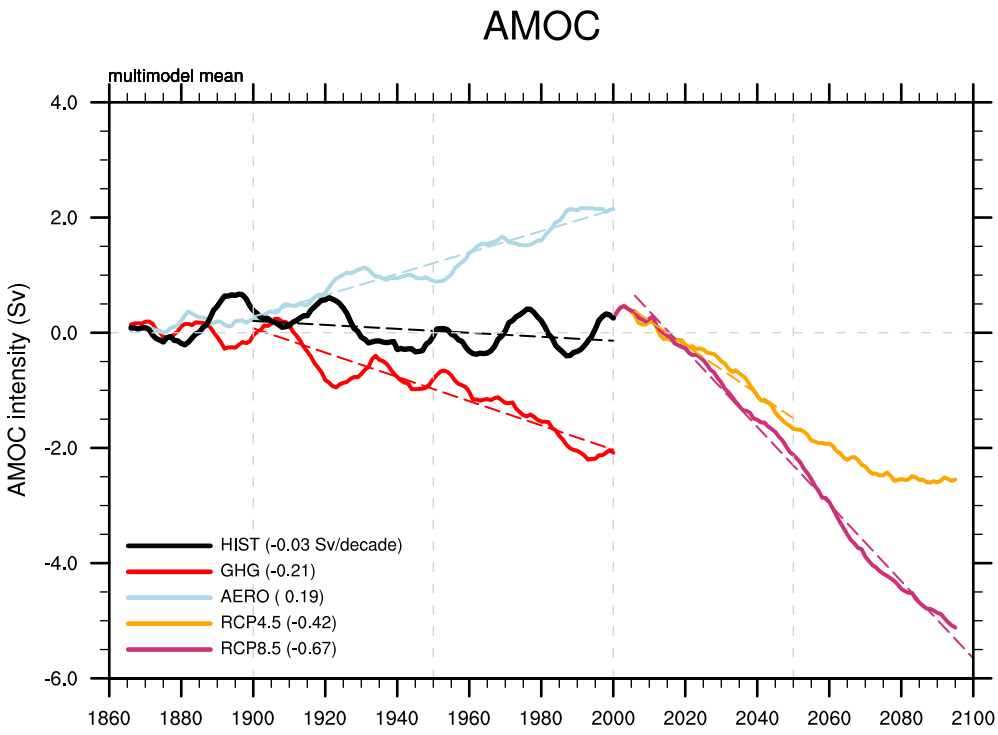

Figure 2.9: Time series of the AMOC intensity (Sv) in the CMIP5 multimodel ensemble runs listed in the figure. AMOC intensity is defined as the maximum volume transport stream function at 30˚N and is calculated based on the multimodel mean of the first realization of each model relative to the average of 1861-1880. The number in the bracket denotes the long-term trend (dashed line) in each experiment.

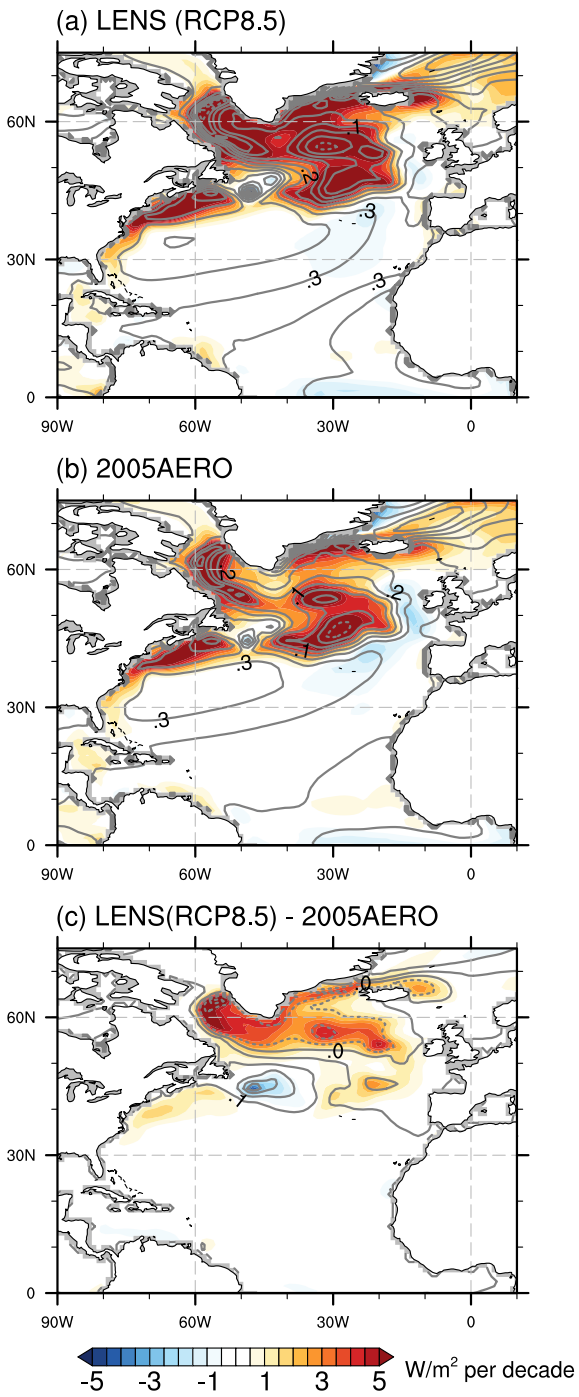

Figure 2.10: Trend of Qnet (shading; W/m^2 per decade) and SST (contours at 0.1K per decade; dashed contours indicate negative trends) of (a) the ensemble mean of (Large Ensemble Project) LENS, (b) the ensemble mean of (aerosol fixed at 2005-level) 2005AERO and (c) LENS minus 2005AERO from 2006 to 2100.

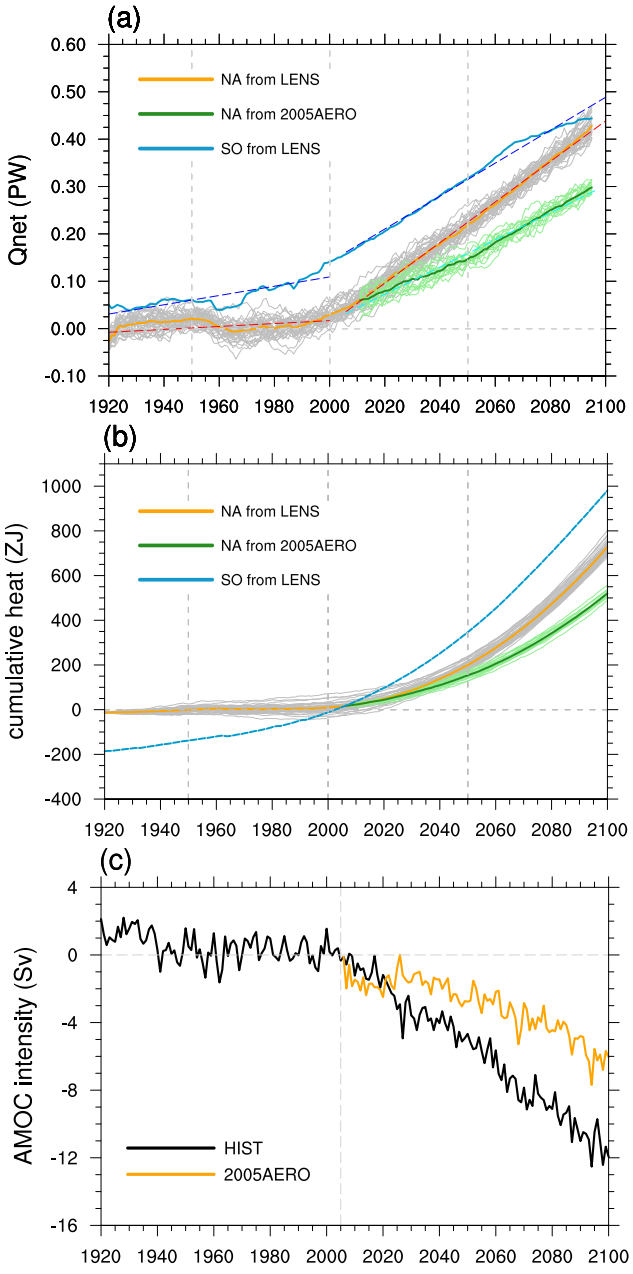

Figure 2.11: Time series of (a) heat uptake and (b) cumulative heat uptake in the NA (orange and green) and SO (blue) relative to the average of 1861-1880 in LENS and 2005AERO. The cumulative heat uptake in the SO is relative to the annual mean of 2006. (c) Time series of the annual mean AMOC intensity in the first realization of LENS (black) and 2005AERO (orange). For LENS, AMOC intensity is relative to the average of 1861-1880. For 2005AERO, the annually AMOC index anomaly is relative to the annual mean of 2006.

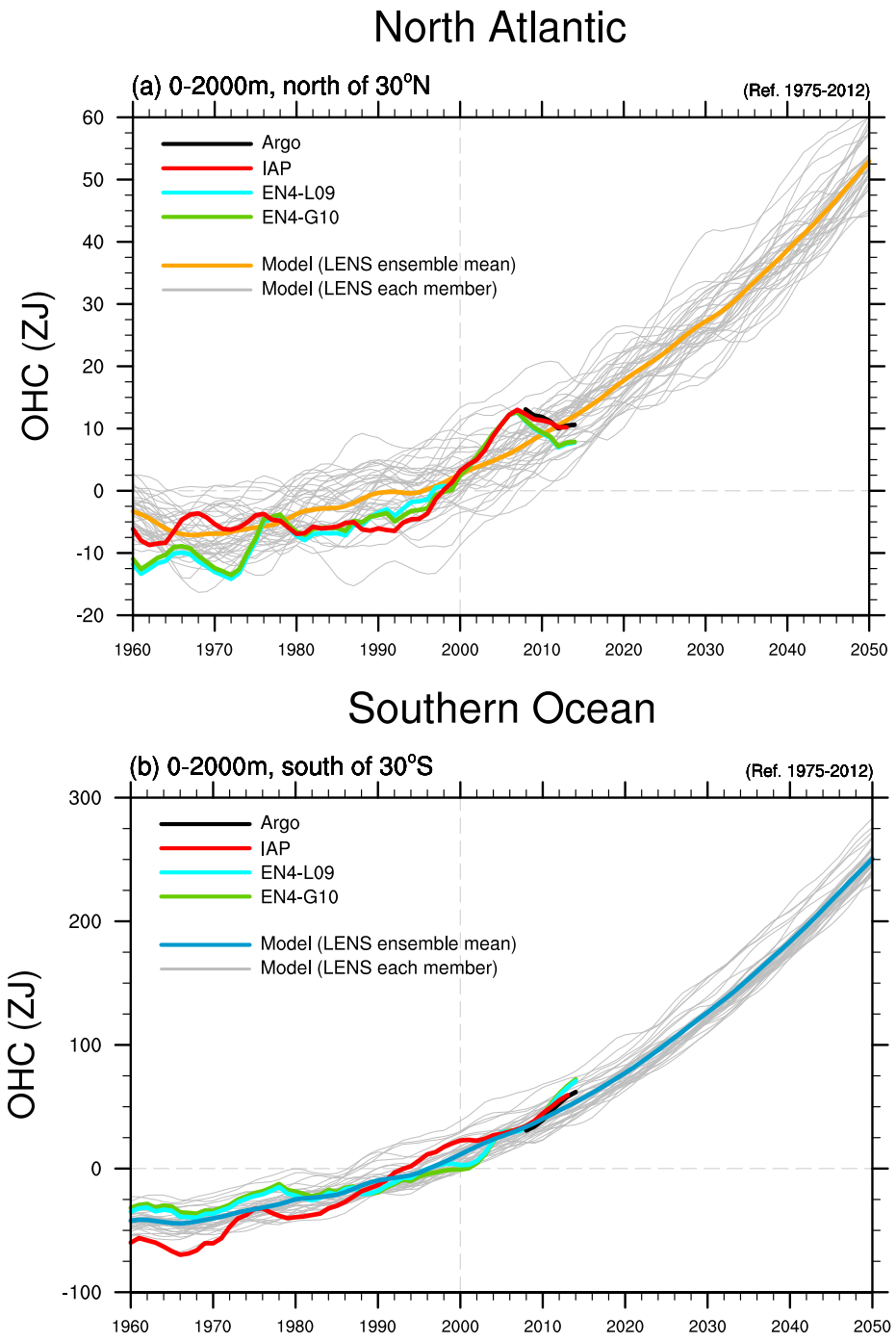

Figure 2.12: Time series of OHC (0-2000m) from observations (Argo, IAP, and EN4) and simulation (LENS) in (a) the NA and (b) the SO. All the time series are relative the 1975-2012 base period. The gray curves denote the OHC from each individual member of LENS. 5-year running mean is applied to the time series.

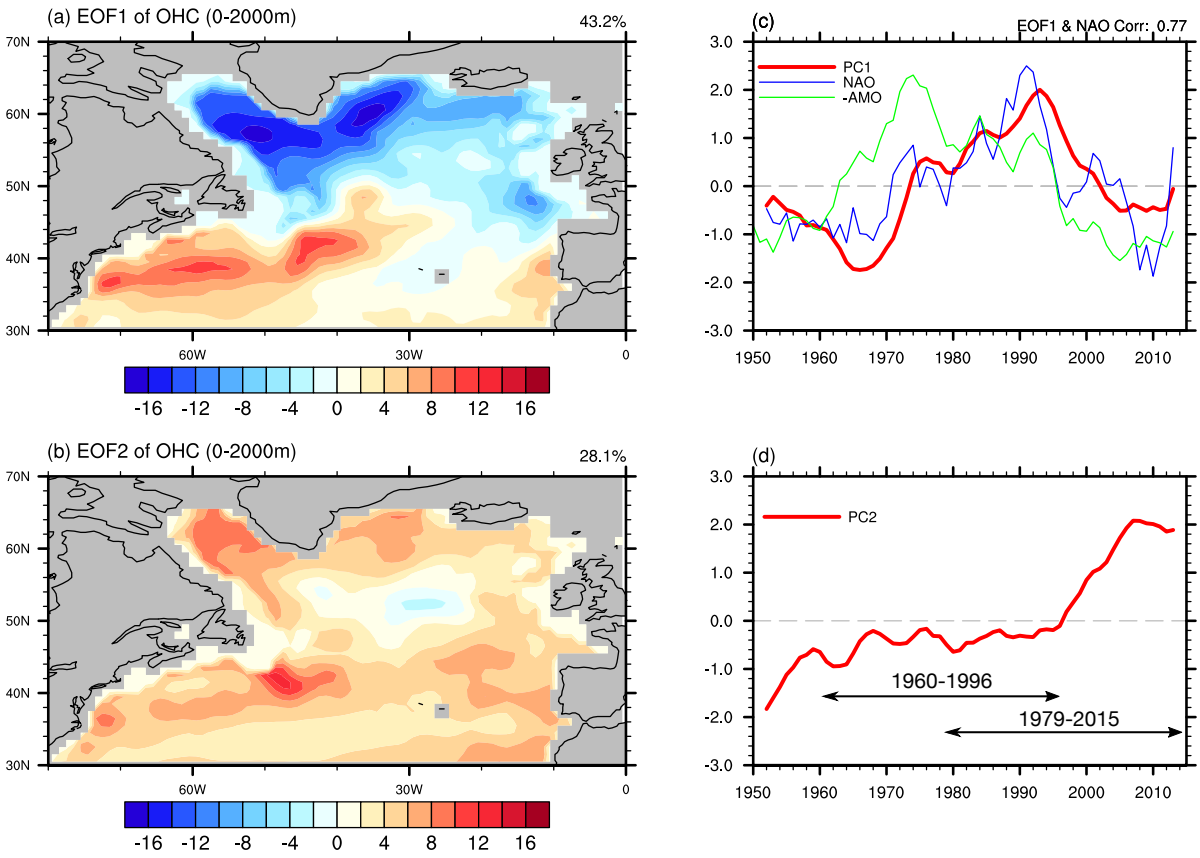

Figure 2.13: First two EOF modes of OHC above 2000m from 1950 to 2015 from IAP data. EOF patterns are shown in (a) and (b). Normalized principal components (PC; red) are shown in (c) and (d). 5-year running mean is applied to the PCs, NAO (blue), and AMO (green). The number at the upper right corner of (c) shows the cross-correlation between PC1 and NAO. The NAO index is from NOAA (https://www.ncdc.noaa.gov/teleconnections/nao/). The AMO index is from the NOAA (https://www.esrl.noaa.gov/psd/data/timeseries/AMO/). The NAO and AMO indices are normalized. Compare with the EN4-G10 data analysis in Figure A4.

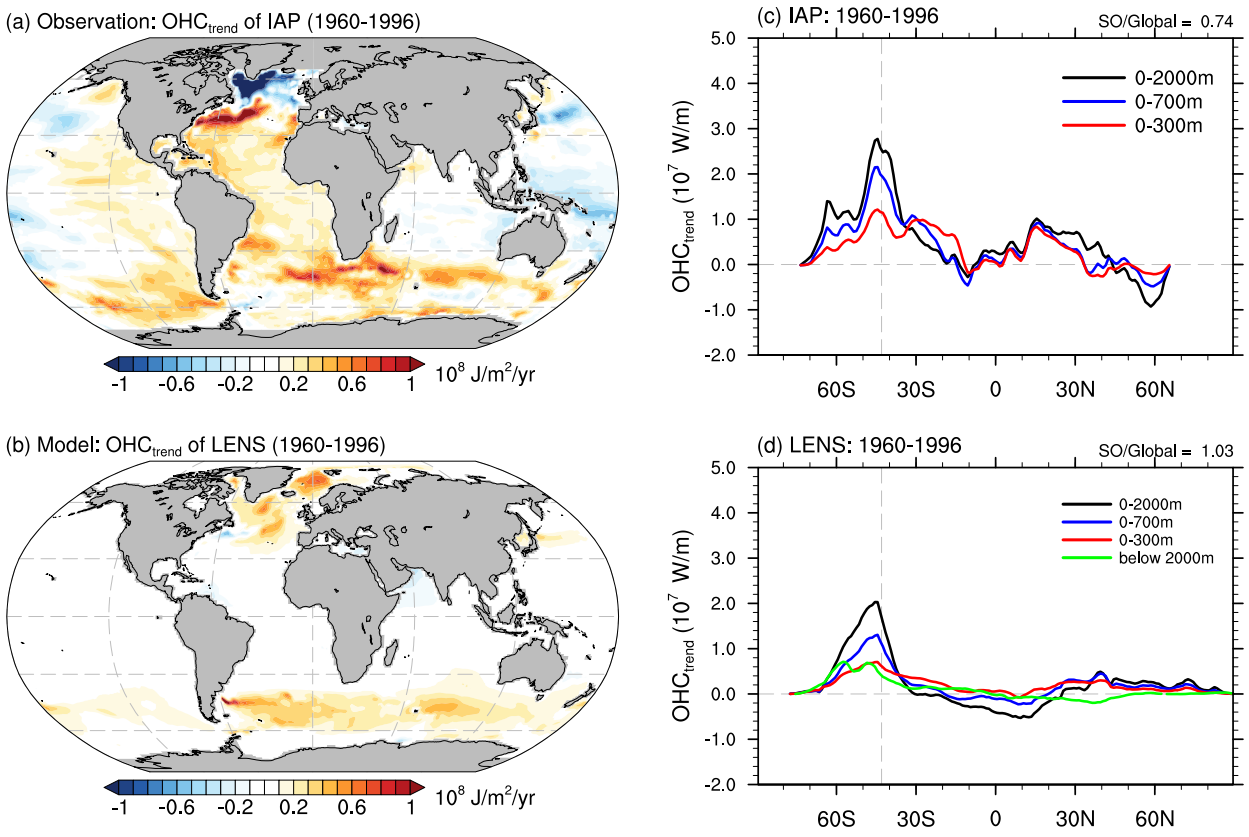

Figure 2.14: 1960-1996 trends in OHC (denoted by OHC_{trend}) above 2000m from (a) IAP data and (b) the ensemble mean of LENS. The zonally integrated OHC trend from (c) IAP data and (d) the ensemble mean of LENS, in different ocean layers. The number at the upper right corner denotes the fraction of SO to global OHC change. Compare with the EN4-G10 data analysis in Figure A5.

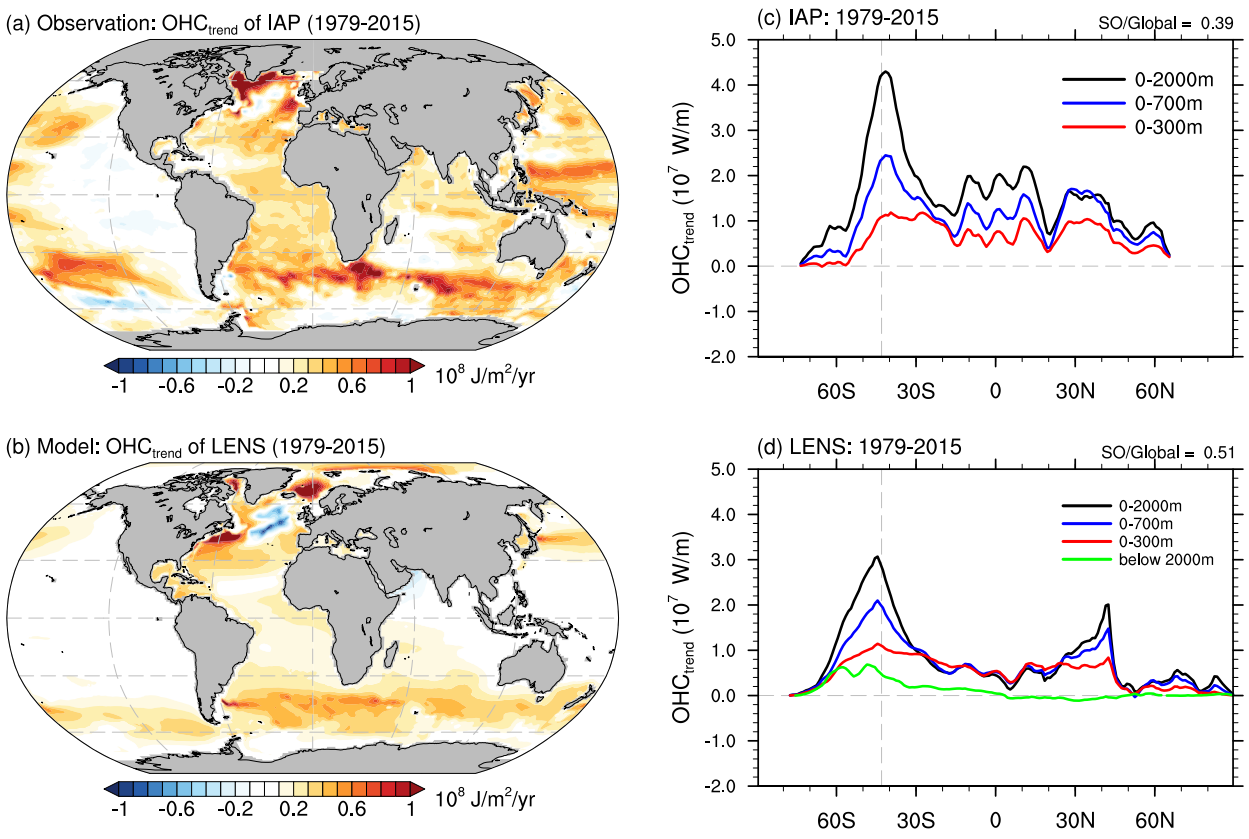

Figure 2.15: Same as Figure 2.14 but the OHC trend is calculated for the period from 1979 to 2015. Also compare with the EN4-G10 data analysis in Figure A5.

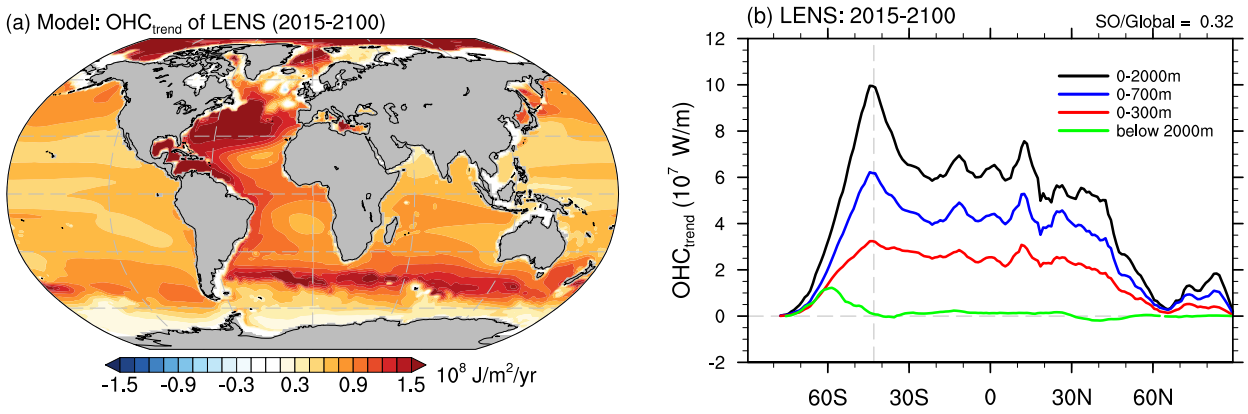

Figure 2.16: (a) OHC trend (denoted by OHC_{trend}) above 2000m from the ensemble mean of LENS over 2015-2100. (b) Zonally integrated OHC trend in different layers, as in Figure 2.14. The number at the upper right corner denotes the fraction of SO to global OHC change.

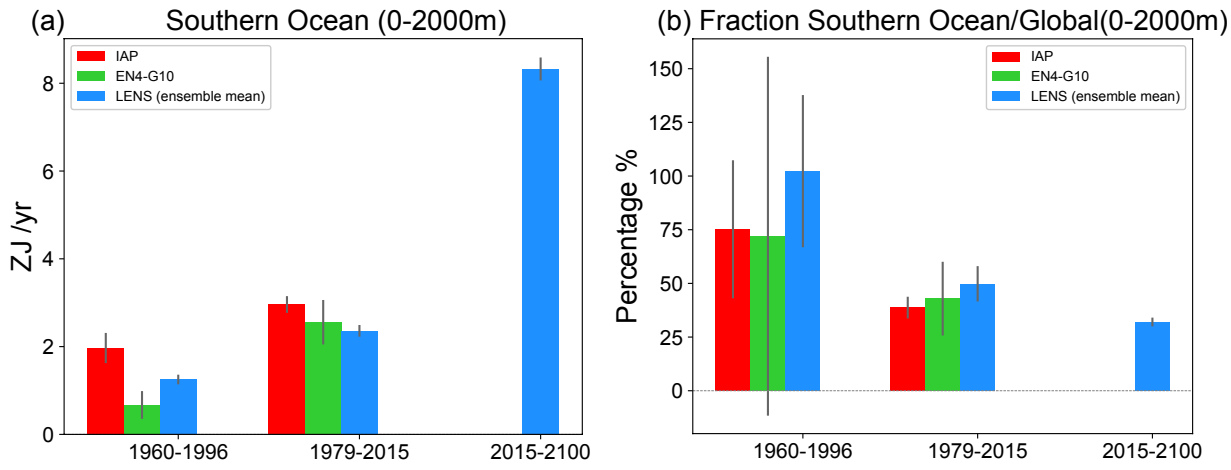

Figure 2.17: (a) OHC trend above 2000m in the SO and (b) fraction of the SO to global OHC change from observations (IAP and EN4-G10) and model (the ensemble mean of LENS). The error bars denote 95% confidence interval.

Chapter 3

Effects of Buoyancy and Wind Forcing on Southern Ocean Climate Change

3.1 Abstract

Observations show that since the 1950s, the Southern Ocean has stored a large amount of anthropogenic heat and has freshened at the surface. These patterns can be attributed to two components of surface forcing: poleward-intensified westerly winds and increased buoyancy flux from freshwater and heat. Here we separate the effects of these two forcing components by using a novel partial-coupling technique. We show that buoyancy forcing dominates the overall response in the temperature and salinity structure of the Southern Ocean. Wind stress change results in changes in subsurface temperature and salinity that are closely related to intensified residual meridional overturning circulation. As an important result, we show that buoyancy and wind forcing result in opposing changes in salinity: the wind-induced surface salinity increase due to upwelling of saltier subsurface water offsets surface freshening due to amplification of the global hydrological cycle. Buoyancy and wind forcing further lead to different vertical structures of Antarctic Circumpolar Current (ACC) transport change; buoyancy forcing causes an ACC transport increase (3.1±1.6 Sv; 1Sv ≡ $10^6 m^3 s^{-1}$) by increasing the meridional density gradient across the ACC in the upper 2000m, while the wind-induced response is more barotropic, with the whole column transport increased by 8.7±2.3 Sv. While previous research focused on the wind

effect on ACC intensity, we show that surface horizontal current acceleration within the ACC is dominated by buoyancy forcing. These results shed light on how the Southern Ocean might change under global warming, contributing to more reliable future projections.

3.2 Introduction

Observations have revealed a complex set of changes in the Southern Ocean over the past few decades. The most pronounced is subsurface warming in the Southern Ocean (Purkey and Johnson 2010; Rhein et al. 2013; Roemmich et al. 2015; Desbruyères et al. 2016; Cheng et al. 2016; Shi et al. 2018), which illustrates the important role of the Southern Ocean in slowing the global surface warming rate. This significant warming can be traced back to the 1950s (Gille 2002, 2008). A broad-scale salinity decrease in the surface, mode, and intermediate waters in the Southern Ocean has also occurred since 1950 (Durack and Wijffels 2010). The change in surface buoyancy flux, which is the combination of heat flux and freshwater flux, supports the temperature and salinity changes physically (Swart et al. 2018). Moreover, the Southern Ocean has experienced significant surface wind stress change (Swart and Fyfe 2012). In particular, observations show poleward-intensified westerly winds associated with a positive tendency of the Southern Annular Mode (SAM) index (Thompson 2002; Marshall 2003), which has been found to be forced by both stratospheric ozone depletion (Gillett 2003; Waugh et al. 2013) and anthropogenic greenhouse gas emissions (Fyfe and Saenko 2006). The observed poleward shift in Southern Hemisphere westerlies occurs mostly in austral summer, and is compensated by opposing shifts in other seasons (Lee and Feldstein 2013; Swart et al. 2015).

Manabe et al. (1990) found in a modeling study that the Southern Ocean dominates anthropogenic heat uptake. Based on CMIP5 models, more than 70% of anthropogenic heat is

absorbed by the Southern Ocean (south of 30˚S, occupying 30% of global surface ocean area) during the historical period (Frölicher et al. 2015; Shi et al. 2018). In the Southern Ocean, deep water upwells along isopycnals that connect the deep ocean to the sea surface, where water masses can interact with the atmosphere, exchanging heat before returning to the ocean interior. Armour et al. (2016) showed that the upwelling of pristine, older deep water with stable temperature under a warming atmosphere leads to greater heat transfer to the ocean because of the increasing ocean-atmosphere temperature difference. Shi et al. (2018) showed that the compensating effects of greenhouse gases and anthropogenic aerosols in the Northern Hemisphere leads to small ocean heat uptake in the subpolar North Atlantic, resulting in dominance of the Southern Hemisphere in global ocean heat uptake. The subsurface warming or ocean heat content (OHC) increase in the Southern Ocean corresponds to enhanced ocean heat uptake at the surface (peaking around 55˚S-60˚S), while most subsurface warming occurs further equatorward, peaking around 40˚S-45˚S (Roemmich et al. 2015; Frölicher et al. 2015; Armour et al. 2016). The equatorward displacement of maximum subsurface warming relative to maximum heat uptake is attributed to the background meridional overturning circulation (MOC), which redistributes the absorbed heat (Armour et al. 2016; Liu et al. 2018). The warmed water is advected northward by Ekman transport, eventually resulting in enhanced warming on the northern flank of the Antarctic Circumpolar Current (ACC) and delayed warming on the southern flank (Armour et al. 2016). Moreover, amplification of the global hydrological cycle, manifested as increased atmospheric freshwater fluxes over the high-latitude oceans, is an important factor driving the observed surface freshening of the Southern Ocean (Durack and Wijffels 2010; Helm et al. 2010; Durack et al. 2012). More recent studies suggest that the freshening also stems from equatorward wind-driven sea ice transport (Haumann

et al. 2016) and enhanced Antarctic glacial melt (Jacobs 2002; Paolo et al. 2015; Bronselaer et al. 2018; Bintanja et al. 2013; Swart and Fyfe 2013).

Southern Ocean circulations, that is, the MOC and the ACC, are affected by the overlying strong westerly winds. Mesoscale eddies can offset the effects of surface wind stress change on the MOC and ACC due to eddy-compensation and eddy-saturation, respectively (Morrison and Hogg 2013). High-resolution ocean models show that wind-driven MOC intensification is partially compensated by an eddy-induced MOC; the compensating ratio is about 50% (Gent 2016). In addition, several modeling studies have shown that the ocean state approaches the fully eddy-saturated regime, with the response of ACC transport insensitive to wind perturbation (Meredith and Hogg 2006; Hallberg and Gnanadesikan 2006; Farneti et al. 2010). Similarly, the observationally-based study of Böning et al. (2008) suggested that, because of eddy saturation, the ACC transport and associated isopycnal tilt are largely unaffected by the poleward-intensified westerly winds. Recent studies (Meredith et al. 2012; Dufour et al. 2012; Morrison and Hogg 2013) find that surface wind stress change is indeed capable of driving weak but significant changes in ACC transport, associated with changes in the zonal barotropic current rather than with changes in the density structure (Zika et al. 2013; Langlais et al. 2015).

In order to isolate the effect of wind forcing change on the Southern Ocean, several studies have used the wind pattern derived from global warming experiments as a perturbation (Fyfe et al. 2007; Spence et al. 2010). They find that poleward-intensified westerly winds enhance Southern Ocean warming north of the ACC and lead to cooling south of the ACC at depth, primarily controlling the spatial pattern of the warming signal. Buoyancy forcing change has also been shown to affect the Southern Ocean. For example, heating and/or freshening of the Southern Ocean can increase ocean stratification, allowing warming in the atmosphere to accelerate and ocean heat

storage to slow (Russell et al. 2006). The surface intensified warming also results in a reduction in the diffusive and advective, southward and upward eddy heat transport (Morrison et al. 2016). Buoyancy forcing can also influence ACC transport by altering upper layer stratification and the cross-stream density gradient (Hogg 2010). Hence it is essential to understand the relative importance of wind and buoyancy forcing in Southern Ocean climate change and the fingerprint (forced response) of change associated with each forcing component.

In this study, we explore the respective effects of buoyancy and wind (momentum) forcing on transient climate change in the Southern Ocean by using partial-coupling model simulations (Liu et al. 2018) in which wind stress fields are prescribed. Fyfe et al. (2007) pioneered a similar approach to separating buoyancy and wind forcing effects, but their simple energy-balance model of the atmosphere limited the simulation skill, especially regarding the hydrological cycle and salinity. Liu et al. (2018) mainly focus on the Eulerian mean and eddy-induced MOC change due to buoyancy and wind forcing. Here, we examine the fingerprint of buoyancy and wind forcing in ocean circulation, temperature, salinity, and sea-ice changes in idealized experiments with quadrupled atmospheric CO_2. Previous studies largely focused on the response of the Southern Ocean to changes in westerly winds, whereas we find that buoyancy forcing dominates the overall response in the temperature and salinity structure of the Southern Ocean. Buoyancy forcing accounts for 80% of the total heat storage change within a quadrupled CO_2 experiment, and wind forcing accounts for the rest, the pattern of which is closely linked with the strengthened residual MOC due to intensified westerly winds. As an important result, we find that buoyancy and wind forcing have opposite impacts on salinity: surface salinity increase over the Southern Ocean driven by stronger wind-driven upwelling of saline waters in the MOC can substantially offset surface freshening due to a global water cycle amplification. Moreover, we find that the changes in

subsurface temperature driven by buoyancy forcing can further intensify the horizontal (circumpolar) circulation due to a change in the meridional density gradient, whereas wind stress changes create a more barotropic increase in circumpolar transport. The surface horizontal velocity acceleration is primarily driven by buoyancy forcing. Understanding the relative responses to these two forcing changes is crucial to understanding observed long-term change in the Southern Ocean.

The rest of the paper is organized as follows. Section 2 describes the models, experiments, data and methods used in this study. Section 3 discusses the response of Southern Ocean temperature to wind change and surface buoyancy forcing. Section 4 discusses the change of salinity and sea ice due to both forcing components. Section 5 further investigates the ACC response, including transport and position. Section 6 provides discussion and conclusions.

3.3 Data and Methods

3.3.1 CESM and partial coupling experiments

We use the Community Earth System Model (CESM), version 1.0.5, from the National Center for Atmospheric Research (NCAR) (Hurrell et al. 2013). The model consists of the version 5 of the Community Atmosphere Model (CAM5), run at a nominal 2˚ resolution (1.9˚ latitude x 2.5˚ longitude) with 26 vertical layers, and version 2 of Parallel Ocean Program (POP2), which has a nominal resolution of 0.5˚ in latitude and 1˚ in longitude over the Southern Ocean. The Community Land Model, version 4, and Community Ice Code, version 4, are coupled with the atmosphere and ocean model. The ocean model employs a temporally and spatially varying specification of the Gent-McWilliams eddy parameterization (Gent and McWilliams 1990). For tracers, such as temperature, the horizontal diffusion follows the Redi isoneutral diffusion operator as represented by the GM parameterization, and the vertical diffusion follows the K-profile

parameterization (Large et al. 1994). NCAR CESM is widely used and has been extensively evaluated against observations and other climate models (Kay et al. 2015, 2016; Cheng and Zhu 2016; Bracegirdle et al. 2018; Beadling et al. 2019).

Here we employ a partial coupling technique (Lu and Zhao 2012; Liu et al. 2015, 2018) to isolate the effects of the wind-induced Southern Ocean climate change. In the partial coupling experiments, variables at the air-sea interface (e.g. wind stress) from fully coupled runs are prescribed in the ocean model in order to disable the targeted feedback. Here we use a fully coupled, preindustrial control run (CTRL) as the baseline run, which starts from AD 1850 scenario. We also use a fully coupled, abruptly quadrupled CO_2 ($4\times CO_2$) run, which branches from CTRL, with the atmospheric CO_2 concentration instantly quadrupled from the 1850 level and kept constant through the 90-yr simulation. Next, we conduct a suite of partial-coupling experiments with prescribed wind stress and surface wind speed from the above-mentioned fully coupled cases (CTRL and $4\times CO_2$) at the daily frequency of air-sea coupling. Here, winds can affect surface heat uptake and interior ocean heat redistribution either by changing ocean circulation via momentum flux (dynamic effect) or by modifying ocean-atmosphere thermal coupling through the wind speed in the bulk formula of turbulent (latent and sensible) heat fluxes (thermal dynamic effect). Wind stress (τ), wind speed (w) and CO_2 level (c) are the variables of interest. To target climate response without wind change, we quadruple the atmospheric CO_2 level (c4) with prescribed wind stress (τ1) and speed (w1) from CTRL; we call this 'τ1w1c4' to specify wind from CTRL and CO_2 level from $4\times CO_2$. The definition of each term is shown in Table 3.1. In sum, we have three partially coupled experiments: τ1w1c1, τ1w1c4, and τ4w1c4. The transient response of the Southern Ocean to wind stress change under quadrupled CO_2 can be obtained by taking the difference between the simulations with and without wind stress changes:

$$Wstr = (\tau 4w1c4 - \tau 1w1c4). \quad (3.1)$$

The buoyancy forcing response can be obtained by taking the difference between the simulations with and without changing the external CO_2 forcing, while keeping the surface wind stress and speed from CTRL:

$$Buoy = (\tau 1w1c4 - \tau 1w1c1). \quad (3.2)$$

Buoy includes effects due to changes in surface heat flux and freshwater flux. We have previously shown, using this partial coupling technique, that the surface wind speed effect on surface heat and freshwater fluxes has a minimal effect on Southern Ocean climate change (Liu et al. 2018). Therefore, in this paper, we focus on the wind stress effect (Wstr) and the buoyancy forcing effect (Buoy), both of which we show have significant impacts. In this partial coupling technique, we represent the total effect (Total) as the linear sum of Wstr and Buoy:

$$Total = Wstr + Buoy = (\tau 4w1c4 - \tau 1w1c1). \quad (3.3)$$

The experiments using from the partial-coupling experiments are summarized in Table 3.2.

Surface wind is coherent with other fields, such as surface heat flux. The coherence can intertwine the wind-induced and buoyancy-induced responses. In order to disrupt this coherence and to separate responses due to wind change and buoyancy flux change, wind stress and speed are shifted forward by one year during the partial coupling. In addition, the partial coupling technique can generate a climate drift by disrupting air-sea interaction. The climate drift due to partial coupling can be largely eliminated by computing the difference between partially coupled runs because the same drift is present in all runs. The responses for Total are compared with the fully coupled experiment ($4\times CO_2$ – CTRL; Figure B1). The Total case largely reproduces $4\times CO_2$ – CTRL in ocean temperature, salinity, and circumpolar velocity, with a discrepancy mainly at intermediate depth in salinity change. The similarities between the Total case and fully coupled

run indicate that the overall effects can be largely represented by a linear combination of Buoy and Wstr (Eq. 3.3). We also compare the Southern Ocean temperature, salinity, and density structure in the partially coupled CESM simulation (τ1w1c1) with the mean state from Argo profiling float observations (2005-2018; Section 2.3). The mean state from CESM agrees roughly with observations (Figure B2). The zonal-mean CESM and Argo density structures are very similar (Figure B2c). However, CESM shows steeper isothermal slopes in the ACC compared to Argo, resulting in deeper penetration of heat to the north of the ACC than is observed. The salinity minimum is located at a shallower depth in CESM than in Argo, which may confine the CESM salinity change within the upper layer. Lastly, the ACC volume transport through the Drake Passage from τ1w1c1 is 166.6 Sv, which falls within the range (173.3 ± 10.7 Sv) observed from the cDrake experiment by Donohue et al. (2016). More details about the CESM1 model configuration and setup can be found in Liu et al. (2018). We analyze changes over years 41-90, which represents the slow (multi-decades) response (Ferreira et al. 2015) to wind and buoyancy forcing.

3.3.2 Flux-anomaly-forced model intercomparison (FAFMIP) experiment

In addition to the CESM partial coupling experiments, this study also uses the output of FAFMIP experiments from four models: ACCESS-CM2 (Hirst et al. 2015), MIROC6 (Tatebe et al. 2019), MPI-ESM1-2-HR (Gutjahr et al. 2019), and MRI-ESM2-0 (Yukimoto et al. 2019). FAFMIP is part of the Coupled Model Intercomparison Project Phase 6 (CMIP6). The FAFMIP experiments, branched from pre-industrial conditions (piControl), prescribe a set of surface flux perturbations for the ocean. These perturbations are obtained from the ensemble-mean changes

simulated at the time of doubled CO_2 by CMIP5 AOGCMs under the 1pctCO2 scenario (CO_2 increases by 1% each year). This study examines FAFMIP experiments: FAF-Wstr (faf-stress), imposing perturbation surface wind stress; FAF-Heat, imposing perturbation surface heat flux; and FAF-Water, imposing perturbation surface freshwater flux (Gregory et al. 2016). For FAF-Heat, the heat flux perturbation yields a strong negative feedback due to SST warming. In order to avoid this negative feedback and to require all of the prescribed heat flux perturbation to enter the ocean, Bouttes and Gregory (2014) used a passive tracer of ocean temperature to prevent the atmosphere from feeling the SST change due to the heat flux perturbation. More details about the treatment of heat flux perturbations can be found in Gregory et al. (2016).

All FAFMIP experiments considered here were run for 70 years. We show the anomalies of the 41-70 year average relative to the climatology from piControl. In addition, we linearly combine the results from FAF-Heat and FAF-Water as FAF-Buoy to represent a buoyancy forcing experiment. FAF-All represents the sum of FAF-Wstr and FAF-Buoy. FAF-Wstr and our CESM Wstr runs may be directly compared to evaluate the model dependency. Because of the differences in the experimental design, however, further studies are needed to understand how to compare FAF-Buoy and our CESM Buoy runs.

3.3.3 Observations

We use temperature and salinity products from the World Ocean Atlas 2018 (WOA; https://www.nodc.noaa.gov/OC5/woa18/). WOA is a uniformly formatted and quality-controlled data set based on the World Ocean Database. Objectively analyzed climatologies of temperature and salinity (1955-1964, 1965-1974, 1975-1984, and 2005-2017) are used in this study. Long-term ocean temperature and salinity changes are calculated as the difference between the 2005-2017

mean and the mean over the 1955-1984 base period. We also use the monthly gridded Argo temperature and salinity data (Roemmich and Gilson 2009; http://www.argo.ucsd.edu) to show the trend from 2005 through 2018. The data are on a 1˚x1˚ grid with 58 vertical pressure levels from the surface to 2000 m. The annual mean trend from 2005 to 2018 is calculated to represent the recent temperature and salinity changes in the Southern Ocean.

3.3.4 Latitude of mean ACC transport

Fixed sea surface height contours are often used to track ACC frontal displacements. This method is problematic because of large-scale steric expansion under global warming. To minimize the effect of steric expansion, we apply the method of Gille (2014) to find the latitude of mean ACC transport. Zonal ocean velocity at the surface (U_g) is related to the meridional gradient of sea surface height (SSH) through the geostrophic relationship:

$$U_g = -\frac{g}{f}\frac{\partial \mathrm{SSH}}{\partial y}, \tag{3.4}$$

where g is gravity, f is the Coriolis parameter, and y is the meridional length. The ACC fronts are expected to correspond to strong geostrophic velocities. Next, weighted by surface velocity, the mean latitude of the surface transport is computed as

$$\bar{\theta} = \frac{\int_{\theta_S}^{\theta_N} \theta U_g \, d\theta}{\int_{\theta_S}^{\theta_N} U_g \, d\theta}, \tag{3.5}$$

where $\bar{\theta}$ is the surface velocity weighted average latitude, θ_N and θ_S are the northern and southern integration limits of latitude, and U_g is zonal velocity calculated from Eq. 3.4. The mean latitude

of the ACC is sensitive to the integration limits (Gille 2014), so we estimate uncertainty by conducting a Monte Carlo test with 1000 realizations, in which two integration limits are randomly perturbed using Gaussian random numbers with mean values at 40˚S and 60˚S, respectively, and a standard deviation of 5˚ latitude.

We also use the independent method from Sen Gupta et al. (2009) and Meijers et al. (2012) to locate the position of the mean ACC, which is calculated at each longitude as the mean latitude within the latitude range defined by 50% of the maximum transport.

3.4 Southern Ocean Temperature Change

Buoy and Wstr under abrupt quadrupling of CO_2 create different zonal mean warming patterns in the Southern Ocean (Figure 3.1c, d). For Buoy, the upper ocean temperature increases by around 3˚C on the northern flank of the ACC and further north (Figure 3.1c). The warming decays with depth mainly along the climatological isopycnals (contours). South of the ACC, warming in the surface layer is weaker (by an average of 1.2˚C between 60˚S and 75˚S), likely due to continuous upwelling by the background ocean circulation of old deep water without a temperature anomaly (Armour et al. 2016). The ocean takes up heat where the deep water outcrops (Figure 3.1a, c). The Ekman transport then advects the warmed water equatorward, where it is subducted and warms the thermocline between 20˚S and 50˚S (Roemmich et al. 2015; Liu et al. 2018; Shi et al. 2018). The meridional gradient in temperature change across the ACC leads to greater thermal-expansion-induced sea level rise in the north than in the south (Bouttes and Gregory 2014), resulting in enhanced zonal geostrophic velocity in the upper layer (Figure 3.7b). We further discuss the important implications of this result in section 5.

Wind-stress change (Wstr) also contributes to surface and subsurface warming between 40˚S and 55˚S, with a maximum warming of over 1˚C (Figure 3.1d). Consistent with Fyfe et al. (2007), the wind forcing also induces subsurface cooling both south and north of the warmed region, a tri-pole pattern distinct from that of Buoy. This wind-driven subsurface temperature change is due to a combination of adiabatic and diabatic processes. The wind-stress curl change is positive south of 58˚S, negative within the ACC, and positive again but with small magnitude north of 35˚S (Figure 3.1b), leading to corresponding anomalous Ekman suction/pumping (Figure 3.1d). At higher latitudes, the isopycnal displacements (contours in Figure 3.1d) account for the warming and cooling patterns in different layers. The wind-forced, deepened isopycnals from 40˚S to 60˚S enhance the subsurface warming that is due to Buoy (Figure 3.1c). At lower latitudes, wind-forced, shoaling isopycnals are responsible for the cooling patch from 200 m to 1000 m. The superposition of ocean vertical velocity change on climatological temperature illustrates this adiabatic heave process (Figure B3a). Furthermore, the poleward shift and intensification of surface wind stress (red curve in Figure 3.1b) leads to anomalous Ekman transport: enhanced equatorward Ekman transport at higher latitudes and reduced equatorward Ekman transport at lower latitudes (cyan vectors in Figure 3.1d). Therefore, there is an ocean heat transport convergence in the surface layer in the vicinity of the ACC, which accounts for the surface warming induced by wind-stress change. Meanwhile, the wind-induced intensified residual MOC leads to a loss in surface heat flux around 45˚S and a gain around 60˚S (Liu et al. 2018). Within the ACC, the wind change reinforces the ocean warming due to Buoy. The wind-driven warming has a relatively small amplitude over the Southern Ocean compared with warming due to buoyancy forcing (Figure B4): about one-fifth of Southern Ocean OHC change integrated between 30˚S and

90˚S is driven by wind forcing (Figure B4d). In fact, for the global ocean, most OHC change is found in Buoy (Figure B4e), associated with ocean heat uptake.

The subsurface temperature change from FAFMIP experiments (Figure 3.2a, b) is broadly consistent with the results from CESM1 (Figure 3.1c, d), which confirms the fingerprints of change driven by Buoy and Wstr, respectively. Furthermore, different FAFMIP models also show similar warming patterns (Figure B5). The observed subsurface warming in WOA and Argo is centered near 38˚-42˚S and is mainly located within the main thermocline layer (Figure B6a, c), which is consistent with the model results (Figure 3.1c). The weak subsurface cooling patch in observations between 400 and 1200 m and from 20˚-30˚S seems to be driven by wind stress change (Figure 3.1d). For the surface temperature response, the observations show surface cooling at higher latitudes, especially regions south of the Subantarctic Front in the Pacific since the 1980s (Bindoff et al. 2013; Jones et al. 2013), which differs from the simulations. Although a number of studies have recently explored this difference between observed and simulated historical changes in the Southern Ocean (Bitz and Polvani 2012; Pauling et al. 2016; Kostov et al. 2017; Purich et al. 2018; Zhang et al. 2019; Rye et al. 2020; Haumann et al. 2020), the exact causes of this discrepancy are not fully understood.

3.5 Southern Ocean Salinity and Sea-Ice change

The Southern Ocean zonal mean salinity changes in the CESM partial-coupling experiments, driven by Buoy and Wstr, are shown in Figure 3.1. For Buoy (Figure 3.1e), the surface salinity change is dominated by strong surface freshening south of 35˚S and strong surface salinification north of 35˚S. The top panels of Figure 3.3 show the fifty-year average salinity in the surface layer (0-50 m) for experiments τ1w1c1, τ1w1c4, and τ4w1c4. Freshening due to Buoy

(Figure 3.3d) is widespread in the Southern Ocean with the highest amplitudes in the Amundsen Sea, the Weddell Sea, and the Indian sector near the Antarctic coast. Moreover, the resemblance between zonal mean climatology (contours in Figure 3.1e) and the salinity change due to buoyancy forcing (shading in Figure 3.1e) indicates a strong global water cycle intensification under global warming: salinity decreases in precipitation-dominated (subpolar) regions and salinity increases in evaporation-dominated (subtropical) regions (green curve in Figure 3.1a). However, in Buoy (Figure 3.1e), the boundary between positive and negative salinity change (around 35˚S) is much farther north than in previous observational and coupled model studies (Durack and Wijffels 2010; Böning et al. 2008; Swart et al. 2018), in which the boundary latitude is around 45˚S (Figure B6b, d). In the remainder of this section, we show that this boundary is mainly set by wind forcing since the combined results from Buoy and Wstr are in fact consistent with previous work.

The salinity change due to Wstr is dominated by salinification in the surface layer not only around the Antarctic coast but also in the vicinity of the ACC (Figs. 3.1f and 3.3e), which partially offsets the freshening driven by Buoy (Figure 3.1e and 3.3d). Precipitation minus evaporation (P-E) increases at higher latitudes (Figure 3.3g), which seems to be associated with a wind-induced sea-ice coverage decrease (Figure 3.5e), facilitating direct interaction between the atmosphere and ocean. Thus the increased Ekman upwelling, bringing saltier water from the deep ocean to the surface, overwhelms surface freshening due to increased freshwater flux from the atmosphere, leading to a surface layer salinity increase in the coastal region. The enhanced Ekman transport at higher latitudes (70˚S – 55˚S) then advects saltier water northward, leading to a salinity increase in the vicinity of the ACC. The decline of sea ice cover results in less freshwater flux from sea ice melt (Figure 3.5e), which further increases surface salinity in the vicinity of the ACC. The weakened northward Ekman transport from 45˚S to 20˚S also contributes to the surface salinity

increase at mid-latitudes. This wind-induced subsurface salinity change pattern is similar to that of temperature change (Figure 3.1d), although the salinity change occurs in a shallower layer because the climatological salinity (Figure B3b) is more stratified than the climatological temperature in the upper layer (Figure B3a). In addition, at 40˚S, salinity has a minimum at around 700m (Antarctic Intermediate Water), so the wind-driven downward movements of isopycnals intensify the salinification above the minimum salinity layer and diminish salinification below. Therefore, pronounced salinity changes are shallower than the subsurface temperature changes. Hence we conclude that the mean stratification is critical for setting the warming and salinification patterns in the Southern Ocean.

For the zonal mean salinity change in the upper layer, the FAFMIP models show change consistent with CESM1: surface freshening due to Buoy and salinification due to Wstr (Figure 3.2c, d). Maps of each model's salinity change in the upper 50 m also show the consistency in broadly distributed freshening due to buoyancy forcing and salinification due to wind forcing (Figure B7). At intermediate depth from 40˚-60˚S, all four FAF-Buoy runs (Figure B8) and Buoy from CESM1 (Figure 3.1e) show a salinity increase. In the FAFMIP models, buoyancy forcing can be further decomposed into a heat flux perturbation and a freshwater flux perturbation. The salinification at depth mostly results from surface heat uptake (Figure B9c), which strongly increases stratification and restricts subduction of fresh water masses. Surface heat uptake contributes little to the surface salinity decrease, which is dominated by freshwater flux change (Figure B9b). The heat uptake effect on salinity change shows large intermodel variation. For example, ACCESS-CM2 and MPI-ESM1-2-HR show very large salinification along the salinity minimum, while MIROC6, MRI-ESM2-0, and our CESM1 show a much weaker increase in salinity. The large intermodel spread may be related to biases in mean stratification of salinity, a

topic that deserves further investigation. In addition, FAF-Buoy leads to freshening between 20˚S and 35˚S in the upper layer (Figure 3.2c), while salinification is found in the same region in Buoy (Figure 3.1e). The result from Buoy is consistent with surface P-E change (green curve in Figure 3.1a), and surface P-E change from FAF-Water (Figure B9a) is consistent with results from Buoy, while it is still unclear how FAF-Water gives rise to a much broader freshening in the Southern Ocean.

For the total response to quadrupled CO_2, we linearly combine the results from Buoy and Wstr (Figure 3.4). At higher latitudes, the surface layer is dominated by freshening due to more freshwater flux from the atmosphere (Figure 3.3f, g), which overwhelms the upwelling of saltier water driven by wind. This can be attributed to the imposed strong CO_2 forcing ($4\times CO_2$) which strongly warms the atmosphere. At mid-latitudes (40˚-50˚), the salinity change is dominated by wind forcing. Overall, the combined response from Buoy and Wstr is broadly consistent with observed long-term surface salinity change (Figure B6) and previous studies (Durack and Wijffels 2010; Swart et al. 2018). A discrepancy at intermediate depths from 20˚S to 40˚S appears to be associated with model drift due to prescribing surface wind stress since the fully coupled run ($4\times CO_2$ - CTRL) shows a different pattern of salinity change (Figure B1).

The atmospheric warming due to increased CO_2 in the partial-coupling experiments restricts sea ice formation such that the ice edge is farther south, especially in winter (Figure 3.5a, b). Interestingly, the wind stress changes also lead to reduced sea ice coverage (solid red contour in Figure 3.5a) because the enhanced vertical advection of heat driven by increased wind-driven upwelling results in SST increase (Figure 3.6a, b) and sea ice retreat (Figure 3.5a). Ferreira et al. (2015) show that the sea ice response to stratospheric ozone depletion depends on the time scale: the fast response is essentially confined to the mixed layer on short (~year) time scales; the slow

time-scale response (years to decades) is driven by ocean interior dynamics. The warming that we show 41-90 years after the CO_2 increase is the slow response. To isolate the fast response, we also show the change over the first two years (Figure 3.6c, d). The sea ice retreat is small during winter (Figure 3.6c), implying that the large seasonal sea ice cover dampens the wind effect on ocean circulation. In austral summer (Figure 3.6d), the sea-ice edge (15% of sea ice coverage) extends northward around the Weddell Sea and most of the coastal regions of East Antarctica. These fast responses are consistent with Purich et al. (2016), showing that during austral summer the enhanced westerly wind leads to increased upwelling of cooler Winter Water just below the surface, which is conducive to increased sea ice coverage. As documented by Ferreira et al. (2015), the effects of wind on SST and sea ice extent are time dependent, leading to increased sea ice extent on short timescales but decreased sea ice extent in the longer term. The intensified wind can increase Antarctic sea ice extent through stronger equatorward Ekman transport, but this effect is overwhelmed gradually by enhanced upwelling of warmer, subsurface water. This non-monotonic time evolution of Southern Ocean SST and sea ice extent driven by wind change, the initial cooling (more sea ice extent) followed by long-term slow warming (less sea ice extent), is well discussed in previous research (Kostov et al. 2017; Holland et al. 2017; Seviour et al. 2016).

3.6 Antarctic Circumpolar Current Response

We now quantify how buoyancy and wind effects contribute to ACC intensity and position. The major ACC fronts coincide with strong geostrophic velocity (U_g), which is calculated from sea surface height (SSH). Zonal geostrophic velocity changes are shown in Figure 3.7. In Buoy, surface geostrophic velocity within the ACC strengthens on average by 1.25 cm/s (+15%). In the Atlantic and Indian sectors, this zonal velocity increase is stronger, which is in line with the zonal

band of warming in the upper 2000 m north of the ACC (Figure B4b). The meridional asymmetry of warming across the ACC results in asymmetric sea level rise through thermal expansion and hence increased zonal geostrophic velocity. Wind-induced change in surface zonal geostrophic velocity is positive overall (Wstr, Figure 3.7c), but is patchy and weaker than the increase due to Buoy. The average velocity increase within the ACC is 0.52 cm/s (+6%). Interestingly, the surface horizontal circulation change within the ACC is dominated by buoyancy forcing.

The zonal mean patterns of zonal velocity change due to buoyancy and wind stress forcing changes for the whole water column are shown in Figure 3.8. For Buoy, zonal velocity change is predominantly baroclinic, confined to the upper ocean (above 1500 m) (Figure 3.8a), associated with density change across the ACC. Buoy increases the eastward ACC transport in the upper layer from 45˚S to 60˚S and creates more westward transport from 35˚S to 45˚S (Figure 3.8a), consistent with maximum warming at 45˚S (Figure 3.1c). Freshening in the south and salinification in the north (Figure 3.1e) would act to reduce the eastward ACC transport. Therefore, the spatial pattern of Southern Ocean heat uptake is responsible for the intensification of Buoy-driven circumpolar transport. In contrast, the wind stress-induced changes in the ACC have an equivalent barotropic structure, in which surface pressure is coherent with bottom pressure (Hughes et al. 2014). While it is vertically sheared, the zonal velocity increase due to wind stress penetrates to the ocean bottom (Figure 3.8b). The excess wind-driven momentum is transferred downward by the eddy buoyancy flux and balanced by bottom form drag (Marshall et al. 2017). The FAFMIP results (Figure 3.8c, d) agree with CESM1. FAF-Buoy leads to a weaker and shallower zonal velocity increase compared to Buoy from CESM1, which seems to be related to the relatively weaker warming (Figure 3.2a) due to smaller external radiative forcing.

Whether the ACC shifts in latitude in response to increased atmospheric CO_2 is a commonly posed question, especially given the well-documented poleward shift of the westerly winds under warming (Gille 2008; Böning et al. 2008; Downes et al. 2011; Meijers et al. 2011; Kim and Orsi 2014; Gille 2014). We calculate the position of the ACC (Figure 3.9) using two methods, from Gille (2014) and Meijers et al. (2012). Using the Gille (2014) method (Figure 3.9a), Buoy accounts for a 0.3˚ southward shift of the mean ACC with a standard deviation of 0.9˚ as determined from 1000 Monte Carlo realizations. Similarly, Wstr accounts for a 0.3˚ southward shift with a standard deviation of 0.6˚. In the Monte Carlo realizations, the northern and southern integration limits are randomly perturbed using Gaussian random numbers with a standard deviation of 5˚ latitude. The large range indicates the sensitivity of the mean ACC position to the choice of northern and southern integration limits in this method. Using the Meijer et al. (2012) method to calculate the ACC location (Figure 3.9b), Buoy leads to a 0.3˚±0.1˚ southward shift of ACC core and Wstr leads to a 0.4±0.1˚ southward shift, with the uncertainty range here determined from temporal variability. Using this method, the ACC shifts due to both Buoy and Wstr are statistically significant at the 95% level. The southward shift primarily takes place in the Atlantic and Indian sectors where surface fronts are strong. For comparison, the westerly wind position, based on the Gille (2014) method (substituting zonal wind stress for U_g in Eq. (3.5)), shifts southward by 1.2˚±0.3˚ in latitude (Figure 3.9c). All seasons show southward wind shifts, with maximum southward shift (2.1˚±1.3˚) in austral summer (December through February; not shown). This southward shift in annual mean wind is about 3 or 4 times greater than the southward shift in ACC position.

3.7 Discussion and Conclusion

The Southern Ocean is regarded as a key player in the response of the global climate system to external forcing such as the anthropogenic emissions of CO_2. External CO_2 forcing gives rise to buoyancy flux change and surface wind stress change, which can lead to changes in ocean circulation and tracers. Previous studies largely focused on the response of the Southern Ocean to changes in westerly wind, whereas in this study we note that buoyancy forcing can play an even more critical role in Southern Ocean climate change. Using a novel partial coupling technique in CESM1, we separate the effects of buoyancy and wind (momentum) forcing on Southern Ocean temperature, salinity, and circulation changes under quadrupled CO_2. Since the external CO_2 forcing is large, buoyancy forcing dominates the Southern Ocean warming, with more warming on the northern than on the southern flank of the ACC due to the mean MOC. Buoyancy forcing also dominates surface freshening in the Southern Ocean. We find that the surface salinity increase over the Southern Ocean driven by wind forcing can substantially offset surface freshening driven by buoyancy forcing. Furthermore, buoyancy forcing leads to an increase in baroclinic transport within the ACC associated with an increase in the cross-stream density gradient. In contrast, wind stress change increases barotropic transport by altering the zonal momentum balance. Buoyancy forcing changes dominate the surface horizontal circulation acceleration.

About 80% of the total heat storage change to the south of 30˚S from the quadrupling CO_2 case is attributed to buoyancy forcing, which includes the increase in the surface heat flux. The warming/cooling pattern driven by wind forcing is associated with deepening/shoaling of isopycnals. For salinity change, interestingly, buoyancy and wind forcing result in opposing changes, especially within the mixed layer. The surface freshening induced by buoyancy forcing is mainly attributed to more freshwater flux from the atmosphere, which is consistent with previous

studies (e.g. Swart et al. 2018). The wind stress change, however, leads to surface salinity increase, driven by increased Ekman upwelling of saltier deep water and northward Ekman advection. This wind-induced salinity increase offsets the freshening due to buoyancy forcing. At higher latitudes, the surface layer is dominated by buoyancy forcing, whereas at mid-latitudes (40˚S-50˚S), the salinity change is dominated by wind forcing. Hence the relative strength of buoyancy and wind forcing can significantly affect the pattern of salinity change. Accurate surface forcing is crucial to understanding the fingerprint of salinity change, in addition to the fingerprint of temperature change. Salinity change occurs at a shallower depth than temperature change, due to shallower stratification in mean salinity compared with temperature.

Buoyancy and wind forcing both trigger retreat of sea ice extent around the Antarctic, especially during austral winter when sea ice is formed (Figure 3.5b). Thus, the northward advection of freshwater due to sea ice is reduced (Figure 3.5c,d,e; Haumann et al. 2016; Abernathey et al. 2016). For wind forcing, the intensified upwelling of warmer subsurface water restricts the formation of sea ice, which overcompensates the equatorward extension of sea ice driven by intensified Ekman transport. Several modeling studies have shown that meltwater from the Antarctic ice sheet can cause significant global sea level rise, reduction of global mean atmospheric warming, and more stratified ocean surface water (de Lavergne et al. 2014; Fogwill et al. 2015; Bronselaer et al. 2018). Interestingly, even without an interactive ice sheet in our model (CESM1), we still find large-scale surface freshening driven by buoyancy forcing (Figure 3.1e), which is consistent with results from Pauling et al. (2016). The observed SST cooling and expansion of Southern Ocean sea ice extent is reproduced by neither the idealized FAFMIP nor our CESM simulations, which seems to be a common issue in models. The poleward intensified westerly winds could lead to an initial surface cooling (Kostov et al. 2017; Holland et al. 2017),

which would last only a few years. Surface freshening is also used in other studies to explain observed sea-ice expansion, SST cooling, and subsurface warming, and is associated with a reduction of deep convection (Bintanja et al. 2013; De Lavergne et al. 2014; Purich et al. 2018). Bronselaer et al. (2020) and Rye et al. (2020) argue that Antarctic glacial melt is essential to recent Southern Ocean climate trends. However, some studies argue that the melting of the Antarctic ice sheet is too weak to trigger sea-ice expansion (Swart and Fyfe 2013; Pauling et al. 2016; Haumann et al. 2020), and the enhanced northward freshwater transport by the sea ice is found to be the predominant cause of the recent observed trends in the high-latitude Southern Ocean (Haumann et al. 2020). Natural variability is also an important factor. For instance, Zhang et al. (2019) found that natural multidecadal variability in Southern Ocean convection may have strongly contributed to the observed temperature and sea-ice trend. More work is required to explore the exact cause of the historical trends in the Southern Ocean and contribute to reliable future projections.

An increase in ACC transport that is weaker than expected given the increased winds in these experiments is consistent with recent studies (Morrison and Hogg 2013; Dufour et al. 2012; Farneti et al. 2015; Langlais et al. 2015). For example, in Bishop et al.'s (2016) high-resolution ocean model, a 41% increase in zonal wind stress led to only about a 6% increase in ACC transport; the weakness of the transport response was attributed to eddy saturation due to stronger baroclinicity and instability in the ACC. In our Wstr experiment, we find a 5% (8.7±2.3 Sv) increase in Drake Passage transport in response to a 19% increase in westerly winds (+0.036 N/m^2), supporting the eddy saturation hypothesis. (Here the uncertainty denotes interannual variability.) Hogg (2010) and Stössel et al. (2015) point out that the strength of mean ACC strongly depends on the surface buoyancy flux. In our study, we find that buoyancy forcing causes a positive but weaker Drake Passage transport change (3.1±1.6 Sv) by increasing the meridional density gradient

due to stronger warming on the northern flank of the ACC than to the south. More importantly, we find that wind and buoyancy forcing lead to different vertical structures of ACC transport change. While previous research has focused on the effect of wind on ACC change, we find that the surface horizontal current acceleration within the ACC is dominated by buoyancy forcing, rather than change in wind. We show that wind changes create a more barotropic increase in circumpolar transport, manifested as an intensified zonal circumpolar current from the surface to the bottom. For buoyancy forcing, ACC strength is mainly governed by changes in the density structure, in other words, by the baroclinic thermal wind transport. Farneti et al. (2015) evaluate the Drake Passage transport change due to wind forcing and buoyancy forcing for 1958–2007 in a suite of cases from the second phase of the Coordinated Ocean-ice Reference Experiments (CORE-II). They find that wind forcing dominates the increase in transport despite eddy saturation. Buoyancy forcing in their experiments, however, leads to a weak reduction in transport, which is inconsistent with our results. They attribute this reduction in transport to a flattening of the isopycnals. We also find flattening of isopycnals in Buoy (Figure 3.1c). However, the surface pressure gradient force from 45˚S to 60˚S increases in our experiments due to the asymmetric warming across the ACC, hence leading to a zonal transport increase in the upper layer (Figure 3.7a). One possible explanation for the discrepancy is that Farneti et al.'s (2015) global mean surface heat flux during their recent five decades is 2.63 W m^{-2}, which is much smaller than in our $4\times CO_2$ experiment (6.25 W m^{-2} for the first 10-year average), so the ACC response to the meridional gradient of warming is not significant in their simulations. As a caveat, the resolution of our model is not fine enough to resolve mesoscale eddies, so the results shown here are based on eddy parameterization. Future investigations should consider how eddy resolution contributes to Southern Ocean responses to buoyancy and wind forcing.

Estimates of the shift in the ACC position can be biased if based on fixed SSH contours, which are strongly affected by large-scale steric expansion associated with warming and freshening of the Southern Ocean. By using two independent methods from Gille (2014) and Meijers et al. (2012), associated with meridional gradient of SSH or streamfunction, we show Buoy and Wstr each result in 0.3˚±0.1˚ southward shifts. The significance of the shift is based on the method from Meijers et al. (2012). The small southward shift from Buoy and Wstr may be associated with the shift of the Subtropical Front north of the ACC, which is strongly surface intensified and confined in the upper layer (Graham et al. 2012). In addition, we find that the southward shifts of the mean ACC mainly occur in the eastern Atlantic and Indian sectors where the fronts are strongest.

We diagnosed the distinct patterns of Southern Ocean change driven by buoyancy and wind forcing only due to an unrealistically strong anthropogenic forcing. The $4\times CO_2$ forcing (around 7 W m^{-2}) in our experiments is much stronger than the actual well-mixed GHG radiative forcing (2.83±0.29 W m^{-2}) in 2011 relative to 1750 (Myhre et al. 2013), and is comparable to the radiative forcing (8.5 W m^{-2}) from Representative Concentration Pathway (RCP) 8.5 in the year 2100. The wind stress change (+0.036 N/m^2) in our simulation is a little smaller than that in RCP8.5, at 0.047 N/m^2 (2080-2100 anomaly relative to the piControl runs from the ensemble mean of 27 CMIP5 models). Even so, the fingerprint of change due to the separate effects of buoyancy and wind forcing can help us better understand the long-term change in the Southern Ocean. In reality, stratospheric ozone depletion, which is not considered in our study, can also give rise to poleward-intensified westerlies (Thompson 2002). In the future, the relative strength and importance of buoyancy and wind forcing are likely to change due to the recovery of stratospheric ozone, which can weaken the westerlies. Reduction in anthropogenic aerosols might intensify the westerlies (e.g.

Shi et al. 2018). Therefore, the Southern Ocean responses are likely to evolve with changes in these forcing terms. For instance, since we find surface salinity change is determined by the compensation between buoyancy and wind forcing effects, we would expect a distinct salinity change pattern in the future relative to the historical change as the relative strength of buoyancy and wind forcing evolves.

3.8 Acknowledgments

J.-R. Shi is supported by U.S. National Science Foundation (AGS-1637450) and the Southern Ocean Carbon and Climate Observations and Modeling project (SOCCOM) under National Science Foundation Award (PLR-1425989). L.D.T. and S.T.G. are also supported by SOCCOM, and S.T.G. received additional support from NSF Award OCE-1658001. W.L. is supported by the Regents' Faculty Fellowship, and also by the Alfred P. Sloan Foundation as a Research Fellow. We thank the CMIP6 groups and the FAFMIP group for producing and making available their model output, which is available from https://esgf-node.llnl.gov/projects/cmip6/. The Argo data used here were collected and made freely available by the International Argo Program and by the national programs that contribute to it (http://argo.ucsd.edu). The World Ocean Atlas 2018 products are available on the NOAA National Oceanographic Data Center website (https://www.nodc.noaa.gov/OC5/woa18/).

Chapter 3, in full, is a reprint of the material as it appears in *Journal of Climate*, 2020: Jia-Rui Shi, Lynne D. Talley, Shang-Ping Xie, Wei Liu, Sarah T. Gille, "Effects of Buoyancy and Wind Forcing on Southern Ocean Climate Change". The dissertation author was the primary investigator and author of this paper.

Table 3.1: Notations for partial-coupling experiments using NCAR CESM1. In partial coupling, wind stress and wind speed are shifted forward by one year.

Names	Note
τ1	Wind stress from CTRL
τ4	Wind stress from 4×CO_2
w1	Wind speed from CTRL
c1	1×CO_2 (preindustrial level) emission (CTRL)
c4	4×CO_2 emission (4×CO_2)
τ1w1c1	Partial coupling with CTRL variables
τ1w1c4	Partial coupling with quadrupled CO_2
τ4w1c4	Partial coupling with τ4 and quadrupled CO_2
CTRL	Fully coupled, preindustrial control run
4×CO_2	Fully coupled, abruptly quadrupled CO_2

Table 3.2: Buoyancy and wind forcing effects derived from experiments using the CESM1 partial-coupling technique. The differences between individual pairs of partial-coupling experiments reveal the contributions from Buoy and Wstr. The total effect of wind and buoyancy forcing is Total (Buoy + Wstr, or τ4w1c4 - τ1w1c1).

Effects	Note	Derivation
Buoy	Buoyancy forcing effect	τ1w1c4 - τ1w1c1
Wstr	Wind forcing effect	τ4w1c4 - τ1w1c4
Total = Buoy + Wstr	Total effect	τ4w1c4 - τ1w1c1

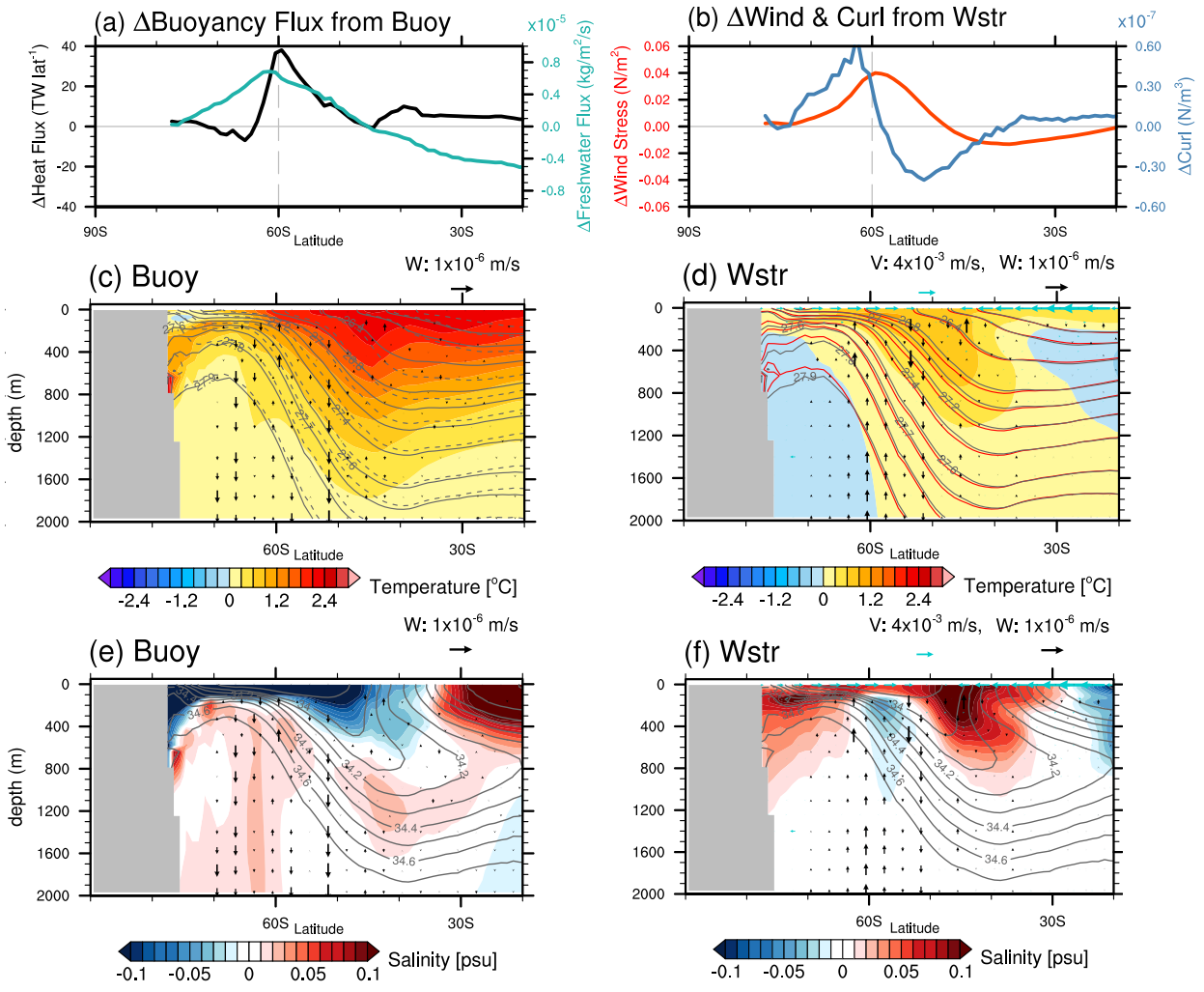

Figure 3.1: Change of (a) zonally-integrated surface heat flux (black) and zonal mean of precipitation minus evaporation (green) due to buoyancy forcing (Buoy) and (b) zonal mean of zonal wind stress (red) and wind-stress curl (light blue) due to wind stress forcing (Wstr) over the Southern Ocean for CESM1, calculated as the average of years 41-90 minus the preindustrial control. The same averaging is used in subsequent figures unless otherwise specified. Zonal mean temperature change (shading) in the upper 2000 m in (c) Buoy and (d) Wstr for CESM1. Climatological isopycnals are shown as contours: dashed gray contours are from τ1w1c1, solid gray contours from τ1w1c4, and red contours from τ4w1c4. Zonal mean salinity change (shading) in the upper 2000m for (e) Buoy and (f) Wstr, with climatological salinity profiles shown as contours. Vertical velocity and meridional surface velocity changes are shown as black and cyan vectors, respectively. All velocity variables include the eddy-induced velocity.

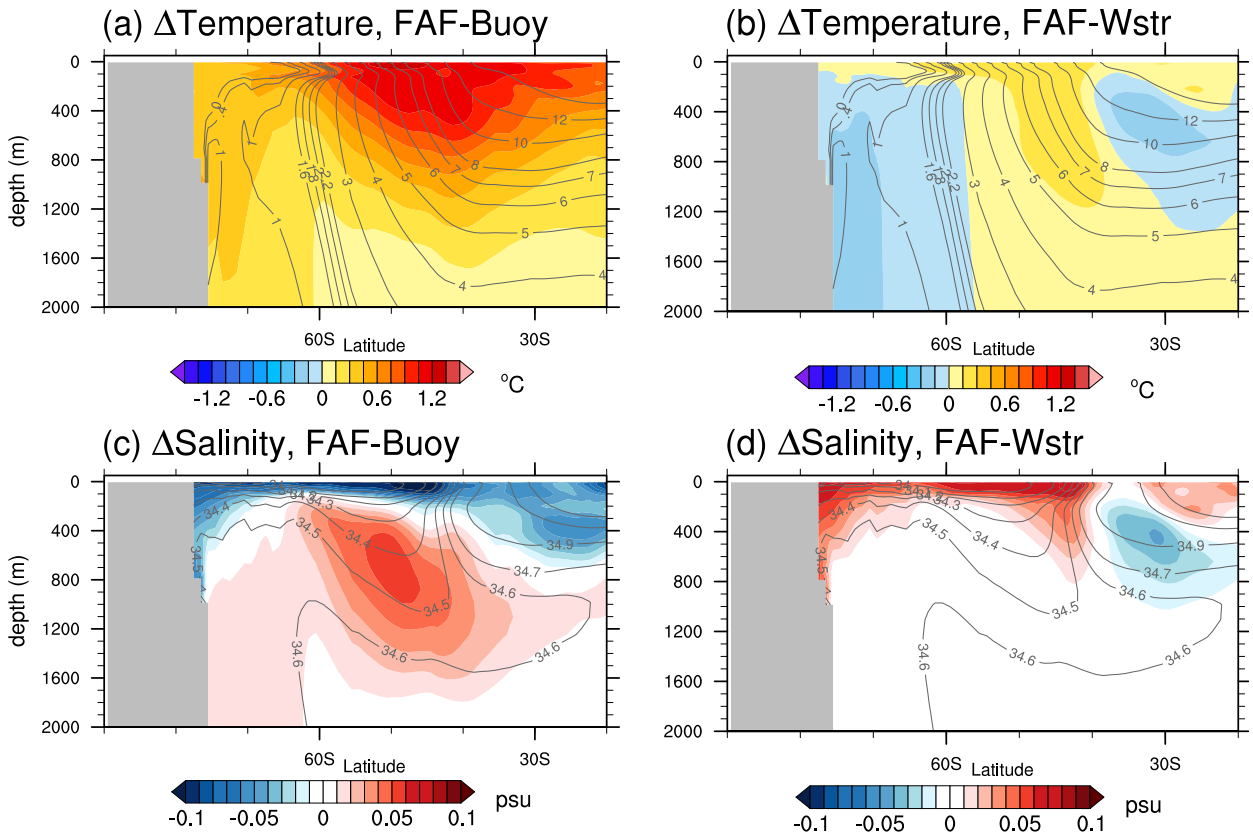

Figure 3.2: Zonal mean temperature change in the upper 2000m from the ensemble mean of FAFMIP experiments: (a) FAF-Buoy, (b) FAF-Wstr. (c) and (d) as in (a) and (b), but showing corresponding zonal mean salinity change. The anomalies represent the difference between the 41-70 year average and the climatology from the corresponding preindustrial control run. Contours show the 30-year climatology.

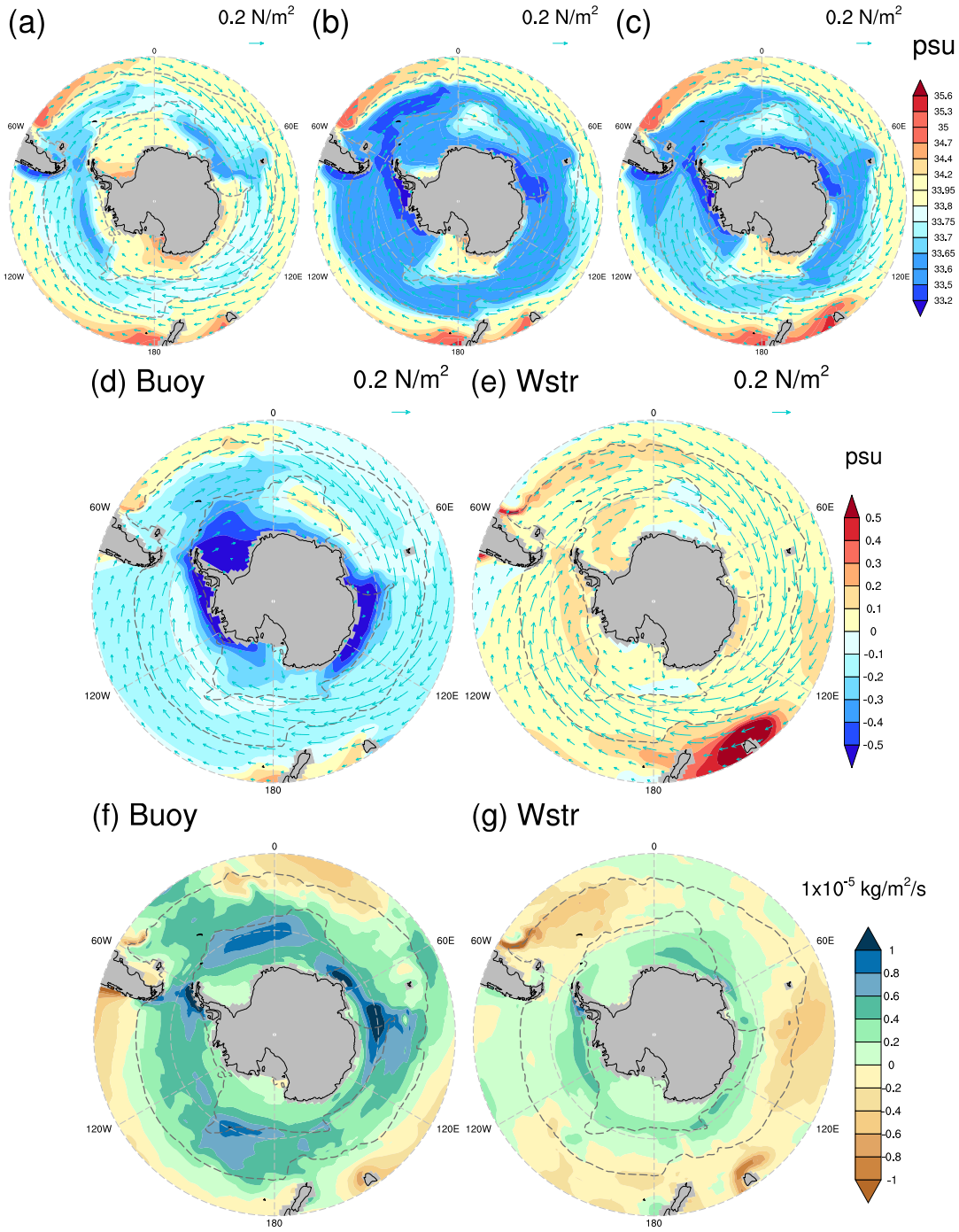

Figure 3.3: Fifty-year climatological salinity within the upper 50m for: (a) τ1w1c1, (b) τ1w1c4 and (c) τ4w1c4 (see Table 3.1 for definitions). Change of salinity in the surface layer (0-50 m) in (d) Buoy and (e) Wstr. Change of precipitation minus evaporation over the Southern Ocean in (f) Buoy and (g) Wstr. The dashed gray contours indicate the northernmost and southernmost barotropic streamfunctions passing through the Drake Passage from preindustrial control, indicating the ACC envelope. Cyan vectors indicate climatological surface wind stress from preindustrial control.

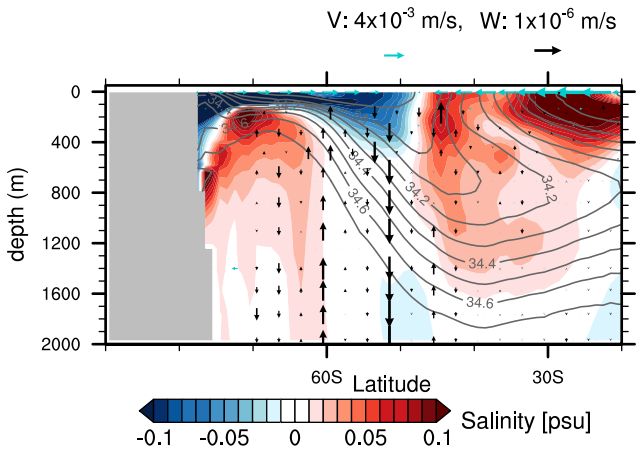

Figure 3.4: Zonal mean salinity change (shading) in the upper 2000 m for Total. Climatological salinity profiles are shown as gray contours. Vertical velocity and meridional surface velocity changes are shown as black and cyan vectors, respectively.

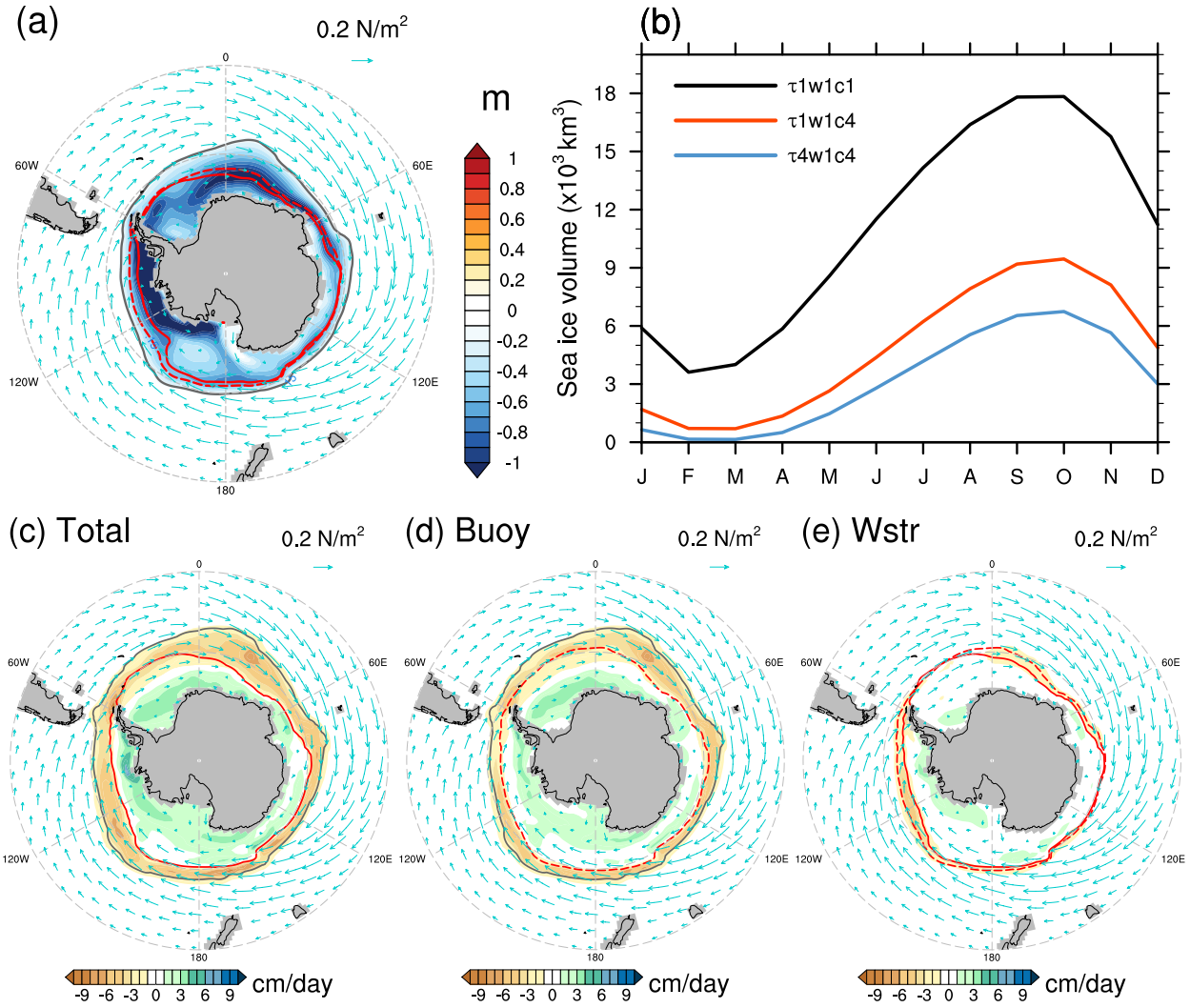

Figure 3.5: (a) September sea ice thickness change in Total (shaded); sea ice edges (contours) based on 15% sea ice fraction from different experiments: τ1w1c1 (gray), τ1w1c4 (dashed red), and τ4w1c4 (solid red). (b) Annual cycle of sea ice volume in the Southern Hemisphere. Annual mean freshwater flux change from sea ice in response to (c) Total, (d) Buoy, and (e) Wstr. Positive values indicate more freshwater flux entering the ocean due to sea ice melting. Cyan vectors show climatological surface wind stress from τ1w1c1.

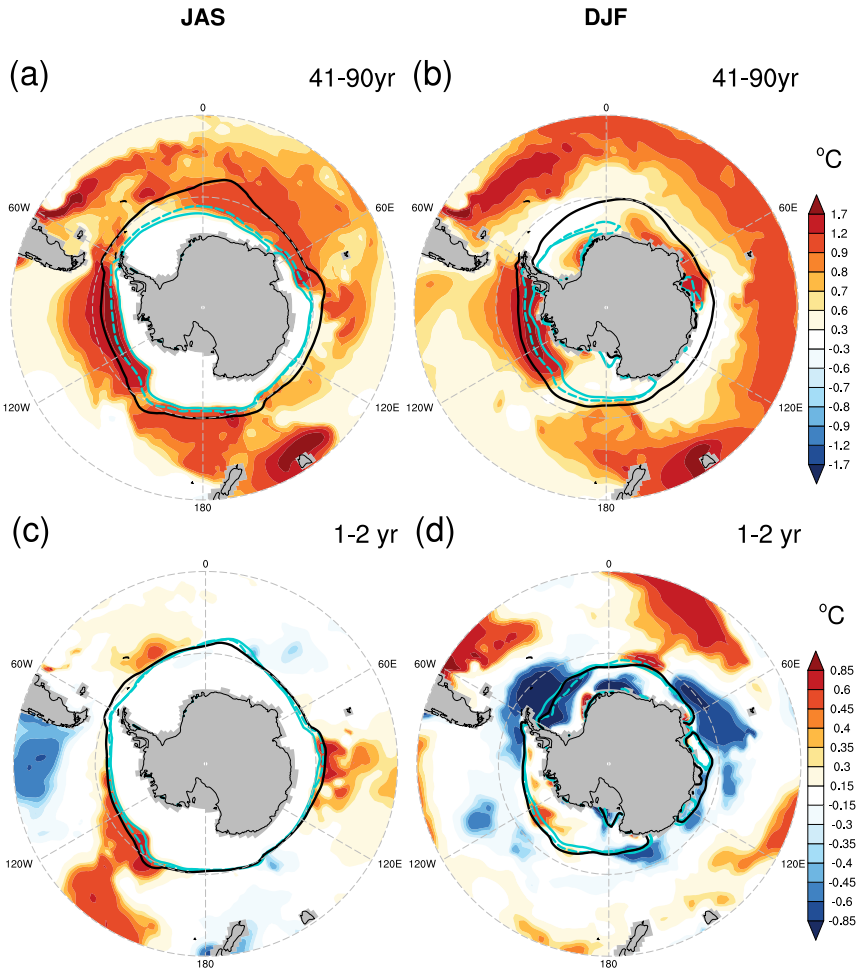

Figure 3.6: Changes of SST (shading) and sea-ice edge (contours) due to Wstr for different periods and seasons. Changes in years 41-90 relative to the control run for (a) JAS and (b) DJF. (c)-(d) as in (a)-(b), but for changes in the first two years. Black contour indicates the sea-ice edge from τ1w1c1, dashed cyan contour indicates sea-ice edge when CO_2 is quadrupled without wind change (τ1w1c4), and solid cyan contour indicates sea-ice edge when both CO_2 and wind changes (τ4w1c4).

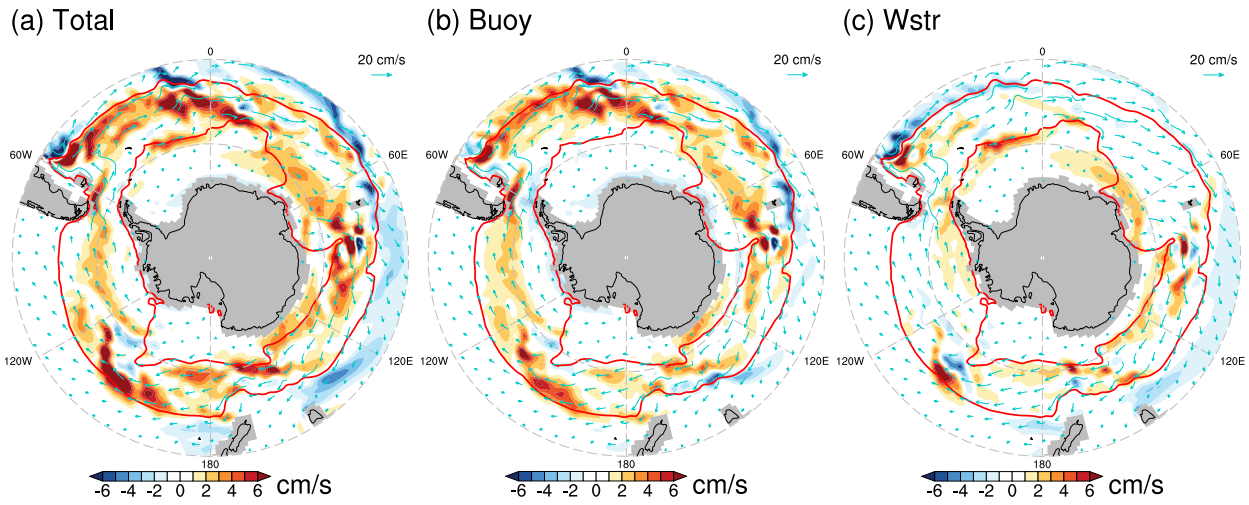

Figure 3.7: Change of surface zonal geostrophic velocity (U_g) (shaded) for (a) Total, (b) Buoy, and (c) Wstr. Climatological ocean velocities in the surface layer (0-50 m) are shown as cyan vectors. The red contours show the ACC envelope. The velocity fields are shown in Figure B10.

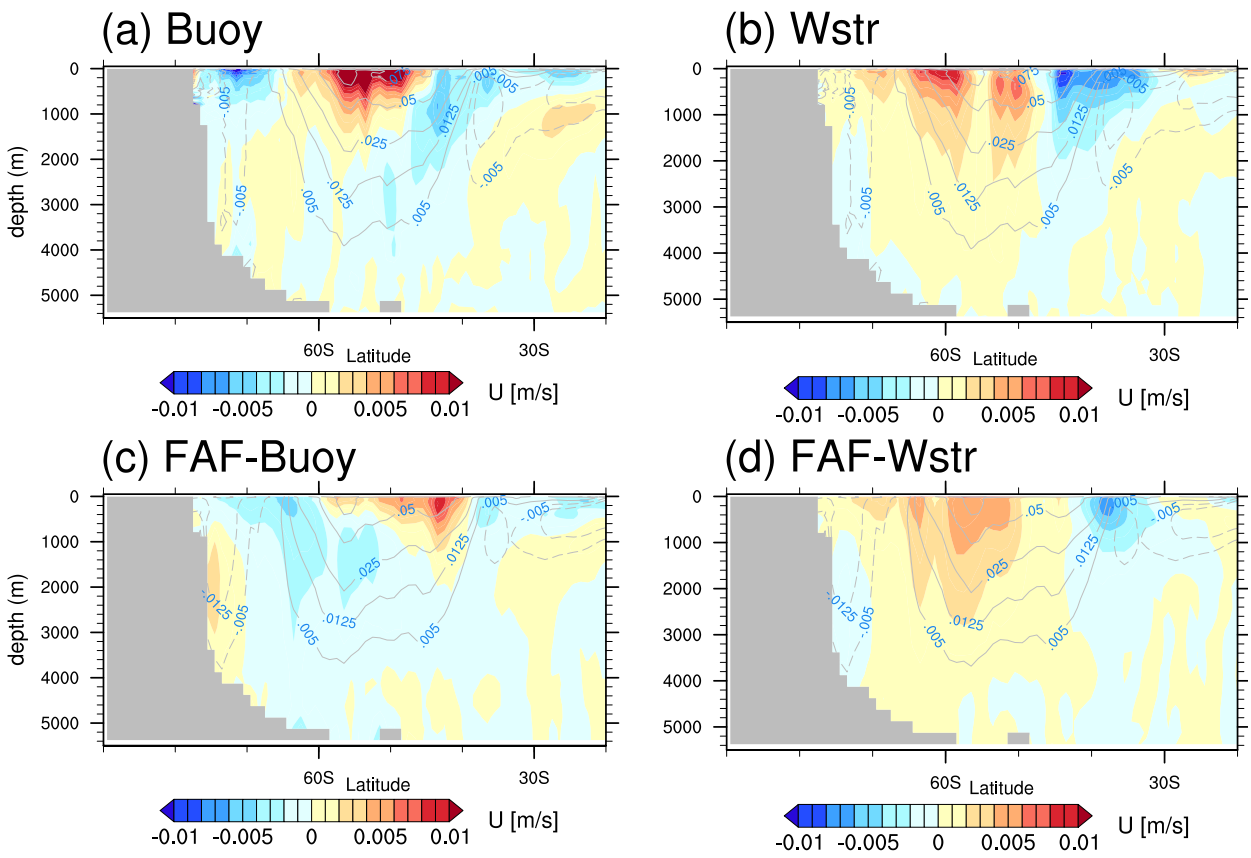

Figure 3.8: Zonal mean of zonal velocity change in response to (a) Buoy and (b) Wstr from CEMS1 partial-coupling experiment and (c) FAF-Buoy and (d) FAF-Wstr from FAFMIP. The contours indicate zonal-mean climatology of zonal velocity from preindustrial control.

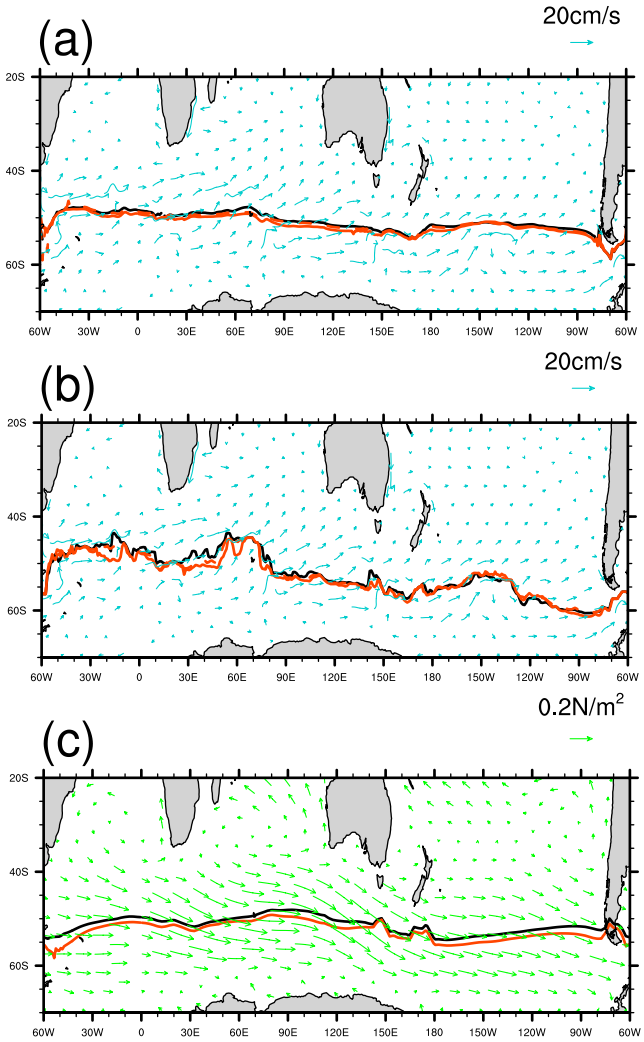

Figure 3.9: (a) Positions of the mean ACC, based on the weighted mean zonal surface geostrophic velocity at each longitude. (b) Position of ACC core based on the method from Meijers et al. (2012). ACC position from τ1w1c1 (black); τ1w1c4 (dashed red); τ4w1c4 (solid red). Climatological ocean velocity in the upper 50m in the preindustrial control (cyan vectors). (c) similar to (a), but positions of weighted mean center of zonal surface wind stress. Climatological surface wind stress from preindustrial control (green vectors).

Chapter 4

Acceleration of the Southern Ocean Zonal Flow

4.1 Abstract

The Southern Ocean circulation redistributes heat, carbon, and other properties across ocean basins. It is unclear how the Antarctic Circumpolar Current (ACC) has changed in response to global warming because the remote Southern Ocean was poorly observed prior to the 1990s. Theoretically, eddy saturation could render the ACC insensitive to the increasing wind stress. Here we document a robust acceleration of Southern Ocean zonal flow at latitudes 48˚S-58˚S since 1993 (satellite altimetry) and since 2005 (Argo floats). This zonal acceleration is reproduced in a hierarchy of climate models, including an ocean-eddy-resolving model. Anthropogenic buoyancy change is the dominant driver, as heat gain north of the ACC, counterbalanced by upwelling of deep water within and south of the ACC, causes zonal acceleration in the upper layer due to increased baroclinicity, while strengthened wind stress is of secondary importance. Continued ocean warming could further accelerate eastward flow in the Southern Ocean.

4.2 Introduction

The Southern Ocean, often defined as the ocean south of about 30˚S, has experienced pronounced subsurface warming, widespread surface freshening, increasing anthropogenic carbon, and changes in oxygen and chlorofluorocarbons over the past several decades of observations (Gille 2008; Böning et al. 2008; Roemmich et al. 2015; Durack and Wijffels 2010; Sabine 2004; Talley et al. 2016; Waugh et al. 2013). Modeling studies suggest that greenhouse gas (GHG) increase and stratospheric ozone depletion, are major drivers of Southern Ocean change (Fyfe 2006; Sigmond et al. 2011; Swart et al. 2018; Shi et al. 2018). The strength of the Southern Ocean overturning circulation plays an important role in regulating the exchange of anthropogenic heat at the sea surface and in redistributing oceanic tracers (Manabe et al. 1990; Armour et al. 2016; Shi et al. 2018, 2020). Moreover, horizontal ocean circulation, including the Antarctic Circumpolar Current (ACC) and subtropical gyres in the Southern Ocean, moves water thousands of kilometers, facilitating the exchange of ocean properties across ocean basins (Rintoul 2018). Hence, quantifying how and understanding why the Southern Ocean horizontal circulation changes in the context of global warming is vital to interpreting past climate change and for reliable future climate projections.

Previous studies of changing Southern Ocean circulation have focused mostly on the effect of changes in the zonal winds, which are shifting poleward and intensifying under global warming. These studies have concluded that the Southern Ocean's large zonal transport, including the ACC, is insensitive to the increasing wind stress (Hallberg and Gnanadesikan 2006; Meredith and Hogg 2006; Farneti et al. 2010; Downes et al. 2011; Meredith et al. 2012; Marshall et al. 2017), and that the additional energy imparted by the wind increase mostly goes into mesoscale eddies, an effect known as eddy saturation (Munday et al. 2013). Analyses of Argo profiling float and historical

oceanographic data carried out a decade ago showed little change in ACC isopycnal slopes and transport during recent decades even as the winds strengthened (Böning et al. 2008). On the other hand, a more recent analysis, using data-assimilating models and a longer record of observations, shows increasing Southern Ocean kinetic energy over recent decades, with speculated attribution to increased wind energy (Hu et al. 2020). It has been shown that subtropical gyre changes in water properties and currents are dominantly forced by sea surface warming rather than wind stress change (Wang et al. 2015). We have recently shown, using the Community Earth System Model (CESM) with eddy parameterization (Gent and Mcwilliams 1990; Gent and Danabasoglu 2011), that buoyancy forcing due to ocean warming should significantly accelerate the zonal flow in the upper layer, i.e. 0-2,000 m, in the Southern Ocean, in contrast to much weaker acceleration induced by increased wind stress (Shi et al. 2020). The background Southern Ocean meridional overturning circulation, comprised of the upwelling of pristine deep water at higher latitudes (55˚S-60˚S) and northward Ekman transport, redistributes the absorbed heat under global warming and results in delayed warming on the southern flank of the ACC and enhanced warming on the northern flank (Armour et al. 2016; Liu et al. 2018). This uneven warming distribution increases the meridional density gradient and enhances zonal geostrophic velocity in the upper layer (Shi et al. 2020).

Is there observational evidence of these simulated heat and transport changes? Argo float observations show remarkable north-south asymmetry in warming over the 0-2,000 m layer in the Southern Ocean between 2006 and 2013 (Roemmich et al. 2015). This warming has continued, as shown here, and continues to be much greater north of the ACC than within and south of the ACC (see Figure 4.1 below). Associated with this warming distribution, we show here a robust and statistically significant acceleration of the Southern Ocean zonal flow between 48˚S and 58˚S, based on satellite altimeter and Argo float data. We compare the observed buoyancy and velocity

changes with historical simulations from the sixth phase of the Coupled Model Intercomparison Project (CMIP6) models and CESM large ensemble simulations, and show the role of external buoyancy forcing in driving acceleration of Southern Ocean eastward flow. This conclusion is also supported by a CESM eddy-resolving model. Using a hierarchy of idealized general circulation model (GCM) simulations, we find that the magnitude and spatial pattern of the observed zonal flow changes are more likely to arise from buoyancy forcing changes than from wind stress changes.

4.3 Methods

4.3.1 Observations

The Argo program, consisting of a global array of 3,800 free-drifting profiling floats, provides systematic coverage of global ocean temperature and salinity of the upper 2000 m since 2005 (Roemmich et al. 2015), before which the sampling was spatially and temporally sparse, especially in the Southern Hemisphere. Here we used the monthly gridded Argo temperature and salinity data (Roemmich and Gilson 2009) from 2005 to 2018 to examine recent trends and to compute dynamic height and geostrophic velocity relative to 2000 dbar:

$$D = -\frac{1}{g}\int_{p_0}^{p}\frac{1}{\rho}\,dp \tag{4.1}$$

$$U_g(p) - U_g(p_0) = -\frac{g}{f}\frac{\partial D}{\partial y} \tag{4.2}$$

where D is the dynamic height at pressure p relative to reference pressure p_o, g is the acceleration due to gravity, ρ is density, and f is the Coriolis parameter. The relative zonal geostrophic velocity is the velocity relative to the velocity at the reference level, p_o. Here we use 2000 dbar as the

reference level with no motion, $U_g(p_0) = 0$. The data are on a 1˚x1˚ grid with 58 vertical levels from the surface to 2000 m.

Institute of Atmospheric Physics (IAP), Met Office Hadley Centre (EN4), and World Ocean Atlas 2018 (WOA18) datasets (temperature and salinity) were used to examine the trends of potential temperature and geostrophic velocity for longer periods. The calculation of geostrophic velocity is the same as that for Argo data (Eq. 4.1 and 4.2). These observationally-based products include shipboard, mechanical bathythermograph, XBT, and Argo profiles. IAP provides monthly mean ocean temperature and salinity from 1940 through 2018 (Cheng et al. 2018). The data are on a regular 1˚x1˚ grid with 41 vertical depth levels in the upper 2000 m. The EN4 (version EN4.2.1) is a subsurface temperature and salinity dataset for the global oceans, spanning 1900 to present with monthly timesteps (Good et al. 2013). The XBT bias was corrected by using the methods from Gouretski and Reseghetti (2010). The data are on a regular 1˚x1˚ grid with 42 vertical depth levels in the upper 2000 m. WOA18 is a uniformly formatted and quality-controlled data set based on the World Ocean Database. Objectively analyzed climatologies of temperature and salinity (Locarnini et al. 2019) (1955-1964, 1965-1974, 1975-1984, 1985-1994, 1995-2004, and 2005-2017) were used in this study to calculate geostrophic velocity for corresponding decades. The data are on a 1˚x1˚ grid from the surface to 5350 m depth. Here we focus on the fields in the upper 2000 m.

Satellite-based sea surface heights (SSH) relative to the geoid (data from AVISO satellite altimetry) were used to investigate dynamic changes of the ocean surface. The surface geostrophic velocity is:

$$U_g(surface) = -\frac{g}{f}\frac{\partial \eta}{\partial y} \tag{4.3}$$

where η is the altimetric sea surface height. The spatial resolution of the product is 1/4˚ (720 latitude × 1440 longitude). Observed altimeter trends (1993-2018) were smoothed to spectral wavenumber 42 (2.5˚ x 2.5˚ resolution) to remove higher frequencies from the field (e.g., as in Fasullo and Nerem 2018), and then remapped to 1˚x1˚ for comparison with other observations.

4.3.2 CMIP6 simulations

A set of CMIP6 historical simulations (Eyring et al. 2016), including solar, volcanic, anthropogenic aerosol, ozone depletion, land-use change, and greenhouse gas effects, was used here. One of the advantages of CMIP6 compared with CMIP5 is that the CMIP6 historical simulation extends to the near present, the year 2014. Linear trends are calculated over different periods, such as 1979-2014 and 1993-2014, for ocean potential temperature, ocean zonal velocity, and atmospheric surface pressure. Velocity at 2000 m depth is subtracted from the modeled velocity trends to be consistent with geostrophic velocity relative to 2000 dbar calculated from observations. The results from the multi-model ensemble mean of 26 CMIP6 models represent the externally forced responses. Uncertainty ranges stated in the text are ±1 standard deviation across the models. The CMIP6 models used in this study for the ocean potential temperature, zonal velocity, and atmospheric surface pressure are listed in Table C1. We regridded all model output to a regular 1˚x1˚ latitude-longitude grid.

4.3.3 Large ensemble simulations.

We used two sets of large ensemble simulations: the CESM1 Large Ensemble (LENS), and the Canadian ESM version 5 (CanESM5) large ensemble, which is part of CMIP6. LENS includes 40 realizations that start with different initial conditions for the air temperature to drive ensemble

spread, but with the identical radiative forcing (Kay et al. 2015). The effects of external forcing and internal climate variability can be isolated by analyzing the ensemble mean and deviations, respectively. All the external anthropogenic and natural forcings are applied to force the fully coupled model following historical (1920-2005) and the Representative Concentration Pathway 8.5 (RCP8.5) scenarios (2006-2100). Similarly, CanESM5 includes 25 members with different atmospheric initial conditions under historical (1850-2014) and future radiative forcing scenarios (RCP8.5: 2015-2100) (Swart et al. 2019). The linear trends are calculated for ocean zonal velocity and surface geostrophic velocity based on sea surface height from these two sets of large ensemble simulations. Uncertainty ranges stated in the text are ±1 standard deviation across the realizations, representing the internal variability.

4.3.4 CESM high-resolution and standard-resolution simulations.

The CESM high-resolution simulation (CESM1-HR or CESM1-CAM5-SE-HR) used in this study is version 1.3 at 0.25˚ resolution for the atmosphere and land, and 0.1˚ resolution for the ocean and sea-ice components, performed under the umbrella of the International Laboratory for High-Resolution Earth System Prediction. The transient simulation with RCP8.5 extension, spanning from 1950 to 2050, is part of the High-Resolution Model Intercomparison Project (HighResMIP). Mesoscale eddies in the ocean are resolved in CESM1-HR. To diagnose the sensitivity of our results to the model resolution, we also used CESM version 1.3 standard-resolution simulation (CESM1-SR or CESM1-CAM5-SE-LR) for comparison. The atmosphere and ocean model in CESM1-SR has an approximate grid spacing of about 1 degree, with other setups the same as CESM1-HR. The ocean model employs a temporally and spatially varying

specification of the Gent-McWilliams eddy parameterization (Gent and Mcwilliams 1990; Gent and Danabasoglu 2011). We investigated long-term trends of zonal velocity for 1979-2018 and 1993-2018, and discussed whether the parameterized and resolved mesoscale eddies affect our conclusions.

4.3.5 Idealized GCMs.

Here we employed a partial coupling technique (Liu et al. 2015) to isolate the effects of the atmosphere-warming-induced and wind-change-induced Southern Ocean climate change. We used the CESM version 1.0.5, in which version 5 of the Community Atmosphere Model (CAM5) runs at a nominal 2˚resolution (1.9˚latitude x 2.5˚longitude) with 26 vertical layers, and version 2 of Parallel Ocean Program (POP2) runs at a nominal resolution of 0.5˚in latitude and 1˚in longitude over the Southern Ocean. The Community Land Model, version 4, and Community Ice Code, version 4, are coupled with the atmosphere and ocean model. A temporally and spatially varying specification of the Gent-McWilliams eddy parameterization is employed in the ocean model. First, we ran a fully coupled, preindustrial control run (CTRL) as the baseline, which starts from the AD 1850 scenario. We then ran a simulation (CESM1_ΔBuoy) with the atmospheric CO_2 level quadrupled but prescribing the surface wind from CTRL. The transient response to surface buoyancy change can be obtained by taking the difference between CESM1_ΔBuoy and CTRL. To isolate the effect of the wind change under global warming, we also ran a simulation (CESM1_ΔWind) with the atmospheric CO_2 level quadrupled and prescribing the surface wind from a fully-coupled, abruptly quadrupled CO_2 run. Sea surface temperature (SST) and sea surface salinity (SSS) interact with atmosphere and evolve in time. Therefore, the responses to wind change can be obtained by taking the difference between CESM1_ΔWind and CESM1_ΔBuoy.

More details about this CESM1 model configuration and setup can be found in Liu et al. (2018). All of these cases were run for 90 years, listed in Table 4.1. The Southern Ocean zonal velocity and potential temperature shown in figures (Figures 4.4 and 4.5) are changes due to surface buoyancy and wind change over years 41-90.

We also used an ocean-only general circulation model (OGCM) to investigate the changes driven by surface warming and wind change. The OGCM utilized in this study is the MIT General Circulation Model (MITgcm). The model is based on the LLC90 grid (Forget et al. 2015) and the horizontal resolution is 1˚x1/3˚ at low and high latitudes and gradually changes to 1˚x1˚ at midlatitudes. The model has 50 layers in the vertical direction, with the layer thicknesses ranging from 10 m at the surface to 456m at the ocean bottom. Isopycnal diffusion and eddy-induced mixing were parameterized with the GM/Redi scheme (Redi 1982; Gent and Mcwilliams 1990). The vertical mixing follows the GGL90 turbulent kinetic energy vertical mixing scheme (Gaspar et al. 1990). The initial state, as well as surface forcing fields such as 6-hourly zonal and meridional surface wind speed, 2-m air temperature and specific humidity, downward longwave and shortwave, and precipitation, are obtained from the Estimating the Circulation and Climate of the Ocean Version 4 Release 4 (ECCO v4r4) (Forget et al. 2015). The model is first integrated forward from 1 January 1992 to 31 December 2017. The monthly climatological SST, SSS, surface wind stress and air-sea fluxes including surface net heat flux, surface net short wave flux surface net freshwater flux are stored as new forcing fields. With these new forcing fields, the model is further integrated for 100 years to reach a quasi-equilibrium state. Variants of this configuration have been successfully used to address ocean dynamic and thermodynamic processes (Peng et al. 2019, 2020).

To assess the specific oceanic response to global warming-induced SST and wind stress changes (denote as Δ), we performed three experiments with the MITgcm, listed in Table 4.2. The

multi-model (Table C2) ensemble mean ΔSST and ΔWind used in the experiments are calculated as the years 100-140 mean difference between CMIP6 abrupt-4×CO2 and pre-industrial control (piControl) experiments. Restarting from the spun-up solution of year 100, the three experiments are integrated forward an additional 140 years; the results shown in this study are the average of the last 40 years (100–140) of each experiment. In the control run (MITgcm_CTL), we forced the model using the present-day monthly climatological wind field (WindClim), and the SST and SSS are strongly restored to the current monthly climatological SST (SSTClim) and SSS (SSSClim). The restoring timescale is 10 days for SST (~50W/m^2/K for the 10 m upper layer) and SSS. The output of MITgcm_CTL is thus the ocean state forced by current forcing fields. In the MITgcm_ΔSST, the forcing fields are the same as MITgcm_CTL but SST is restored to the prescribed SSTClim+ΔSST. The difference, MITgcm_ΔSST minus MITgcm_CTL, yields the oceanic response to ΔSST induced by the increases of greenhouse gas concentrations. In the MITgcm_ΔWind, wind stress is restored to WindClim+ΔWind, and SST/SSS are restored to SSTClim/SSSClim. The difference between MITgcm_ΔWind and MITgcm_CTL isolates the impacts of wind stress change.

4.4 Observed acceleration of Southern Ocean zonal flow

Zonally-averaged sea level has been rising at all latitudes in the Southern Ocean over the 26 years since 1993, based on AVISO satellite altimetric surface height (Figure 4.1a). The greatest sea level rise has been found in the subtropical Southern Hemisphere north of 50°S, where it matches the global mean sea level rise. The maximum sea level rise was at about 45°S. In contrast, between 65°S and 50°S, sea level increase has been slower than the global mean. When examined over just the more recent Argo observation period starting in 2005, the subtropical increase was

greater and the subpolar increase was smaller, yielding a larger meridional gradient in the trend. The increasing sea level is attributable to thermal expansion, and its pattern to greater warming in the subtropics than in the ACC latitudes, based on gridded Argo temperature data (Roemmich and Gilson 2009) (Figure 4.1b). Subsurface zonal mean warming is maximum at about 45˚S on the northern flank of the broad, climatological, zonal mean eastward flow (Figure 4.1b). On the southern flank, the warming rate is insignificant or much slower, attributed to the upwelling of deep water (Armour et al. 2016; Shi et al. 2020).

Acceleration of the eastward zonal geostrophic flow is associated with the increasing sea level gradient and hence meridional pressure gradient between 45°S and 60°S (Figure 4.1c, based on AVISO satellite altimetric height). The acceleration is concentrated around 48˚S-58˚S, south of the maximum mean flow, hence shifting the flow poleward. The 2005-2018 acceleration is almost double that of 1993-2018. Zonal geostrophic velocity shows negative (westward) trends on the north and south sides of the significant positive trend. Thus, the Southern Ocean's eastward flow has also intensified and narrowed.

Acceleration of the zonal geostrophic velocity is also apparent from the independent Argo temperature and salinity data (Roemmich and Gilson 2009), which also show its decay with depth (Figs. 4.1d and 4.2b). This baroclinic structure is consistent with buoyancy forcing that creates stronger warming in the upper layer north of the ACC (Figure 4.1b) as opposed to wind forcing changes (Shi et al. 2020).

The surface zonal geostrophic velocity (U_g) from AVISO altimetry, averaged between 48˚S and 58˚S, increased from 1993 to 2018 (Figure 4.2). The 26-year trend was 0.74 ± 0.27 cm/s per century (Figure 4.3c). The corresponding trend from Argo, from 2005 to 2018, was a comparable 0.82 ± 0.24 cm/s per century (Figure 4.3c). In addition to the long-term eastward acceleration, the

AVISO-based surface zonal velocity shows strong decadal variability, which may bias the long-term trend estimates. In particular, the spike around the year 2000 is likely due to natural variability, based on an empirical orthogonal function (EOF) analysis of U_g (Figure C1). Attempts to estimate the ACC trend from AVISO would be inclusive prior to 2010 when the surface zonal flow first exceeded the 2000 peak (Figure 4.2a).

To examine Southern Ocean zonal acceleration for a longer period, we examine datasets from the Institute of Atmospheric Physics (IAP), Met Office Hadley Centre (EN4), and World Ocean Atlas 2018 (WOA18), which include many decades of ship-based hydrographic data (Figure 4.2a). All three show a significant eastward acceleration of the geostrophic flow relative to 2,000 dbar since 1993 (Figure 4.3c), matching the AVISO and Argo results. EN4, which has large oscillations, shows a larger U_g trend of 1.00 ± 0.20 cm/s per century compared with the smoother IAP trend of 0.50 ± 0.14 cm/s per century. The change from WOA18 (2005–2017 mean minus 1995–2004 mean) is 0.15 cm/s, equivalent to a trend of 1.20 cm/s per century.

For longer periods, the evidence for acceleration is even stronger. The trend in Southern Ocean zonal geostrophic velocity from IAP, spanning 1979 to 2018 (Figure 4.4a), is similar to the Argo trend (Figure 4.1d). Maximum warming is located on the northern flank of the ACC (Armour et al. 2016) (Figure C2a). South of the maximum warming, eastward zonal flow is intensified with stronger vertical shear. North of the maximum warming, negative change (weakened eastward or intensified westward flow) occurs along the boundary between eastward and westward flows, indicating a southward shift of zonal flow. To quantify the net acceleration, we calculate the eastward baroclinic transport in the upper 2,000 m based on IAP since 1940 (Figure C3). For all regions of eastward flow, the net intensification is 2.2 ± 0.3 Sv/century. Eastward transport

weakens at a rate of -2.7 ± 0.3 Sv/century to the north of the ACC (38˚-46˚S), associated with the ACC's poleward shift (Figure C3a).

The consistency across different observational datasets and analyses suggests a robust increase in eastward zonal flow in the latitude band 48˚S to 58˚S, associated with the strongest warming north of the ACC and weak warming within and to the south of the ACC. As a caveat, the Southern Ocean is subject to strong internal climate variability and the observations are sparse. Therefore, we turn to numerical climate model simulations to corroborate the zonal flow acceleration and for attribution of the physical mechanisms.

4.5 Mechanism for acceleration of Southern Ocean zonal flow, using climate models

Acceleration of Southern Ocean zonal flow, demonstrated from observations in the preceding section, is also found in multiple climate simulations that are subjected to anthropogenic forcing, versus their background internal climate variability. We first use the multi-model mean (MMM) of 26 CMIP6 historical simulations, which include multiple anthropogenic forcings (see Methods). For comparison with observations, the difference between the zonal velocity in the upper 100 m and at 2,000 m depth, averaged between 48˚S and 58˚S, shows a long-term linear trend of 0.40 ± 0.30 cm/s per century from 1993 to 2014 (Figure 4.3c). The surface velocity trend from altimetry and simulations is shown in Figure C4.

Internal climate variability and model structure uncertainty create large inter-model variability in CMIP6 (Deser et al. 2012) (Figure 4.3a, c). To separate internal from forced variability, we use the CESM1 40-member Large Ensemble (LENS) (Kay et al. 2015) and the CMIP6 25-member CanESM5 large ensemble (Swart et al. 2019) (Figure 4.3b; Figure C5), to

interpret the observed structure. The meridional structures in both LENS and CanESM5 are similar to the observed AVISO trend (Figure C5), supporting our hypothesis that the observed eastward acceleration is of anthropogenic origin. The velocity trend in LENS, 0.43 ± 0.17 cm/s per century for 1993-2018, is comparable to CMIP6 but with a narrower range (Figure 4.3c). Since the LENS mean trend is larger than the uncertainty, we conclude that external forcing is more important than internal variability for the altimeter era. Hence the CMIP6 MMM and the LENS and CanESM5 large ensemble means confirm the observed long-term trend of Southern Ocean zonal velocity.

The observed zonal velocity change since 1993 includes not only a trend but a large decadal oscillation (Figure 4.2a). This oscillation is not present in the multi-model mean, which suggests that it is internal variability (Figure 4.3a). Individual LENS runs (e.g. thin red in Figure 4.3b) exhibit the forced response (trend) with internal variability that is similar in magnitude to the observed oscillation. The combined external forcing and internal variability make the observed trends larger than model ensemble mean results (Figure 4.3c). For a longer period, for instance, since 1979 when the zonal velocity started climbing from a relatively stable state (Figure 4.3a), the random internal variability is weaker and the forced signal is more evident. Hence the longer-period observed trend is much closer to the ensemble mean results from CMIP6 and LENS (Figure 4.3d).

The models considered thus far are 'standard' resolution (about 1°) with eddy parameterizations, and capture the observed maximum warming around 45˚S (Figure C2) and zonal velocity acceleration around 50˚S (Figure 4.4b). Does model resolution matter? Comparing a standard resolution CESM1-SR with the eddy-resolving CESM1-HR model (see Methods), the zonal mean velocity trends for 1979-2018 (Figure 4.4c, d) and time evolution of zonal velocity (Figure C6) are similar. The small difference in trends is partly attributed to large internal

variability, as shown by LENS. Thus, the eddy parameterizations in the standard resolution ocean models effectively reflect eddy activity under global warming.

Previous studies focused on wind effects on Southern Ocean climate change (Downes et al. 2011; Meredith et al. 2012). Here we demonstrate that the observed zonal flow change (ΔU) is largely due to the meridional gradient of ocean buoyancy change (warming) rather than wind stress change. To compare buoyancy and wind forcing changes, we define two indices: (1) the index 'ΔT' of buoyancy change is the zonal mean upper 2,000 m temperature difference between 45˚S and 60˚S, latitudes where the maximum and minimum of warming occur, respectively; (2) the index 'SAM' of wind stress change is the zonal-mean atmospheric surface pressure difference between 40˚S and 65˚S, which is the Southern Annular Mode index (Marshall 2003). Across the CMIP6 models, the correlation coefficient between the 1979-2014 trends of ΔT and ΔU is 0.71, which is much larger than the correlation of 0.16 between the trends of SAM and ΔU (Figure C7).

To further test attribution of the ocean changes to surface warming versus wind, we performed idealized experiments with two GCMs: the air-sea coupled CESM1 and the ocean-only MITgcm model (see Methods). To isolate the ocean response to warming, we first compared a pre-industrial run of CESM1 ('CTRL') with a run 'CESM1_ΔBuoy' forced by quadrupled atmospheric CO_2 and prescribed winds from CTRL. The quadrupled CO_2 experiment largely reproduces the zonal mean velocity trend from observations and CMIP6 (Figure 4.4e). This result was confirmed with the ocean-only MITgcm, with a control run (MITgcm_CTL) forced by current climatological winds, SST, and SSS. For the buoyancy experiment (MITgcm_ΔSST), the global warming-induced ΔSST, obtained from CMIP6 quadrupled-CO_2 experiments, was added to the current climatological field. MITgcm_ΔSST (Figure 4.4f) captures the principal features from observations, CMIP6, and CESM1_ΔBuoy.

Idealized simulations with surface wind stress changes (CESM1_ΔWind and MITgcm_ΔWind) show only small additional velocity changes (Figure C8) compared with those driven by temperature change. Moreover, the wind-change-induced responses show maximum zonal flow change at mid-depth, unlike the surface-intensified flow change in observations, CMIP6 historical runs, and the buoyancy forcing experiments.

Overall, both sets of idealized simulation results suggest that acceleration of zonal flow in the Southern Ocean is a general feature of the ocean's response to global warming, and that wind changes play a secondary role in shaping the Southern Ocean response.

4.6 Spatial structure of Southern Ocean velocity response

If viewed only as a zonal mean, acceleration of the eastward zonal flow and associated temperature changes (Figs. 4.1 and 4.4) might be interpreted as intensification of a zonally-oriented ACC at all longitudes. However, the accelerations/decelerations and temperature changes are localized to different parts of the Southern Ocean's zonal flows (Figure 4.5), importantly including not only the Subantarctic Front (SAF) of the ACC, but also the Agulhas Return Current (ARC) in the western Indian sector. The strongest mean flows (> 12 cm/s) from AVISO data follow the SAF and the ARC (Figure C9). The SAF and ARC latitudes vary from 40°S to 60°S, resulting in much broader zonally-averaged zonal flow than at any given longitude. Observed zonal flow acceleration occurred mainly along the SAF (Figure 4.5a,b). There is a slight indication of deceleration (westward acceleration) north of and along the SAF in the Atlantic and eastern Indian Oceans, suggesting a poleward shift of the SAF. The maximum SAF acceleration in the Pacific sector might be associated with spin-up of the subtropical gyre (Roemmich et al. 2007), but is likely natural variability based on the first EOF (Figure C1).

The three observational products with longer periods also show SAF-intensification (Figure C10). The long-term trends/change do not show the strong Pacific acceleration. The potential density trends, which govern the geostrophic velocity trends, are dominated by temperature trends. The most zonally-coherent accelerations (as opposed to noisy ones) have the meridional dipole structure, and are strongest where the subtropical temperature trends are strongest.

The CESM1-SR model velocity trend for 1993-2018 is similar to AVISO observations, with a meridional dipolar change in the Atlantic and Indian sectors (Figure 4.5c). Although the zonal means in CESM1-SR and CESM1-HR are similar (Figure 4.4c, d), the horizontal structure is sensitive to ocean model resolution; for instance, the magnitude and regional pattern from CESM1-HR are larger and more concentrated where ocean jets are stronger (Figure 4.5d) compared with CESM1-SR (Figure 4.5c). This meridional structure was also shown in the eddy kinetic energy trends using a multi-model mean (Hu et al. 2020). Here we see that the horizontal warming patterns in both observations and models, including CESM1-SR and CESM1-HR (Figure C10,C11), are tightly linked with velocity change patterns (Figure 4.5).

The maps of observed long-term velocity change resemble both of the idealized buoyancy-driven GCM experiments (Figure 4.5e, f). All have acceleration and poleward shift of eastward flow in the Indian sector. CESM1_ΔBuoy also creates a poleward shift in the Atlantic sector (Figure 4.5e). In contrast, the idealized wind-change-driven GCM experiments accelerate the eastward flow much farther to the south and are much patchier (Figure C12). The wind experiments do create westward acceleration in the subtropics, especially in the Atlantic and Indian sectors, which could contribute to the meridional dipole in acceleration and spin-up of subtropical gyres.

4.7 Summary and discussion

We find statistically significant acceleration of Southern Ocean zonal flow between 48˚S and 58˚S, based on satellite altimeter and hydrographic data since 1993, and supported by multi-decadal hydrographic data analyses reaching back to 1979. The observed acceleration is consistent with the observed greater warming north of the ACC compared with reduced warming within and south of the ACC, and reflects the role of Southern Ocean overturning circulation in oceanic heat redistribution (Armour et al. 2016). Multiple model simulations and idealized experiments support attribution of the acceleration to the warming distribution as opposed to wind changes. Given the continuing role of the Southern Ocean in oceanic heat uptake (Shi et al. 2018) and equatorward heat transport, we expect the zonal acceleration to continue and even increase. For example, the 26-year trend of zonal velocity in the CESM1 LENS model is 0.79 ± 0.17 and 1.31 ± 0.16 cm/s per century for 2020-2045 and 2075-2100 (Figure C13), respectively, which are much larger than the 0.43 ± 0.17 cm/s per century trend for 1993-2018. Further studies are needed to explore how the bathymetry, standing meanders, and zonal deep mixed layer distribution affect the regional or sectoral distribution of the greatest warming north of the ACC and the associated ocean current changes.

4.8 Acknowledgments

J.-R. Shi is supported by U.S. National Science Foundation (AGS-1637450) and the Southern Ocean Carbon and Climate Observations and Modeling project (SOCCOM) under National Science Foundation Award (PLR-1425989). L.D.T. is also supported by SOCCOM. W.L. is supported by the Regents' Faculty Fellowship, and also by the Alfred P. Sloan Foundation as a Research Fellow. Argo data is available at http://www.argo.ucsd.edu. IAP data is available at

https://climatedataguide.ucar.edu/climate-data/ocean-temperature-analysis-and-heat-content-estimate-institute-atmospheric-physics. EN4 data is available at https://www.metoffice.gov.uk/hadobs/en4/. WOA18 data is available at https://www.nodc.noaa.gov/OC5/woa18/. Satellite altimetry data is available at https://www.aviso.altimetry.fr/en/data.html. The CMIP6, CanESM5 large ensemble, CESM1-HR, and CESM1-SR data are available on the Program for Climate Model Diagnostics and Intercomparison's Earth System Grid (https://esgf-node.llnl.gov/search/cmip6/). The CESM LENS simulations are available on the Earth System Grid (www.earthsystemgrid.org).

Chapter 4, in full, has been submitted for publication of the material as it may appear in *Nature Climate Change*: Jia-Rui Shi, Lynne D. Talley, Shang-Ping Xie, Qihua Peng, Wei Liu, "Acceleration of the Southern Ocean Zonal Flow" (2021). The dissertation author was the primary investigator and author of this paper.

Table 4.1: Description of the partial coupling CESM1 experiments.

Names	Note
CTRL	Fully coupled, preindustrial control run
$4\times CO_2$	Fully coupled, abruptly quadrupled CO_2
CESM1_ΔBuoy	Partial coupling with fixed wind stress from $4\times CO_2$ and quadrupled CO_2
CESM1_ΔWind	Partial coupling with fixed wind stress from CTRL and quadrupled CO_2

Table 4.2: Description of the experiments of OGCM.

Experiment	Surface Forcing
MITgcm_CTL	Present-day monthly climatological SST (SSTClim), SSS (SSSClim) and wind stress (WindClim)
MITgcm_ΔSST	Same as MITgcm_CTL but SST is restored to SSTClim+ΔSST
MITgcm_ΔWind	Same as MITgcm_CTL but wind stress is restored to WindClim+ΔWind

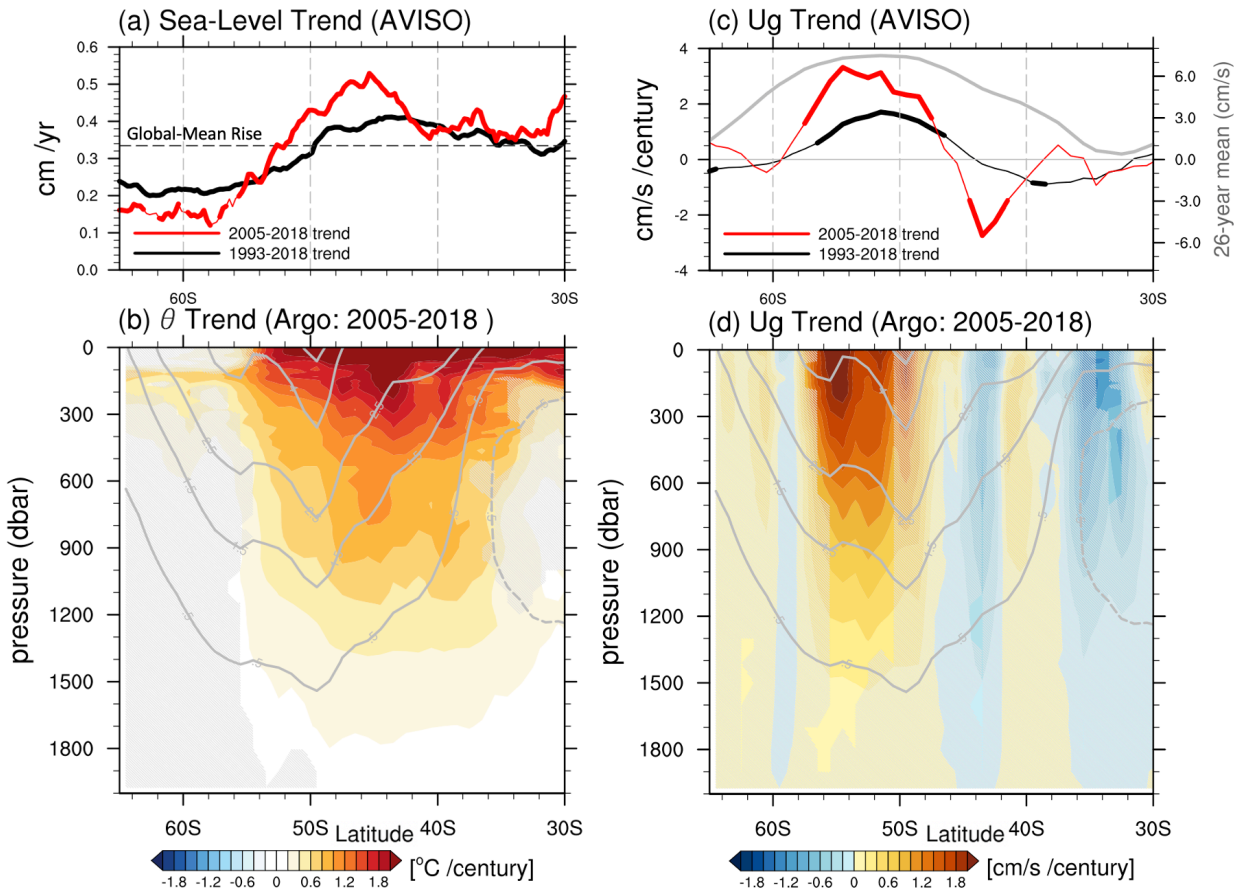

Figure 4.1: (a) Zonal mean sea-level trend from AVISO for 1993-2018 (black) and 2005-2018 (red). The global mean sea-level trend (0.33 cm per year from 1993 to 2018) is the dashed gray line. (b) Potential temperature trend (2005-2018) from Argo. (c) Zonal geostrophic velocity (U_g) trend from AVISO. (d) The same from Argo relative to 2000 dbar. Climatological (26-year mean since 1993) surface U_g (cm/s) from AVISO is represented as a gray curve in (c). Gray contours in (b) and (d) are the climatological U_g based on Argo (cm/s), with solid contours representing eastward flow and dashed contours representing westward flow. Hatched regions (b) and (d) indicate that the trends are not significant at the 95% confidence level from the two-tailed *t*-test. Thick curves in (a) and (c) show latitudes exceeding 95% statistical significance.

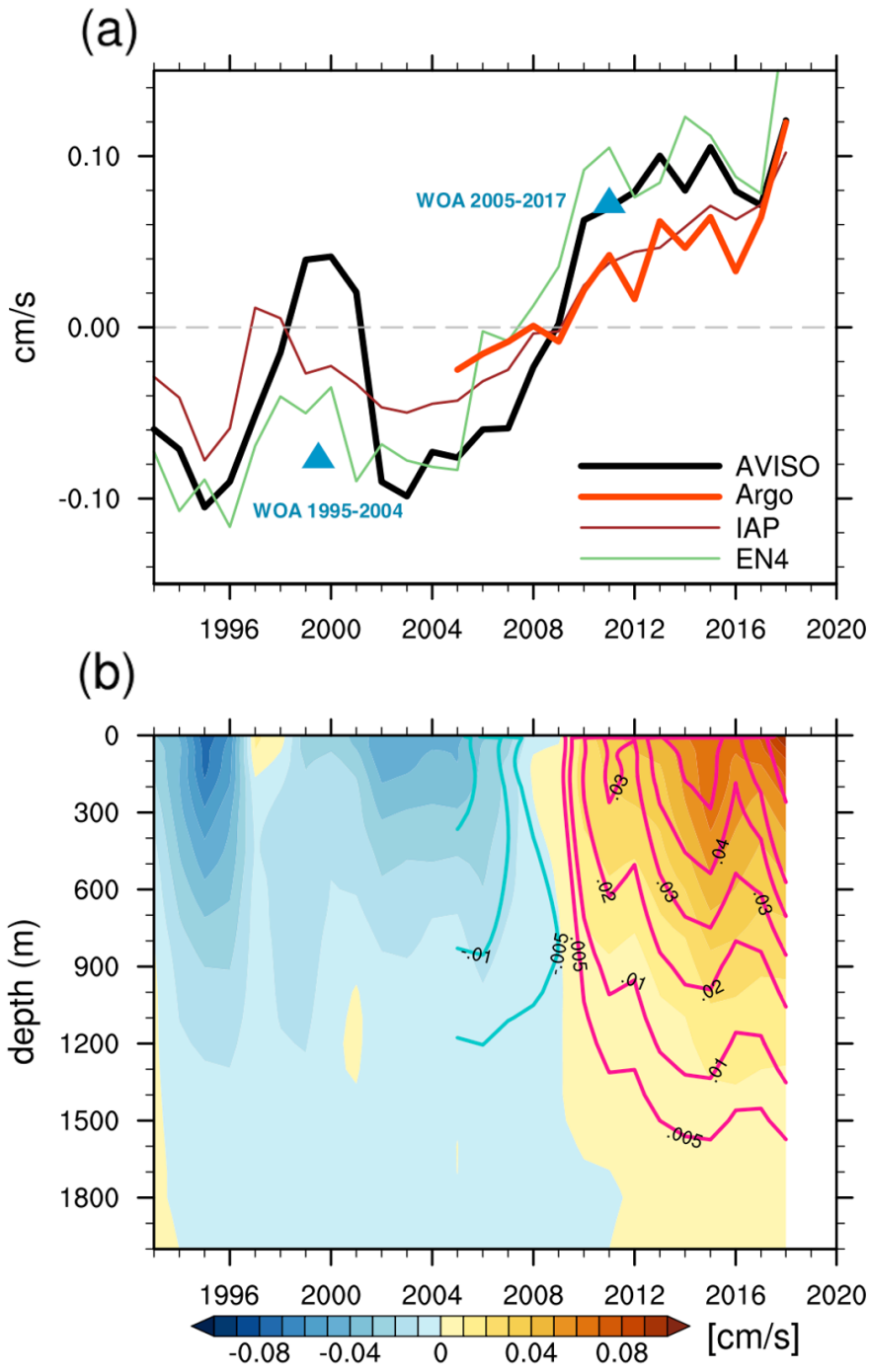

Figure 4.2: (a) Time series of observed surface zonal geostrophic velocity U_g (averaged between 48˚S-58˚S) anomaly from: AVISO (black), IAP (brown), EN4 (green), and Argo (red; since 2005). The blue triangles represent the decadal average of Ug anomaly from WOA18. U_g from ocean measurements are relative to 2000 m depth. (b) Hovmöller diagram of U_g (averaged between 48˚S-58˚S; cm/s) anomaly from IAP (shading) and Argo (contours).

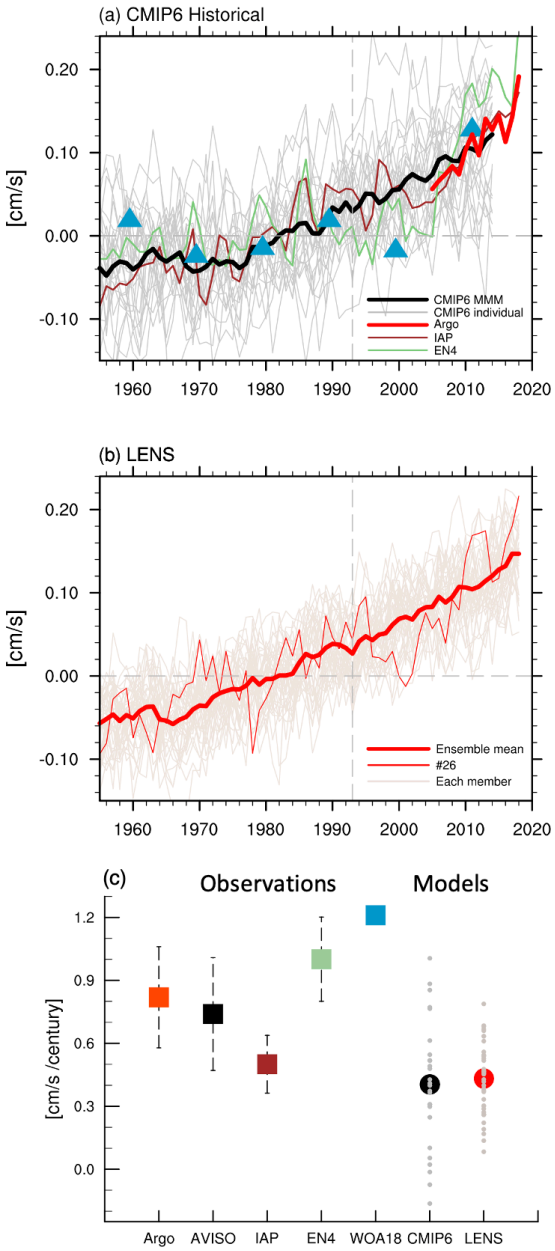

Figure 4.3: (a) Time series of upper 100 m zonal velocity (minus 2000 m velocity and averaged between 48˚S-58˚S) from CMIP6 historical simulations. CMIP6 multi-model mean (MMM) is the black curve, with superimposed observation-based products: IAP (brown), EN4 (green), WOA18 (blue triangle), and Argo (red; since 2005). (b) Time series of upper 100 m zonal velocity relative to the velocity at 2000 m depth from LENS. LENS ensemble mean is shown as the thick red curve and an individual run is shown as the thin red curve. (c) Trend of zonal velocity from observations (squares) and simulations (circles) in (a) and (b) from 1993 to 2018. For Argo, the trend is for 2005-2018. For CMIP6 historical runs, the trend is for 1993-2014. The error bar represents the 95% confidence interval for the linear trend. For WOA18, the changing rate is estimated based on the difference between 2005-2017 and 1995-2004 and then divided by 12 years. Small dots are results from individual runs from CMIP6 and LENS.

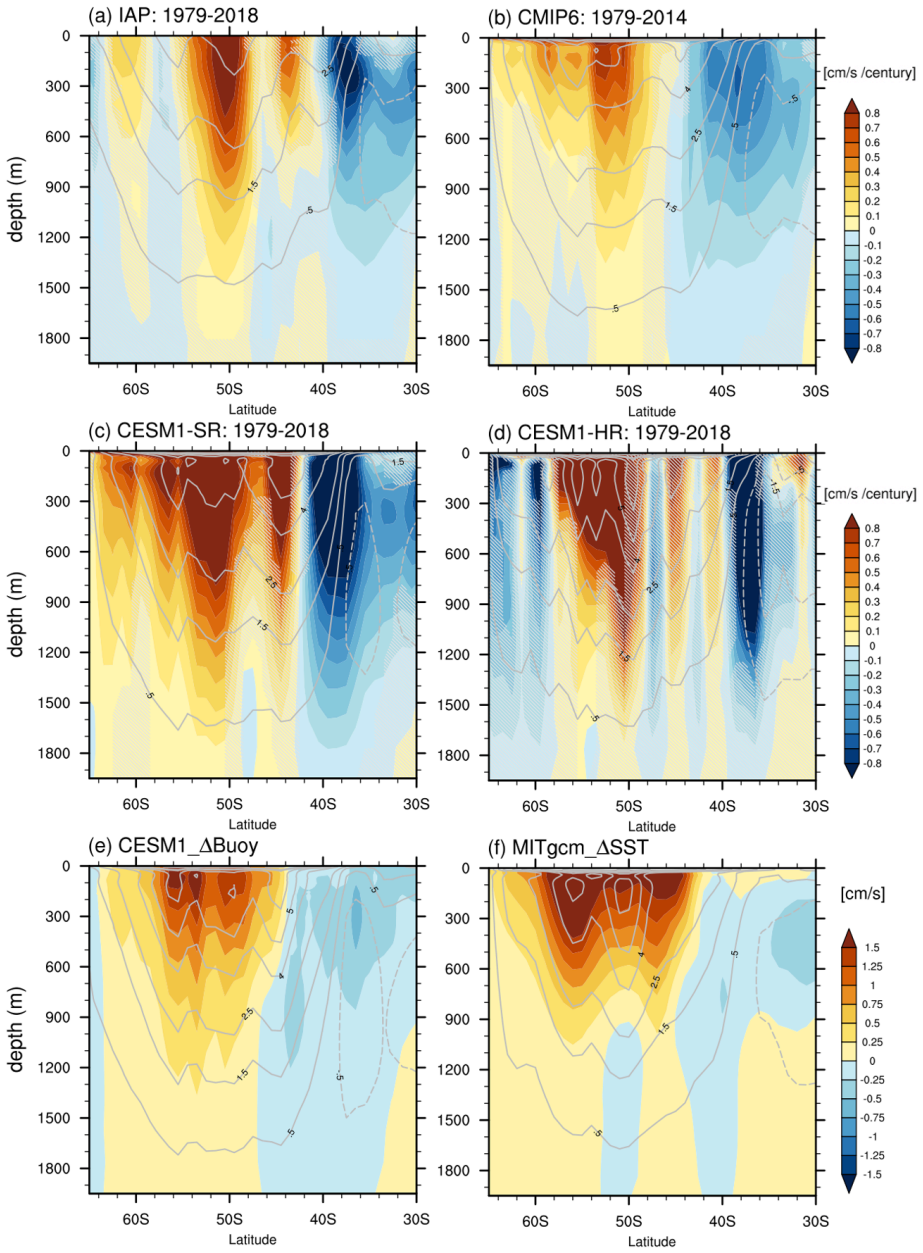

Figure 4.4: (a)-(d) Zonal mean U (U_g for observations) trend from observations: (a) IAP; models: (b) CMIP6 MMM, (c) CESM1-SR, and (d) CESM1-HR. The trend from CMIP6 MMM is from 1979 to 2014, and the rest is from 1979 to 2018. (e) Zonal mean U change from the CESM1_ΔBuoy experiment relative to the control run, averaged over 50 years. (f) Zonal mean U change from the MITgcm_ΔSST experiment relative to the control run. All the velocity changes from model simulations are relative to the velocity at 2000 m depth. Gray contours are the climatological U_g or U (in cm/s) from the corresponding cases. Hatched regions indicate the trends are not significant at the 95% confidence level.

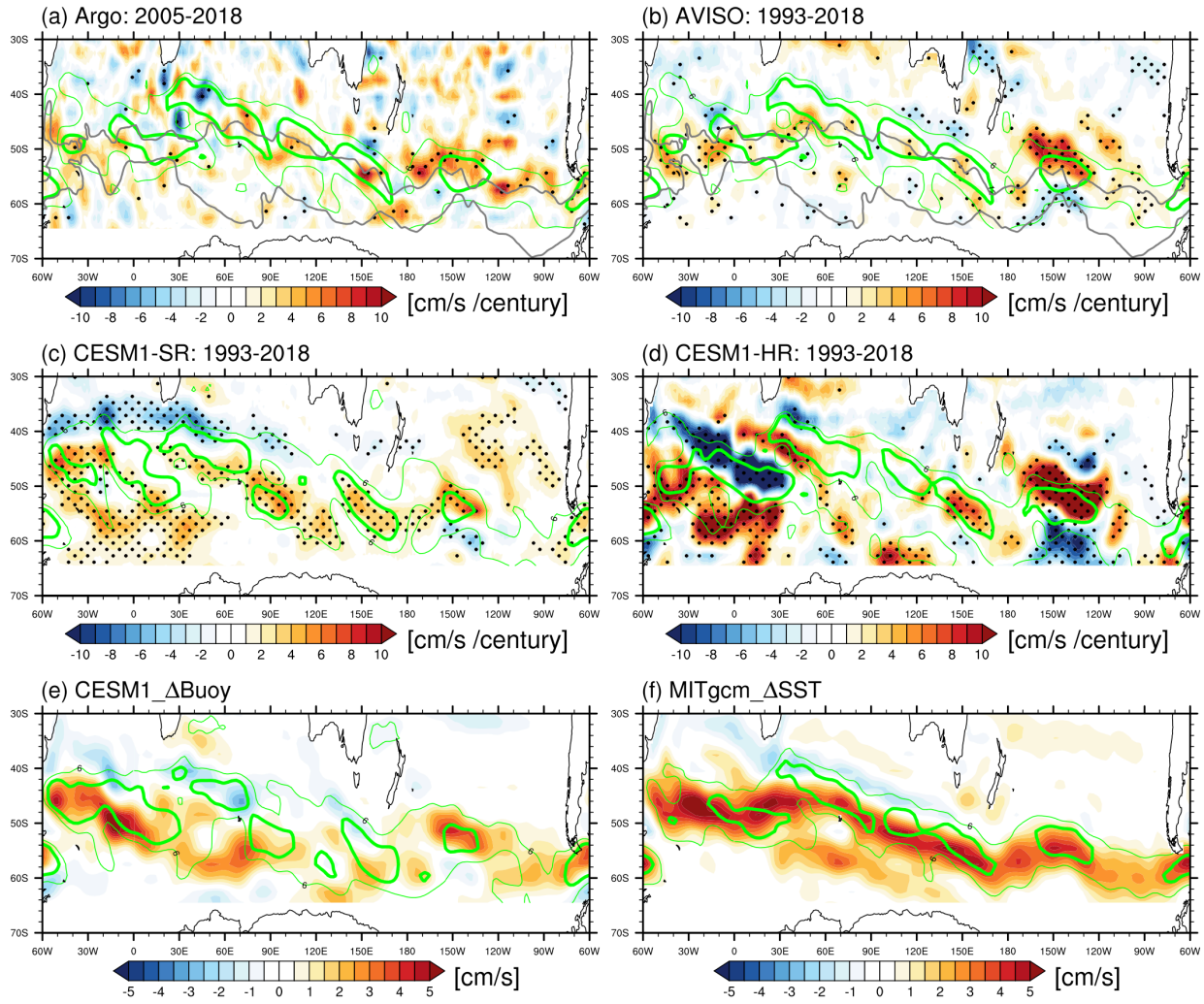

Figure 4.5: (a) Upper 100 m U_g trend from Argo (2005-2018). Gray contours indicate the Subantarctic Front, and Southern ACC Front from north to south (Orsi et al., 1995). (b) Surface U_g trend from AVISO (1993-2018). (c, d) Upper 100 m U trend from CESM1-SR (1° resolution) and CESM1-HR (0.1° resolution). (e, f) Upper 100 m U change from the CESM1_ΔBuoy experiment and the MITgcm_ΔSST experiment relative to their corresponding control runs. Mean zonal velocities of 6 cm/s and 12 cm/s are shown as thin and thick green contours, respectively. Stippling indicates regions exceeding 95% statistical significance computed from the two-tailed *t* test.

Chapter 5

Spatial Pattern of the Southern Ocean Subsurface Warming: The Role of Ocean Jets

5.1 Introduction

By connecting the deeper and upper layers of the global ocean overturning circulation, the Southern Ocean plays a pivotal role in ocean heat uptake (defined as surface heat flux change), heat storage (or ocean heat content; OHC) increase, and slowdown of the global surface warming (Manabe et al. 1990; von Schuckmann et al. 2016; Frölicher et al. 2015; Armour et al. 2016; Shi et al. 2018). Observations have revealed significant subsurface warming in the Southern Ocean (Gille 2002, 2008; Levitus et al. 2005, 2012; Roemmich et al. 2015; Cheng et al. 2016; Böning et al. 2008). From the zonal mean perspective, the maximum warming occurs around 40˚-45˚S (e.g. Swart et al. 2018). The background meridional overturning circulation (MOC) brings up to the surface deep water, taking up heat from the warming atmosphere, and then advects the warmed water northward via Ekman transport (Armour et al. 2016; Liu et al. 2018). This Southern Ocean excess heat content is stored in different regions and layers of the ocean basins (e.g. Sallée 2018).

In addition to the aforementioned zonal-average perspective, narrow zonal currents, such as the Antarctic Circumpolar Current (ACC) and Agulhas Return Current (ARC), are also essential components of Southern Ocean dynamics. Connecting major ocean basins, the eastward currents

forced by the westerly winds and steered by bathymetry help the interbasin exchange of properties through large baroclinic eddies and meanders. In steady state, the unique circulation pattern of the ACC leads to zonally asymmetric patterns in the heat budget (Sun and Watts 2002; Tamsitt et al. 2016): the ACC warms along its equatorward flank (Atlantic and Indian sectors) and cools on its poleward flank (Pacific sector).

The ACC is composed of a series of fronts, characterized by sloping isopycnals and a strong meridional gradient of sea surface temperature or sea surface height (Orsi et al. 1995; Belkin and Gordon 1996; Gille 1994; Dong et al. 2006; Sokolov and Rintoul 2007). A number of studies have noted that the observed warming in the ACC region can be explained by a poleward shift of the fronts (Gille 2002, 2008; Böning et al. 2008). The Southern Annular Mode, an atmospheric pressure seesaw between 40˚S and 65˚S, has shown a positive trend over the past several decades, forced by both ozone depletion and greenhouse warming according to modeling studies (Gillett 2003; Fyfe and Saenko 2006). Poleward shift and intensification of the westerly winds may drive intensification and poleward shift of the subtropical gyres, with associated warming in the western boundary currents and its extension regions (Cai 2006; Roemmich et al. 2007; Wu et al. 2012; Qu et al. 2019). Based on hydrographic profiles, Sallée et al. (2008) showed zonally asymmetric responses of the ACC to a relatively uniform change in the westerlies: poleward movement of the ACC fronts in the Indian sector and equatorward movement in the Pacific sector. However, other studies have shown that the positions of ACC fronts are primarily steered by topography and insensitive to westerly wind change, while the circumpolar Subtropical Front, which includes the ARC, is more sensitive to wind shifts since it is more stratified, and the flow is more baroclinic (Graham et al. 2012). Meijers et al. (2012) reported no significant relationship between latitudinal positions of the westerlies and ACC fronts based on historical simulations from the Coupled Model

Intercomparison Project phase 5 (CMIP5). On the other hand, changes in surface buoyancy flux, such as ocean heat uptake and intensified net freshwater flux due to global warming (Durack and Wijffels 2010), can also lead to ocean circulation change and substantial warming in the Southern Ocean upper layer (Hogg 2010; Fyfe et al. 2007; Liu et al. 2018; Shi et al. 2020; Shi et al. submitted).

Ocean temperature change can be separated into two categories: passive and dynamic temperature change. Here the passive warming does not affect ocean circulation, and reflects the advection of the anomalous warming signal by climatological ocean currents. For example, the passive-tracer simulation from Armour et al. (2016) broadly captures the uneven warming pattern in the Southern Ocean driven by GHG forcing. On the other hand, dynamic temperature change involves the ocean's dynamic adjustment to downward mixing of heat, intensification of upper layer stratification (e.g. Wang et al. 2015), and wind stress change. Based on a comparison between fixed-ocean-current and free-evolving-current simulations, Winton et al. (2013) showed that ocean dynamic adjustment is important for the regional ocean warming pattern. Building on our previous studies (Shi et al. 2020; Shi et al. submitted), we show that the dynamic adjustment to the surface warming is important for shaping the regional responses in the Southern Ocean, while wind stress change has a much weaker impact.

In this study, we aim to explore the spatial pattern and regional response of the Southern Ocean subsurface warming and investigate the dynamic adjustment of the ocean currents to the buoyancy and wind stress change. Based on observations and model simulations, we find that the mean ocean jets strongly anchor the banded subsurface warming pattern: the greatest OHC change occurs on the northern flank of the ACC, which slants southeastward by (2200 kilometers) from the Atlantic to the Pacific. The position (or latitude) of the maximum OHC change in the Southern

Ocean varies among CMIP models. Here we show that the intermodel spread in the position of the maximum OHC change is closely related to the biases in the mean position of the Subantarctic Front (SAF). Particularly, the positions of the mean SAF and maximum OHC change are highly correlated ($R \geq 0.6$) in the regions where the ocean current is strong and zonal. The effect of bathymetry on the spatial warming pattern is also investigated through the comparison among a set of model simulations including flat-bottom cases. The existence of ocean ridges gives rise to more warming on the regional scale. Furthermore, the remarkable gyre-like warming pattern from the low resolution and flat bottom experiment is found to be associated with anomalous southward advection of warm water along the western boundary. In addition, the passive-heat experiment from Flux-Anomaly-Forced Model Intercomparison (FAFMIP) clearly shows the control of mean ocean jets associated with jet-scale overturning circulation on the redistribution of absorbed heat. In turn, the redistributed ocean warming can accelerate the zonal flow, largely reproducing the acceleration from the coupled run which allows the ocean adjustments. We find that the dynamic adjustment, i.e. a poleward shift of ocean jet, mainly takes place in the ARC and limits the northward expansion of the OHC change in the Indian sector. This indicates that the jet dynamics is fundamental to the regional response, and OHC change is in balance with the circulation change.

The rest of the chapter is organized as follows. Section 5.2 describes the models, experiments, data, and methods used in this study. Section 5.3 discusses the warming pattern and its relation with the ocean front via observations and CMIP5/CMIP6 models. Section 5.4 discusses the effects of bathymetry on the regional warming pattern. Section 5.5 discusses control of mean ocean jets and cross-jet secondary circulation on Southern Ocean warming by using FAFMIP experiments. Section 5.6 discusses the dynamic adjustment by comparing the flat bottom run and passive-tracer run. Section 5.7 is a summary.

5.2 Data and Methods

5.2.1 Observations

We use temperature products from the World Ocean Atlas 2018 (WOA18; https://www.nodc.noaa.gov/OC5/woa18/), which is a uniformly formatted and quality controlled data set based on the World Ocean Database. Objectively analyzed climatologies of temperature (Locarnini et al. 2019) in decades (1955-1964, 1965-1974, 1975-1985, and 2005-2017) at standard depth levels are used in this study. The data are on a 1˚ x 1˚ latitude-longitude grid. The second data set is the monthly mean temperature product from the Institution of Atmospheric Physics (IAP) (Cheng et al. 2016, 2017) from 1940 to 2017 on a regular 1˚x1˚ grid with 41 vertical levels in the upper 2000 m. The IAP temperature product includes shipboard, mechanical bathythermograph, XBT, and Argo temperature profiles. Long-term ocean temperature changes in the upper 2000 m are calculated as the difference between the 2005–2017 mean and the mean over the 1955–1984 base period.

5.2.2 CMIP5 and CMIP6 models and simulations

Simulated ocean subsurface temperature is compared with observations to assess the validity of simulations. We analyze outputs of climate model simulations from the World Climate Research Program's CMIP5 (Taylor et al. 2012) and CMIP6 (Eyring et al. 2016). For the analyzed historical period, 1955-2017, we choose the CMIP5 Historical experiment (1955-2005) and representative concentration pathway 4.5 (RCP4.5; 2006-2017) scenario from 27 models (Table 5.1). For CMIP6 models, historical simulations extend to the near present, the year 2014. Therefore, in order to show the change from 1955-1984 to 2005-2017, we append outputs from

societal development pathway 2-4.5 (SSP2-4.5) simulations of Scenario Model Intercomparison Project (2015-2017) (O'Neill et al. 2016) to the Historical outputs. CMIP6 Historical runs used in this study are listed in Table 5.2. We also analyze the preindustrial control (piControl) and abruptly quadrupled CO_2 ($4xCO_2$) simulations of 30 CMIP5/CMIP6 models (Tables 5.1 and 5.2). The $4xCO_2$ represents an idealized global warming scenario in which the atmospheric CO_2 concentration is instantaneously quadrupled from its preindustrial value and held fixed for several decades. We examine the changes in ocean temperature by calculating the difference between abrupt$4xCO_2$ and piControl runs for the average of years 41-90.

5.2.3 Flat-bottom experiment from CESM1

We use the Community Earth System Model (CESM), version 1.0.6, from the National Center for Atmospheric Research (NCAR) (Hurrell et al. 2013). We chose a relatively coarse resolution, T31_g37, due to the limitation of computational resources. The model consists of version 4 of the Community Atmosphere Model (CAM4), run at a nominal 3.7˚ resolution both latitudinally and longitudinally, and version 2 of the Parallel Ocean Program (POP2), which uses a displaced pole grid and has a spatial resolution of approximately 1.6˚ latitudinally and 3.6˚ longitudinally that varies in space. The ocean model employs a temporally and spatially varying specification of the Gent–McWilliams (GM) eddy parameterization (Gent and Mcwilliams 1990). For tracers, such as temperature, the horizontal diffusion follows the Redi isoneutral diffusion operator as represented by the GM parameterization, and vertical mixing uses the K-profile parameterization (Large et al. 1994).

We first conducted two experiments, one pre-industrial control (named PI) and the other with abrupt quadrupling of CO_2 (named Cx4). We also conducted another pair of experiments by

using a flat bottom (FB) restarting from the spun-up solution of year 150: one with a flat bottom at around 2,400m level with pre-industrial atmospheric CO_2 level (named PI_FB), and the other with the same flat bottom but forced with instantly quadrupled CO_2 (named Cx4_FB). In the flat-bottom runs, all the continents are retained and the ocean plateaus shallower than 2,400m, such as Kerguelen, Campbell, and Malvinas Plateaus, are also retained with all of their realistic topography. Deeper than 2,400m, the ocean is filled with a flat top to remove the ridges including Mid-Atlantic Ridge, Scotia Ridge, Southwest and Southeast Indian Ridges, and Pacific-Antarctic Ridge (Figure 5.6b). Each experiment is integrated for 60 years to study the transient climate response to greenhouse forcing. We show the anomalies of the 41–60yr average relative to the climatology from corresponding control runs, i.e. Cx4 – PI and Cx4_FB – PI_FB.

5.2.4 FAFMIP experiments

This study also uses the output of the FAFMIP experiments from model MRI-ESM2.0 (Yukimoto et al. 2019), in which the outputs from the passive tracer experiment are currently available. The FAFMIP experiments, branched from pre-industrial conditions, prescribe a set of surface flux perturbations for the ocean. These perturbations are obtained from the ensemble-mean changes in net surface heat flux and wind stress simulated at the time of doubled CO_2 by CMIP5 AOGCMs under the 1pctCO_2 scenario (CO_2 increases by 1% each year). This study examines three FAFMIP experiments: (1) FAF-Heat (named Total-Heat here), imposing perturbation surface heat flux; (2) FAF-Passiveheat (named Passive-Heat), as in Total-Heat, but temperature change is treated as a passive tracer without effects on density and ocean circulation; (3) FAF-Stress (named Wind-Stress-Change), imposing perturbation surface wind stress (Gregory et al. 2016). Comparison of Passive-Heat with Total-Heat reflects the ocean adjustment to the added

heat. All FAFMIP experiments considered here were run for 70 years. We show the anomalies of the 51–70-yr average relative to the climatology from piControl.

Although the passive tracer of the added heat does not change the ocean circulation, the redistribution of excess heat can be used to calculate the geostrophic velocity, which reflects the circulation change potentially driven by the added heat. Here we calculate the geostrophic velocity from Passive-Heat to show the velocity change forced by the added heat. The method of calculating the geostrophic velocity is the same as the method used in Shi et al. submitted, but uses 5,500 m as the reference level of no motion. For Passive-Heat, the dynamic height is computed by using piControl temperature + added tracer and piControl salinity. Geostrophic velocities from piControl, FAF-Heat, and FAF-Stress are also calculated by using the ocean temperature and salinity from the corresponding cases. The changes in geostrophic velocities shown in this chapter are the differences between FAF runs and piControl.

5.3 Observed and Simulated Changes in OHC

The Southern Ocean map of upper 2000 m OHC long-term change is shown in Figure 5.1. To quantify historical changes in the Southern Ocean subsurface temperature, we calculated the difference between the 2005-2017 mean and the mean over a 1955-1984 base period from the WOA18 and IAP datasets. The observed OHC changes over the Southern Ocean (Figure 5.1a, b) show concentrated warming between 35˚S~55˚S with a narrow-banded warming pattern. The previous studies mainly focus on the zonal-mean subsurface temperature change (Swart et al. 2018; Shi et al. 2020), demonstrating that maximum warming found around 40˚S~45˚S is associated with background northward Ekman transport (Armour et al. 2016; Liu et al. 2018). The observed OHC changes display a distinctive warming pattern in the zonal direction. The maximum

warming is predominantly to the north of the Subantarctic Front (SAF), while the warming within the ACC is much weaker. Moreover, the southeast slanted warming band, from the Atlantic to the Pacific, is broadly consistent with the slanted mean ACC axis. This indicates that the major ACC fronts or ACC dynamics anchor the banded subsurface warming pattern. Moreover, the strongest warming in the Indian sector seems to be associated with the poleward shift of ARC, which is discussed in Section 5.5. As a caveat, the two observational products are not identical with respect to Southern Ocean OHC change: 1) the IAP analysis shows a stronger and wider warming band than the WOA18 analysis; 2) A cooling band just to the south of the maximum warming band, extending from the Indian sector to the Pacific sector, appears only in the WOA18 analysis. This cooling band appears in an earlier trend analysis (e.g. Rhein et al. 2013), which was based on WOA09 (Levitus et al. 2009) but its source has not yet been elucidated. Overall, both WOA18 and IAP show more warming in the Atlantic and Indian sectors than in the Pacific sector.

The CMIP5 and CMIP6 multi-model ensemble means of upper 2000 m OHC historical changes are shown in Figure 5.1c and 5.1d, respectively, to compare with observations. The simulated warming patterns from historical all-forcing experiments, which include greenhouse gas, anthropogenic aerosol, ozone depletion, solar, and land-use change effects, broadly resemble the observation-based patterns of change (Figure 5.1a, b). The simulated results also show a warming band with a clear zonal asymmetry. Different models in the ensembles produce maximum subsurface warming at different latitudes (not shown), so the multi-model ensemble mean OHC change has a much wider warming pattern than any given model or observations. The surface heat flux change (ocean heat uptake, OHU; colored contours in Figure 5.1c, d) is anti-correlated with subsurface warming: the ocean gains heat where less warming takes place; the ocean releases heat where maximum warming occurs, such as around the Agulhas Current, Brazil Current, east of

Kerguelen Island, and East Australian Current. This suggests that regional warming is associated with anomalous ocean heat transport rather than forced by localized heat uptake. We also show the OHC change and OHU from CMIP5/CMIP6 4xCO_2 experiments as representative of the greenhouse gas effect (Figure 5.1e, f). The spatial patterns of OHC change and OHU are consistent with those from historical runs (Figure 5.1c, d). This suggests that the ocean warming and OHU patterns are primarily driven by the greenhouse gas effect.

Next, we address the control of the major ocean front on the warming pattern using a set of CMIP5/CMIP6 4xCO_2 runs in which the forced responses are much larger than the background internal variability. Here we define the front of the ACC, the SAF, as the sea surface height going through the Drake Passage at the point 67.5˚W, 57.5˚S. We then convert the mean zonal velocity and change of ocean temperature from the latitude coordinate to the coordinate along the so-defined SAF. The "streamwise" coordinate covers the regions from 10˚ south to 10˚ north of the latitude of the SAF for each longitude. The global zonal mean and streamwise mean of temperature change with mean zonal velocity are shown in Figure 5.2. Compared with the global zonal mean pattern, the streamwise mean clearly shows the enhanced subsurface warming in the northern half of the eastward ocean jet with an increased meridional gradient of temperature. This is also true for the sectorial responses (not shown).

In the maps of OHC change (Figure 5.3), the positions of maximum OHC change (black curve) and mean SAF (cyan curve) are positively correlated (Figure 5.4) within each CMIP5/CMIP6 model. The correlation coefficient is 0.83 for the multi-model mean. Based on the map of topography (Figure 5.5a), the SAF is steered by the ocean ridges, plateaus, and continents. The maximum warming is located on the northern flank of SAF at all longitudes (Figure 5.5b). The spike from 150˚E to 180˚ shown in Figure 5.5b is due to substantial warming spots east of

Australia and New Zealand associated with the spin-up of the subtropical gyre (e.g. Roemmich et al. 2007 discussed the spin-up to the east of New Zealand), and further increases the displacement between the positions of maximum warming and SAF in the Pacific sector. Compared with the Pacific sector, the displacements are much smaller in the Atlantic and Indian sectors where the zonal flow is stronger. The scatter plot between the latitudes of maximum warming and SAF from 30˚W to 120˚E (box in Figure 5.5a) shows a remarkable linear relation across models, with R = 0.81 (Figure 5.5d). This indicates that the model with a more northward located SAF is associated with a more northward appearance of subsurface warming. Similarly, we calculate the correlation across models for each 5˚ longitudes (Figure 5.5c). We find that the positions of SAF and maximum OHC change are highly and positively correlated where the currents are more zonal. Near the Mid-Atlantic Ridge, Kerguelen Plateau, and Campbell Plateau, the positive correlations are largely disrupted by the strong meridional motions such as meanders, which generate deviations from zonal-mean properties.

5.4 Effects of bathymetry

Bathymetry alters and steers the eastward-flowing ACC (Gille 1994; Thompson and Sallée 2012). For instance, the Kerguelen Plateau pushes the northern part of the ACC northward in the Indian sector and restricts the position of the ARC (Wang et al. 2016c). By setting the maximum depth at 2,400m, our flat bottom simulation only retains major shallower features such as the Kerguelen, Campbell, and Malvinas Plateaus (Figure 5.6b). Based on the barotropic streamfunction from the simulation with the "realistic" bottom (not shown), the ACC intensifies in volume transport because of the reduced bathymetric form drag and becomes more zonal in the flat bottom experiment. The difference in sea surface height in the subtropical gyre is small

between realistic and flat bottom runs (Figure 5.6b) as the water column in the subtropical region is more upper layer stratified and its connection with bathymetry is weak. In contrast, the ocean ridges are important for the circumpolar currents. The ocean ridges, such as the Mid-Atlantic Ridge and Southwest Indian Ridge, generate meanders (Figure 5.6a) which facilitate the meridional property exchange associated with the high eddy kinetic energy in the lee of topography (e.g. Thompson and Sallée 2012). In the flat bottom simulation, the deviations from the zonal flow by topographic steering are largely removed, except the downstream of major topographic features at the Antarctic Peninsula, Kerguelen Plateau, and Campbell Plateau. Overall, the ocean flow in the flat bottom run is stronger and more zonal than that from the realistic bottom case.

Figures 5.6c and d compare the OHC changes induced by $4xCO_2$ from realistic and flat bottom models. Both warming patterns show the banded structure along and to the north the SAF (same with definition in Section 5.3). At low resolution with realistic bathymetry, the ACC is limited to the north of 50˚S in the Atlantic sector, confining the OHC increase to the northern flank of the narrow ACC. Moreover, the realistic bottom model produces more small-scale warming structures located at the meandering jets in the Atlantic and Indian sectors (Figure 5.6c) around the Mid-Atlantic Ridge and Southwest Indian Ridge. Here we pick two meridional transects (15˚W and 45˚E) in the vicinity of these two ocean ridges to look at the vertical structure of warming and meridional velocity change (Figure 5.7). More concentrated, penetrated warming occurs in the realistic bottom model (Figure 5.7a, c) than the flat bottom model (Figure 5.7b, d). For realistic bottom runs, the anomalies of meridional velocity bring warm water poleward. The meridional velocity change in the flat bottom model is much weaker.

The broad-scale warming structure from the flat bottom model is more zonal, consistent with its zonally distributed SAF, which is only altered by the continent and plateaus (Figure 5.6d).

Remarkably, the subsurface warming features gyre-like responses with westward intensification. The westward intensified warming is associated with the increase of the southward flow along the western boundary (black arrows in Figure 5.6c, d). This anomalous meridional velocity is part of the Sverdrup response to the poleward shift and intensification of westerly winds over the Southern Ocean. Most importantly, the enhanced ocean density stratification caused by surface buoyancy flux change without wind stress changes intensifies the subtropical gyre shoaling the wind-driven gyre to satisfy the Sverdrup dynamics, as suggested in Wang et al. 2015. South America (Malvinas Plateau), Kerguelen Plateau, and Campbell Plateau act as the western boundaries for the anomalous subtropical gyres, creating three major centers of maximum OHC warming. The Mid-Atlantic Ridge, for example, in the realistic bottom run acts as an additional, submerged western boundary for the surface warming-induced anomalous subtropical gyre, adding complexity to the OHC pattern.

The model resolution affects the bathymetry effect since the "realistic" bottom from the low-resolution model is largely smoothed. Therefore, the meanders and eddy activities associated with the sharp and small topographic obstacles are partly removed in the low-resolution runs. For example, comparing the low-resolution warming patterns (Figure 5.6) with those from CESM standard-resolution (about 1°) and high-resolution (about 0.1°) shown in Chapter 4 (Figure C11), we find more small-scale structures of OHC change in the high-resolution run.

Overall, topography shows steering effects on the ocean fronts and further features the regional warming pattern. However, the physical mechanisms of ocean current adjustments associated with bathymetry are still not fully understood.

5.5 Results from FAFMIP

5.5.1 Mean circulation effects

In this section, we use idealized experiments from FAFMIP, such as the passive tracer experiment, to investigate the effects of mean ocean circulation on subsurface warming. For Passive-Heat, the added heat is redistributed by the mean flow shown in Figure 5.8. The OHU (contours in Figure 5.8a) takes place in the upwelling regions in the high latitudes (Figure 5.9a), while the ocean stores the excess heat in the mid-latitudes (35˚S-55˚S). The mean ocean jets play an important role in anchoring the pattern of heat storage, which mainly appears to the north of the SAF (Figure 5.8a). The streamwise mean along the SAF shows a remarkable meridional gradient in temperature change, straddling the sharp ocean jets (Figure 5.8b). It is also true for each sector, while the Pacific sector shows a smaller gradient in temperature response associated with its weaker zonal velocity compared with those in the Atlantic and Indian sectors (Figure 5.8c,d).

Associated with the ocean jets, the jet-scale overturning circulation (JSOC; Li et al. 2016) is used here to explain the regional warming asymmetry in the meridional direction. The eddy momentum flux converges toward the core latitude of the SAF and decreases with depth (Li and Lee 2017). The Coriolis force of an equatorward velocity is required to balance the acceleration due to the eddy momentum flux convergence. The density field should adjust to the vertical shear of the zonal current to achieve the thermal wind balance. This means that a downward motion should bring down more buoyant water from the surface on the equatorward jet flank and an upward motion should bring up dense water on the poleward flank of the jet. The vertical profile of the mean vertical velocity from piControl confirms the clockwise JSOC in MRI-ESM2.0 (Figure 5.9b). The Atlantic and Indian sectors show a stronger JSOC (Figure 5.9c) than the Pacific sector (Figure 5.9d). Downward transport of the passive tracer of added heat driven by the

descending branch of the JSOC leads to more warming on the equatorward jet flank than on the poleward flank which is dominated by the ascending process. This indicates that the secondary circulation, the JSOC, is important in shaping the cross-front difference in temperature change.

5.5.2 Feedback from the ocean circulation.

Passive tracers induce no change in ocean circulation, while added heat has the potential to change the density field, affecting the geostrophic balance in the horizontal direction if the currents are allowed to evolve. Here, added heat acts as the forcing, and the ocean evolution is regarded as the feedback to the forcing. In the Passive-Heat, the redistribution of tracers can lead to widespread acceleration of zonal geostrophic velocity (Figure 5.10a). The spatial pattern of the acceleration is highly correlated (R = 0.90) with the mean zonal geostrophic velocity (contours in Figure 5.10a). As a possible physical mechanism for this high correlation, the JSOC increases the meridional density gradient across the front and enhances the jet. Here we consider a 1.5-layer isopycnal ocean model, in which the bottom layer of infinite depth outcrops at the surface in the Southern Ocean (Figure 5.11). Assuming that the warming (ΔT_1) is then limited to the first layer north of the outcrop line, the sea level change is proportional to $\Delta T_1 \bar{h}$. Here, $\bar{h}$ is the mean depth of the isopycnal since there is no change in ocean circulation in the passive tracer experiment. As a result, the change in zonal geostrophic velocity, ΔU_g, is proportional to $\overline{U_g}$ assuming that ΔT_1 is spatially uniform to first order.

The Total-Heat driven change includes the active effect of the added heat. The comparison between the Passive-Heat driven and Total-Heat driven circulation change shows the ocean adjustment to the added heat. The acceleration of zonal geostrophic flow in Total-Heat (color in Figure 5.10b) largely resembles the change in Passive-Heat (contours in Figure 5.10b). This

indicates that the mean ocean circulation, which is steered by bathymetry, plays a leading role in determining the broad-scale circulation change. The exception is the ARC, where a meridional dipole pattern appears instead that represents a poleward displacement of the strong ocean front driven by buoyancy change. For comparison, we also show the results driven by wind stress change: the poleward shifting westerlies leads to poleward shifts in ocean fronts in all sectors (Figure 5.10c), and the magnitude of circulation change is the largest in the vicinity of the ARC.

We further focus on the time evolution and vertical structure of circulation change within a small sector of 35˚E-50˚E within the Indian Ocean (the blue box shown in Figure 5.10a). The Hovmöller diagram shows that both the SAF and ARC keep accelerating in time in Passive-Heat (Figure 5.12a). The SAF accelerates in Total-Heat with little displacement in its latitude, while the ARC displaces poleward with no significant change in intensity (Figure 5.12b). The wind-change-induced shift in the front takes place in the first 1~5 years and then remains nearly constant for the rest of the model run (Figure 5.12c). The vertical cross-section shows that the acceleration of zonal flow is mainly attributed to the Passive-Heat (Figure 5.13a). The dipole pattern of velocity change straddling the mean ARC illustrates the poleward shift of the subtropical front in Total-Heat (Figure 5.13b). Wind stress change also induces a poleward shift of the ARC, but little change in the intensity or position of the SAF (Figure 5.13c). The contrasting responses of different fronts are consistent with the results from Graham et al. (2012), who suggested that the meridional variations in the ocean stratification explain these different responses to wind forcing. North of the ACC the water column is more stratified, and the subtropical front or ARC is more surface intensified and baroclinic. Fronts within the ACC are more barotropic, so their connection with bottom topography is strong. Therefore, the ARC is more sensitive and the SAF is less sensitive to change in wind forcing (Graham et al. 2012). In this work, we suggest the different responses

of the subtropical front and ACC apply to the buoyancy forcing. The upper layer temperature increase leads to more stratification to the north of the ACC, which means the subtropical regions become more surface intensified and control of bathymetry on the subtropical front position becomes weaker. Therefore, the ARC is more sensitive to the buoyancy forcing change.

5.6 Dynamic Adjustment

In Sections 5.4 and 5.5, we discussed two "extreme" cases from different model simulations: one is the low-resolution flat bottom experiment from CESM1 and the other is the Passive-Heat experiment from FAFMIP. Their OHC change patterns differ significantly (Figure 5.6d vs. Figure 5.8a), which may help us understand the dynamic adjustment of ocean jets in response to surface warming.

In the low-resolution flat bottom experiment, the orographic effects and meanders are largely removed. The OHC increase is largely westward and southward intensified towards the SAF (Figure 5.6d). The associated dynamic adjustment features anomalous subtropical gyres, which are delineated by major topography acting as western boundaries. In contrast, the OHC increase in the Passive-Heat extends far to the north (Figure 5.8a). The difference in the northward extent of the OHC increase is most pronounced in the Indian sector between Passive-Heat and flat bottom run (or other CMIP runs shown in Figure 5.1). The Total-Heat shows less warming in the Indian sector to the north of the ARC (Figure 5.14a). The Active-Heat, difference between Total-Heat and Passive-Heat, shows the influence of dynamic adjustment on the regional temperature response (Figure 14b). In the chosen cross-section (35˚E-50˚E), the poleward displacement of the ARC limits the northward extent of OHC increase as required by geostrophy, producing a concentrated warming within a narrow latitudinal band (Figure 5.15a vs. 5.15b). The shift induced

by wind stress change also shows a similar, albeit weaker, effect on the ARC and ACC (Figure 5.15c).

Thus, the dynamical adjustments of zonal jets in the Southern Ocean are fundamental to understanding the pattern of OHC change. Surface warming causes the ACC to accelerate and narrow (in the Atlantic sector) or displace southward (in case of ARC), and the OHC pattern forms in geostrophic balance. We plan to conduct an additional passive-tracer case in the flat bottom model to further investigate the connection between the passive response and dynamic adjustment.

5.7 Summary

In this chapter, we demonstrate that the spatial pattern of the Southern Ocean subsurface warming is strongly anchored by the ocean jets by using various sets of model simulations. We find that the observed and simulated OHC change mainly occurs north of the ACC, from the northwest in the Atlantic to the southeast in the Pacific along the ACC tilted axis. The positions of the SAF and the maximum OHC change are highly correlated across CMIP5/CMIP6 models, especially in the region where the flow is more zonal. Based on flat bottom simulations, we show that the bathymetry steers the ocean fronts, which affects the regional pattern of warming.

The meridional overturning circulation associated with the Ekman upwelling and downwelling can explain the zonal mean response of temperature change well, as discussed in Shi et al. 2020. For the regional response, the jet-scale overturning circulation discussed in this chapter creates warming asymmetry across the jet by the downward branch on the northern flank and upward branch on the southern flank. This warming asymmetry driven by jet-scale overturning circulation enhances the zonal flow in order to reach the geostrophic balance. The spatial pattern of this zonal flow acceleration driven by added heat is highly correlated with the mean velocity

field. The poleward displacement of the ARC, which is an extraordinarily strong current and is more surface intensified than the SAF, restricts the subsurface warming to a narrow band along the slanted ocean front. These results demonstrate that jet dynamics is important in shaping the regional responses in the Southern Ocean.

5.8 Acknowledgments

Chapter 5, in part, is a draft in preparation for submission for publication as “Spatial Pattern of the Southern Ocean Subsurface Warming: The Role of Ocean Jets”, by J.-R. Shi, S.-P. Xie, and L. D. Talley. The dissertation author was the primary investigator and author of this material.

Table 5.1: CMIP5 models for the output of ocean potential temperature, zonal velocity, sea surface height, and net surface heat flux in historical, RCP4.5, 4xCO2, and piControl experiments.

Model Names	Historical and RCP4.5	$4xCO_2$ and piControl
ACCESS1-0	√	√
ACCESS1-3	√	√
CCSM4	√	√
CESM1-BGC	√	-
CESM1-CAM5	√	-
CMCC-CM	√	-
CMCC-CMS	√	-
CNRM-CM5	√	√
CSIRO-Mk3-6-0	√	-
CanESM2	√	√
GFDL-CM3	√	√
GFDL-ESM2M	√	√
GISS-E2-R	√	-
HadGEM2-ES	√	√
IPSL-CM5A-LR	√	√
IPSL-CM5A-MR	√	-
IPSL-CM5B-LR	√	√
MIROC-ESM	√	√
MIROC-ESM-CHEM	√	-
MIROC5	√	√
MPI-ESM-LR	√	√
MPI-ESM-MR	√	√
MRI-CGCM3	√	√
NorESM1-M	√	-
NorESM1-ME	√	-
bcc-csm1-1	√	-
bcc-csm1-1-m	√	-

Table 5.2: CMIP6 models for the output of ocean potential temperature, zonal velocity, sea surface height, and net surface heat flux in historical, SSP2-4.5, 4xCO2, and piControl experiments.

Model Names	Historical and SSP2-4.5	$4xCO_2$ and piControl
ACCESS-CM2	-	√
ACCESS-ESM1-5	-	√
BCC-CSM2-MR	√	-
CanESM5	√	√
CESM2	√	√
CESM2-WACCM	√	√
EC-Earth3	√	-
EC-Earth3-Veg	√	√
FGOALS-f3-L	-	√
FIO-ESM-2-0	-	√
GFDL-CM4	√	-
GFDL-ESM4	√	-
IPSL-CM6A-LR	√	√
MIROC6	√	√
MPI-ESM1-2-HR	√	√
MPI-ESM1-2-LR	-	√
MRI-ESM2-0	-	√
NESM3	√	√
SAM0-UNICON	-	√

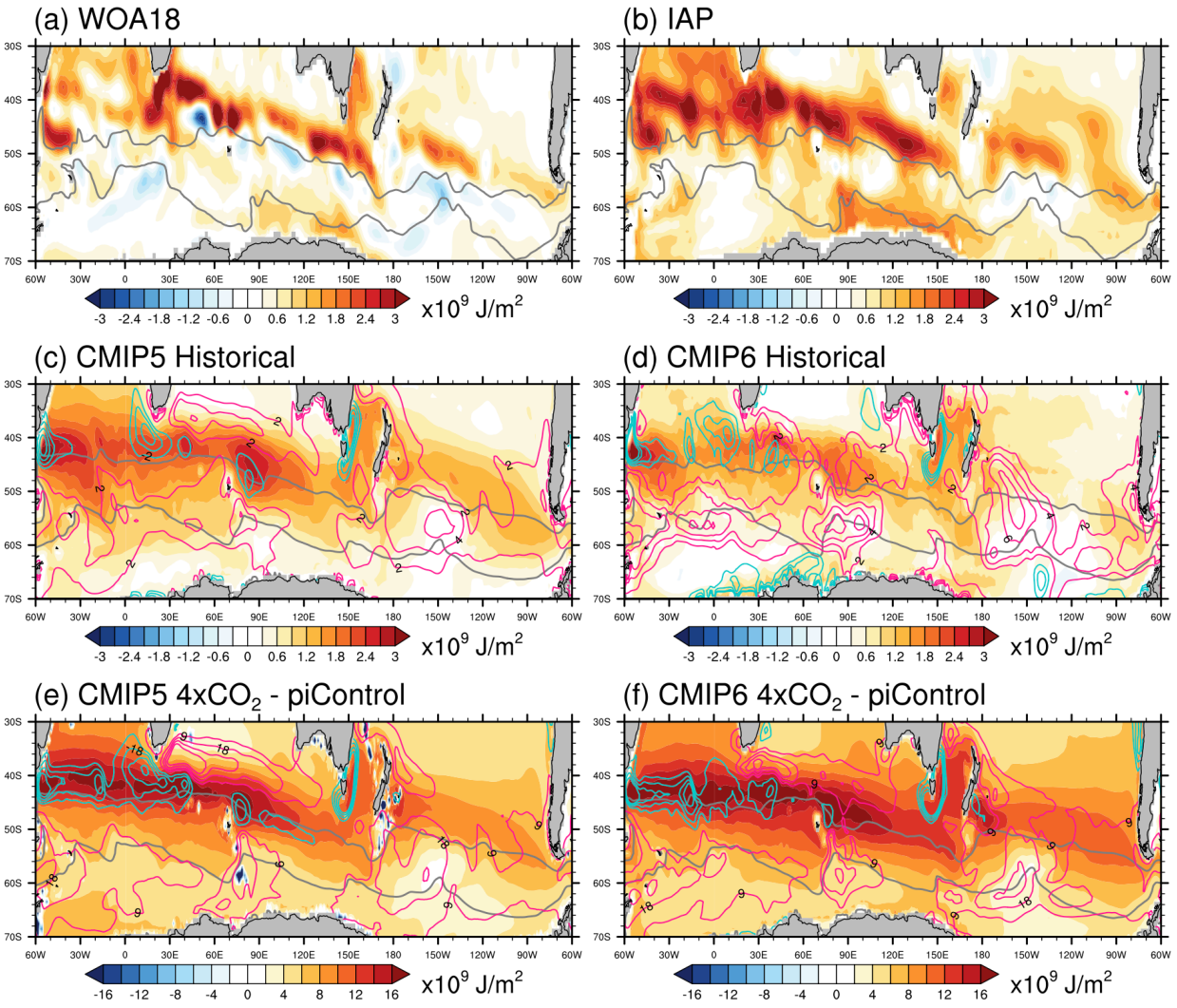

Figure 5.1: OHC change (shading; 10^9 J/m^2) in the upper 2000 m from (a) WOA18, (b) IAP, (c) ensemble mean of CMIP5 Historical runs, and (d) CMIP6 Historical runs. The anomalies represent the difference between the 2005-2017 mean and the mean over the 1955-1984 base period. For (e) CMIP5 and (f) CMIP6 abrupt 4xCO2 experiments, the change in upper 2000 m OHC is the average of years 41-90 minus the pre-industrial control. Gray contours indicate the Subantarctic Front and Southern ACC Front from Orsi et al. (1995) in (a) and (b). In simulations, (c)-(f), the Subantarctic Front and Southern ACC Front are defined as the northmost and southmost mean sea surface height going through the Drake Passage. Colored contours in (c)-(f) indicate surface heat flux change (W/m^2) from the corresponding experiments and periods. Red (cyan) contours mean the anomalous heat flux going into (out of) the ocean.

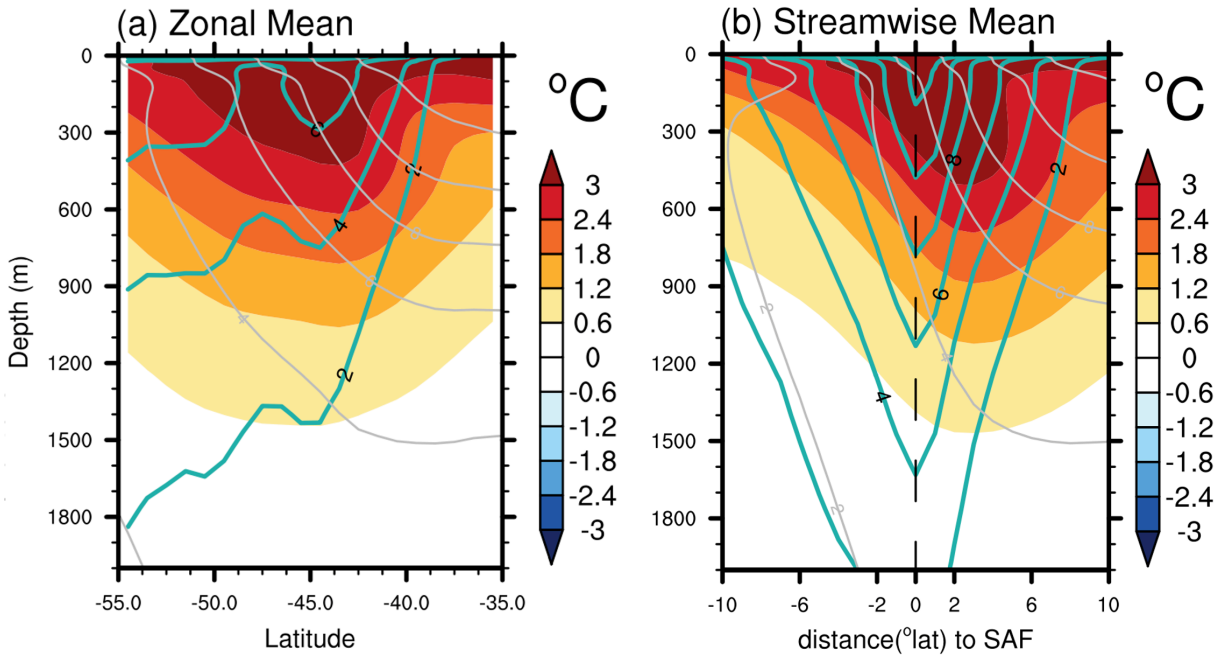

Figure 5.2: Global zonal mean and streamwise mean of the temperature change from 4xCO_2 relative to piControl with mean zonal flow from piControl shown as cyan contours. The streamwise coordinate follows the SAF, spanning from 10˚ south to 10˚ north of the SAF latitude. Gray contours are climatological temperature from piControl.

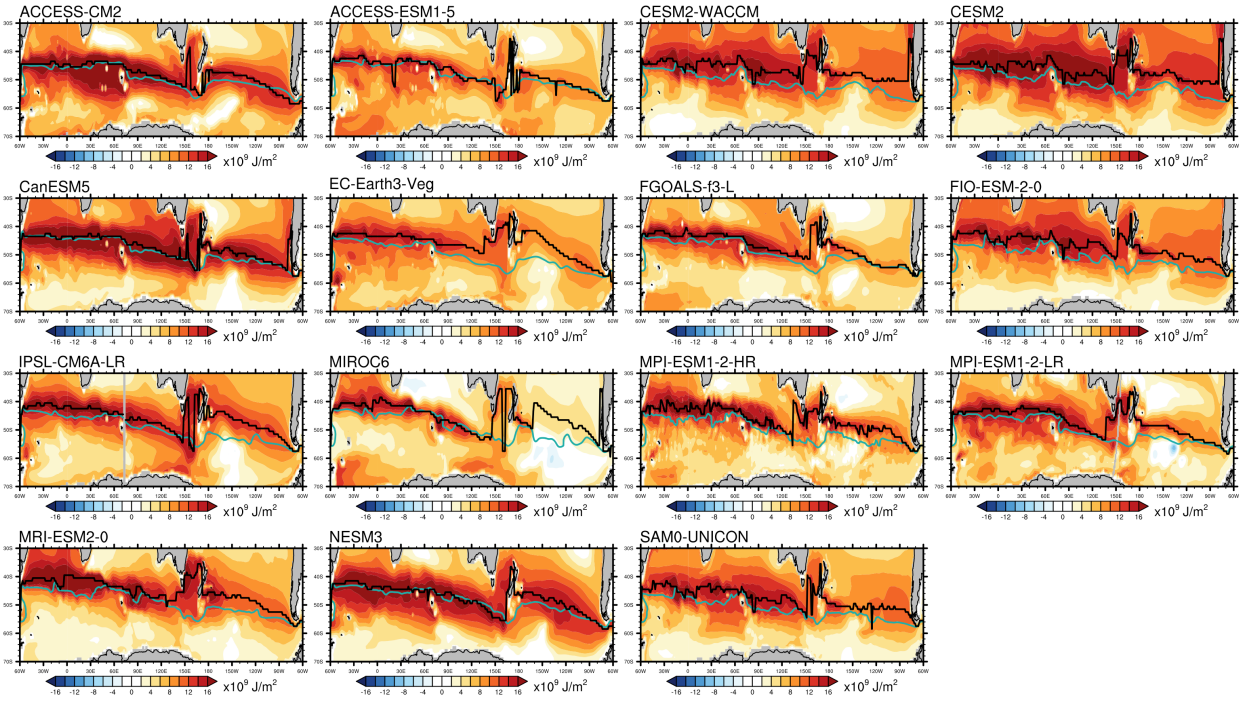

Figure 5.3: Upper 2000 m OHC change (10^9 J/m^2) from CMIP6 4xCO_2 simulations relative to the corresponding piControl. Black curve is the position of maximum OHC change from each model, and cyan curve is the SAF from each model.

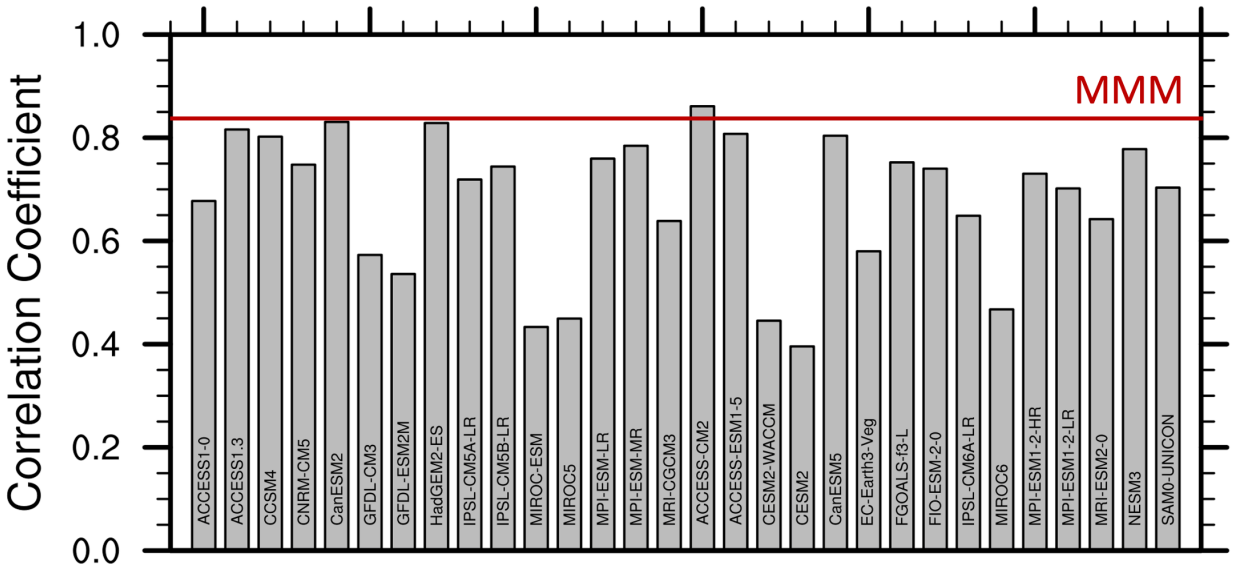

Figure 5.4: Correlation coefficient of positions of the maximum OHC change and the SAF in latitude for each model. The correlation coefficient from the multi-model mean is shown as the red line.

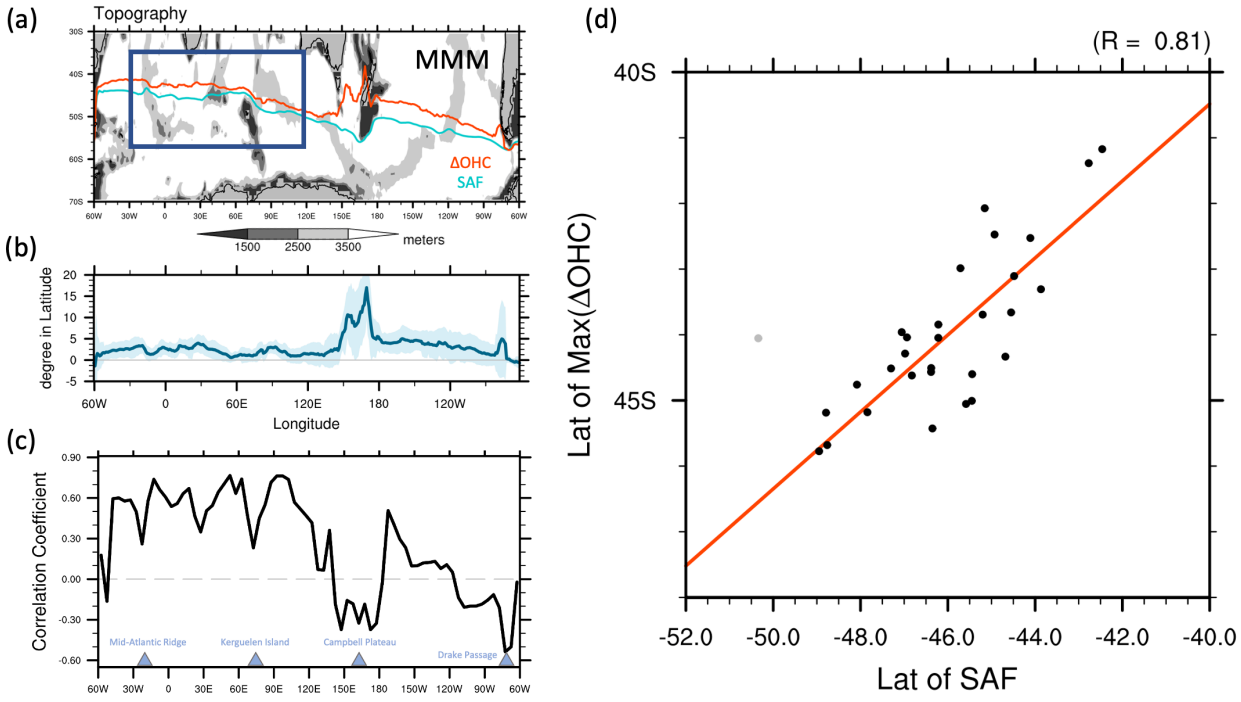

Figure 5.5: (a) Topography from model CESM2 superimposed by positions of the mean SAF (cyan curve) and maximum OHC change within the Southern Ocean (red curve). (b) The displacement between the SAF and maximum OHC change. Positive means that maximum OHC change locates to the north of the SAF. (c) Correlation coefficient of the positions of the SAF and maximum OHC change across CMIP5/CMIP6 models for each 5˚ longitude. (d) Maximum OHC change vs SAF in their positions within the blue box shown in (a). Each dot denotes the result from each model, and the outliner marked as gray dot is from the model GFDL-CM3.

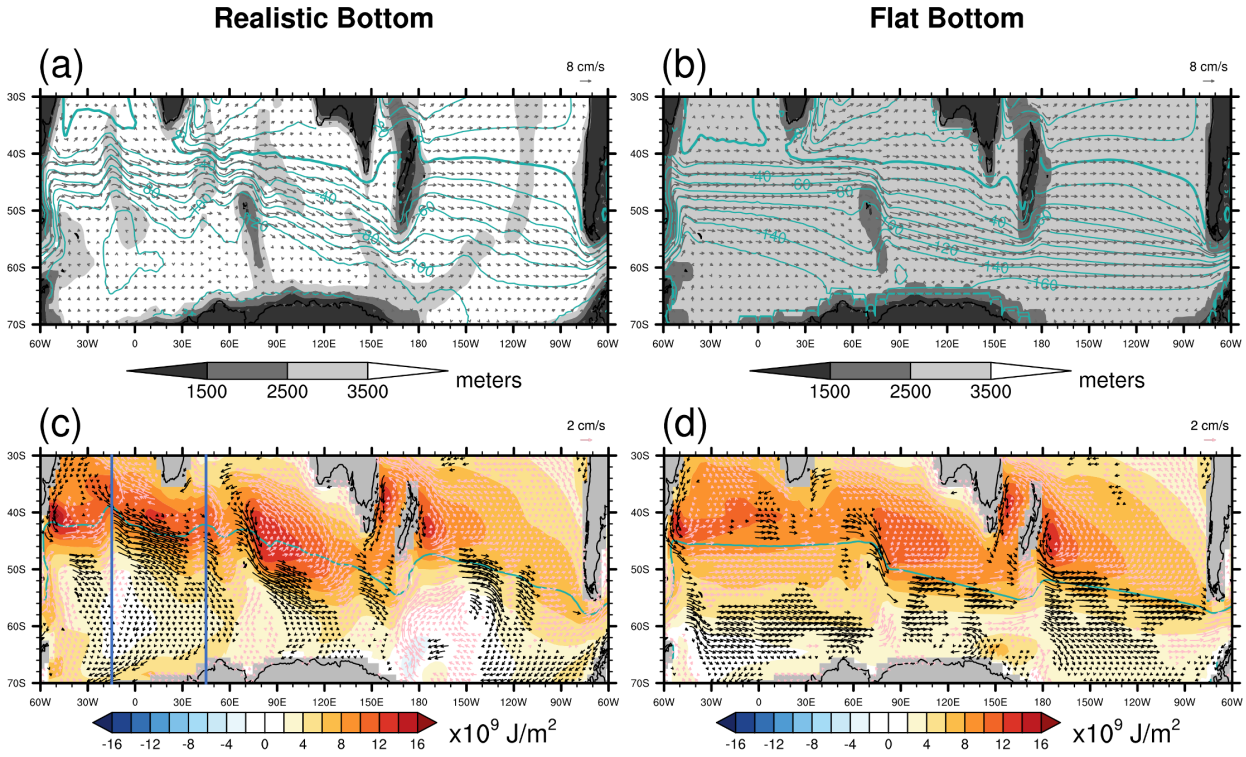

Figure 5.6: Topography from (a) CESM PI simulation with a realistic bottom and (b) PI_FB simulation with a flat bottom, with climatological sea surface height shown as contours. Gray arrows in (a) and (b) are climatological horizontal velocity at 100 m depth from corresponding runs. Upper 2000 m OHC change and ocean velocity change at 100 m from (c) Cx4-PI and (d) Cx4_FB – PI_FB. Black arrows are the poleward meridional velocity anomalies, and pink arrows show the equatorward ones in (c) and (d).

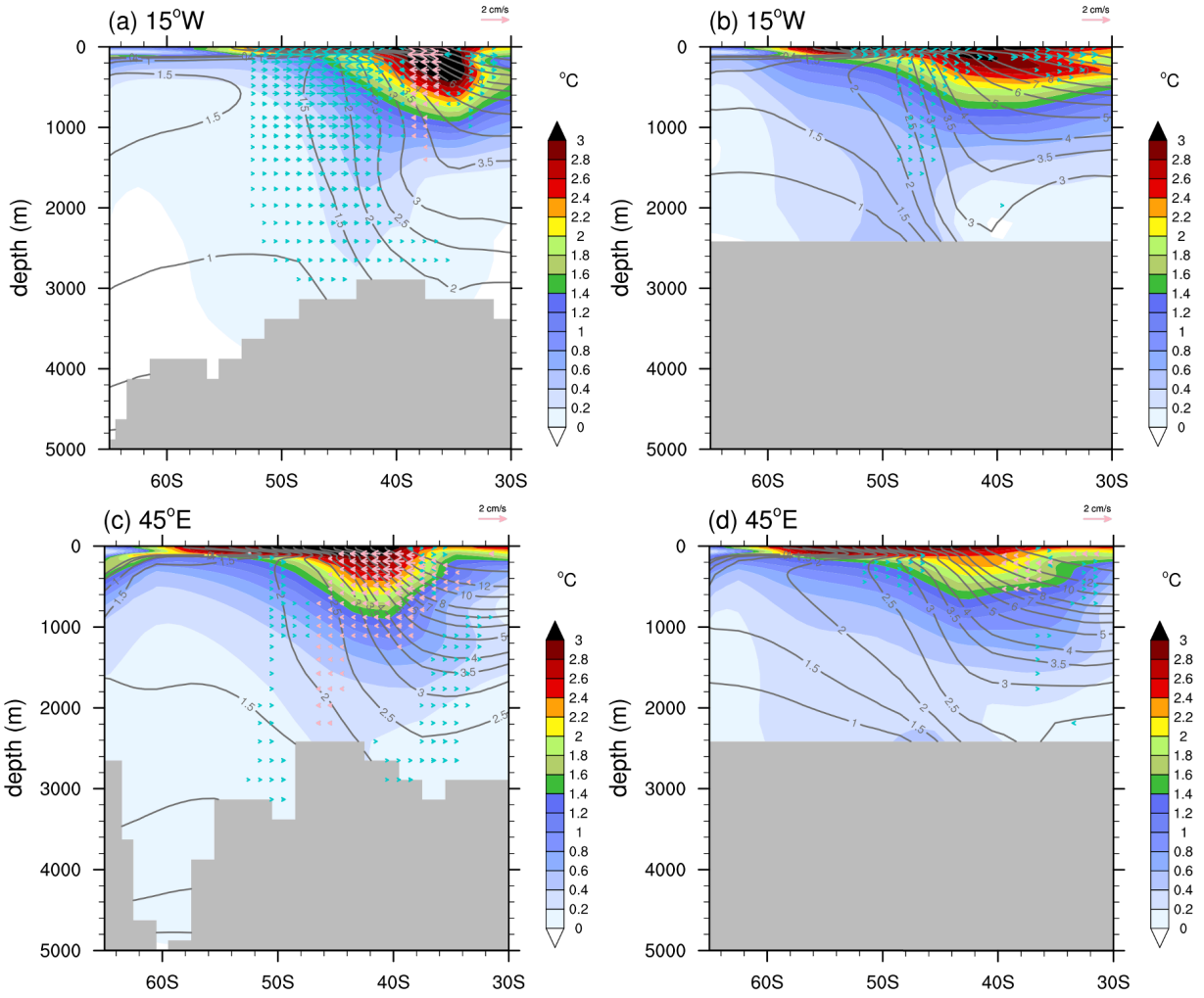

Figure 5.7: (a)-(b), meridional transect along 15˚W for the temperature change and meridional velocity change from realistic and flat bottom simulations. (c)-(d), same with (a)-(b), but for the 45˚E transect. Gray contours are the climatological isothermals from PI and PI_FB. Cyan arrows are the equatorward meridional velocity anomalies, and pink arrows show the equatorward ones.

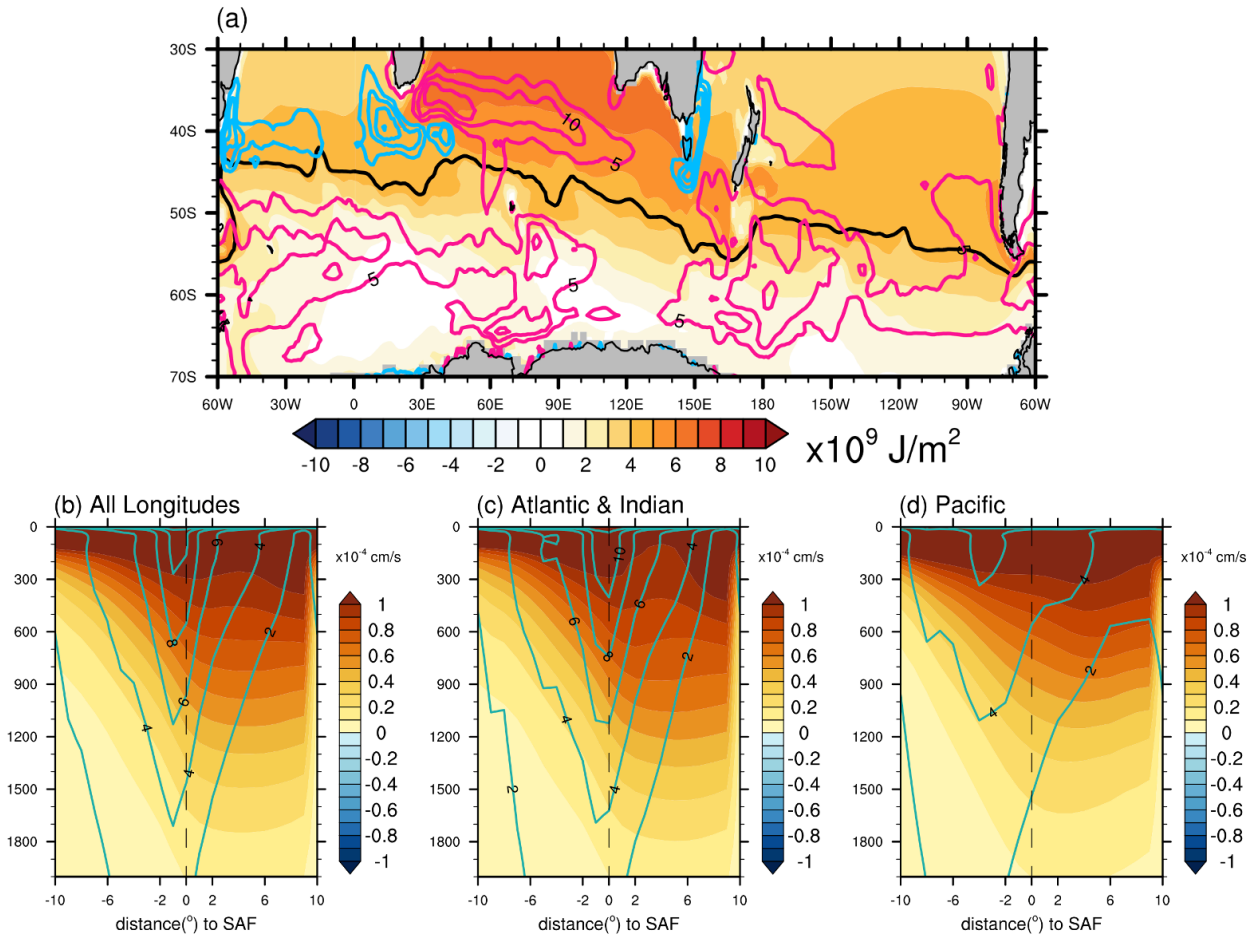

Figure 5.8: (a) OHC change in the upper 2000 m from Passive-Heat relative to piControl. The black curve is the SAF. The colored contours are surface heat flux changes. Streamwise mean of ocean temperature changes from (b) all longitudes, (c) the Atlantic and Indian sectors, and (d) the Pacific sector are superimposed by climatological zonal flow from piControl.

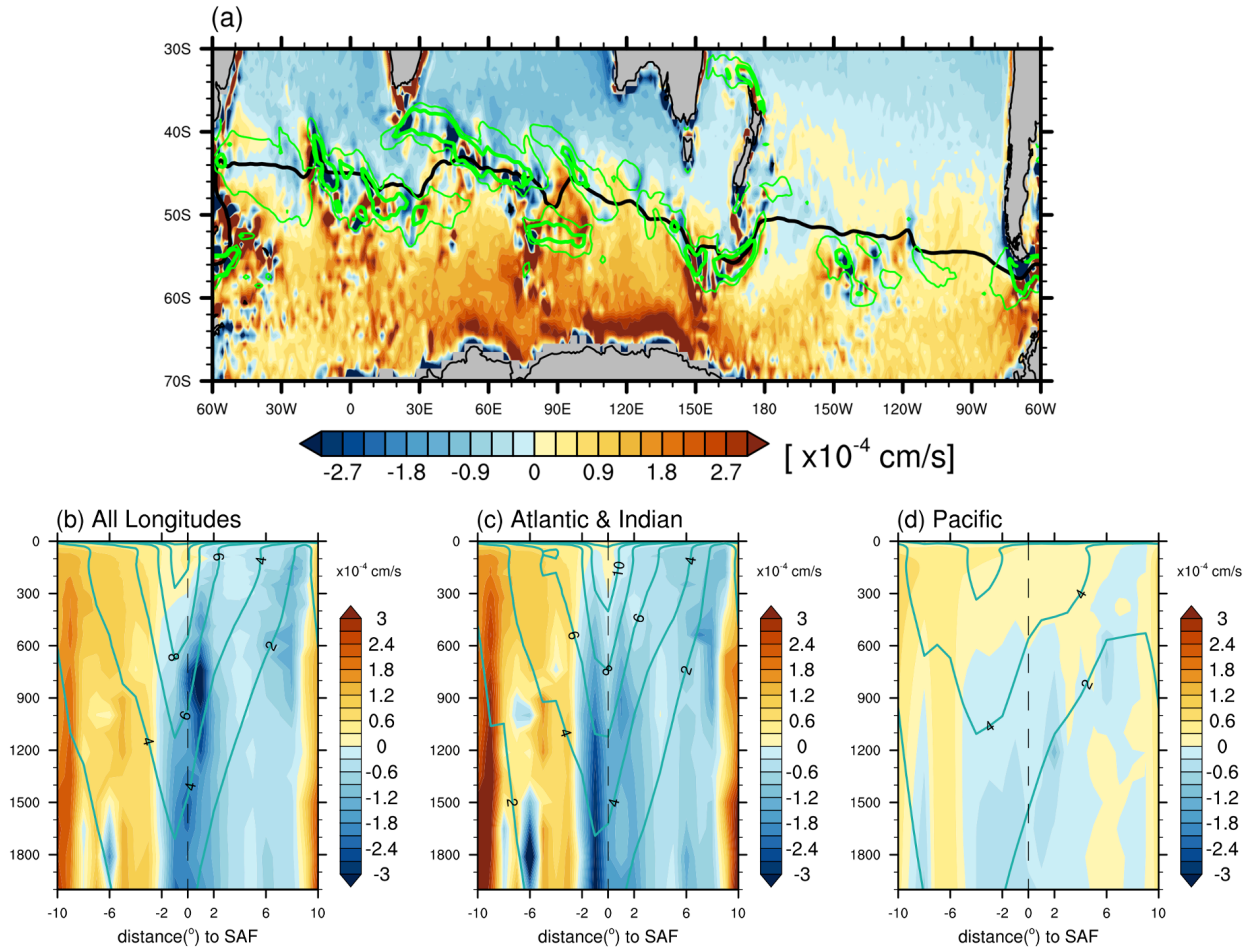

Figure 5.9: Same as Figure 5.8, but for the climatological vertical velocity from piControl. Positive means upwelling vertical velocity.

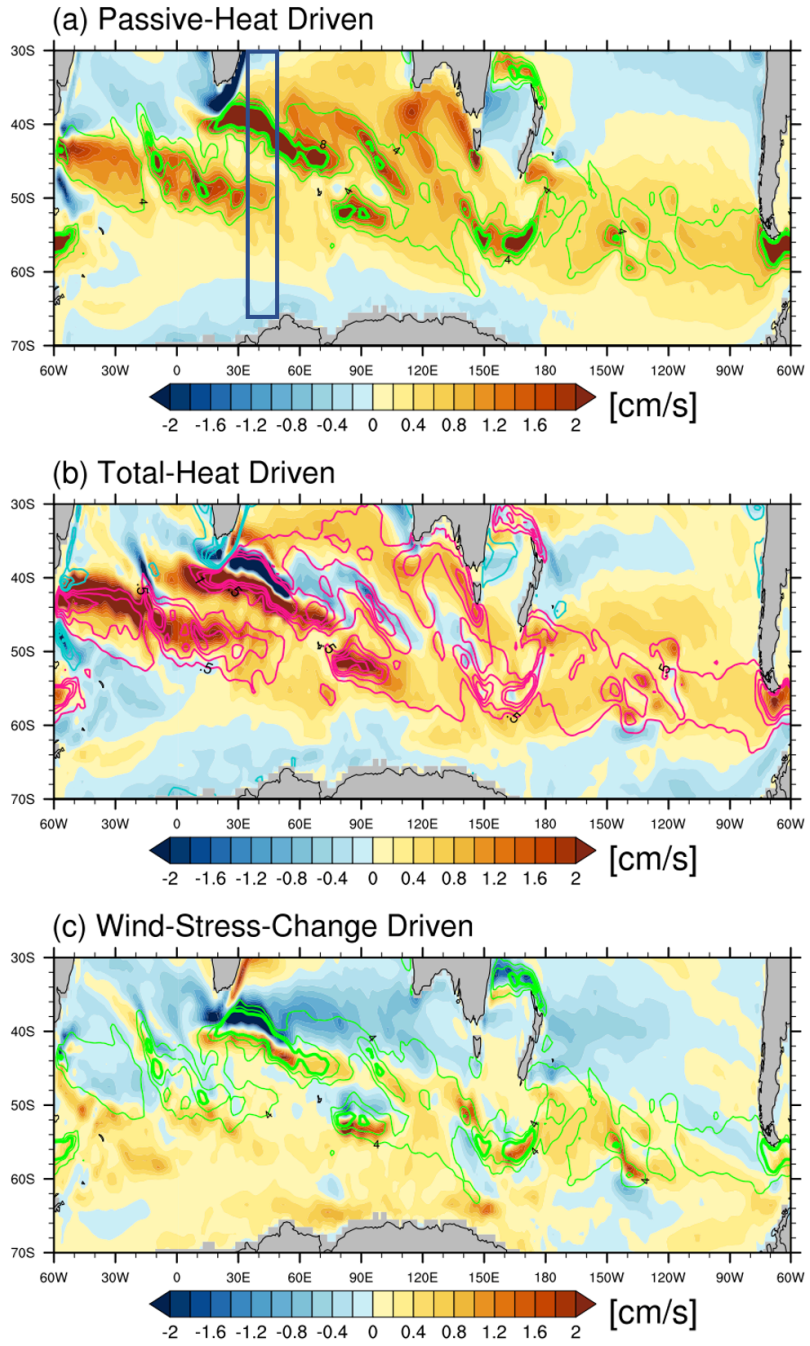

Figure 5.10: Zonal geostrophic velocity change driven by (a) Passive-Heat, (b) Total-Heat, and (c) Wind-Stress-Change. The green contours are climatological zonal velocities. The thick contour is the velocity at 12 cm s^{-1}. The cyan (westward change) and red (eastward change) contours in (b) are the velocity change induced by Passive-Heat, same with (a).

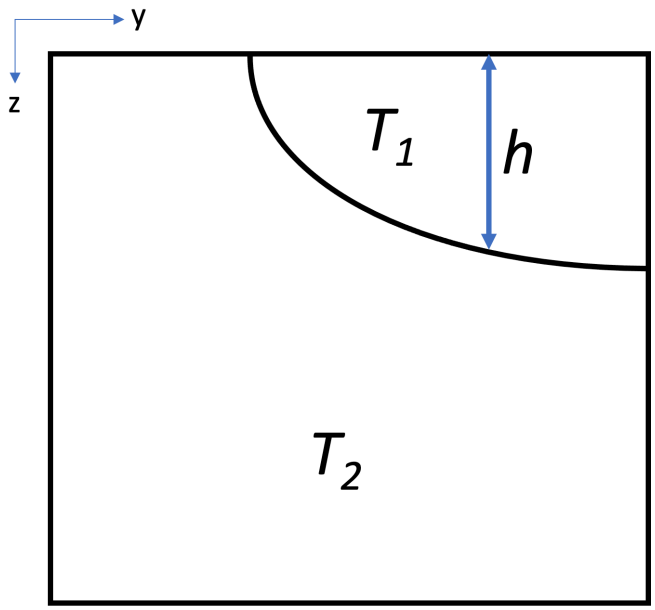

Figure 5.11: Schematic of 1.5-layer isopycnal ocean model with bottom layer outcropping at the surface.

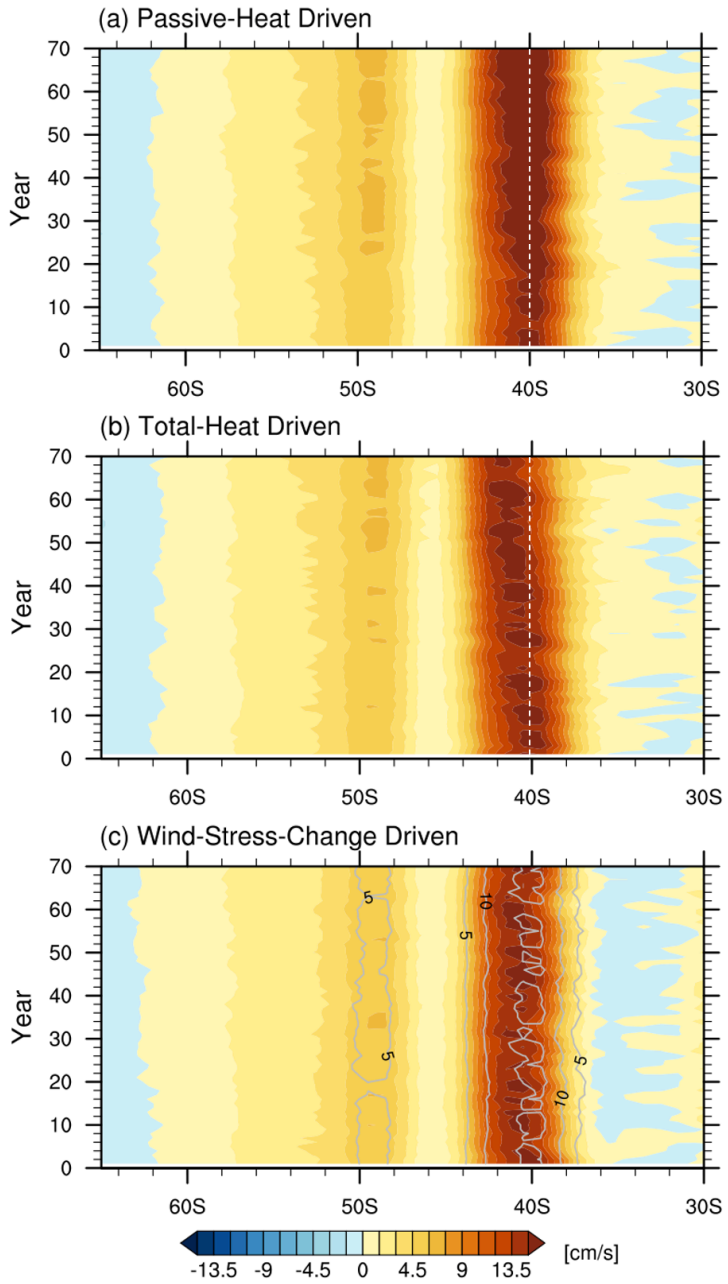

Figure 5.12: Hovmöller diagrams of zonal geostrophic velocity in the first 70 years from the (a) Passive-Heat, (b) Total-Heat, and (c) Wind-Stress-Change simulations, zonally averaged in the Indian sector of 35˚E-50˚E. The velocity from piControl is shown as gray contours in (c).

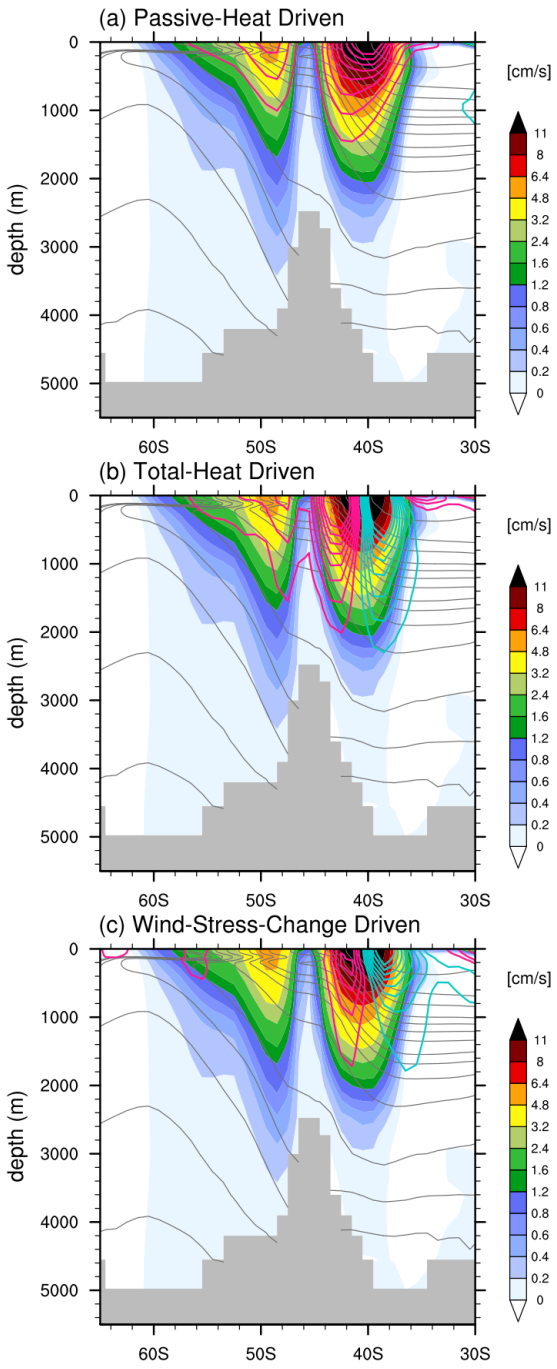

Figure 5.13: Vertical cross-sections of zonal geostrophic velocity change (contours; cm/s) from (a) Passive-Heat, (b) Total-Heat, and (c) Wind-Stress-Change simulations, zonally averaged in the Indian sector of 35˚E-50˚E. The shadings are climatological zonal velocity from piControl.

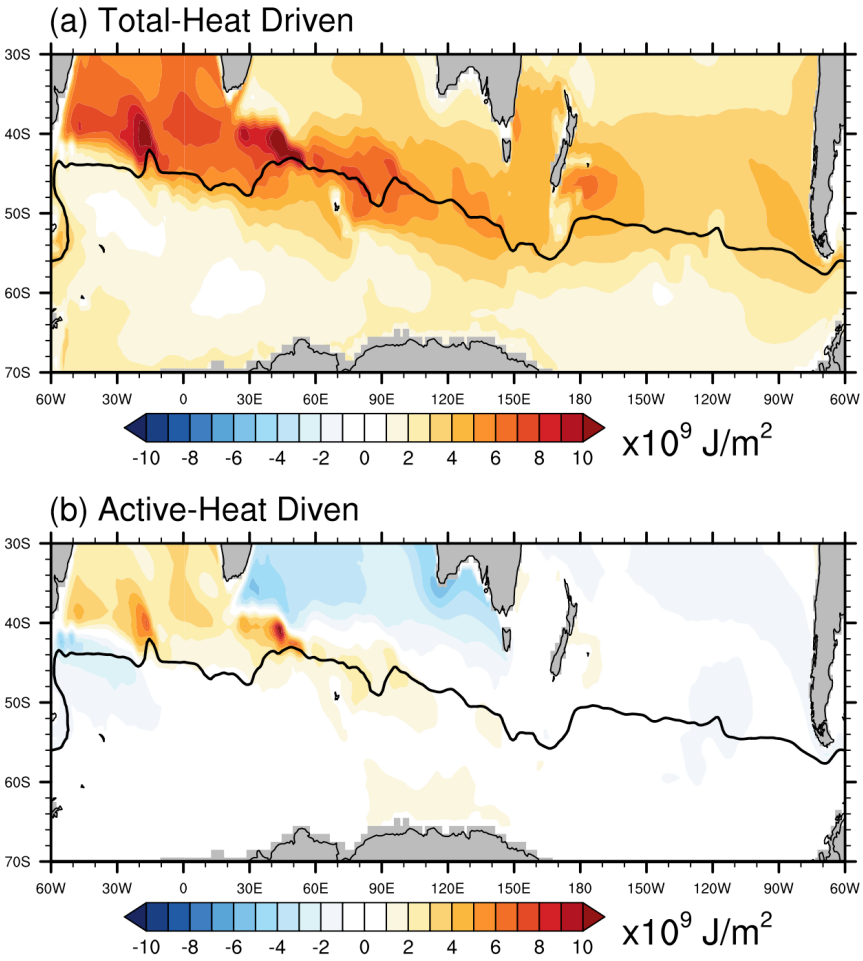

Figure 5.14: OHC change in the upper 2000 m from (a) Total-Heat relative to piControl and (b) Active-Heat, which is the difference between Total-Heat and Passive-Heat. The black curve is the SAF.

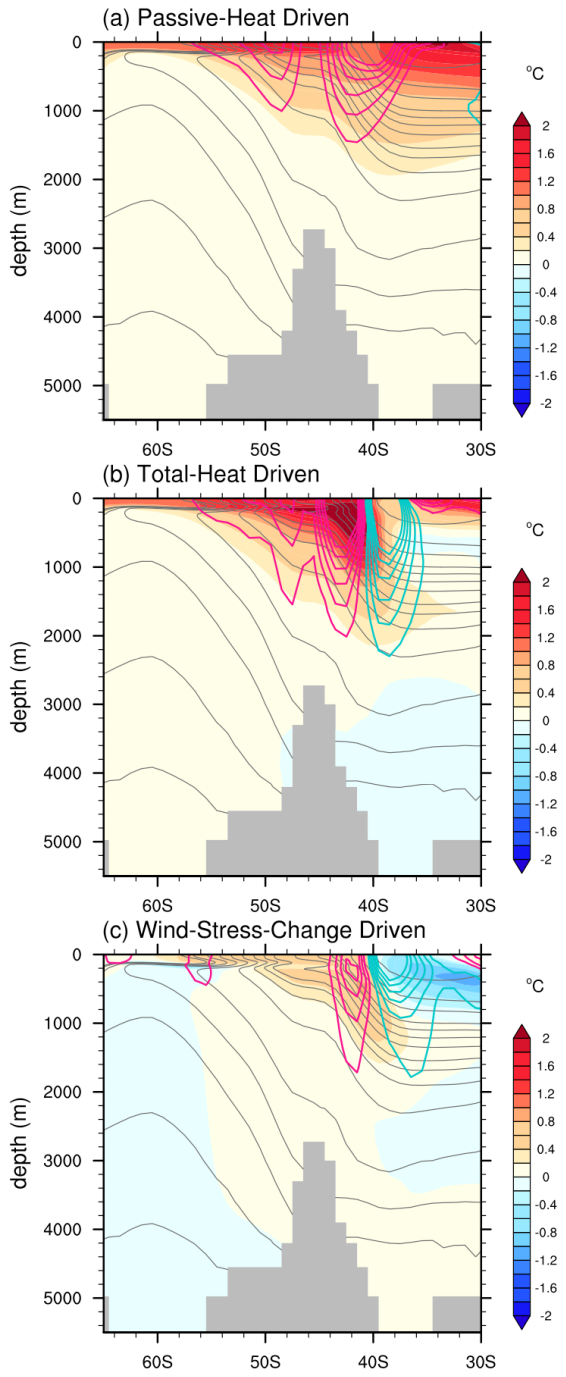

Figure 5.15: Vertical cross-sections of temperature change (shadings; ˚C) from (a) Passive-Heat, (b) Total-Heat, and (c) Wind-Stress-Change simulations, zonally averaged in the Indian sector of 35˚E-50˚E.. Colored contours are changes of zonal geostrophic velocity from corresponding experiments (eastward in red and westward in cyan). Gray contours are mean isothermals from piControl.

Chapter 6

Conclusion

In this dissertation, modern observational data sets and global climate model simulations were utilized to investigate the responses of the Southern Ocean in a changing climate. The main objectives of this work centered on the Southern Ocean subsurface temperature change from the 1-dimensional time evolution (Chapter 2) to the global zonal mean response (Chapters 3 and 4), and further to its spatial pattern and regional response (Chapter 5). The ocean heat content change was found to be linked with atmosphere-ocean interaction, i.e. ocean heat uptake (Chapter 2 and 3), and ocean circulation (Chapters 4 and 5). We found that the large-scale and secondary ocean circulations play an important role in redistributing the absorbed heat and controlling the warming pattern. We further analyzed the effects of buoyancy forcing and wind stress change on the Southern Ocean climate change by using idealized model experiments, and demonstrated that the surface buoyancy forcing change dominates the Southern Ocean subsurface warming and the acceleration of the zonal flow (Chapter 3 to 5). The recent observations from satellite and hydrographic data supported the robust acceleration of the Southern Ocean zonal flow (Chapter 4).

In Chapter 2, we compared the ocean heat uptake and heat storage change in the Southern Ocean and North Atlantic during different time periods (historical vs. future scenarios) driven by different atmospheric forcing agencies (greenhouse gases vs. anthropogenic aerosols). The Southern Ocean accounts for more than 70% of global heat uptake during the historical period, while the contribution from the North Atlantic north of 30˚N is only 6%. This small change in the

North Atlantic is due to the compensation between greenhouse gases and aerosols, associated with weakening (strengthening) of the Atlantic Meridional Overturning Circulation in response to greenhouse gas (aerosol) radiative forcing. In the Southern Ocean, the cooling effect of the anthropogenic aerosols is much weaker. In future scenarios, such as RCP8.5, the Southern Ocean still dominates the heat absorption and heat storage with an exponential increase, while its percentage contribution to global uptake decreases to 48% due to the substantial increase in the ocean heat uptake over the northern North Atlantic.

Motivated by the results of Chapter 2, in Chapter 3 we sought to relate the remarkable Southern Ocean climate change to the surface buoyancy flux change and wind stress change, respectively. To accomplish this goal, we used idealized simulations such as the CESM partial-coupling model simulations and the FAFMIP experiments. Many previous studies focused on the Southern Ocean responses to the poleward-intensified westerly wind, whereas in this study we noted that surface buoyancy flux change can play a more critical role in driving the ocean subsurface warming, salinity change, and an increase in baroclinic transport within the ACC. The surface freshening induced by the buoyancy forcing change is partly compensated by the surface salinity increase due to the enhancement of westerlies, which brings saltier deep water to the surface via increasing Ekman upwelling. More importantly, we showed that the uneven subsurface warming distribution, i.e. more warming to the north of the ACC than within the ACC, increases the meridional density gradient and enhances zonal geostrophic velocity in the upper layer. The wind-change-induced zonal velocity change is more barotropic and smaller in magnitude compared with the responses to the buoyancy forcing change. The acceleration of the Southern Ocean zonal flow found in the model simulations was supported in the observations from satellite altimeter and hydrographic data during recent decades, as discussed in Chapter 4. Multiple model

simulations show that the observed eastward acceleration is of anthropogenic origin, and support attribution of the acceleration to the warming distribution as opposed to the wind changes. We expect the zonal acceleration to continue and increase in the future due to the continuing ocean heat uptake and heat storage in the Southern Ocean.

As the aforementioned conclusions from Chapter 2 to Chapter 4 are largely based on the zonal mean responses, it is important to further investigate the regional responses in the Southern Ocean, which are still not fully understood and full of challenges. In Chapter 5, we focused on the relation between the spatial pattern of the Southern Ocean subsurface warming and mean ocean jets. We showed that banded OHC change structure spanning from the northwest in the Atlantic (~35˚S) to the southeast in the Pacific (~55˚S) is strongly anchored by the mean ocean jets, which are steered by the bathymetry. The secondary ocean circulation, i.e. jet-scale overturning circulation, is used to explain the regional warming pattern: the downwelling branch of the jet-scale overturning circulation leads to more warming on the equatorward jet flank, while the upwelling branch suppresses the warming on the poleward flank. Moreover, the ocean adjustment to warming, such as displacement of ocean fronts, is also an important factor affecting the regional response. Here we showed that the poleward displacement of the Agulhas Return Current, which is more upper layer stratified, provides a concentrated warming pattern in the vicinity of the strong current.

The research presented in this dissertation improves understanding of the physical processes controlling the Southern Ocean climate change. These results can contribute to more reliable future projections and guide future observational strategies, e.g. for the Argo array, to look at the regions showing the “fingerprint” of climate change. However, there are still several outstanding questions stemming from this dissertation. For instance, how do the jet dynamics work

in the ocean adjustment to global warming? How would the topography impact the surface current change? To what extent does the zonal deep mixed layer distribution affect the regional temperature change? Moreover, radiative forcing of anthropogenic aerosols can give rise to remarkable regional responses, such as the changes in North Atlantic temperature and the Atlantic Meridional Overturning Circulation. Can we find more evidence for the regional responses to anthropogenic aerosols in the ocean based on the recent observations and state-of-the-art model simulations? Future work is needed to elucidate the regional details of the response patterns.

Appendix A

Appendix for Chapter 2

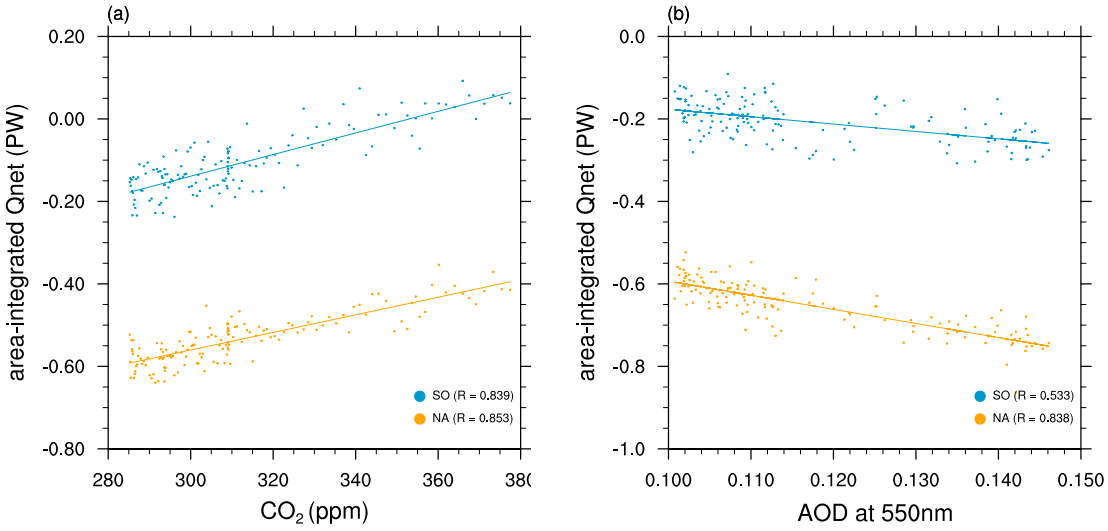

Figure A1: The relationship between area-integrated surface heat flux (Qnet) and (a) atmospheric concentration of CO_2 (ppm), (b) global average of aerosol optical depth (AOD) at 550mn. Each small dot represents annual mean of surface heat flux and CO_2 concentration or AOD. Negative denotes net loss of ocean heat. The results from the Southern Ocean (North Atlantic north of 30˚N) are denoted by blue (orange) points. R is the linear correlation coefficient between area-integrated Qnet and CO_2 (AOD). Data are from GFDL-CM3.

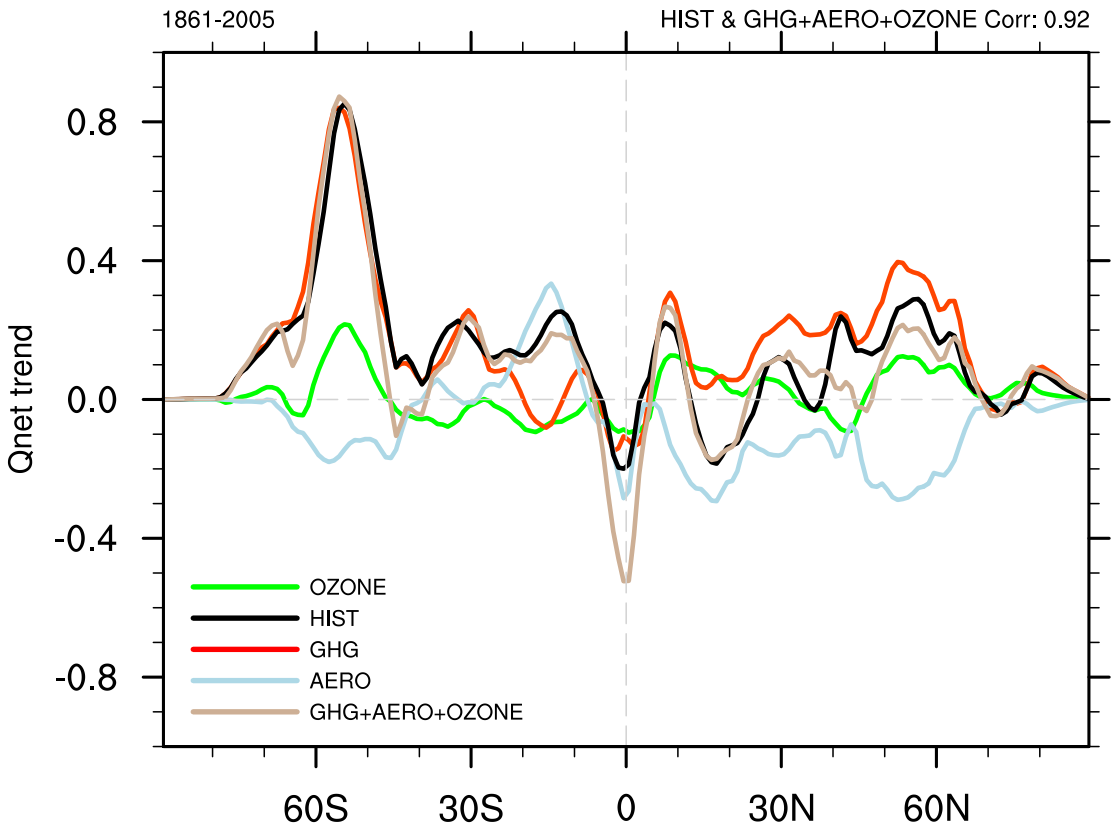

Figure A2: Zonally integrated Qnet trend (in TW/lat per decade) in OZONE (green), GHG (red), AERO (blue) and HIST (black) runs from 1861 to 2005. All the responses are from the ensemble mean of three CMIP5 models with OZONE runs available: CCSM4 (3 members), CESM1-CAM5 (3 members) and GISS-E2-R (5 members). The brown curve denotes the sum of responses of GHG, AERO, and OZONE (GHG+AERO+OZONE).

Figure A3: Time series of the AMOC index (in Sv) in different runs from each CMIP5 model. The number in the bracket denotes the long-term trend (dashed line) for each experiment. An 11-year running mean is applied to the time series.

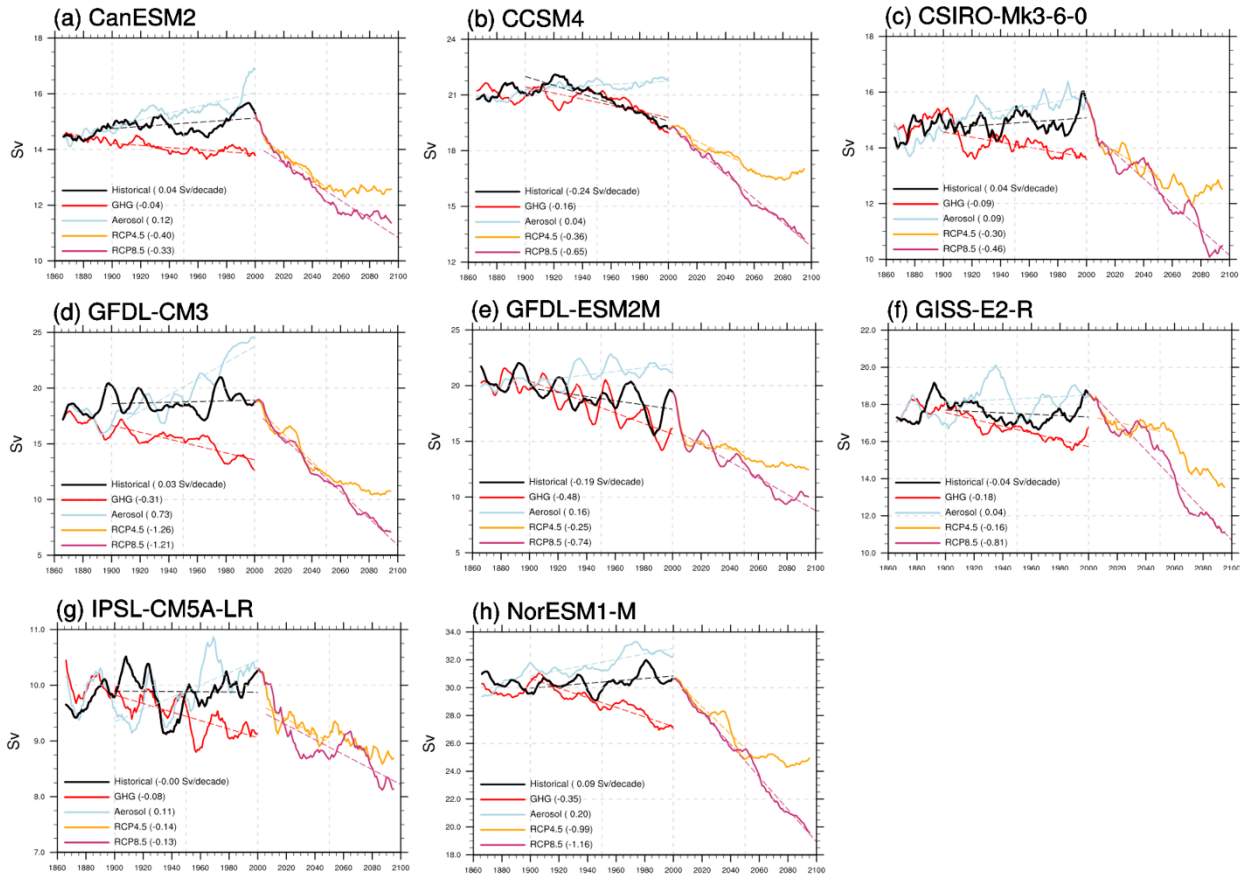

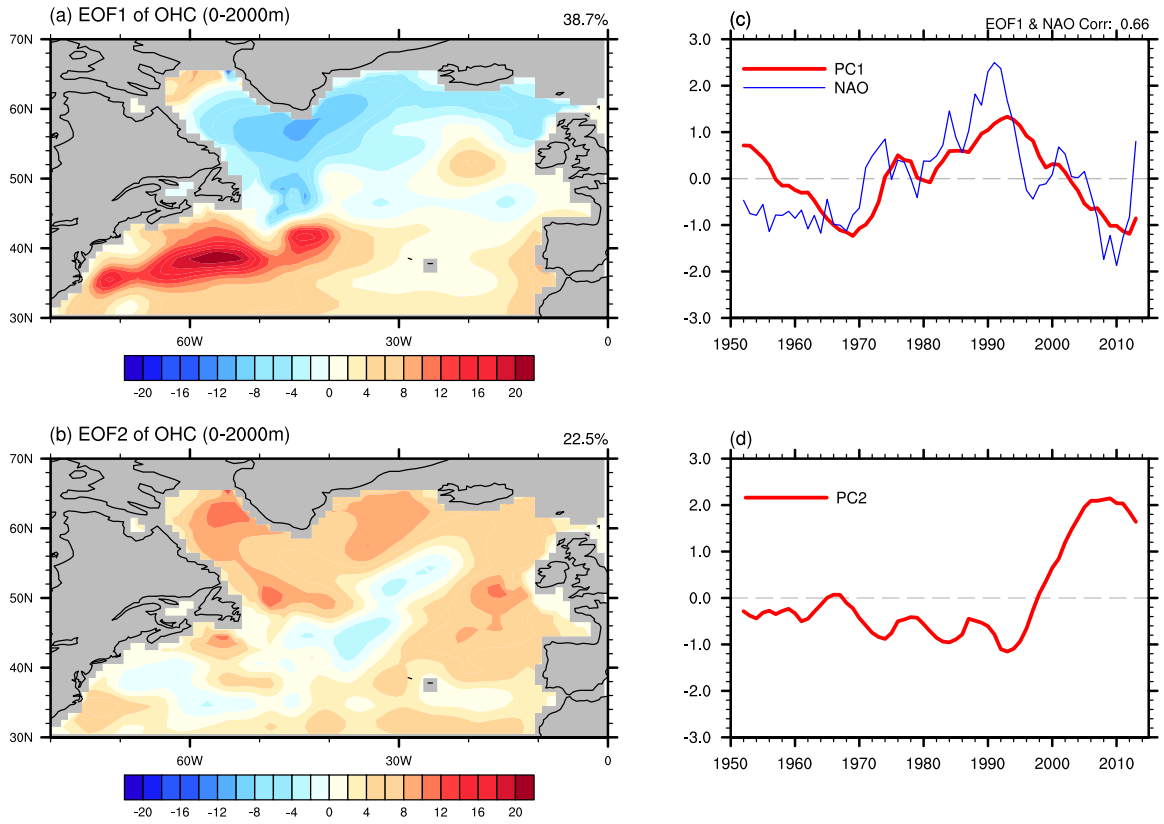

Figure A4: First two EOF modes of OHC above 2000m from 1950 to 2016 from EN4-G10 (observation), to compare with the IAP results in Figure 2.13. EOF patterns are shown in (a) and (b). Normalized principal components (PC; red) are shown in (c) and (d). The number at the upper right corner of (c) shows the cross-correlation between PC1 and NAO (blue). 5-year running mean is applied to the PCs and NAO.

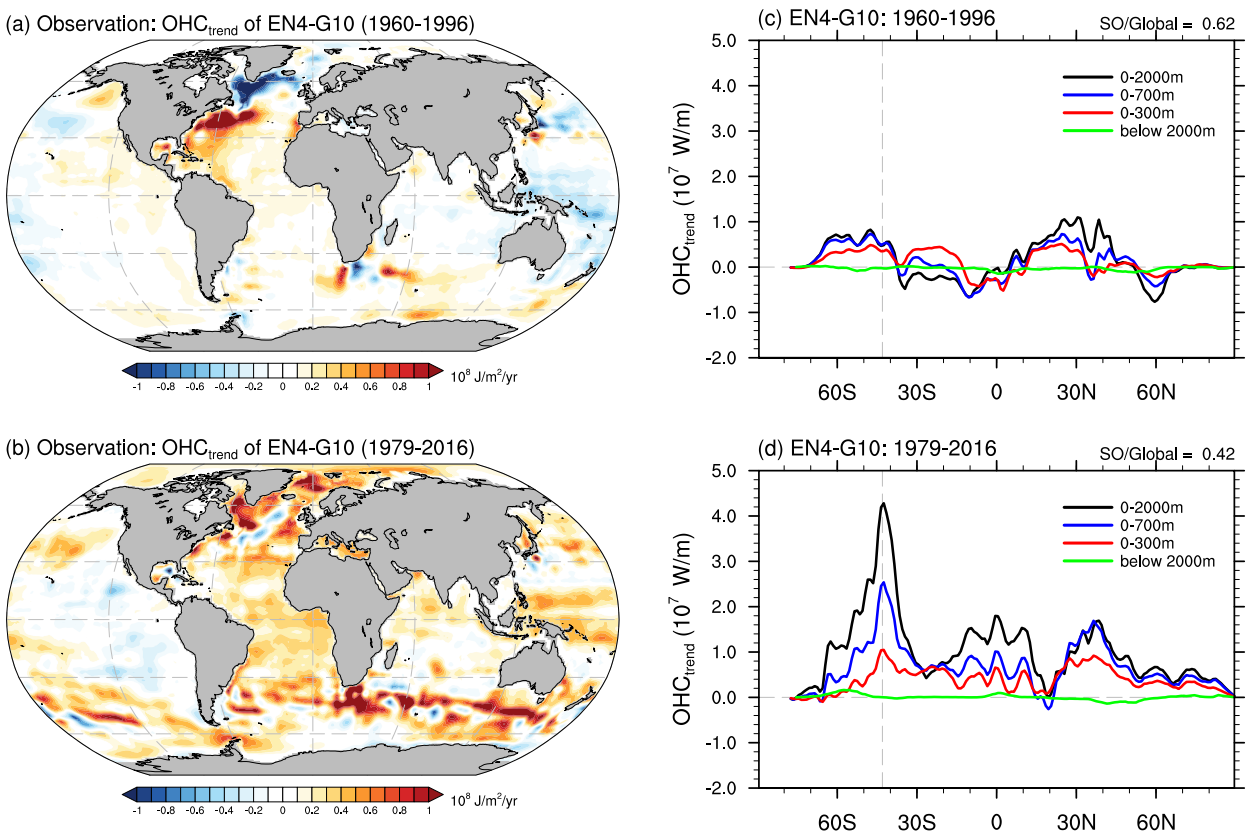

Figure A5: Trend of OHC above 2000m from EN4-G10 over (a) 1960-1996 and (b) 1979-2016. The zonally integrated OHC trend over (c) 1960-1996 and (d) 1979-2016. The number at the upper right corner denotes the fraction of SO to global OHC change. Compare with Figures 2.14 and 2.15.

Appendix B

Appendix for Chapter 3

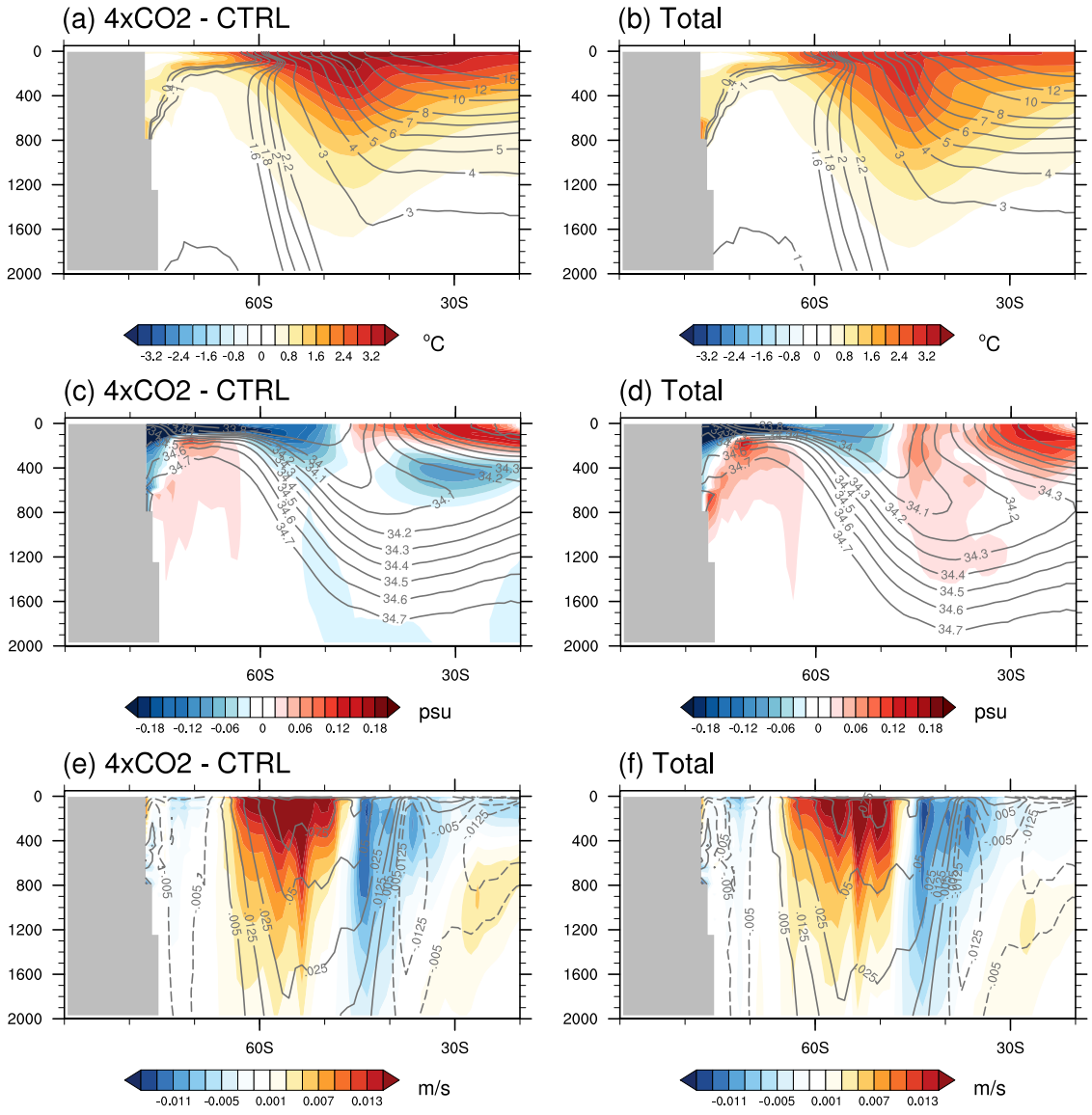

Figure B1: Zonal mean temperature change from (a) 4×CO_2 – CTRL and (b) Total. (c)-(d) as in (a)-(b), but for changes in salinity. (e)-(f) for changes in zonal velocity. Gray contours represent 50-year climatology for each field.

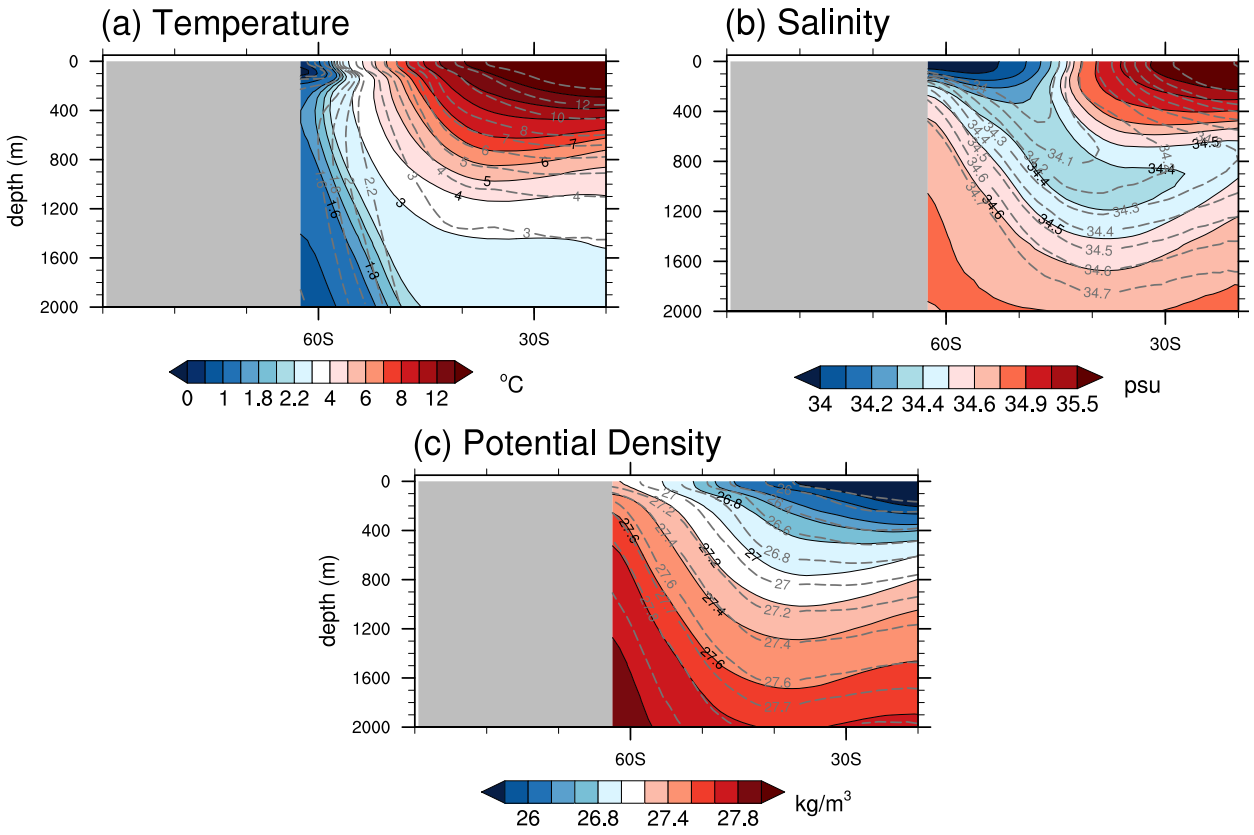

Figure B2: Zonal mean climatological (a) temperature, (b) salinity, and (c) potential density referenced to the sea surface from Argo (shading; 2005-2018 mean) and τ1w1c1 (dashed contours; fifty-year mean).

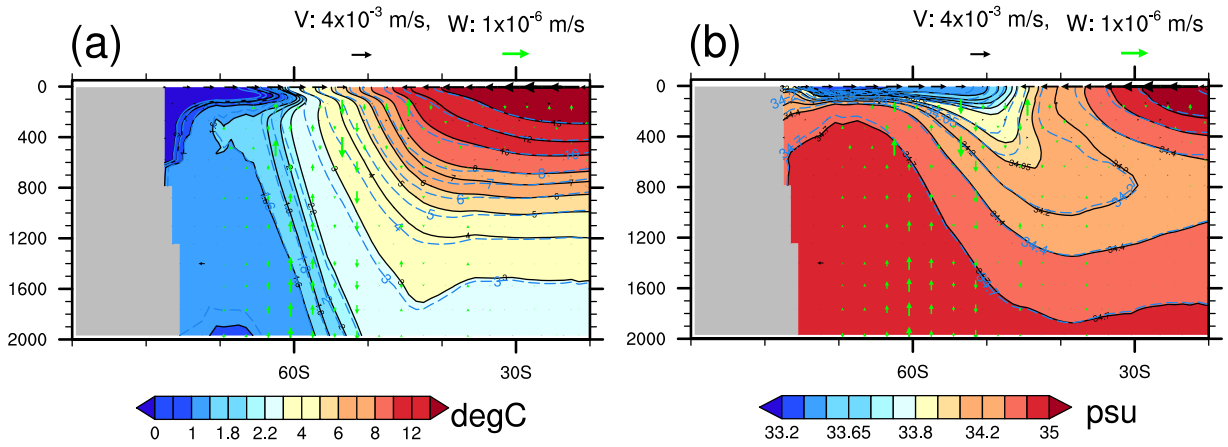

Figure B3: Climatology of zonal mean (shading) (a) temperature and (b) salinity from τ1w1c4. The dashed blue contours show the corresponding climatology from τ4w1c4. Vertical velocity and meridional velocity changes due to Wstr are shown as green and black vectors, respectively.

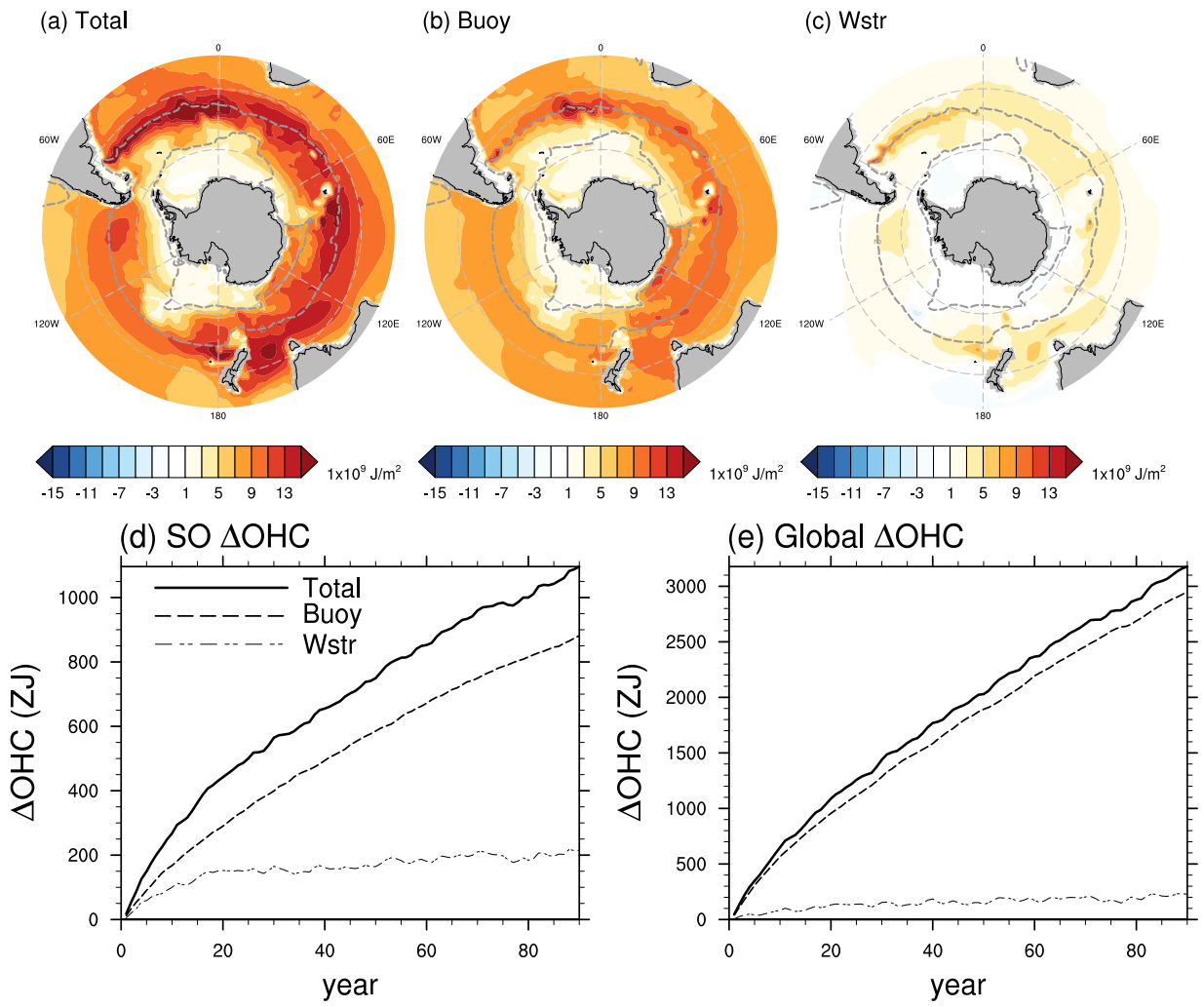

Figure B4: Ocean heat content change for the entire water column for (a) Total, (b) Buoy, and (c) Wstr. Time series of ΔOHC in the (d) Southern Ocean (south of 30˚S) and the (e) global ocean.

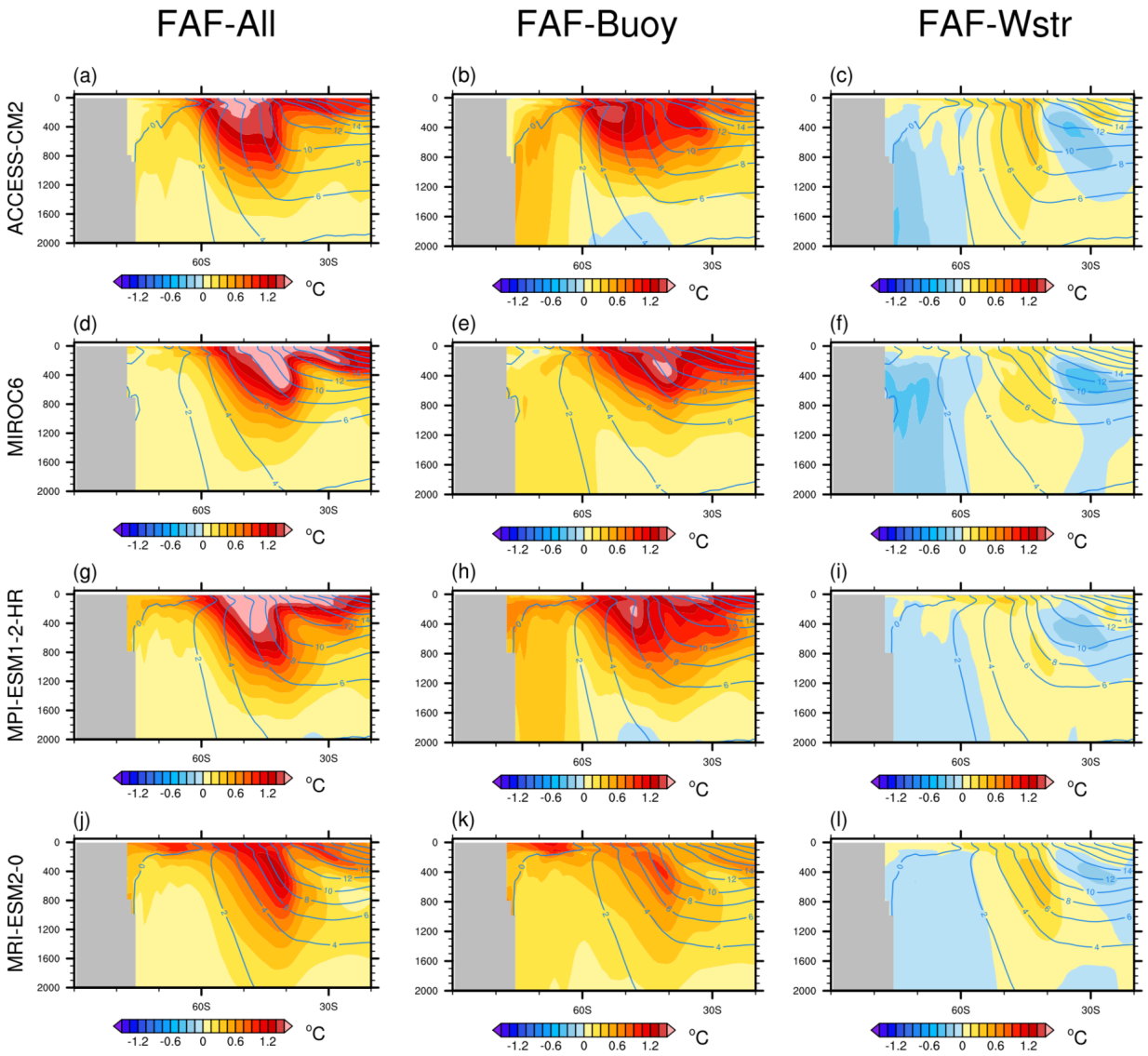

Figure B5: Zonal mean temperature change from each FAFMIP model and experiment. Blue contours indicate 20-year climatology from preindustrial control.

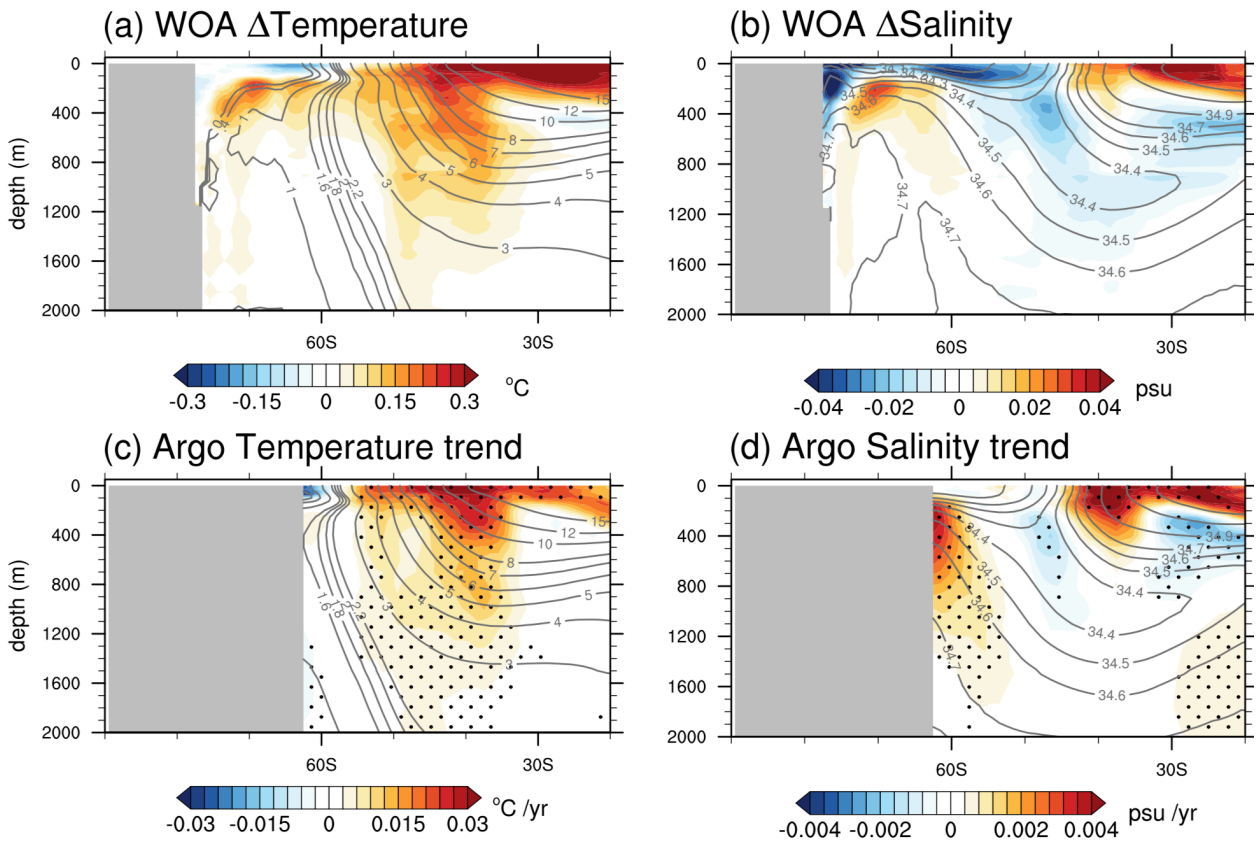

Figure B6: Zonal mean (a) temperature change and (b) salinity change from WOA. The anomalies represent the difference between the 2005-2017 mean and the mean over a 1955-1984 base period. Gray contours are climatology of 1955-1984. Zonal mean (c) temperature trend and (d) salinity trend from 2005 to 2018 from Argo. Stippling indicates regions exceeding 95% statistical significance computed from the two-tailed t test.

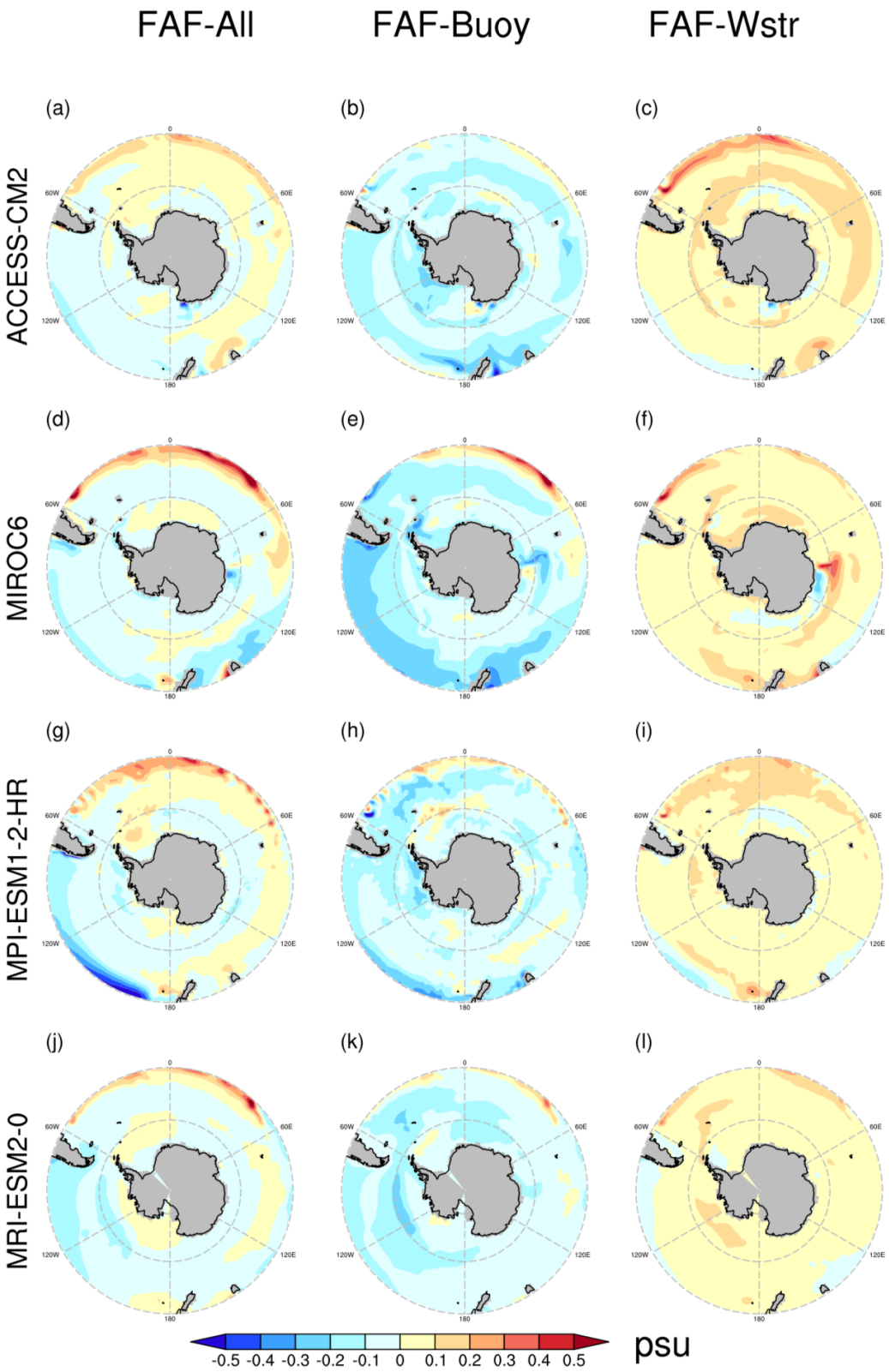

Figure B7: Change of salinity in the surface layer (0-50 m) from each FAFMIP model and experiment.

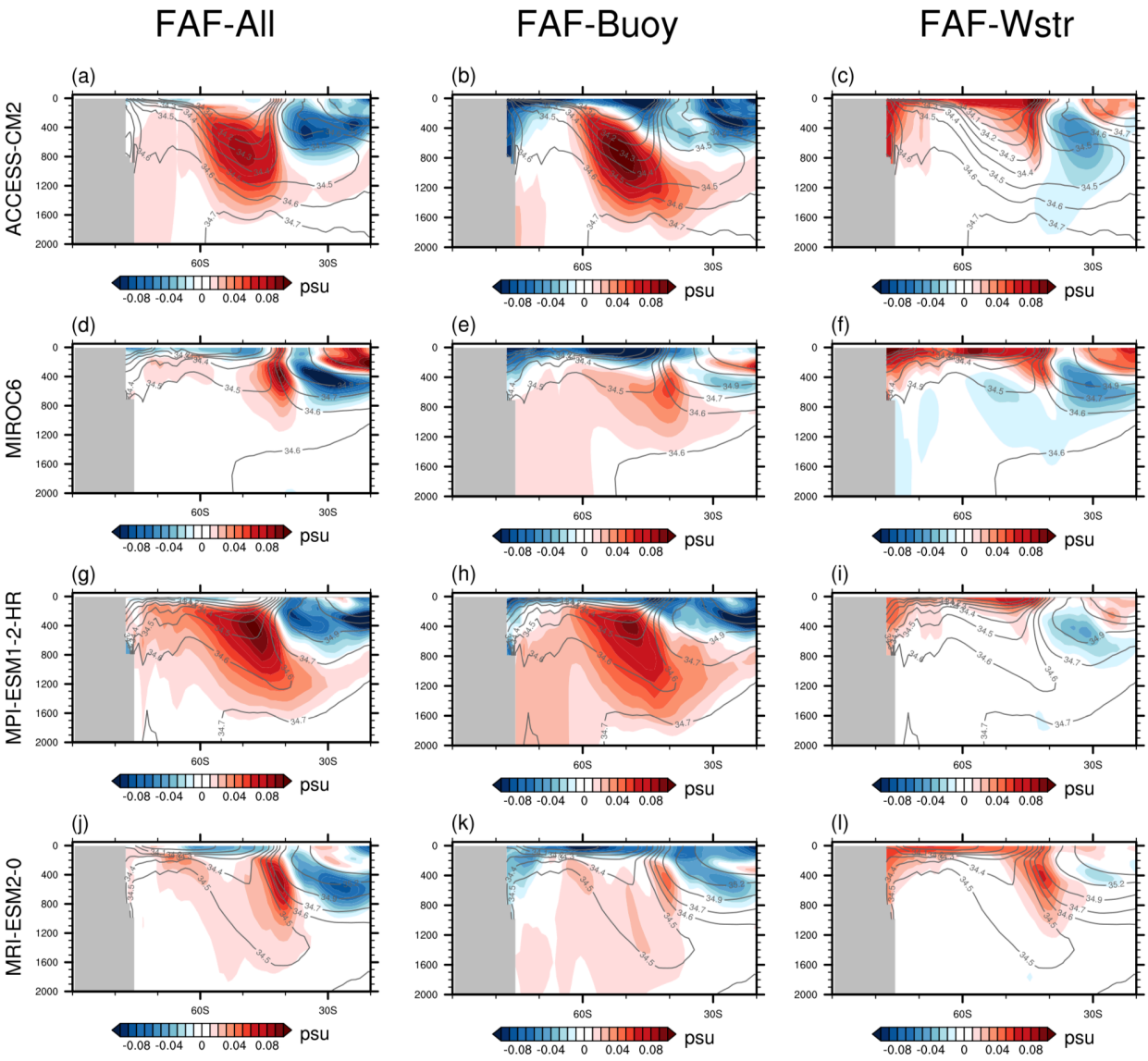

Figure B8: Zonal mean salinity change from each FAFMIP model and experiment. Gray contours indicate 20-year climatology from preindustrial control.

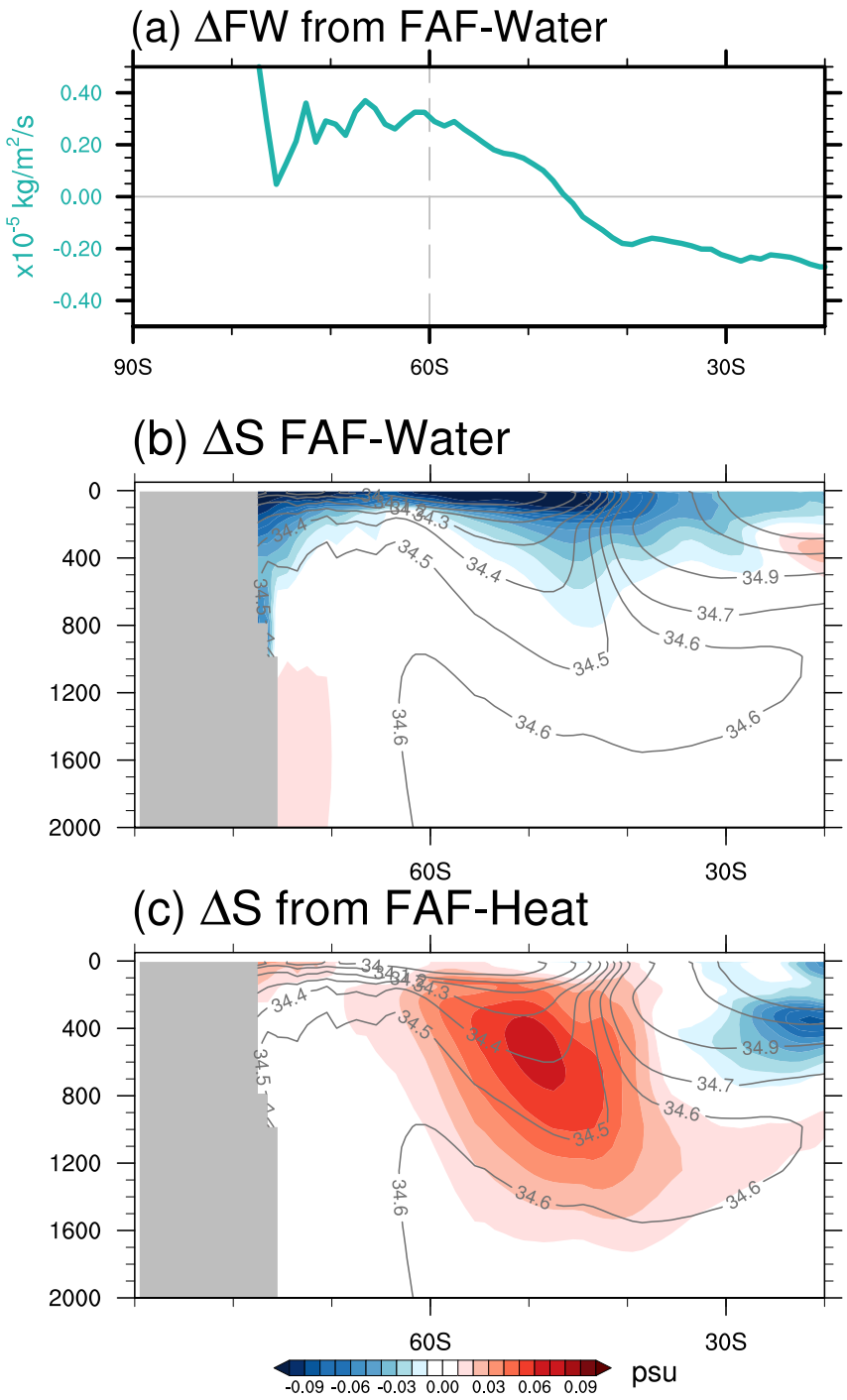

Figure B9: (a) Zonal mean freshwater flux change from FAF-Water and salinity change in the upper 2000 m from (b) FAF-Heat and (c) FAF-Water. Contours are 20-year climatology from preindustrial control run.

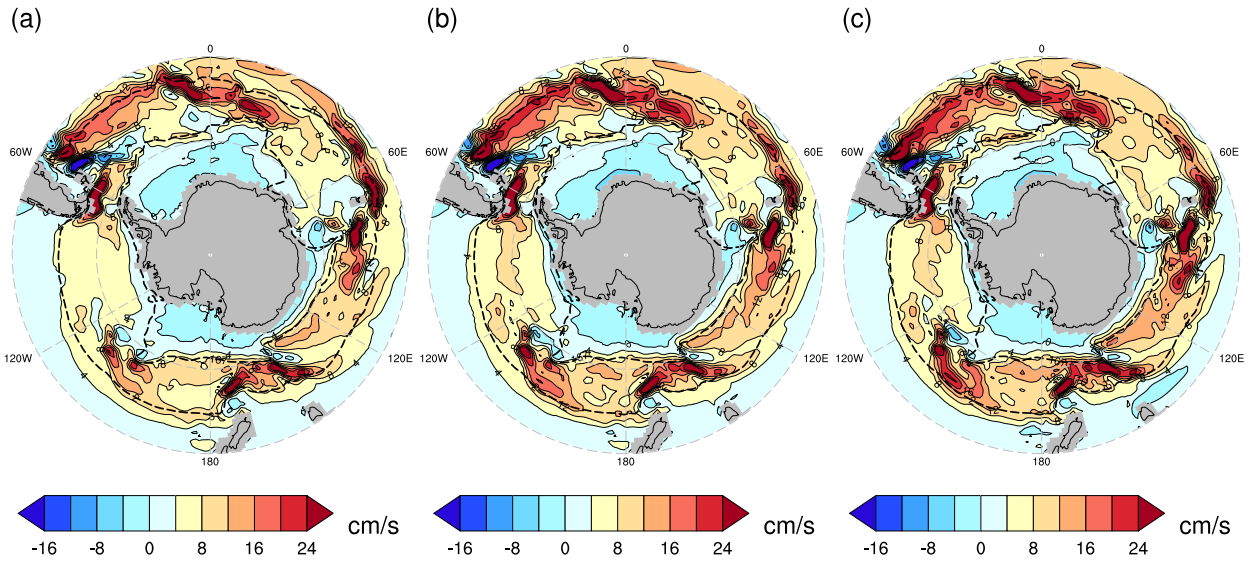

Figure B10: Mean zonal geostrophic velocity (U_g) from (a) τ1w1c1, (b) τ1w1c4, and (c) τ4w1c4.

Appendix C

Appendix for Chapter 4

Table C1: CMIP6 models for the output of ocean potential temperature, zonal velocity, and atmospheric surface pressure in historical simulations.

Model Names	Potential Temp. & U	Surface Pressure
BBC-CSM2-MR	√	√
BCC-ESM1	√	√
CAMS-CSM1-0	√	√
CanESM5	√	√
CAS-ESM2-0	√	√
CESM2	√	√
CESM2-FV2	√	√
CESM2-WACCM	√	√
CESM2-WACCM-FV2	√	√
CMCC-CM2-HR4	√	√
CMCC-CM2-SR5	√	√
EC-Earth3	√	–
EC-Earth3-Veg	√	–
FGOALS-g3	√	√
FIO-ESM-2-0	√	√
GFDL-CM4	√	–
GISS-E2-1-G	√	√
IPSL-CM6A-LR	√	–
MCM-UA-1-0	√	√
MIROC6	√	√
MPI-ESM1-1-2-HAM	√	√
MPI-ESM1-2-LR	√	√
MRI-ESM2-0	√	√
NESM3	√	√
SAM0-UNICON	√	√
TaiESM1	√	√

Table C2: List of CMIP6 models used in OGCM for surface forcing, including SST, SSS and surface wind.

Model Names
ACCESS-CM2
ACCESS-ESM1-5
BCC-CSM2-MR
BCC-ESM1
CAMS-CSM1-0
CanESM5
CAS-ESM2-0
CESM2
CESM2-FV2
CESM2-WACCM
CESM2-WACCM-FV2
CIESM
CNRM-CM6-1
CNRM-ESM2-1
E3SM-1-0
EC-Earth3-Veg
FGOALS-f3-L
GFDL-ESM4
GISS-E2-1-G
HadGEM3-GC31-LL
INM-CM4-8
IPSL-CM6A-LR
MCM-UA-1-0
MIROC6
MIROC-ES2L
MPI-ESM1-2-HR
MRI-ESM2-0
NESM3
SAM0-UNICON
UKESM1-0-LL

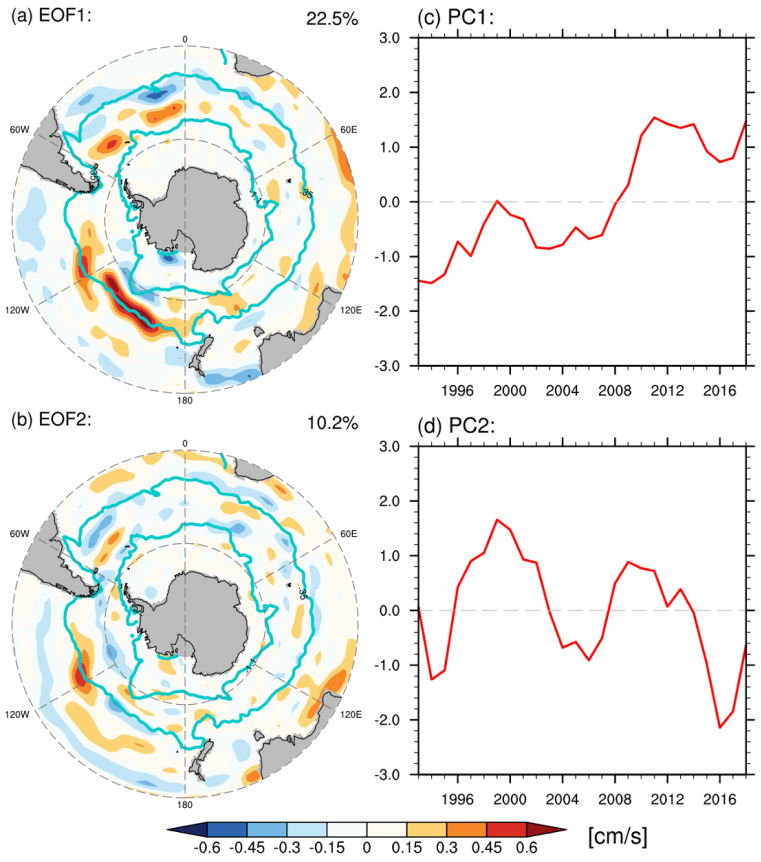

Figure C1: The first two EOF modes of surface U_g from 1993 to 2018 from AVISO data. Shown are (a), (b) EOF patterns and (c), (d) normalized PCs. The cyan contours show the ACC envelope (northernmost and southernmost contours in Drake Passage), based on sea surface height from AVISO.

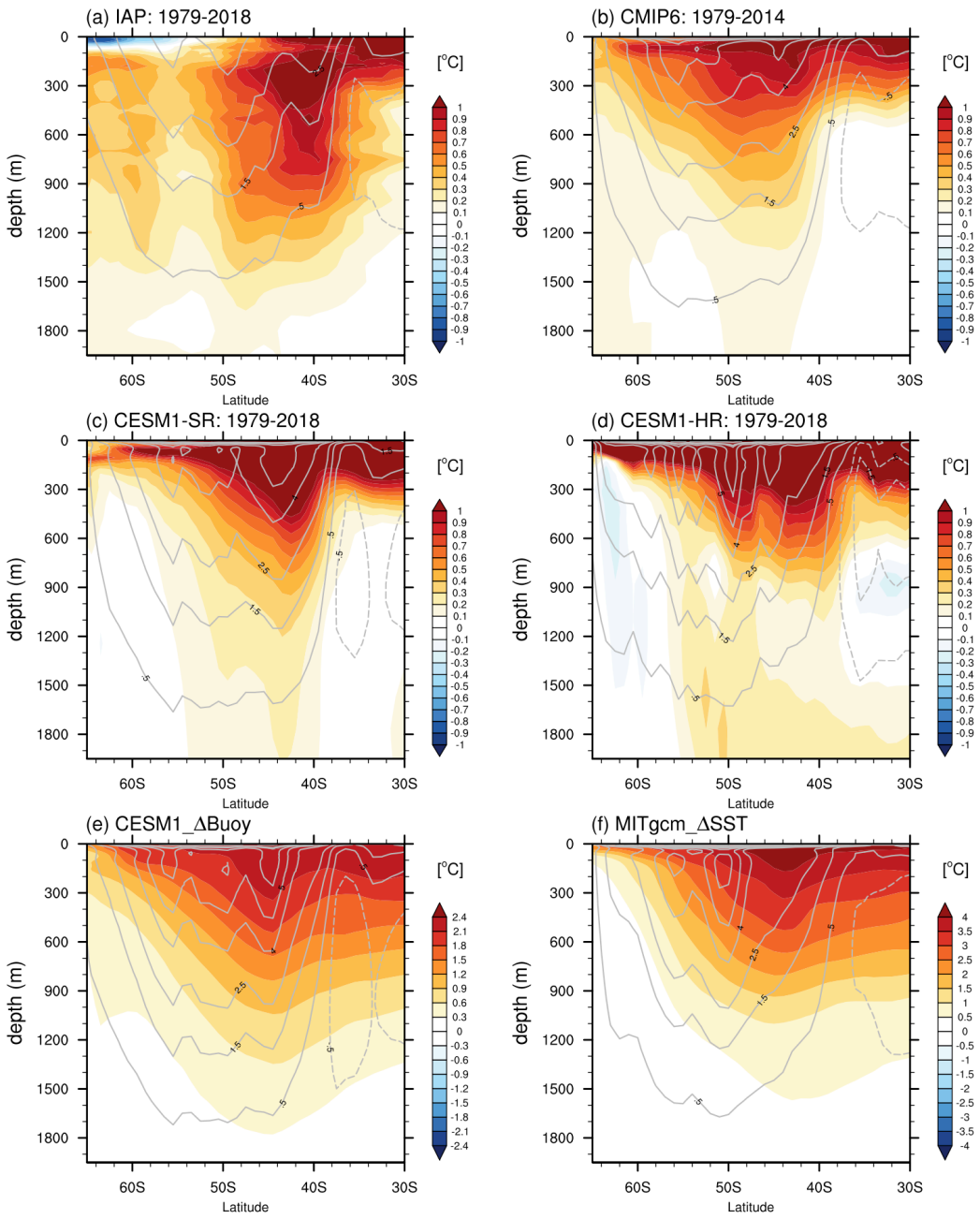

Figure C2: Zonal mean potential temperature trend from (a) IAP (observations), (b) CMIP6 MMM, (c) CESM1-SR, and (d) CESM1-HR. The trend from CMIP6 MMM is from 1979 to 2014, and the rest are from 1979 to 2018. (e) Zonal mean potential temperature change from the CESM1_ΔBuoy experiment relative to the control run. (f) Zonal mean potential temperature change from the MITgcm_ΔSST experiment relative to the control run. Gray contours are the climatological U_g or U (in cm/s) from the corresponding cases.

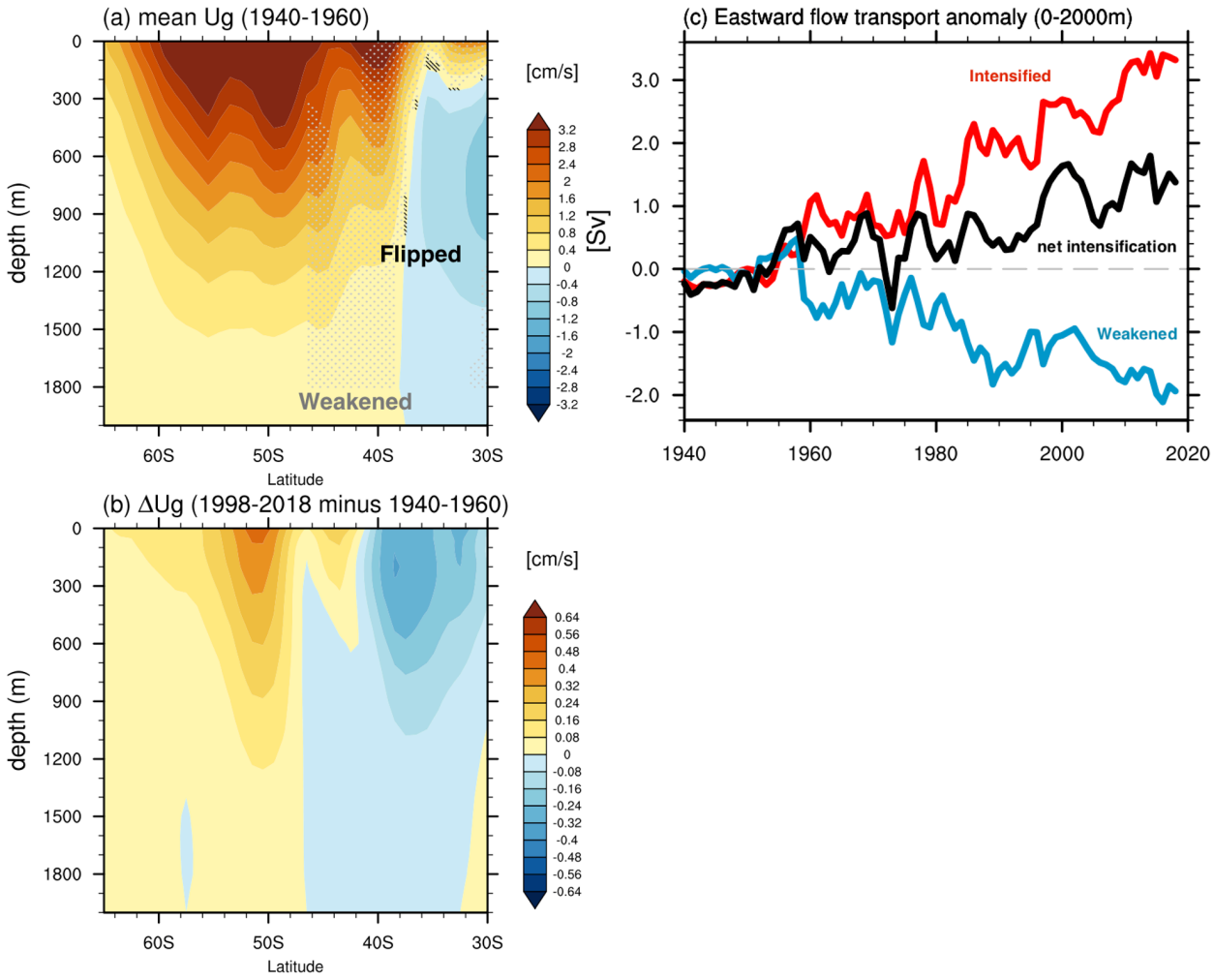

Figure C3: (a) Zonal mean of climatological U_g averaged from 1940 to 1960, from IAP data. (b) The difference ΔU_g between the 1998-2018 and 1940-1960 averages, both from IAP data. Gray dots in (a) indicate the regions where eastward flows are weakened, and black slashes indicate the signs of zonal flow are flipped. Velocity in the regions without stippling is intensified. (c) Eastward flow baroclinic transport in the upper 2000 m from 1940 to 2018 from IAP data. Blue curve shows the weakened eastward transport (weakened regions); red curve shows the intensified eastward transport; black curve is the sum of two curves, showing the net intensification of the eastward flow.

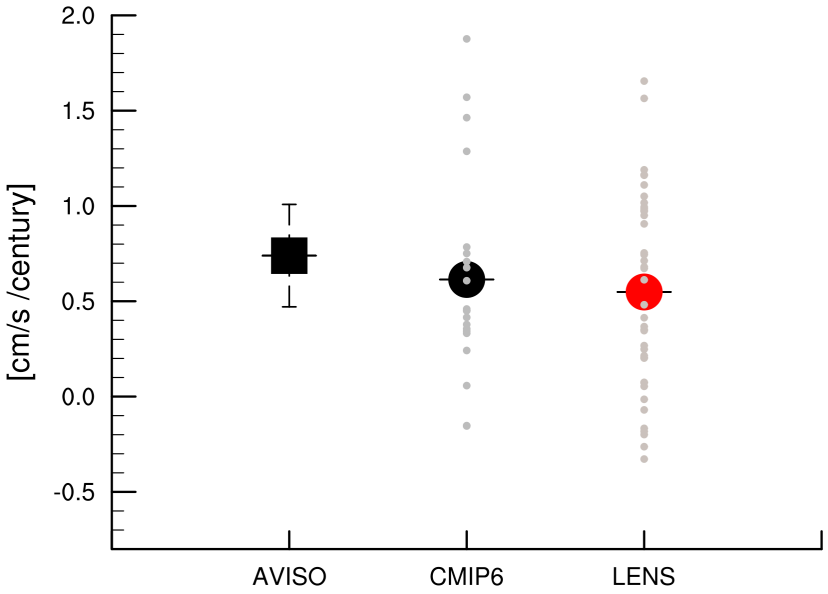

Figure C4: Trend of surface zonal velocity from AVISO (square) and model simulations (circles) for 1993-2018. For CMIP6 historical runs, the trend is for 1993-2014. The error bar represents the 95% confidence interval for the linear trend. Small dots are results from individual runs from CMIP6 and LENS.

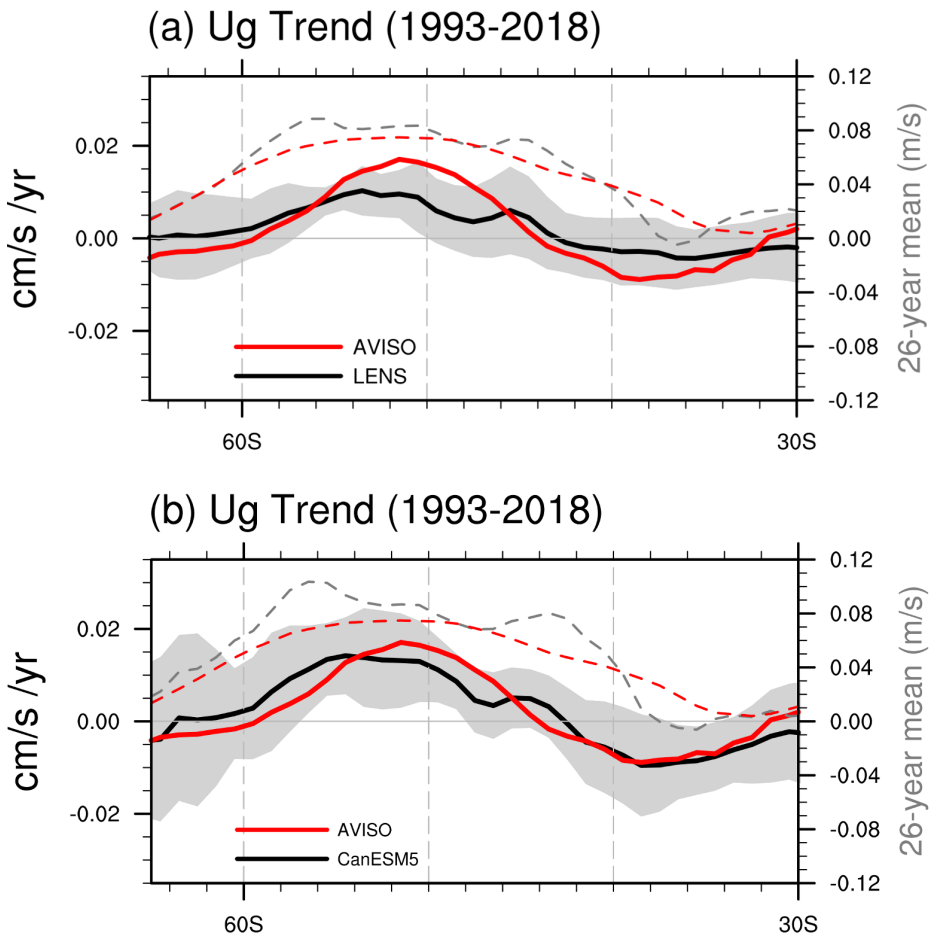

Figure C5: (a) Trend of zonal mean surface U_g (cm/s /yr) from AVISO and LENS for 1993-2018. The black curve is the LENS ensemble mean and shading is ± 1 standard deviation from all of the ensemble members. Dashed curves are climatologies of zonal mean U_g (m/s) from AVISO and LENS. (b) Same as (a) but for the comparison between AVISO and CanESM5 large ensemble simulation.

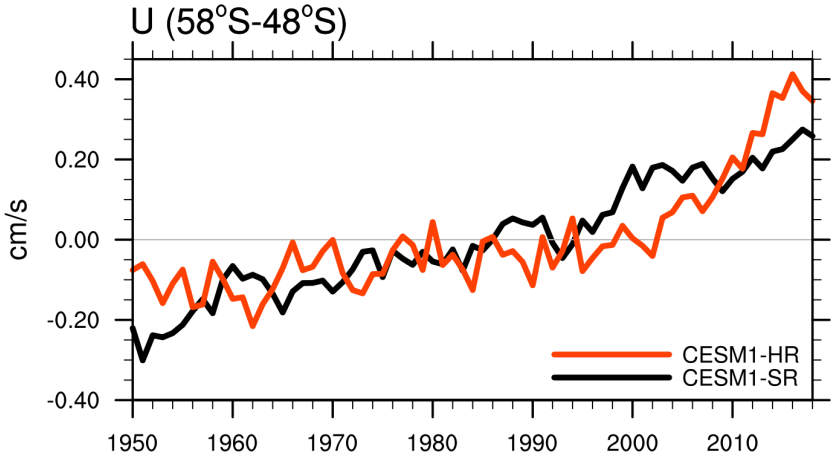

Figure C6: Time evolution of upper 100 m zonal velocity averaged between 58˚S and 48˚S from CESM1-SR (black curve) and CESM1-HR (red curve).

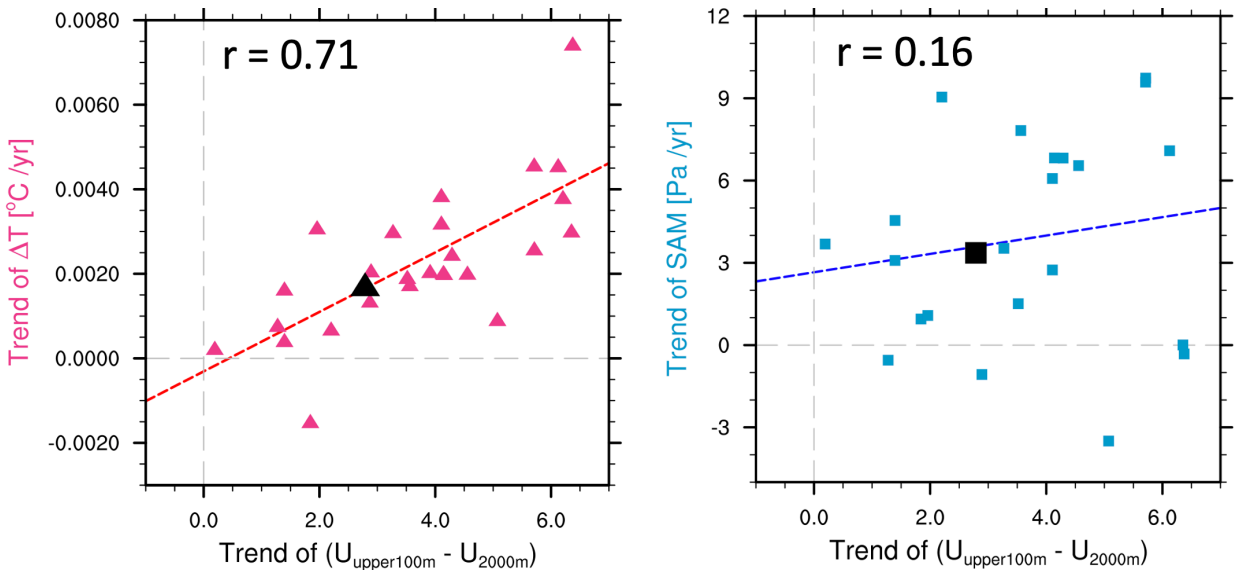

Figure C7: (a) Scatter plot of trend (1979-2014) of upper 100 m zonal velocity relative to 2000 m depth versus trend of temperature difference between 45˚S and 60˚S, along with the linear relationship for the CMIP6 models. Each red triangle indicates the result of each CMIP6 model. The correlation coefficient is 0.71 across models. The black triangle represents the trend from the IAP product. (b) Scatter plot of velocity trend versus SAM. Each blue square indicates the result from each CMIP6 model. The correlation coefficient is 0.16 across models. The black square represents the SAM trend from ERA5 (observations).

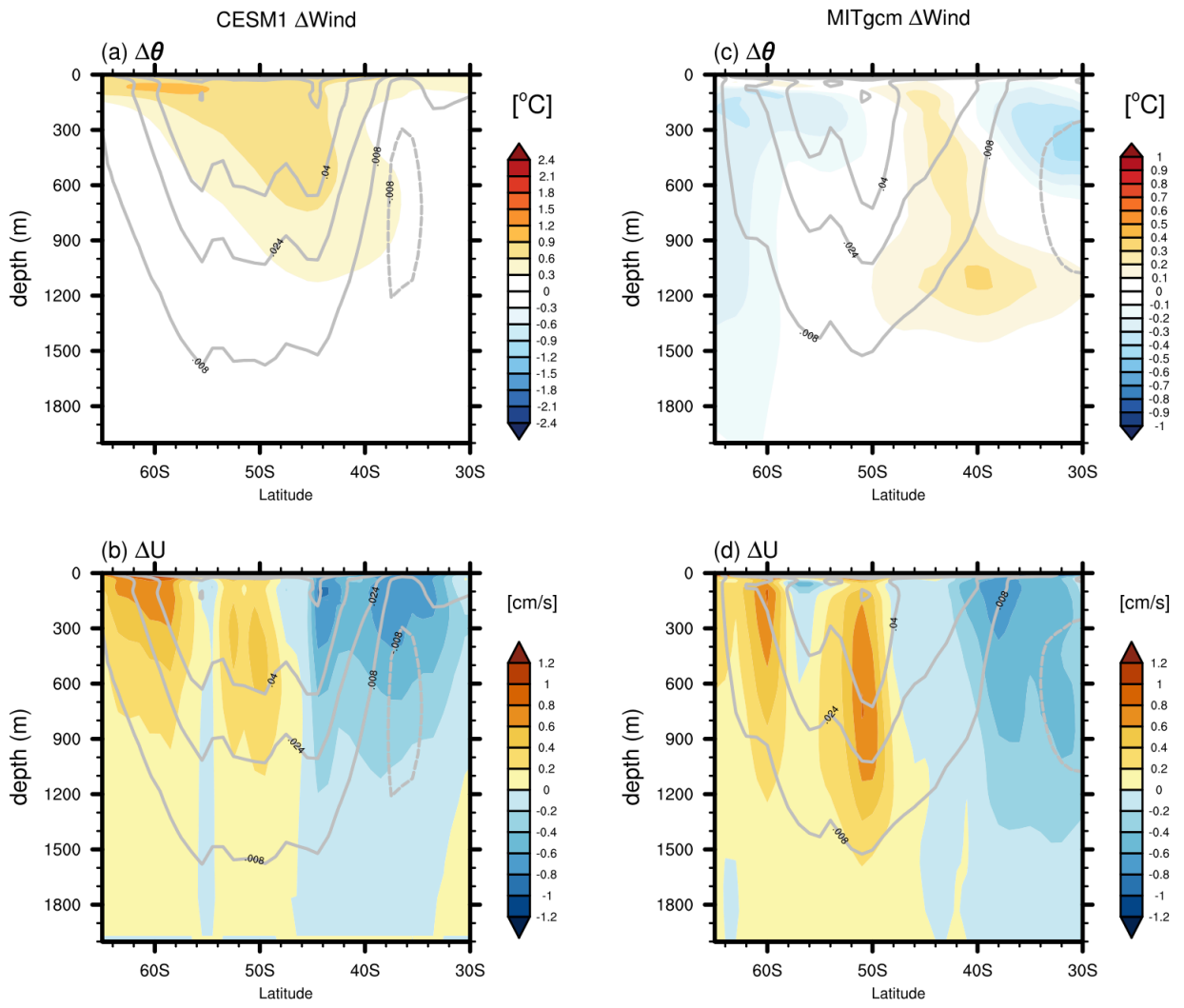

Figure C8: (a, c) Zonal mean potential temperature change and (b, d) U change induced by surface stress change (ΔWind) from CESM1_ΔWind (a, b) relative to CESM1_ΔBuoy and MITgcm_ΔWind (c, d) relative to MITgcm_CTL (Methods). Gray contours are the climatological zonal velocity U (in m/s) from the corresponding cases.

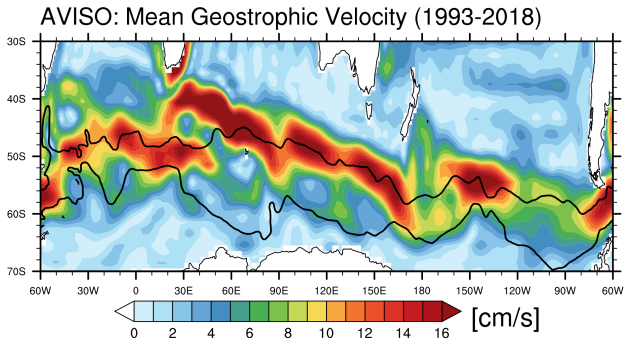

Figure C9: Surface mean geostrophic velocity from AVISO (1993-2018).

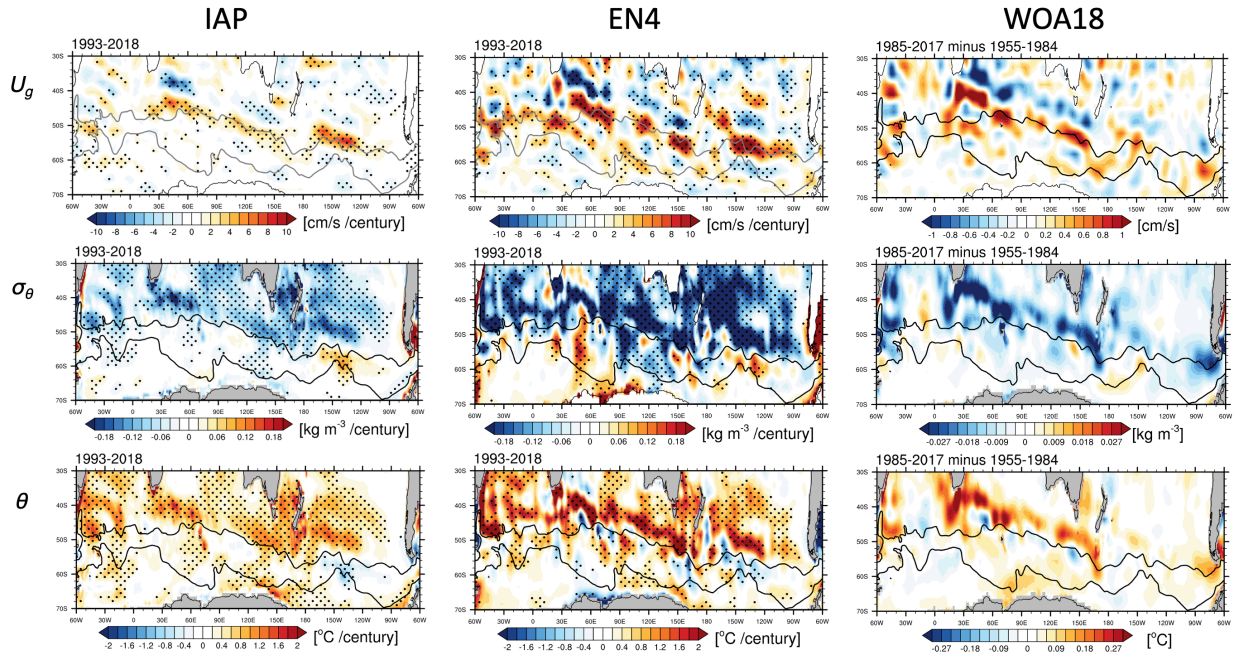

Figure C10: Upper 100 m zonal geostrophic velocity, U_g, trend (1993-2018) from the IAP, EN4 and change from WOA18 (1985-2017 mean minus 1955-1984 mean) (top row). Corresponding trend/change of upper 2000 m averaged potential density and potential temperature are shown in middle row and bottom row, respectively. Gray contours indicate Subantarctic Front and Southern ACC Front from Orsi et al. (1995). Stippling indicates regions exceeding 95% statistical significance computed from the two-tailed *t*-test.

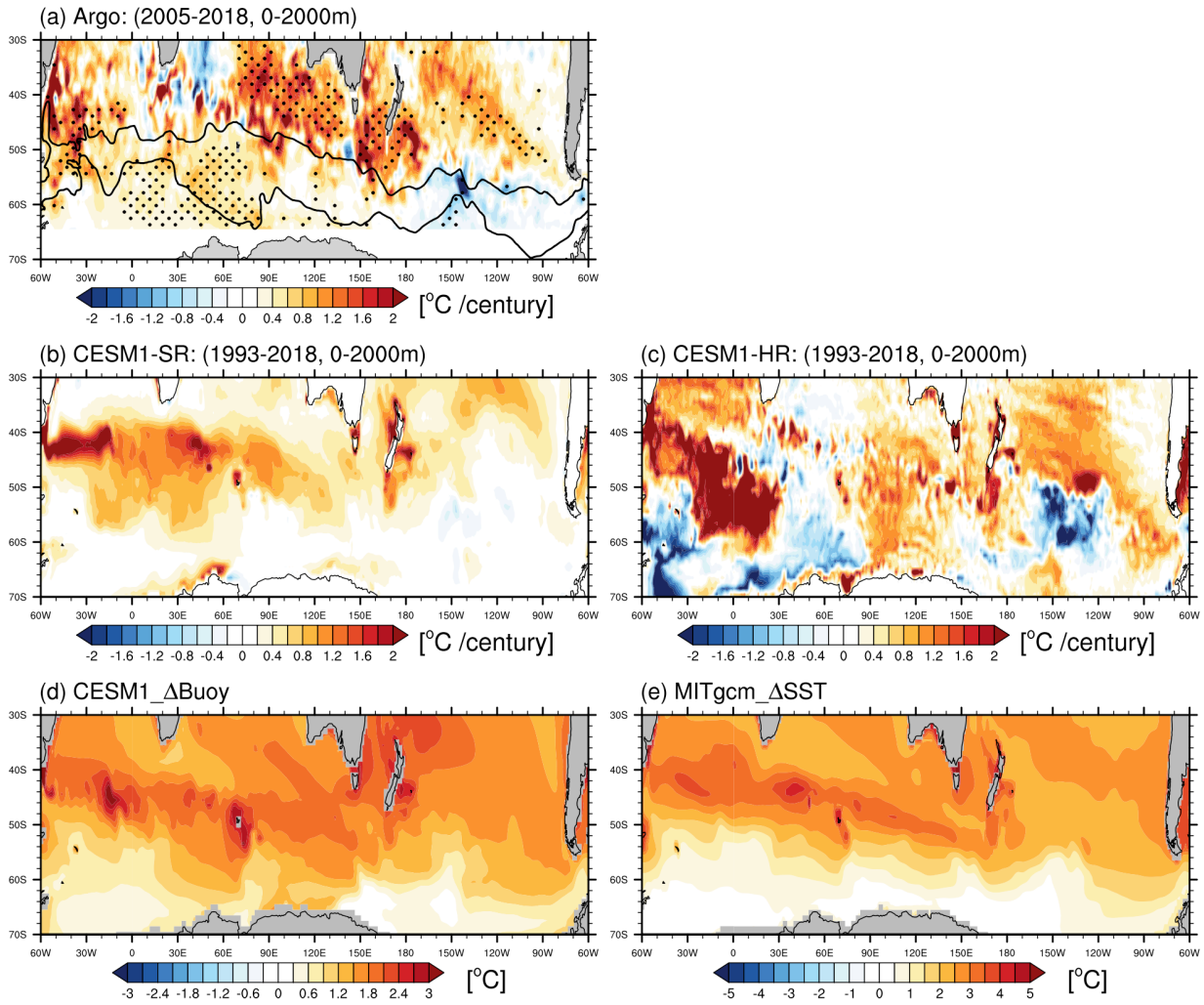

Figure C11: (a) Upper 2000 m potential temperature trend from Argo observations (2005-2018). Black contours indicate the Subtropical Front (STF), Subantarctic Front (SAF), and Southern ACC Front (SACCF) from Orsi et al. (1995). (b, c) Upper 2000 m potential temperature trend from CESM1-SR (b) and CESM1-HR (c). (d, e) Upper 2000 m potential temperature change from the CESM1_ΔBuoy experiment (d) and the MITgcm_ΔSST experiment (e) relative to the corresponding control runs. Stippling indicates regions exceeding 95% statistical significance computed from the two-tailed *t* test.

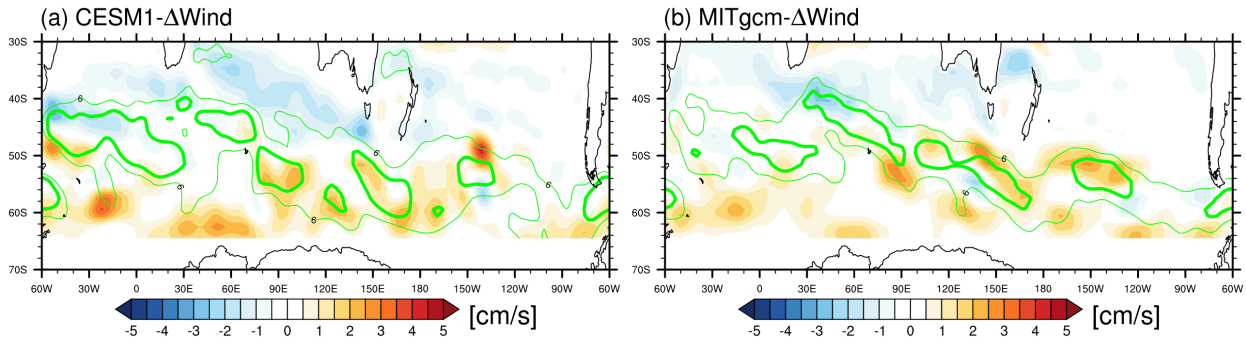

Figure C12: Upper 100 m zonal velocity change driven by wind stress change from (a) CESM1 and (b) MITgcm. Mean zonal velocities of 6 cm/s and 12 cm/s are shown as thin and thick green contours.

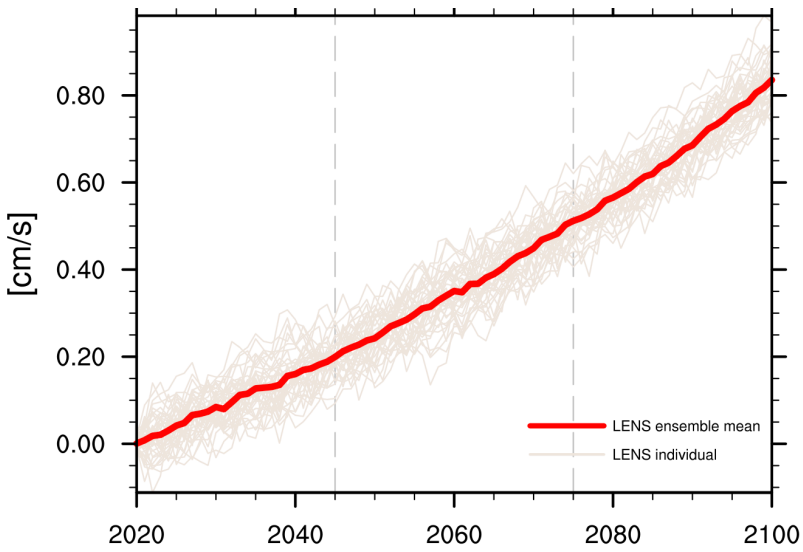

Figure C13: Time series of upper 100 m zonal velocity relative to the velocity at 2000 m depth from LENS from 2020 to 2100. LENS ensemble mean is the red curve.

Chapter 7

Reference

Abernathey, R. P., I. Cerovecki, P. R. Holland, E. Newsom, M. Mazloff, and L. D. Talley, 2016: Water-mass transformation by sea ice in the upper branch of the Southern Ocean overturning. *Nat. Geosci.*, **9**, 596–601, https://doi.org/10.1038/ngeo2749.

Acosta Navarro, J. C., A. M. L. Ekman, F. S. R. Pausata, A. Lewinschal, V. Varma, Ø. Seland, M. Gauss, T. Iversen, A. Kirkevåg, I. Riipinen, and H. C. Hansson, 2017: Future Response of Temperature and Precipitation to Reduced Aerosol Emissions as Compared with Increased Greenhouse Gas Concentrations. *J. Clim.*, **30**, 939–954, https://doi.org/10.1175/JCLI-D-16-0466.1.

Armour, K. C., J. Marshall, J. R. Scott, A. Donohoe, and E. R. Newsom, 2016: Southern Ocean warming delayed by circumpolar upwelling and equatorward transport. *Nat. Geosci.*, **9**, 549–554, https://doi.org/10.1038/ngeo2731.

Beadling, R. L., J. L. Russell, R. J. Stouffer, P. J. Goodman, and M. Mazloff, 2019: Assessing the Quality of Southern Ocean Circulation in CMIP5 AOGCM and Earth System Model Simulations. *J. Clim.*, **32**, 5915–5940, https://doi.org/10.1175/JCLI-D-19-0263.1.

Belkin, I. M., and A. L. Gordon, 1996: Southern Ocean fronts from the Greenwich meridian to Tasmania. *J. Geophys. Res. C Ocean.*, **101**, 3675–3696, https://doi.org/10.1029/95JC02750.

Bindoff, N. L., K. Mirle, M. R. A. Uk, N. G. Canada, D. Gutzler, S. M. Republic, D. M. Uk, T. M. Germany, D. P. Uk, and A. R. France, 2013: Detection and Attribution of Climate Change: from Global to Regional. *Climate Change 2013 - The Physical Science Basis*, Intergovernmental Panel on Climate Change, Ed., Vol. 9781107057 of, Cambridge University Press, 867–952.

Bintanja, R., G. J. Van Oldenborgh, S. S. Drijfhout, B. Wouters, and C. A. Katsman, 2013: Important role for ocean warming and increased ice-shelf melt in Antarctic sea-ice expansion. *Nat. Geosci.*, **6**, 376–379, https://doi.org/10.1038/ngeo1767.

Bishop, S. P., P. R. Gent, F. O. Bryan, A. F. Thompson, M. C. Long, and R. Abernathey, 2016: Southern Ocean Overturning Compensation in an Eddy-Resolving Climate Simulation. *J. Phys. Oceanogr.*, **46**, 1575–1592, https://doi.org/10.1175/JPO-D-15-0177.1.

Bitz, C. M., and L. M. Polvani, 2012: Antarctic climate response to stratospheric ozone depletion in a fine resolution ocean climate model. *Geophys. Res. Lett.*, **39**, 1–5, https://doi.org/10.1029/2012GL053393.

Böning, C. W., M. Scheinert, J. Dengg, A. Biastoch, and A. Funk, 2006: Decadal variability of subpolar gyre transport and its reverberation in the North Atlantic overturning. *Geophys. Res. Lett.*, **33**, 1–5, https://doi.org/10.1029/2006GL026906.

——, A. Dispert, M. Visbeck, S. R. Rintoul, and F. U. Schwarzkopf, 2008: The response of the Antarctic Circumpolar Current to recent climate change. *Nat. Geosci.*, **1**, 864–869, https://doi.org/10.1038/ngeo362.

Boucher, O. . O., G. Claire, C. Hoose, and A. Jones, 2013: Clouds and Aerosols. *Climate Change 2013 - The Physical Science Basis*, Intergovernmental Panel on Climate Change, Ed., Vol. 9781107057 of, Cambridge University Press, 571–658.

Bouttes, N., and J. M. Gregory, 2014: Attribution of the spatial pattern of CO_2 -forced sea level change to ocean surface flux changes. *Environ. Res. Lett.*, **9**, 034004, https://doi.org/10.1088/1748-9326/9/3/034004.

Bracegirdle, T. J., P. Hyder, and C. R. Holmes, 2018: CMIP5 diversity in Southern Westerly jet projections related to historical sea ice area: Strong link to strengthening and weak link to shift. *J. Clim.*, **31**, 195–211, https://doi.org/10.1175/JCLI-D-17-0320.1.

Bronselaer, B., M. Winton, S. M. Griffies, W. J. Hurlin, K. B. Rodgers, O. V. Sergienko, R. J. Stouffer, and J. L. Russell, 2018: Change in future climate due to Antarctic meltwater. *Nature*, **564**, 53–58, https://doi.org/10.1038/s41586-018-0712-z.

——, J. L. Russell, M. Winton, N. L. Williams, R. M. Key, J. P. Dunne, R. A. Feely, K. S. Johnson, and J. L. Sarmiento, 2020: Importance of wind and meltwater for observed chemical and physical changes in the Southern Ocean. *Nat. Geosci.*, **13**, 35–42, https://doi.org/10.1038/s41561-019-0502-8.

Bryan, K., S. Manabe, and M. J. Spelman, 1988: Interhemispheric Asymmetry in the Transient Response of a Coupled Ocean–Atmosphere Model to a CO 2 Forcing. *J. Phys. Oceanogr.*, **18**, 851–867, https://doi.org/10.1175/1520-0485(1988)018<0851:IAITTR>2.0.CO;2.

Buckley, M. W., and J. Marshall, 2016: Observations, inferences, and mechanisms of the Atlantic Meridional Overturning Circulation: A review. *Rev. Geophys.*, **54**, 5–63, https://doi.org/10.1002/2015RG000493.

Cai, W., 2006: Antarctic ozone depletion causes an intensification of the Southern Ocean super-gyre circulation. *Geophys. Res. Lett.*, **33**, 1–4, https://doi.org/10.1029/2005GL024911.

Cheng, L., and J. Zhu, 2016: Benefits of CMIP5 Multimodel Ensemble in Reconstructing Historical Ocean Subsurface Temperature Variations. *J. Clim.*, **29**, 5393–5416, https://doi.org/10.1175/JCLI-D-15-0730.1.

——, K. E. Trenberth, M. D. Palmer, J. Zhu, and J. P. Abraham, 2016: Observed and simulated full-depth ocean heat-content changes for 1970-2005. *Ocean Sci.*, **12**, 925–935, https://doi.org/10.5194/os-12-925-2016.

——, ——, J. Fasullo, T. Boyer, J. Abraham, and J. Zhu, 2017: Improved estimates of ocean heat content from 1960 to 2015. *Sci. Adv.*, **3**, e1601545, https://doi.org/10.1126/sciadv.1601545.

——, G. Wang, J. Abraham, and G. Huang, 2018: Decadal Ocean Heat Redistribution Since the Late 1990s and Its Association with Key Climate Modes. *Climate*, **6**, 91, https://doi.org/10.3390/cli6040091.

Cheng, W., J. C. H. Chiang, and D. Zhang, 2013: Atlantic meridional overturning circulation (AMOC) in CMIP5 Models: RCP and historical simulations. *J. Clim.*, **26**, 7187–7197, https://doi.org/10.1175/JCLI-D-12-00496.1.

Cionni, I., V. Eyring, J. F. Lamarque, W. J. Randel, D. S. Stevenson, F. Wu, G. E. Bodeker, T. G. Shepherd, D. T. Shindell, and D. W. Waugh, 2011: Ozone database in support of CMIP5 simulations: Results and corresponding radiative forcing. *Atmos. Chem. Phys.*, **11**, 11267–11292, https://doi.org/10.5194/acp-11-11267-2011.

Cunningham, S. A., T. Kanzow, D. Rayner, M. O. Baringer, W. E. Johns, J. Marotzke, H. R. Longworth, E. M. Grant, J. J.-M. Hirschi, L. M. Beal, C. S. Meinen, and H. L. Bryden, 2007: Temporal Variability of the Atlantic Meridional Overturning Circulation at 26.5 N. *Science (80-.).*, **317**, 935–938, https://doi.org/10.1126/science.1141304.

Delworth, T. L., and K. W. Dixon, 2006: Have anthropogenic aerosols delayed a greenhouse gas-induced weakening of the North Atlantic thermohaline circulation? *Geophys. Res. Lett.*, **33**, 3–6, https://doi.org/10.1029/2005GL024980.

——, F. Zeng, L. Zhang, R. Zhang, G. A. Vecchia, and X. Yang, 2017: The central role of ocean dynamics in connecting the North Atlantic oscillation to the extratropical component of the Atlantic multidecadal oscillation. *J. Clim.*, **30**, 3789–3805, https://doi.org/10.1175/JCLI-D-16-0358.1.

Desbruyères, D. G., S. G. Purkey, E. L. McDonagh, G. C. Johnson, and B. A. King, 2016: Deep and abyssal ocean warming from 35 years of repeat hydrography. *Geophys. Res. Lett.*, **43**, 10,356-10,365, https://doi.org/10.1002/2016GL070413.

Deser, C., A. Phillips, V. Bourdette, and H. Teng, 2012: Uncertainty in climate change projections: The role of internal variability. *Clim. Dyn.*, **38**, 527–546, https://doi.org/10.1007/s00382-010-0977-x.

——, A. S. Phillips, I. R. Simpson, N. Rosenbloom, D. Coleman, F. Lehner, A. G. Pendergrass, P. DiNezio, and S. Stevenson, 2020: Isolating the Evolving Contributions of Anthropogenic Aerosols and Greenhouse Gases: A New CESM1 Large Ensemble Community Resource. *J. Clim.*, **33**, 7835–7858, https://doi.org/10.1175/JCLI-D-20-0123.1.

Ding, Y., J. A. Carton, G. A. Chepurin, G. Stenchikov, A. Robock, L. T. Sentman, and J. P. Krasting, 2014: Ocean response to volcanic eruptions in Coupled Model Intercomparison Project 5 simulations. *J. Geophys. Res. Ocean.*, **119**, 5622–5637, https://doi.org/10.1002/2013JC009780.

Dong, S., J. Sprintall, and S. T. Gille, 2006: Location of the Antarctic Polar Front from AMSR-E Satellite Sea Surface Temperature Measurements. *J. Phys. Oceanogr.*, **36**, 2075–2089, https://doi.org/10.1175/JPO2973.1.

Donohue, K. A., K. L. Tracey, D. R. Watts, M. P. Chidichimo, and T. K. Chereskin, 2016: Mean Antarctic Circumpolar Current transport measured in Drake Passage. *Geophys. Res. Lett.*, **43**, 11,760-11,767, https://doi.org/10.1002/2016GL070319.

Downes, S. M., A. S. Budnick, J. L. Sarmiento, and R. Farneti, 2011: Impacts of wind stress on the Antarctic Circumpolar Current fronts and associated subduction. *Geophys. Res. Lett.*, **38**, 3–8, https://doi.org/10.1029/2011GL047668.

Drijfhout, S., G. J. van Oldenborgh, and A. Cimatoribus, 2012: Is a decline of AMOC causing the warming hole above the North Atlantic in observed and modeled warming patterns? *J. Clim.*, **25**, 8373–8379, https://doi.org/10.1175/JCLI-D-12-00490.1.

Duchez, A., E. Frajka-Williams, S. A. Josey, D. G. Evans, J. P. Grist, R. Marsh, G. D. McCarthy, B. Sinha, D. I. Berry, and J. J.-M. Hirschi, 2016: Drivers of exceptionally cold North Atlantic Ocean temperatures and their link to the 2015 European heat wave. *Environ. Res. Lett.*, **11**, 074004, https://doi.org/10.1088/1748-9326/11/7/074004.

Dufour, C. O., J. Le Sommer, J. D. Zika, M. Gehlen, J. C. Orr, P. Mathiot, and B. Barnier, 2012: Standing and Transient Eddies in the Response of the Southern Ocean Meridional Overturning to the Southern Annular Mode. *J. Clim.*, **25**, 6958–6974, https://doi.org/10.1175/JCLI-D-11-00309.1.

Durack, P. J., and S. E. Wijffels, 2010: Fifty-Year Trends in Global Ocean Salinities and Their Relationship to Broad-Scale Warming. *J. Clim.*, **23**, 4342–4362, https://doi.org/10.1175/2010JCLI3377.1.

Durack, P. J., S. E. Wijffels, and R. J. Matear, 2012: Ocean Salinities Reveal Strong Global Water Cycle Intensification During 1950 to 2000. *Science (80-.).*, **336**, 455–458, https://doi.org/10.1126/science.1212222.

Exarchou, E., T. Kuhlbrodt, J. M. Gregory, and R. S. Smith, 2015: Ocean heat uptake processes: A model intercomparison. *J. Clim.*, **28**, 887–908, https://doi.org/10.1175/JCLI-D-14-00235.1.

Eyring, V., and Coauthors, 2013: Long-term ozone changes and associated climate impacts in CMIP5 simulations. *J. Geophys. Res. Atmos.*, **118**, 5029–5060, https://doi.org/10.1002/jgrd.50316.

Eyring, V., S. Bony, G. A. Meehl, C. A. Senior, B. Stevens, R. J. Stouffer, and K. E. Taylor,

2016: Overview of the Coupled Model Intercomparison Project Phase 6 (CMIP6) experimental design and organization. *Geosci. Model Dev.*, **9**, 1937–1958, https://doi.org/10.5194/gmd-9-1937-2016.

Farneti, R., T. L. Delworth, A. J. Rosati, S. M. Griffies, and F. Zeng, 2010: The Role of Mesoscale Eddies in the Rectification of the Southern Ocean Response to Climate Change. *J. Phys. Oceanogr.*, **40**, 1539–1557, https://doi.org/10.1175/2010JPO4353.1.

——, and Coauthors, 2015: An assessment of Antarctic Circumpolar Current and Southern Ocean meridional overturning circulation during 1958–2007 in a suite of interannual CORE-II simulations. *Ocean Model.*, **93**, 84–120, https://doi.org/10.1016/j.ocemod.2015.07.009.

Fasullo, J. T., and R. S. Nerem, 2018: Altimeter-era emergence of the patterns of forced sea-level rise in climate models and implications for the future. *Proc. Natl. Acad. Sci. U. S. A.*, **115**, 12944–12949, https://doi.org/10.1073/pnas.1813233115.

Ferreira, D., J. Marshall, C. M. Bitz, S. Solomon, and A. Plumb, 2015: Antarctic ocean and sea ice response to ozone depletion: A two-time-scale problem. *J. Clim.*, **28**, 1206–1226, https://doi.org/10.1175/JCLI-D-14-00313.1.

Fogwill, C. J., S. J. Phipps, C. S. M. Turney, and N. R. Golledge, 2015: Sensitivity of the Southern Ocean to enhanced regional Antarctic ice sheet meltwater input. *Earth's Futur.*, **3**, 317–329, https://doi.org/10.1002/2015EF000306.

Forget, G., J.-M. Campin, P. Heimbach, C. N. Hill, R. M. Ponte, and C. Wunsch, 2015: ECCO version 4: an integrated framework for non-linear inverse modeling and global ocean state estimation. *Geosci. Model Dev. Discuss.*, **8**, 3653–3743, https://doi.org/10.5194/gmdd-8-3653-2015.

Forster, P., V. Ramaswamy, P. Artaxo, T. Berntsen, R. Betts, D.W. Fahey, J. Haywood, J. Lean, D.C. Lowe, G. Myhre, J. Nganga, R. Prinn, G. Raga, M. S. and R. V. D., 2007: Changes in Atmospheric Constituents and in Radiative Forcing. In: Climate Change 2007: The Physical Science Basis. *Climate Change 2007*, Cambridge Univ. Press.

Frölicher, T. L., J. L. Sarmiento, D. J. Paynter, J. P. Dunne, J. P. Krasting, and M. Winton, 2015: Dominance of the Southern Ocean in Anthropogenic Carbon and Heat Uptake in CMIP5 Models. *J. Clim.*, **28**, 862–886, https://doi.org/10.1175/JCLI-D-14-00117.1.

Fyfe, J. C., 2006: Southern Ocean warming due to human influence. *Geophys. Res. Lett.*, **33**, 1–4, https://doi.org/10.1029/2006GL027247.

——, and O. A. Saenko, 2006: Simulated changes in the extratropical Southern Hemisphere winds and currents. *Geophys. Res. Lett.*, **33**, 1–4, https://doi.org/10.1029/2005GL025332.

——, ——, K. Zickfeld, M. Eby, and A. J. Weaver, 2007: The Role of Poleward-Intensifying Winds on Southern Ocean Warming. *J. Clim.*, **20**, 5391–5400, https://doi.org/10.1175/2007JCLI1764.1.

Gaspar, P., Y. Grégoris, and J.-M. Lefevre, 1990: A simple eddy kinetic energy model for simulations of the oceanic vertical mixing: Tests at station Papa and long-term upper ocean study site. *J. Geophys. Res.*, **95**, 16179, https://doi.org/10.1029/JC095iC09p16179.

Gent, P. R., 2016: Effects of Southern Hemisphere Wind Changes on the Meridional Overturning Circulation in Ocean Models. *Ann. Rev. Mar. Sci.*, **8**, 79–94, https://doi.org/10.1146/annurev-marine-122414-033929.

——, and J. C. Mcwilliams, 1990: Isopycnal Mixing in Ocean Circulation Models. *J. Phys. Oceanogr.*, **20**, 150–155, https://doi.org/10.1175/1520-0485(1990)020<0150:IMIOCM>2.0.CO;2.

——, and G. Danabasoglu, 2011: Response to increasing Southern Hemisphere winds in CCSM4. *J. Clim.*, **24**, 4992–4998, https://doi.org/10.1175/JCLI-D-10-05011.1.

Gille, S. T., 1994: Mean sea surface height of the Antarctic Circumpolar Current from Geosat data: Method and application. *J. Geophys. Res.*, **99**, 18255, https://doi.org/10.1029/94JC01172.

——, 2002: Warming of the Southern Ocean Since the 1950s. *Science (80-.).*, **295**, 1275–1277, https://doi.org/10.1126/science.1065863.

——, 2008: Decadal-Scale Temperature Trends in the Southern Hemisphere Ocean. *J. Clim.*, **21**, 4749–4765, https://doi.org/10.1175/2008JCLI2131.1.

——, 2014: Meridional displacement of the Antarctic Circumpolar Current. *Philos. Trans. R. Soc. A Math. Phys. Eng. Sci.*, **372**, 20130273, https://doi.org/10.1098/rsta.2013.0273.

Gillett, N. P., 2003: Simulation of Recent Southern Hemisphere Climate Change. *Science (80-.).*, **302**, 273–275, https://doi.org/10.1126/science.1087440.

Gleckler, P. J., P. J. Durack, R. J. Stouffer, G. C. Johnson, and C. E. Forest, 2016: Industrial-era global ocean heat uptake doubles in recent decades. *Nat. Clim. Chang.*, **6**, 394–398, https://doi.org/10.1038/nclimate2915.

Good, S. A., M. J. Martin, and N. A. Rayner, 2013: EN4: Quality controlled ocean temperature and salinity profiles and monthly objective analyses with uncertainty estimates. *J. Geophys. Res. Ocean.*, **118**, 6704–6716, https://doi.org/10.1002/2013JC009067.

Gould, J., D. Roemmich, S. Wijffels, H. Freeland, M. Ignaszewsky, X. Jianping, S. Pouliquen, Y. Desaubies, U. Send, K. Radhakrishnan, K. Takeuchi, K. Kim, M. Danchenkov, P. Sutton, B. King, B. Owens, and S. Riser, 2004: Argo profiling floats bring new era of in situ ocean observations. *Eos, Trans. Am. Geophys. Union*, **85**, 185, https://doi.org/10.1029/2004EO190002.

Gouretski, V., and F. Reseghetti, 2010: On depth and temperature biases in bathythermograph data: Development of a new correction scheme based on analysis of a global ocean database. *Deep. Res. Part I Oceanogr. Res. Pap.*, **57**, 812–833,

https://doi.org/10.1016/j.dsr.2010.03.011.

Graham, R. M., A. M. De Boer, K. J. Heywood, M. R. Chapman, and D. P. Stevens, 2012: Southern Ocean fronts: Controlled by wind or topography? *J. Geophys. Res. Ocean.*, **117**, 1–14, https://doi.org/10.1029/2012JC007887.

Gregory, J. M., K. W. Dixon, R. J. Stouffer, A. J. Weaver, E. Driesschaert, M. Eby, T. Fichefet, H. Hasumi, A. Hu, J. H. Jungclaus, I. V. Kamenkovich, A. Levermann, M. Montoya, S. Murakami, S. Nawrath, A. Oka, A. P. Sokolov, and R. B. Thorpe, 2005: A model intercomparison of changes in the Atlantic thermohaline circulation in response to increasing atmospheric CO 2 concentration. *Geophys. Res. Lett.*, **32**, n/a-n/a, https://doi.org/10.1029/2005GL023209.

——, N. Bouttes, S. M. Griffies, H. Haak, W. J. Hurlin, J. Jungclaus, M. Kelley, W. G. Lee, J. Marshall, A. Romanou, O. A. Saenko, D. Stammer, and M. Winton, 2016: The Flux-Anomaly-Forced Model Intercomparison Project (FAFMIP) contribution to CMIP6: investigation of sea-level and ocean climate change in response to CO2 forcing. *Geosci. Model Dev.*, **9**, 3993–4017, https://doi.org/10.5194/gmd-9-3993-2016.

Gulev, S. K., M. Latif, N. Keenlyside, W. Park, and K. P. Koltermann, 2013: North Atlantic Ocean control on surface heat flux on multidecadal timescales. *Nature*, **499**, 464–467, https://doi.org/10.1038/nature12268.

Sen Gupta, A., A. Santoso, A. S. Taschetto, C. C. Ummenhofer, J. Trevena, and M. H. England, 2009: Projected Changes to the Southern Hemisphere Ocean and Sea Ice in the IPCC AR4 Climate Models. *J. Clim.*, **22**, 3047–3078, https://doi.org/10.1175/2008JCLI2827.1.

Gutjahr, O., D. Putrasahan, K. Lohmann, J. H. Jungclaus, J. S. Von Storch, N. Brüggemann, H. Haak, and A. Stössel, 2019: Max Planck Institute Earth System Model (MPI-ESM1.2) for the High-Resolution Model Intercomparison Project (HighResMIP). *Geosci. Model Dev.*, **12**, 3241–3281, https://doi.org/10.5194/gmd-12-3241-2019.

Hallberg, R., and A. Gnanadesikan, 2006: The Role of Eddies in Determining the Structure and Response of the Wind-Driven Southern Hemisphere Overturning: Results from the Modeling Eddies in the Southern Ocean (MESO) Project. *J. Phys. Oceanogr.*, **36**, 2232–2252, https://doi.org/10.1175/JPO2980.1.

Hansen, J., M. Sato, P. Kharecha, and K. von Schuckmann, 2011: Earth's energy imbalance and implications. *Atmos. Chem. Phys.*, **11**, 13421–13449, https://doi.org/10.5194/acp-11-13421-2011.

Haumann, F. A., N. Gruber, M. Münnich, I. Frenger, S. Kern, F. Alexander Haumann, N. Gruber, M. Münnich, I. Frenger, and S. Kern, 2016: Sea-ice transport driving Southern Ocean salinity and its recent trends. *Nature*, **537**, 89–92, https://doi.org/10.1038/nature19101.

——, ——, and ——, 2020: Sea-Ice Induced Southern Ocean Subsurface Warming and Surface Cooling in a Warming Climate. *AGU Adv.*, **1**, https://doi.org/10.1029/2019AV000132.

Held, I. M., and B. J. Soden, 2006: Robust Responses of the Hydrological Cycle to Global Warming. *J. Clim.*, **19**, 5686–5699, https://doi.org/10.1175/JCLI3990.1.

Helm, K. P., N. L. Bindoff, and J. A. Church, 2010: Changes in the global hydrological-cycle inferred from ocean salinity. *Geophys. Res. Lett.*, **37**, 2–6, https://doi.org/10.1029/2010GL044222.

Heuzé, C., 2017: North Atlantic deep water formation and AMOC in CMIP5 models. *Ocean Sci.*, **13**, 609–622, https://doi.org/10.5194/os-13-609-2017.

Hirst, T., D. Bi, H. Yan, S. Marsland, M. Dix, and A. Sullivan, 2015: The ACCESS-CM2 coupled climate model – status and plans including contribution to CMIP6. Hobart, CSIRO.

Hogg, A. M. C., 2010: An Antarctic Circumpolar Current driven by surface buoyancy forcing. *Geophys. Res. Lett.*, **37**, 1–5, https://doi.org/10.1029/2010GL044777.

Holland, M. M., L. Landrum, Y. Kostov, and J. Marshall, 2017: Sensitivity of Antarctic sea ice to the Southern Annular Mode in coupled climate models. *Clim. Dyn.*, **49**, 1813–1831, https://doi.org/10.1007/s00382-016-3424-9.

Holte, J., L. D. Talley, J. Gilson, and D. Roemmich, 2017: An Argo mixed layer climatology and database. *Geophys. Res. Lett.*, **44**, 5618–5626, https://doi.org/10.1002/2017GL073426.

Hu, S., J. Sprintall, C. Guan, M. J. McPhaden, F. Wang, D. Hu, and W. Cai, 2020: Deep-reaching acceleration of global mean ocean circulation over the past two decades. *Sci. Adv.*, **6**, 1–9, https://doi.org/10.1126/sciadv.aax7727.

Hughes, C. W., J. Williams, A. C. Coward, and B. A. De Cuevas, 2014: Antarctic circumpolar transport and the southern mode: A model investigation of interannual to decadal timescales. *Ocean Sci.*, **10**, 215–225, https://doi.org/10.5194/os-10-215-2014.

Hurrell, J. W., and Coauthors, 2013: The community earth system model: A framework for collaborative research. *Bull. Am. Meteorol. Soc.*, **94**, 1339–1360, https://doi.org/10.1175/BAMS-D-12-00121.1.

Hwang, Y.-T., S.-P. Xie, C. Deser, and S. M. Kang, 2017: Connecting Tropical Climate Change with Southern Ocean Heat Uptake. *Geophys. Res. Lett.*, 9449–9457, https://doi.org/10.1002/2017GL074972.

IPCC, 2013: *Climate Change 2013: The Physical Science Basis. Contribution of Working Group I to the Fifth Assessment Report of the Intergovernmental Panel on Climate Change*. Cambridge University Press, 1535 pp.

Jackson, L. C., K. A. Peterson, C. D. Roberts, and R. A. Wood, 2016: Recent slowing of Atlantic overturning circulation as a recovery from earlier strengthening. *Nat. Geosci.*, **9**, 518–522, https://doi.org/10.1038/ngeo2715.

Jacobs, S. S., 2002: Freshening of the Ross Sea During the Late 20th Century. *Science (80-.).*,

297, 386–389, https://doi.org/10.1126/science.1069574.

Jones, G. S., P. A. Stott, and N. Christidis, 2013: Attribution of observed historical near-surface temperature variations to anthropogenic and natural causes using CMIP5 simulations. *J. Geophys. Res. Atmos.*, **118**, 4001–4024, https://doi.org/10.1002/jgrd.50239.

Kang, S. M., and S. P. Xie, 2014: Dependence of climate response on meridional structure of external thermal forcing. *J. Clim.*, **27**, 5593–5600, https://doi.org/10.1175/JCLI-D-13-00622.1.

Kay, J. E., and Coauthors, 2015: The Community Earth System Model (CESM) Large Ensemble Project: A Community Resource for Studying Climate Change in the Presence of Internal Climate Variability. *Bull. Am. Meteorol. Soc.*, **96**, 1333–1349, https://doi.org/10.1175/BAMS-D-13-00255.1.

Kay, J. E., C. Wall, V. Yettella, B. Medeiros, C. Hannay, P. Caldwell, and C. Bitz, 2016: Global Climate Impacts of Fixing the Southern Ocean Shortwave Radiation Bias in the Community Earth System Model (CESM). *J. Clim.*, **29**, 4617–4636, https://doi.org/10.1175/JCLI-D-15-0358.1.

Kim, H., and S.-I. An, 2013: On the subarctic North Atlantic cooling due to global warming. *Theor. Appl. Climatol.*, **114**, 9–19, https://doi.org/10.1007/s00704-012-0805-9.

Kim, Y. S., and A. H. Orsi, 2014: On the variability of antarctic circumpolar current fronts inferred from 1992-2011 altimetry. *J. Phys. Oceanogr.*, **44**, 3054–3071, https://doi.org/10.1175/JPO-D-13-0217.1.

Kostov, Y., J. Marshall, U. Hausmann, K. C. Armour, D. Ferreira, and M. M. Holland, 2017: Fast and slow responses of Southern Ocean sea surface temperature to SAM in coupled climate models. *Clim. Dyn.*, **48**, 1595–1609, https://doi.org/10.1007/s00382-016-3162-z.

Kuhlbrodt, T., and J. M. Gregory, 2012: Ocean heat uptake and its consequences for the magnitude of sea level rise and climate change. *Geophys. Res. Lett.*, **39**, 1–6, https://doi.org/10.1029/2012GL052952.

Langlais, C. E., S. R. Rintoul, and J. D. Zika, 2015: Sensitivity of Antarctic Circumpolar Current Transport and Eddy Activity to Wind Patterns in the Southern Ocean*. *J. Phys. Oceanogr.*, **45**, 1051–1067, https://doi.org/10.1175/JPO-D-14-0053.1.

Large, W. G., J. C. McWilliams, and S. C. Doney, 1994: Oceanic vertical mixing: A review and a model with a nonlocal boundary layer parameterization. *Rev. Geophys.*, **32**, 363–403, https://doi.org/10.1029/94RG01872.

De Lavergne, C., J. B. Palter, E. D. Galbraith, R. Bernardello, and I. Marinov, 2014: Cessation of deep convection in the open Southern Ocean under anthropogenic climate change. *Nat. Clim. Chang.*, **4**, 278–282, https://doi.org/10.1038/nclimate2132.

Lee, S., and S. B. Feldstein, 2013: Detecting Ozone- and Greenhouse Gas–Driven Wind Trends

with Observational Data. *Science (80-.).*, **339**, 563–567, https://doi.org/10.1126/science.1225154.

Levitus, S., J. Antonov, and T. Boyer, 2005: Warming of the world ocean, 1955-2003. *Geophys. Res. Lett.*, **32**, 1–4, https://doi.org/10.1029/2004GL021592.

——, J. I. Antonov, T. P. Boyer, R. A. Locarnini, H. E. Garcia, and A. V. Mishonov, 2009: Global ocean heat content 1955-2008 in light of recently revealed instrumentation problems. *Geophys. Res. Lett.*, **36**, 1–5, https://doi.org/10.1029/2008GL037155.

——, ——, ——, O. K. Baranova, H. E. Garcia, R. A. Locarnini, A. V. Mishonov, J. R. Reagan, D. Seidov, E. S. Yarosh, and M. M. Zweng, 2012: World ocean heat content and thermosteric sea level change (0-2000m), 1955-2010. *Geophys. Res. Lett.*, **39**, 1–5, https://doi.org/10.1029/2012GL051106.

Li, Q., and S. Lee, 2017: A Mechanism of Mixed Layer Formation in the Indo–Western Pacific Southern Ocean: Preconditioning by an Eddy-Driven Jet-Scale Overturning Circulation. *J. Phys. Oceanogr.*, **47**, 2755–2772, https://doi.org/10.1175/JPO-D-17-0006.1.

——, ——, and A. Griesel, 2016: Eddy Fluxes and Jet-Scale Overturning Circulations in the Indo–Western Pacific Southern Ocean. *J. Phys. Oceanogr.*, **46**, 2943–2959, https://doi.org/10.1175/JPO-D-15-0241.1.

Liu, W., J. Lu, and S.-P. Xie, 2015: Understanding the Indian Ocean response to double CO2 forcing in a coupled model. *Ocean Dyn.*, **65**, 1037–1046, https://doi.org/10.1007/s10236-015-0854-6.

——, S.-P. Xie, and J. Lu, 2016: Tracking ocean heat uptake during the surface warming hiatus. *Nat. Commun.*, **7**, 10926, https://doi.org/10.1038/ncomms10926.

——, J. Lu, S.-P. P. Xie, A. Fedorov, W. Liu, J. Lu, S.-P. P. Xie, and A. Fedorov, 2018: Southern Ocean Heat Uptake, redistribution, and storage in a warming climate: The role of meridional overturning circulation. *J. Clim.*, **31**, 4727–4743, https://doi.org/10.1175/JCLI-D-17-0761.1.

Locarnini, R.A., A.V. Mishonov, O.K. Baranova, T.P. Boyer, M.M. Zweng, H.E. Garcia, J.R. Reagan, D. Seidov, K.W. Weathers, C.R. Paver, and I. V. S., 2019: *World Ocean Atlas 2018, Volume 1: Temperature.* 52 pp.

Lozier, M. S., S. Leadbetter, R. G. Williams, V. Roussenov, M. S. C. Reed, and N. J. Moore, 2008: The spatial pattern and mechanisms of heat-content change in the North Atlantic. *Science (80-.).*, **319**, 800–803, https://doi.org/10.1126/science.1146436.

Lu, J., and B. Zhao, 2012: The Role of Oceanic Feedback in the Climate Response to Doubling CO 2. *J. Clim.*, **25**, 7544–7563, https://doi.org/10.1175/JCLI-D-11-00712.1.

Manabe, S., K. Bryan, and M. J. Spelman, 1990: Transient Response of a Global Ocean-Atmosphere Model to a Doubling of Atmospheric Carbon Dioxide. *J. Phys. Oceanogr.*, **20**,

722–749, https://doi.org/10.1175/1520-0485(1990)020<0722:TROAGO>2.0.CO;2.

——, R. J. Stouffer, M. J. Spelman, and K. Bryan, 1991: Transient responses of a coupled ocean–atmosphere model to gradual changes of atmospheric CO2. Part I. Annual mean response. *J. Clim.*, **4**, 785–818, https://doi.org/https://doi.org/10.1175/1520-0442(1991)004<0785:TROACO>2.0.CO;2.

Marshall, D. P., M. H. P. Ambaum, J. R. Maddison, D. R. Munday, and L. Novak, 2017: Eddy saturation and frictional control of the Antarctic Circumpolar Current. *Geophys. Res. Lett.*, **44**, 286–292, https://doi.org/10.1002/2016GL071702.

Marshall, G. J., 2003: Trends in the Southern Annular Mode from observations and reanalyses. *J. Clim.*, **16**, 4134–4143, https://doi.org/10.1175/1520-0442(2003)016<4134:TITSAM>2.0.CO;2.

Marshall, J., K. C. Armour, J. R. Scott, Y. Kostov, U. Hausmann, D. Ferreira, T. G. Shepherd, and C. M. Bitz, 2014: The ocean's role in polar climate change: asymmetric Arctic and Antarctic responses to greenhouse gas and ozone forcing. *Philos. Trans. R. Soc. A Math. Phys. Eng. Sci.*, **372**, 20130040, https://doi.org/10.1098/rsta.2013.0040.

——, J. R. Scott, K. C. Armour, J.-M. Campin, M. Kelley, and A. Romanou, 2015: The ocean's role in the transient response of climate to abrupt greenhouse gas forcing. *Clim. Dyn.*, **44**, 2287–2299, https://doi.org/10.1007/s00382-014-2308-0.

McCarthy, G. D., I. D. Haigh, J. J. M. Hirschi, J. P. Grist, and D. A. Smeed, 2015: Ocean impact on decadal Atlantic climate variability revealed by sea-level observations. *Nature*, **521**, 508–510, https://doi.org/10.1038/nature14491.

Meijers, A. J. S., N. L. Bindoff, and S. R. Rintoul, 2011: Frontal movements and property fluxes: Contributions to heat and freshwater trends in the Southern Ocean. *J. Geophys. Res. Ocean.*, **116**, 1–17, https://doi.org/10.1029/2010JC006832.

——, E. Shuckburgh, N. Bruneau, J. B. Sallee, T. J. Bracegirdle, and Z. Wang, 2012: Representation of the Antarctic Circumpolar Current in the CMIP5 climate models and future changes under warming scenarios. *J. Geophys. Res. Ocean.*, **117**, 1–19, https://doi.org/10.1029/2012JC008412.

Menary, M. B., C. D. Roberts, M. D. Palmer, P. R. Halloran, L. Jackson, R. A. Wood, W. A. Müller, D. Matei, and S. K. Lee, 2013: Mechanisms of aerosol-forced AMOC variability in a state of the art climate model. *J. Geophys. Res. Ocean.*, **118**, 2087–2096, https://doi.org/10.1002/jgrc.20178.

Meredith, M. P., and A. M. Hogg, 2006: Circumpolar response of Southern Ocean eddy activity to a change in the Southern Annular Mode. *Geophys. Res. Lett.*, **33**, L16608, https://doi.org/10.1029/2006GL026499.

——, A. C. Naveira Garabato, A. M. Hogg, and R. Farneti, 2012: Sensitivity of the Overturning Circulation in the Southern Ocean to Decadal Changes in Wind Forcing. *J. Clim.*, **25**, 99–

110, https://doi.org/10.1175/2011JCLI4204.1.

Morrison, A. K., and A. Hogg, 2013: On the Relationship between Southern Ocean Overturning and ACC Transport. *J. Phys. Oceanogr.*, **43**, 140–148, https://doi.org/10.1175/JPO-D-12-057.1.

——, O. A. Saenko, A. M. Hogg, and P. Spence, 2013: The role of vertical eddy flux in Southern Ocean heat uptake. *Geophys. Res. Lett.*, **40**, 5445–5450, https://doi.org/10.1002/2013GL057706.

——, S. M. Griffies, M. Winton, W. G. Anderson, and J. L. Sarmiento, 2016: Mechanisms of Southern Ocean Heat Uptake and Transport in a Global Eddying Climate Model. *J. Clim.*, **29**, 2059–2075, https://doi.org/10.1175/JCLI-D-15-0579.1.

Munday, D. R., H. L. Johnson, and D. P. Marshall, 2013: Eddy Saturation of Equilibrated Circumpolar Currents. *J. Phys. Oceanogr.*, **43**, 507–532, https://doi.org/10.1175/JPO-D-12-095.1.

Myhre, G., D. Shindell, F.-M. Bréon, W. Collins, J. Fuglestvedt, J. Huang, D. Koch, J.-F. Lamarque, D. Lee, B. Mendoza, T. Nakajima, A. Robock, G. Stephens, T. Takemura, and H. Zhang, 2013: Anthropogenic and Natural Radiative Forcing. *Clim. Chang. 2013 Phys. Sci. Basis. Contrib. Work. Gr. I to Fifth Assess. Rep. Intergov. Panel Clim. Chang.*, 659–740, https://doi.org/10.1017/ CBO9781107415324.018.

O'Neill, B. C., C. Tebaldi, D. P. Van Vuuren, V. Eyring, P. Friedlingstein, G. Hurtt, R. Knutti, E. Kriegler, J. F. Lamarque, J. Lowe, G. A. Meehl, R. Moss, K. Riahi, and B. M. Sanderson, 2016: The Scenario Model Intercomparison Project (ScenarioMIP) for CMIP6. *Geosci. Model Dev.*, **9**, 3461–3482, https://doi.org/10.5194/gmd-9-3461-2016.

Orsi, A. H., T. Whitworth, and W. D. Nowlin, 1995: On the meridional extent and fronts of the Antarctic Circumpolar Current. *Deep. Res. Part I*, **42**, 641–673, https://doi.org/10.1016/0967-0637(95)00021-W.

Paolo, F. S., H. A. Fricker, and L. Padman, 2015: Volume loss from Antarctic ice shelves is accelerating. *Science (80-.).*, **348**, 327–331, https://doi.org/10.1126/science.aaa0940.

Pauling, A. G., C. M. Bitz, I. J. Smith, and P. J. Langhorne, 2016: The Response of the Southern Ocean and Antarctic Sea Ice to Freshwater from Ice Shelves in an Earth System Model. *J. Clim.*, **29**, 1655–1672, https://doi.org/10.1175/JCLI-D-15-0501.1.

Peng, Q., S. P. Xie, D. Wang, X. T. Zheng, and H. Zhang, 2019: Coupled ocean-atmosphere dynamics of the 2017 extreme coastal El Niño. *Nat. Commun.*, **10**, 1–10, https://doi.org/10.1038/s41467-018-08258-8.

——, S.-P. Xie, D. Wang, Y. Kamae, H. Zhang, S. Hu, X.-T. Zheng, and W. Wang, 2020: Eastern Pacific Wind Effect on the Evolution of El Niño: Implications for ENSO Diversity. *J. Clim.*, **33**, 3197–3212, https://doi.org/10.1175/JCLI-D-19-0435.1.

Purich, A., W. Cai, M. H. England, and T. Cowan, 2016: Evidence for link between modelled trends in Antarctic sea ice and underestimated westerly wind changes. *Nat. Commun.*, **7**, 10409, https://doi.org/10.1038/ncomms10409.

——, M. H. England, W. Cai, A. Sullivan, and P. J. Durack, 2018: Impacts of broad-scale surface freshening of the Southern Ocean in a coupled climate model. *J. Clim.*, **31**, 2613–2632, https://doi.org/10.1175/JCLI-D-17-0092.1.

Purkey, S. G., and G. C. Johnson, 2010: Warming of global abyssal and deep Southern Ocean waters between the 1990s and 2000s: Contributions to global heat and sea level rise budgets. *J. Clim.*, **23**, 6336–6351, https://doi.org/10.1175/2010JCLI3682.1.

Qu, T., I. Fukumori, and R. A. Fine, 2019: Spin-Up of the Southern Hemisphere Super Gyre. *J. Geophys. Res. Ocean.*, **124**, 154–170, https://doi.org/10.1029/2018JC014391.

Redi, M. H., 1982: Oceanic Isopycnal Mixing by Coordinate Rotation. *J. Phys. Oceanogr.*, **12**, 1154–1158, https://doi.org/10.1175/1520-0485(1982)012<1154:OIMBCR>2.0.CO;2.

Rhein, M., S. R. Rintoul, S. Aoki, E. Campos, D. Chambers, R. A. Feely, S. Gulev, G. C. Johnson, S. A. Josey, A. Kostianoy, C. Mauritzen, D. Roemmich, L. D. Talley, and F. Wang, 2013: Observations: Ocean. *Climate Change 2013 - The Physical Science Basis*, Intergovernmental Panel on Climate Change, Ed., Cambridge University Press, 255–316.

Rintoul, S. R., 2018: The global influence of localized dynamics in the Southern Ocean. *Nature*, **558**, 209–218, https://doi.org/10.1038/s41586-018-0182-3.

Riser, S. C., and Coauthors, 2016: Fifteen years of ocean observations with the global Argo array. *Nat. Clim. Chang.*, **6**, 145–153, https://doi.org/10.1038/nclimate2872.

Roberts, C. D., L. Jackson, and D. McNeall, 2014: Is the 2004 – 2012 reduction of the Atlantic meridional overturning circulation significant ? *Geophys. Res. Lett.*, **41**, 1–7, https://doi.org/10.1002/2014GL059473.

Robson, J., P. Ortega, and R. Sutton, 2016: A reversal of climatic trends in the North Atlantic since 2005. *Nat. Geosci.*, **9**, 513–517, https://doi.org/10.1038/ngeo2727.

Roemmich, D., and J. Gilson, 2009: The 2004–2008 mean and annual cycle of temperature, salinity, and steric height in the global ocean from the Argo Program. *Prog. Oceanogr.*, **82**, 81–100, https://doi.org/10.1016/j.pocean.2009.03.004.

——, J. Gilson, R. Davis, P. Sutton, S. Wijffels, and S. Riser, 2007: Decadal Spinup of the South Pacific Subtropical Gyre. *J. Phys. Oceanogr.*, **37**, 162–173, https://doi.org/10.1175/JPO3004.1.

——, J. Church, J. Gilson, D. Monselesan, P. Sutton, and S. Wijffels, 2015: Unabated planetary warming and its ocean structure since 2006. *Nat. Clim. Chang.*, **5**, 2–7, https://doi.org/10.1038/nclimate2513.

Rotstayn, L. D., M. A. Collier, A. Chrastansky, S. J. Jeffrey, and J.-J. Luo, 2013: Projected effects of declining aerosols in RCP4.5: unmasking global warming? *Atmos. Chem. Phys.*, **13**, 10883–10905, https://doi.org/10.5194/acp-13-10883-2013.

——, M. A. Collier, D. T. Shindell, and O. Boucher, 2015: Why does aerosol forcing control historical global-mean surface temperature change in CMIP5 models? *J. Clim.*, **28**, 6608–6625, https://doi.org/10.1175/JCLI-D-14-00712.1.

Rugenstein, M. A. A., M. Winton, R. J. Stouffer, S. M. Griffies, and R. Hallberg, 2013: Northern High-Latitude Heat Budget Decomposition and Transient Warming. *J. Clim.*, **26**, 609–621, https://doi.org/10.1175/JCLI-D-11-00695.1.

Russell, G. L., and D. Rind, 1999: Response to CO 2 Transient Increase in the GISS Coupled Model : Regional Coolings in a Warming Climate. *J. Clim.*, **12**, 531–539, https://doi.org/https://doi.org/10.1175/1520-0442(1999)012<0531:RTCTII>2.0.CO;2.

Russell, J. L., K. W. Dixon, A. Gnanadesikan, R. J. Stouffer, and J. R. Toggweiler, 2006: The Southern hemisphere westerlies in a warming world: Propping open the door to the deep ocean. *J. Clim.*, **19**, 6382–6390, https://doi.org/10.1175/JCLI3984.1.

Rye, C. D., J. Marshall, M. Kelley, G. Russell, L. S. Nazarenko, Y. Kostov, G. A. Schmidt, and J. Hansen, 2020: Antarctic Glacial Melt as a Driver of Recent Southern Ocean Climate Trends. *Geophys. Res. Lett.*, **47**, 1–9, https://doi.org/10.1029/2019GL086892.

Sabine, C. L., 2004: The Oceanic Sink for Anthropogenic CO2. *Science (80-.).*, **305**, 367–371, https://doi.org/10.1126/science.1097403.

Sallée, J.-B., 2018: Southern Ocean Warming. *Oceanography*, **31**, 52–62, https://doi.org/10.5670/oceanog.2018.215.

von Schuckmann, K., M. D. Palmer, K. E. Trenberth, A. Cazenave, D. Chambers, N. Champollion, J. Hansen, S. A. Josey, N. Loeb, P.-P. Mathieu, B. Meyssignac, and M. Wild, 2016: An imperative to monitor Earth's energy imbalance. *Nat. Clim. Chang.*, **6**, 138–144, https://doi.org/10.1038/nclimate2876.

Seviour, W. J. M., A. Gnanadesikan, and D. W. Waugh, 2016: The transient response of the Southern Ocean to stratospheric ozone depletion. *J. Clim.*, **29**, 7383–7396, https://doi.org/10.1175/JCLI-D-16-0198.1.

Sheffield, J., and Coauthors, 2013: North American Climate in CMIP5 experiments. Part I: Evaluation of historical simulations of continental and regional climatology. *J. Clim.*, **26**, 9209–9245, https://doi.org/10.1175/JCLI-D-12-00592.1.

Shi, J.-R., S.-P. Xie, and L. D. Talley, 2018: Evolving Relative Importance of the Southern Ocean and North Atlantic in Anthropogenic Ocean Heat Uptake. *J. Clim.*, **31**, 7459–7479, https://doi.org/10.1175/JCLI-D-18-0170.1.

——, L. D. Talley, S.-P. Xie, W. Liu, and S. T. Gille, 2020: Effects of Buoyancy and Wind

Forcing on Southern Ocean Climate Change. *J. Clim.*, **33**, 10003–10020, https://doi.org/10.1175/JCLI-D-19-0877.1.

Shindell, D. T., G. Faluvegi, L. Rotstayn, and G. Milly, 2015: Spatial patterns of radiative forcing and surface temperature response. *J. Geophys. Res. Atmos.*, **120**, 5385–5403, https://doi.org/10.1002/2014JD022752.

Sigmond, M., M. C. Reader, J. C. Fyfe, and N. P. Gillett, 2011: Drivers of past and future Southern Ocean change: Stratospheric ozone versus greenhouse gas impacts. *Geophys. Res. Lett.*, **38**, 3–7, https://doi.org/10.1029/2011GL047120.

Smeed, D. A., G. D. McCarthy, S. A. Cunningham, E. Frajka-Williams, D. Rayner, W. E. Johns, C. S. Meinen, M. O. Baringer, B. I. Moat, A. Duchez, and H. L. Bryden, 2014: Observed decline of the Atlantic meridional overturning circulation 2004-2012. *Ocean Sci.*, **10**, 29–38, https://doi.org/10.5194/os-10-29-2014.

Smith, D. M., B. B. B. Booth, N. J. Dunstone, R. Eade, L. Hermanson, G. S. Jones, A. A. Scaife, K. L. Sheen, and V. Thompson, 2016: Role of volcanic and anthropogenic aerosols in the recent global surface warming slowdown. *Nat. Clim. Chang.*, **6**, 936–940, https://doi.org/10.1038/nclimate3058.

Sokolov, S., and S. R. Rintoul, 2007: Multiple jets of the antarctic circumpolar current South of Australia. *J. Phys. Oceanogr.*, **37**, 1394–1412, https://doi.org/10.1175/JPO3111.1.

Spence, P., J. C. Fyfe, A. Montenegro, and A. J. Weaver, 2010: Southern ocean response to strengthening winds in an eddy-permitting global climate model. *J. Clim.*, **23**, 5332–5343, https://doi.org/10.1175/2010JCLI3098.1.

Stössel, A., D. Notz, F. A. Haumann, H. Haak, J. Jungclaus, and U. Mikolajewicz, 2015: Controlling high-latitude Southern Ocean convection in climate models. *Ocean Model.*, **86**, 58–75, https://doi.org/10.1016/j.ocemod.2014.11.008.

Sun, C., and D. R. Watts, 2002: Heat flux carried by the Antarctic circumpolar current mean flow. *J. Geophys. Res. C Ocean.*, **107**, 2–1, https://doi.org/10.1029/2001JC001187.

Swart, N. C., and J. C. Fyfe, 2012: Observed and simulated changes in the Southern Hemisphere surface westerly wind-stress. *Geophys. Res. Lett.*, **39**, n/a-n/a, https://doi.org/10.1029/2012GL052810.

——, and ——, 2013: The influence of recent Antarctic ice sheet retreat on simulated sea ice area trends. *Geophys. Res. Lett.*, **40**, 4328–4332, https://doi.org/10.1002/grl.50820.

——, J. C. Fyfe, N. Gillett, and G. J. Marshall, 2015: Comparing Trends in the Southern Annular Mode and Surface Westerly Jet. *J. Clim.*, **28**, 8840–8859, https://doi.org/10.1175/JCLI-D-15-0334.1.

——, S. T. Gille, J. C. Fyfe, and N. P. Gillett, 2018: Recent Southern Ocean warming and freshening driven by greenhouse gas emissions and ozone depletion. *Nat. Geosci.*, **11**, 836–

841, https://doi.org/10.1038/s41561-018-0226-1.

——, and Coauthors, 2019: The Canadian Earth System Model version 5 (CanESM5.0.3). *Geosci. Model Dev. Discuss.*, **5**, 1–68, https://doi.org/10.5194/gmd-2019-177.

Talley, L. D., G. L. Pickard, W. J. Emery, and J. H. Swift, 2011: *Descriptive physical oceanography: An introduction*. 6th ed. Academic Press, London,.

——, and Coauthors, 2016: Changes in Ocean Heat, Carbon Content, and Ventilation: A Review of the First Decade of GO-SHIP Global Repeat Hydrography. *Ann. Rev. Mar. Sci.*, **8**, 185–215, https://doi.org/10.1146/annurev-marine-052915-100829.

Tamsitt, V., L. D. Talley, M. R. Mazloff, and I. Cerovečki, 2016: Zonal Variations in the Southern Ocean Heat Budget. *J. Clim.*, **29**, 6563–6579, https://doi.org/10.1175/JCLI-D-15-0630.1.

Tatebe, H., and Coauthors, 2019: Description and basic evaluation of simulated mean state, internal variability, and climate sensitivity in MIROC6. *Geosci. Model Dev.*, **12**, 2727–2765, https://doi.org/10.5194/gmd-12-2727-2019.

Taylor, K. E., R. J. Stouffer, and G. a Meehl, 2012: An Overview of CMIP5 and the Experiment Design. *Bull. Am. Meteorol. Soc.*, **93**, 485–498, https://doi.org/10.1175/BAMS-D-11-00094.1.

Terray, L., 2012: Evidence for multiple drivers of North Atlantic multi-decadal climate variability. *Geophys. Res. Lett.*, **39**, 6–11, https://doi.org/10.1029/2012GL053046.

Thompson, A. F., and J. B. Sallée, 2012: Jets and Topography: Jet Transitions and the Impact on Transport in the Antarctic Circumpolar Current. *J. Phys. Oceanogr.*, **42**, 956–972, https://doi.org/10.1175/JPO-D-11-0135.1.

Thompson, D. W. J., 2002: Interpretation of Recent Southern Hemisphere Climate Change. *Science (80-.).*, **296**, 895–899, https://doi.org/10.1126/science.1069270.

——, S. Solomon, P. J. Kushner, M. H. England, K. M. Grise, and D. J. Karoly, 2011: Signatures of the Antarctic ozone hole in Southern Hemisphere surface climate change. *Nat. Geosci.*, **4**, 741–749, https://doi.org/10.1038/ngeo1296.

Thorpe, R. B., J. M. Gregory, T. C. Johns, R. A. Wood, and J. F. B. Mitchell, 2001: Mechanisms determining the Atlantic thermohaline circulation response to greenhouse forcing in a non-flux-adjusted coupled climate model. *J. Clim.*, **14**, 3102–3116, https://doi.org/10.1175/1520-0442(2001)014<3102:MDTATC>2.0.CO;2.

Toggweiler, J. R., and B. Samuels, 1995: Effect of drake passage on the global thermohaline circulation. *Deep Sea Res. Part I Oceanogr. Res. Pap.*, **42**, 477–500, https://doi.org/10.1016/0967-0637(95)00012-U.

Trenberth, K. E., J. T. Fasullo, and M. A. Balmaseda, 2014: Earth's Energy Imbalance. *J. Clim.*,

27, 3129–3144, https://doi.org/10.1175/JCLI-D-13-00294.1.

Valdivieso, M., and Coauthors, 2017: An assessment of air–sea heat fluxes from ocean and coupled reanalyses. *Clim. Dyn.*, **49**, 983–1008, https://doi.org/10.1007/s00382-015-2843-3.

Wang, G., S. P. Xie, R. X. Huang, and C. Chen, 2015: Robust warming pattern of global subtropical oceans and its mechanism. *J. Clim.*, **28**, 8574–8584, https://doi.org/10.1175/JCLI-D-14-00809.1.

Wang, G., L. Cheng, J. Abraham, and C. Li, 2017: Consensuses and discrepancies of basin-scale ocean heat content changes in different ocean analyses. *Clim. Dyn.*, 1–17, https://doi.org/10.1007/s00382-017-3751-5.

Wang, H., S. P. Xie, and Q. Liu, 2016a: Comparison of climate response to anthropogenic aerosol versus greenhouse gas forcing: Distinct patterns. *J. Clim.*, **29**, 5175–5188, https://doi.org/10.1175/JCLI-D-16-0106.1.

——, ——, H. Tokinaga, Q. Liu, and Y. Kosaka, 2016b: Detecting cross-equatorial wind change as a fingerprint of climate response to anthropogenic aerosol forcing. *Geophys. Res. Lett.*, **43**, 3444–3450, https://doi.org/10.1002/2016GL068521.

Wang, J., M. R. Mazloff, and S. T. Gille, 2016c: The Effect of the Kerguelen Plateau on the Ocean Circulation. *J. Phys. Oceanogr.*, **46**, 3385–3396, https://doi.org/10.1175/JPO-D-15-0216.1.

Waugh, D. W., F. Primeau, T. DeVries, and M. Holzer, 2013: Recent Changes in the Ventilation of the Southern Oceans. *Science (80-.).*, **339**, 568–570, https://doi.org/10.1126/science.1225411.

Weaver, A. J., M. Eby, M. Kienast, and O. A. Saenko, 2007: Response of the Atlantic meridional overturning circulation to increasing atmospheric CO 2 : Sensitivity to mean climate state. *Geophys. Res. Lett.*, **34**, https://doi.org/10.1029/2006GL028756.

Westervelt, D. M., L. W. Horowitz, V. Naik, J. C. Golaz, and D. L. Mauzerall, 2015: Radiative forcing and climate response to projected 21st century aerosol decreases. *Atmos. Chem. Phys.*, **15**, 12681–12703, https://doi.org/10.5194/acp-15-12681-2015.

Winton, M., S. M. Griffies, B. L. Samuels, J. L. Sarmiento, and T. L. Frölicher, 2013: Connecting Changing Ocean Circulation with Changing Climate. *J. Clim.*, **26**, 2268–2278, https://doi.org/10.1175/JCLI-D-12-00296.1.

Wood, R. a, A. B. Keen, J. F. B. Mitchell, and J. M. Gregory, 1999: Changing spatial structure of the thermohaline circulation in response to atmospheric CO2 forcing in a climate model. *Nature*, **399**, 572–575, https://doi.org/10.1038/21170.

Wu, L., W. Cai, L. Zhang, H. Nakamura, A. Timmermann, T. Joyce, M. J. McPhaden, M. Alexander, B. Qiu, M. Visbeck, P. Chang, and B. Giese, 2012: Enhanced warming over the global subtropical western boundary currents. *Nat. Clim. Chang.*, **2**, 161–166,

https://doi.org/10.1038/nclimate1353.

Xie, S.-P., C. Deser, G. a Vecchi, J. Ma, H. Teng, and A. T. Wittenberg, 2010: Global Warming Pattern Formation: Sea Surface Temperature and Rainfall*. *J. Clim.*, **23**, 966–986, https://doi.org/10.1175/2009JCLI3329.1.

——, B. Lu, and B. Xiang, 2013: Similar spatial patterns of climate responses to aerosol and greenhouse gas changes. *Nat. Geosci.*, **6**, 828–832, https://doi.org/10.1038/ngeo1931.

——, C. Deser, G. A. Vecchi, M. Collins, T. L. Delworth, A. Hall, E. Hawkins, N. C. Johnson, C. Cassou, A. Giannini, and M. Watanabe, 2015: Towards predictive understanding of regional climate change. *Nat. Clim. Chang.*, **5**, 921–930, https://doi.org/10.1038/nclimate2689.

Xu, Y., J. F. Lamarque, and B. M. Sanderson, 2015: The importance of aerosol scenarios in projections of future heat extremes. *Clim. Change*, 1–14, https://doi.org/10.1007/s10584-015-1565-1.

Yukimoto, S., H. Kawai, T. Koshiro, N. Oshima, K. Yoshida, S. Urakawa, H. Tsujino, M. Deushi, T. Tanaka, M. Hosaka, S. Yabu, H. Yoshimura, E. Shindo, R. Mizuta, A. Obata, Y. Adachi, and M. Ishii, 2019: The meteorological research institute Earth system model version 2.0, MRI-ESM2.0: Description and basic evaluation of the physical component. *J. Meteorol. Soc. Japan*, **97**, 931–965, https://doi.org/10.2151/jmsj.2019-051.

Zhang, L., T. L. Delworth, W. Cooke, and X. Yang, 2019: Natural variability of Southern Ocean convection as a driver of observed climate trends. *Nat. Clim. Chang.*, **9**, 59–65, https://doi.org/10.1038/s41558-018-0350-3.

Zhang, W., and X.-H. Yan, 2017: The Subpolar North Atlantic Ocean Heat Content Variability and its Decomposition. *Sci. Rep.*, **7**, 13748, https://doi.org/10.1038/s41598-017-14158-6.

Zhang, X., F. W. Zwiers, G. C. Hegerl, F. H. Lambert, N. P. Gillett, S. Solomon, P. A. Stott, and T. Nozawa, 2007: Detection of human influence on twentieth-century precipitation trends. *Nature*, **448**, 461–465, https://doi.org/10.1038/nature06025.

Zika, J. D., J. Le Sommer, C. O. Dufour, J.-M. Molines, B. Barnier, P. Brasseur, R. Dussin, T. Penduff, D. Iudicone, A. Lenton, G. Madec, P. Mathiot, J. Orr, E. Shuckburgh, and F. Vivier, 2013: Vertical Eddy Fluxes in the Southern Ocean. *J. Phys. Oceanogr.*, **43**, 941–955, https://doi.org/10.1175/JPO-D-12-0178.1.